

DATING AND CHARACTERIZING LATE HOLOCENE
EARTHQUAKES USING PALEOMAGNETICS

Thesis by

Stephen Lowell Salyards

In Partial Fulfillment of the Requirements
for the Degree of
Doctor of Philosophy

California Institute of Technology
Pasadena, California

1989

(Submitted June 17, 1988)

© 1989

Stephen Lowel Salyards

All Rights Reserved

Acknowledgments

I have been fortunate to have received much assistance in my time at the California Institute of Technology and it is a pleasant responsibility to recognize this help.

First, I thank Kerry Sieh and Joseph Kirschvink for their guidance, suggestions, flexibility, knowledge and insight and that occasional push to get me going. I also thank them for their time and patience in critically reading this thesis. Their effort made this thesis a better product.

I also thank Clarence Allen and Robert Clayton, both for reviewing this thesis and serving on the examination committee and for advice and guidance while I have been at Caltech.

Paleomagnetic sampling is more efficient when sampling is done by a team, and so I have the pleasure of thanking numerous people who have helped with sample collection. By far my greatest thanks goes to Charles Budney who assisted me in collecting over 200 samples on several collecting trips. Robin Chang also helped me on multiple collecting trips. I received additional assistance from Michael Gardish, Heidi Houston, Eme Burt, Janice Peters, Catie Helm, Joe Kirschvink, Mark Fahnestock, Jim Conca, Norm Brown, Harold Magistrale, Scott King, Joanne Salyards, Diane Donovan and Carol Prentice. In addition, I thank Kerry and

Carol for helping with surveying.

I also appreciate the help of Kenneth Verosub, at U.C. Davis, in supplying me with a listing of the Fish Lake data and the help of Richard Hoblitt, at the U.S.G.S. C.V.O, in sharing his data from Mt. St. Helens.

Science does not happen in a vacuum, and I had the pleasure of interacting with many who stimulated my thinking. I appreciate the discussions, ideas, and suggestions from Rob Ripperdan, Robin Chang and Janet Boley and for their and Joe's work in keeping the paleomagnetism lab operating. In matters theoretical, and involving finite element calculations, I thank Leslie Sonders, Craig Jones and Scott King. Leslie and Craig have kept me honest and Scott has helped tremendously with the nitty-gritty of the finite element calculations. They have answered my dumb questions with a straight face.

Many others have contributed to my time at the Seismological Laboratory. My classmates provided the most valuable support network and I thank John Louie, Ann Mori, Dave Scott, and Richard Stead for this. In addition, all of the office personal, Dee, Nancy, Janet, Sue, Amy, Ann and Ann have always been ready to help when I needed it.

Outside of Caltech have been many others that were understanding about my time commitments and helped keep me sane. I thank all of you, but in particular I thank Roger Anderson. For me, he has fulfilled his objective of not letting school drive me completely crazy. In addition, I

thank all of the other students that I have been in Bible studies with and all of my family at Knox Presbyterian Church, especially the Young Adults group. They have all helped me keep my sights on the real objective. A.M.G.D.

Finally, and most importantly, I thank my family for all of their love and support. My parents, Lowell and Margaret Salyards were understanding and the support did not go unnoticed. My grandparents, Francis and Ilda Lord, probably first inspired me to attend Caltech and their love and words of wisdom are appreciated. And finally, I thank my wife Joanne. In addition to the help with sample collection, data measurement and the fine work she put in helping me to complete this thesis, I thank her for her love, understanding, patience, and support.

In addition, I am indebted to all who have supported this research and my tenure at Caltech. Fellowship support from a National Science Foundation Graduate Fellowship and the Beno Gutenberg Fellowship from the Seismological Laboratory allowed me to branch off in this unlikely direction. These awards allowed me freedom to work on the ideas which led to this thesis. This work was supported by the following grants: U.S.G.S.- 14-08-0001-G1086, 14-08-0001-G1370, 14-08-0001-G1184, 14-08-0001-21980, 14-08-0001-21981, 14-08-0001-21854, 14-08-0001-21210, and NSF ERA-8351370, ERA-8121377.

Abstract

In this thesis I apply paleomagnetic techniques to paleoseismological problems. I investigate the use of secular-variation magnetostratigraphy to date prehistoric earthquakes; I identify liquefaction remanent magnetization (LRM), and I quantify coseismic deformation within a fault zone by measuring the rotation of paleomagnetic vectors.

In Chapter 2 I construct a secular-variation reference curve for southern California. For this curve I measure three new well-constrained paleomagnetic directions: two from the Pallett Creek paleoseismological site at A.D. 1397-1480 and A.D. 1465-1495, and one from Panum Crater at A.D. 1325-1365. To these three directions I add the best nine data points from the Sternberg secular-variation curve, five data points from Champion, and one point from the A.D. 1480 eruption of Mt. St. Helens. I derive the error due to the non-dipole field that is added to these data by the geographical correction to southern California. Combining these yields a secular variation curve for southern California covering the period A.D. 670 to 1910, with the best coverage in the range A.D. 1064 to 1505.

In Chapter 3 I apply this curve to a problem in southern California. Two paleoseismological sites in the

Salton trough of southern California have sediments deposited by prehistoric Lake Cahuilla. At the Salt Creek site I sampled sediments from three different lakes, and at the Indio site I sampled sediments from four different lakes. Based upon the coinciding paleomagnetic directions I correlate the oldest lake sampled at Salt Creek with the oldest lake sampled at Indio. Furthermore, the penultimate lake at Indio does not appear to be present at Salt Creek. Using the secular variation curve I can assign the lakes at Salt Creek to broad age ranges of A.D. 800 to 1100, A.D. 1100 to 1300, and A.D. 1300 to 1500. This example demonstrates the large uncertainties in the secular-variation curve and the need to construct curves from a limited geographical area.

Chapter 4 demonstrates that seismically induced liquefaction can cause resetting of detrital remanent magnetization and acquisition of a liquefaction remanent magnetization (LRM). I sampled three different liquefaction features, a sandbody formed in the Elsinore fault zone, diapirs from sediments of Mono Lake, and a sandblow in these same sediments. In every case the liquefaction features showed stable magnetization despite substantial physical disruption. In addition, in the case of the sandblow and the sandbody, the intensity of the natural remanent magnetization increased by up to an order of magnitude.

In Chapter 5 I apply paleomagnetism to measuring the tectonic rotations in a 52 meter long transect across the

San Andreas fault zone at the Pallett Creek paleoseismological site. This site has presented a significant problem because the brittle long-term average slip-rate across the fault is significantly less than the slip-rate from other nearby sites. I find sections adjacent to the fault with tectonic rotations of up to 30° . If interpreted as block rotations, the non-brittle offset was 14.0 ± 2.8 , -2.1 meters in the last three earthquakes and 8.5 ± 1.0 , -0.9 meters in the last two. Combined with the brittle offset in these events, the last three events all had about 6 meters of total fault offset, even though the intervals between them were markedly different.

In Appendix 1 I present a detailed description of my standard sampling and demagnetization procedure.

In Appendix 2 I present a detailed discussion of the study at Panum Crater that yielded the well-constrained paleomagnetic direction for use in developing secular variation curve in Chapter 2. In addition, from sampling two distinctly different clast types in a block-and-ash flow deposit from Panum Crater, I find that this flow had a complex emplacement and cooling history. Angular, glassy "lithic" blocks were emplaced at temperatures above 600° C. Some of these had cooled nearly completely, whereas others had cooled only to 450° C, when settling in the flow rotated the blocks slightly. The partially cooled blocks then finished cooling without further settling. Highly vesicular, breadcrusted pumiceous clasts had not yet cooled

to 600°C at the time of these rotations, because they show a stable, well clustered, unidirectional magnetic vector.

Table of Contents

	Page
Acknowledgments	iii
Abstract	vi
List of Illustrations	xii
List of Tables	xv
Chapter 1: Introduction	1
Chapter 2 - A Secular Variation Reference Curve for Southern California	4
Abstract	4
Introduction	5
The DuBois Curve	8
The Sternberg Curve	10
The Fish Lake, Oregon, Curve	14
Individual Sites	19
Panum Crater	19
Pallett Creek	22
Sunset Crater	25
Mt. St. Helens	26
Construction of a SVC for southern California	27
Error in the dipole assumption	27
SV reference curve for so. Calif.	37
Discussion	39
Chapter 3 - Paleomagnetic Correlation and Dating of the Prehistoric Sediments of Lake Cahuilla and Measurement of Their Tectonic Rotation	43
Abstract	43
Introduction	43
Sample Collection	46
Correlation and magnetostratigraphy	51
Measurement of tectonic rotations	67
Chapter 4 - Resetting of Detrital Remanent Magnetization by Liquefaction	74
Abstract	74
Introduction	75
Results from a liquefied sandbody on the Elsinore fault	76
Results from soft-sediment diapirs at Mono Lake	85
Results from sandblows	92
Discussion	94

	Page
Chapter 5 - Paleomagnetic Measurement of Non-brittle Deformation across the San Andreas Fault at Pallett Creek	100
Abstract	100
Introduction	101
Problems at Pallett Creek	104
Study site	106
Data collection	110
Results	117
Interpretation	143
Discussion	162
Implications	166
Summary	170
References	172
Appendix 1 - Collection, Preparation, and Measurement of Soft-Sediment Paleomagnetic Samples	181
Introduction	181
Sampling	181
Tools	181
Sampling procedure	183
Preparation	185
Measurement	187
Facilities	187
Demagnetization procedure	188
Interpretation	189
Orthogonal Vector Demagnetization Diagrams	190
Appendix 2 - Paleomagnetic Constraints on the Depositional and Thermal History of a Block-and-ash Flow from Panum Crater, California	192
Abstract	192
Introduction	193
Setting	194
The problem	198
Data collection and results	199
Discussion	209

List of Illustrations

	Page
Chapter 2	
Figure 1. DuBois SV Curve	9
2. Sternberg SV Curve	12
3. Index map of sample sites	15
4. Verosub and others SV Curve	16
5. Map of Panum Crater block-and-ash flow	21
6. Demagnetization diagram of pumice sample	23
7. Equal-area plot of pumice samples	24
8. Translation errors with longitude	31
9. Translation errors with latitude	33
10. Translation errors	35
11. Southern California Secular Variation Curve	38
12. Comparison of so. Calif. SVC with published SVC's	40
Chapter 3	
Figure 1. Index map of sample localities	45
2. Map of the Indio site	47
3. View of trench wall 16	49
4. Map of Salt Creek site	50
5. Demagnetization diagram of lake A sample	52
6. Equal-area plot of lake B samples	53
7. Demagnetization diagram of lake E sample	55
8. Equal-area plot of upper lake E samples	56
9. Equal-area plot of lower lake E samples	57
10. Equal-area plots of lakes 1, 2, and 3 samples	60
11. Equal-area plot of lakes 1, 2, and 3 with lake E	61
12. Equal-area plot of lakes 1, 2, and 3 with lake B	62
13. So. Calif. SVC with lake directions	64
14. So. Calif. SVC with inclination corrected lake directions	65
15. Map of Indio excavation 13	69
16. Demagnetization diagram of sample from excavation 13	70
17. Equal-area plot of sample groups showing tectonic rotations	73
Chapter 4	
Figure 1. Map of sample sites	77
2. Drawing of the Glen Ivy sandbody	79
3. Demagnetization diagrams of Glen Ivy samples	80
4. Equal-area plot of sandbody samples	82
5. Equal-area plot of sandbody and source bed samples	83
6. NRM Intensities of liquefied features and their source beds	84
7. Drawing of the Mono Lake diapirs	87
8. Demagnetization diagram of diapir sample	88

	Page
9. Equal-area plot of diapirs and their source bed	89
10. Equal-area plot of sandblow samples	95
11. So. Calif. SVC with liquefaction features	98
 Chapter 5	
Figure 1. Fence lines deformed in 1906 earthquake	103
2. Map of the Pallett Creek site showing fault geometry	105
3. Stratigraphic section at Pallett Creek	109
4. Map of surface breakage and location of samples	111
5. Demagnetization diagrams of typical samples	115
6. Map of the Fort Ross fence deformed in the 1906 earthquake	118
7. Group declinations	122
8. Group directions with independent group errors	128
9. Group directions with mean centered errors	133
10. Detail of group declinations near control group	137
11. Group rotations	139
12. Diagrams of modes of deformation	144
13. Cumulative non-brittle offset calculated using block rotations	147
14. Diagram of finite-element grid	151
15. Finite-element calculation of simple shear deformation	153
16. Finite-element calculation of different fault geometries	155
17. Finite-element calculation using boundary conditions	159
18. Pallett Creek total cumulative offset	164
19. Diagram of possible reasons for deformation distribution	168
 Appendix 2	
Figure 1. Map of Mono and Inyo Craters	195
2. Map of Panum Crater block-and-ash flow	196
3. Demagnetization diagram of pumice sample	200
4. Equal-area plot of pumice samples	201
5. Demagnetization diagram of lithic sample	202
6. Demagnetization diagrams of two-component lithic samples	204
7. Equal-area plot of one component lithic samples	205
8. Equal-area plots of two component lithic samples	206

	Page
9. Demagnetization diagrams of site 2 samples	208
10. Equal-area plots of site 2 samples	210
11. Equal-area plots comparing group directions to pumice direction	213

List of Tables

	Page
Chapter 2	
Table 1. Data used from Sternberg	13
Chapter 3	
Table 1. Group mean directions from excavation 13	71
Chapter 4	
Table 1. Group mean directions of liquefaction features	85
Chapter 5	
Table 1. Group average declinations	120
2. Single block rotations	126
3. Block rotations	126
4. Independent group statistics	130
5. Rotations	141

Chapter 1

Introduction

Paleoseismologists are concerned with answering two basic questions about an earthquake: its date and the nature of its source. All of the chapters of this dissertation use paleomagnetism to address these two basic questions. This work demonstrates that paleomagnetism can be an important tool for resolving paleoseismic questions.

All of the paleoseismic applications of paleomagnetism that I discuss in this thesis have corresponding applications in traditional paleomagnetism. For example, my dating of young sediments by secular variation of the earth's magnetic field is analogous to dating older rocks by reversal magnetostratigraphy. The rotation of paleomagnetic directions during individual earthquakes is analogous to rotation of large blocks over millions of years.

The combination of secular variation magnetostratigraphy with the resetting of detrital remanent magnetization by liquefaction produces a method to date an earthquake, not just bracket the age with units above and below the earthquake horizon.

In Chapter 2 I present the basic technique of secular variation magnetostratigraphy and develop a secular variation reference curve for southern California. I have collected well-constrained data from both published and

unpublished sources, as well as my own measurements.

In Chapter 3, I apply magnetic field directions and secular variation magnetostratigraphy, using the curve I constructed in the preceding chapter, to make stratigraphic correlations between two paleoseismologic sites. In addition, sampling at one of the sites provides an opportunity to measure rotations due to deformation near a fault zone, a concept developed in a later chapter.

Chapter 4 discusses the resetting of detrital remanent magnetization by liquefaction. In each of three different types of liquefaction or soft-sediment deformation there is good evidence of a Liquefaction Remanent Magnetization (LRM). This chapter closes with the observation that using an LRM direction to date an earthquake is problematical because of the deformation near a fault zone.

Non-brittle deformation across a fault zone is investigated in Chapter 5. Detailed sampling across the San Andreas fault zone at the Pallett Creek paleoseismological site enables measurement of the rotation of young sediments during the last three earthquakes.

The chapters are written to be as independent as possible. Even so, development of data and ideas in some chapters are dependent on data and concepts present in other chapters. This dependence dictated the order of the chapters.

Appendix 1 details the standard steps involved in acquisition, preparation, processing and interpretation of

the samples. This is included as an appendix for two reasons. First, all the samples used in the main part of this thesis were handled in a similar manner, so the details need be discussed only once. Second, this work represents the collection and processing of one of the largest sets of soft-sediment samples ever collected, and I have gained much experience and insight that can benefit others using these techniques.

Appendix 2 presents a detailed discussion of the paleomagnetic study of a pyroclastic flow deposit near Panum Crater. In addition to the well-constrained magnetic field direction that I use in Chapter 2, I also obtain constraints on the thermal and depositional history of this block-and-ash flow from Panum Crater.

All of these chapters show the usefulness, and limitations, of paleomagnetism as a paleoseismological tool. Paleomagnetism has the ability to address questions important in paleoseismology and may be most useful in mapping non-brittle deformation. In the area of secular variation magnetostratigraphy, the reference curve will require refinement but shows potential as a dating tool. This thesis represents the introduction of these techniques to paleoseismology.

Chapter 2

A Secular Variation Reference Curve for Southern California**Abstract**

Secular variation of the earth's magnetic field provides a paleomagnetic dating technique that is used in a manner similar to reversal magnetostratigraphy. Like reversal magnetostratigraphy, a reference time scale is needed to be able to date materials. I use well-dated, well-constrained magnetic directions to construct a secular variation curve for southern California for the last 1400 years. For this curve I use 9 archeomagnetic directions from the southwestern United States (Sternberg, 1982), 5 paleomagnetic directions from the Sunset Crater volcanic field (Champion, 1980), the direction of the Mt. St. Helens eruption beginning in 1480 (Hoblitt, pers. com.), and three well-dated directions I have measured in southern California. Because the earth's magnetic field is not a dipole, and prehistoric non-dipole components of the field are not known, error is introduced by translating the magnetic field direction measured at one geographic site to the direction that existed contemporaneously at another. I find the magnitude of this error, based on the current magnetic field, for translation in latitude and longitude. From these data, and utilizing these constraints on the

errors, I construct a secular variation curve for southern California. Other published SV curves for the western United States are consistent with my curve, and I show that differences between the other curves are within the error of the measurements.

Introduction

Magnetostratigraphy using the magnetic-polarity time scale is a well-established method of paleomagnetic dating. In this technique a measured pattern of rock magnetic polarities is matched to a known reference pattern of polarity reversals to determine the age of the rocks. This method requires a preliminary estimate of the age of the section by paleontologic or isotopic dating. Because the geomagnetic field reverses every million years or so, on the average, the magnetic polarity scale is most useful for resolving dates to within 10^5 to 10^6 years.

Secular variation of the earth's magnetic field represents a shorter-term variation of magnetostratigraphy, with periods on the order of a few thousand years. It therefore has a maximum potential value in geochronology for resolving the ages of deposits to within a few decades or centuries.

Resolution of ages with this precision is a particularly attractive goal to scientists interested in understanding earthquakes, volcanic eruptions and other

surficial geologic processes that occur every few hundred to thousands of years. My goal in this chapter is to construct a secular variation curve for southern California that will be useful for dating local geological events of the past two millennia.

Two approaches to determining the secular variation of the earth's magnetic field are commonly employed. One technique is the sampling of a sedimentary section to obtain a continuous record of the secular variation. This method usually suffers from poor time control on individual layers in the section, sediment magnetic instability and indeterminate core orientation. The second approach uses directions of magnetically stable samples from well-dated localities. Although the age and magnetic values are well-controlled, problems exist because of the geographic scatter of sampling localities and the lack of a continuous record. In spite of these problems the latter approach still provides the best-constrained data and is the technique I will depend on most in this chapter.

The disadvantages of each of these approaches illustrate the types of problems that are inherent in this work. The most basic requirement is for magnetically stable material. Fire hearths from archaeological sites and volcanic flows have the greatest potential since they acquire a thermal remanent magnetization (TRM). Generally sediments also produce satisfactory results, but their detrital remanent magnetization is a weaker form of

magnetization and any chemical overprints can contribute to instability.

A second problem with constructing a secular variation curve is obtaining good temporal coverage and control. Sedimentary sections that contain no hiatuses provide the best opportunity to obtain a continuous record, but magnetic stability and good age control are the drawbacks. When sampling different sites, the lack of data in a particular age range will produce a gap in the curve. Even worse, if the ages of the sites are not well constrained the temporal order of the samples may not be known. This problem is compounded when datable material is sparse and dates on the material are imprecise.

A third problem is due to slight irregularities in the shape of the earth's magnetic field. Although it is best approximated by a dipole, non-dipole irregularities result in different apparent magnetic poles or virtual geomagnetic poles (VGP) for individual sites. The main implication of this is that a secular variation curve determined at one locality will not precisely match that determined at another. This error increases with distance between sites, so it is best to calibrate the curve with data from near the area of interest.

To eliminate all of these problems the ideal locality to sample for a secular variation study would be a single small volcanic field with eruptive flows every decade. Unfortunately, these are at best rare, and probably non-

existent. Therefore, the two approaches described above try to use the advantages of each approach while minimizing the problems.

Attempts to establish secular variation curves are numerous. They include the efforts of Wolfman (1979), Lund and Banerjee (1979, 1985), Creer and Tucholka (1982).

Three curves have been constructed for the western United States. These curves by DuBois (1974), Sternberg (1982, 1983) and Verosub and others (1986) span roughly the past 1,500 to 13,000 years. Major features of each curve agree with the others (Sternberg, 1983, Verosub and Mehringer, 1984, Verosub and others, 1986). In addition to these curves, several sites have provided dated, stable magnetic directions for individual rock units and strata that can be used to construct a curve for southern California.

In this chapter I will evaluate the available data and supplement them with a few new observations to construct a reference curve for use in the other chapters of this thesis. The objective is to derive one reference curve with the greatest temporal and directional control.

The DuBois Curve

The first southwestern U.S. magnetic reference curve was published by R. L. DuBois (1974) (figure 1). This curve is based on measurements from 157 archaeomagnetic features, such as hearths, from archaeological sites throughout Arizona,

Dubois SV Curve

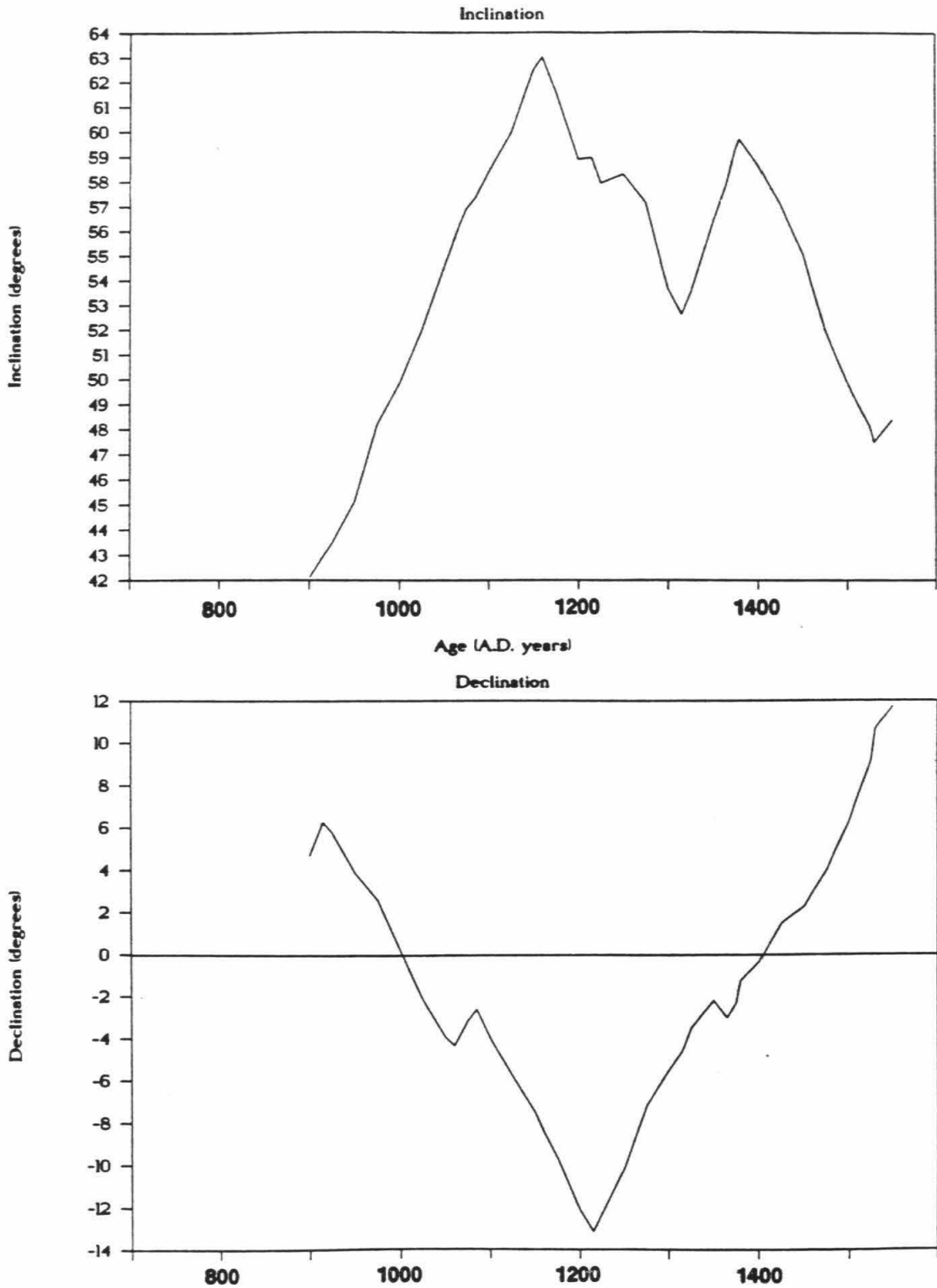


Figure 1
Secular variation (SV) curve from DuBois (1974). No data points of confidence limits were published.

New Mexico and southern Colorado.

Hearths are good paleomagnetic targets since their magnetization is usually a strong and stable thermal remanent magnetization (TRM). Furthermore, the dates of construction of these archaeological sites are often well-constrained by dendrochronologic dating of the wood used in the construction of the associated dwelling structures.

Figure 1 shows Dubois' declination and inclination curves derived from these data. Unfortunately, evaluation of DuBois's curve is difficult because only the curve, and not the ages of the sites that contributed to the curve, nor the paleomagnetic directions and uncertainties, was published. The Dubois curve is, therefore, mainly of historical interest and can not be used to assemble a reference curve for southern California.

The Sternberg Curve

Sternberg's (1982, 1983) archaeomagnetic secular variation curve is the best-documented curve for the southwestern United States. Sternberg has age and directional paleomagnetic data from 85 archaeological features at 26 sites. Most of these directions are from hearths, but a few burned walls are included in his data.

The most significant problem in archeomagnetic work is constraining the age of the hearth sampled. As mentioned before, dating the construction and beginning of inhabitation of a site is commonly accomplished by

dendrochronology. However, the magnetic direction of the hearth is acquired the last time it was heated, so for sites with a long or unknown length of habitation this could lead to large uncertainties in the age of the magnetization. Sternberg interpreted this to be the cause of the large spread in some of his age data.

To compensate for these uncertainties, and to allow use of all of his data, Sternberg (1983) applied a high-frequency moving-average filter to his data to produce his secular variation curve. This smoothing technique weighted each data point by the inverse of its error in both age and direction (see Sternberg, 1983, for a detailed description). Therefore, a direction with a large directional uncertainty was weighted less than a well-constrained direction. Likewise, a sample with a large age span might be included in several windows, but weighted less than a sample completely within the time window. His preferred smoothed SV curve is shown in figure 2 with the assigned uncertainties. The advantage to this method is that all the data are used in proportion to their reliability in both time and space. The disadvantage is that, in the process of smoothing, the best points are contaminated somewhat by the less certain points.

For my purposes, I chose to use only the best constrained of Sternberg's (1982) data (table 1). My criteria are that the data point must have a paleomagnetic uncertainty of no more than 5 degrees and a range in

STERNBERG SV CURVE

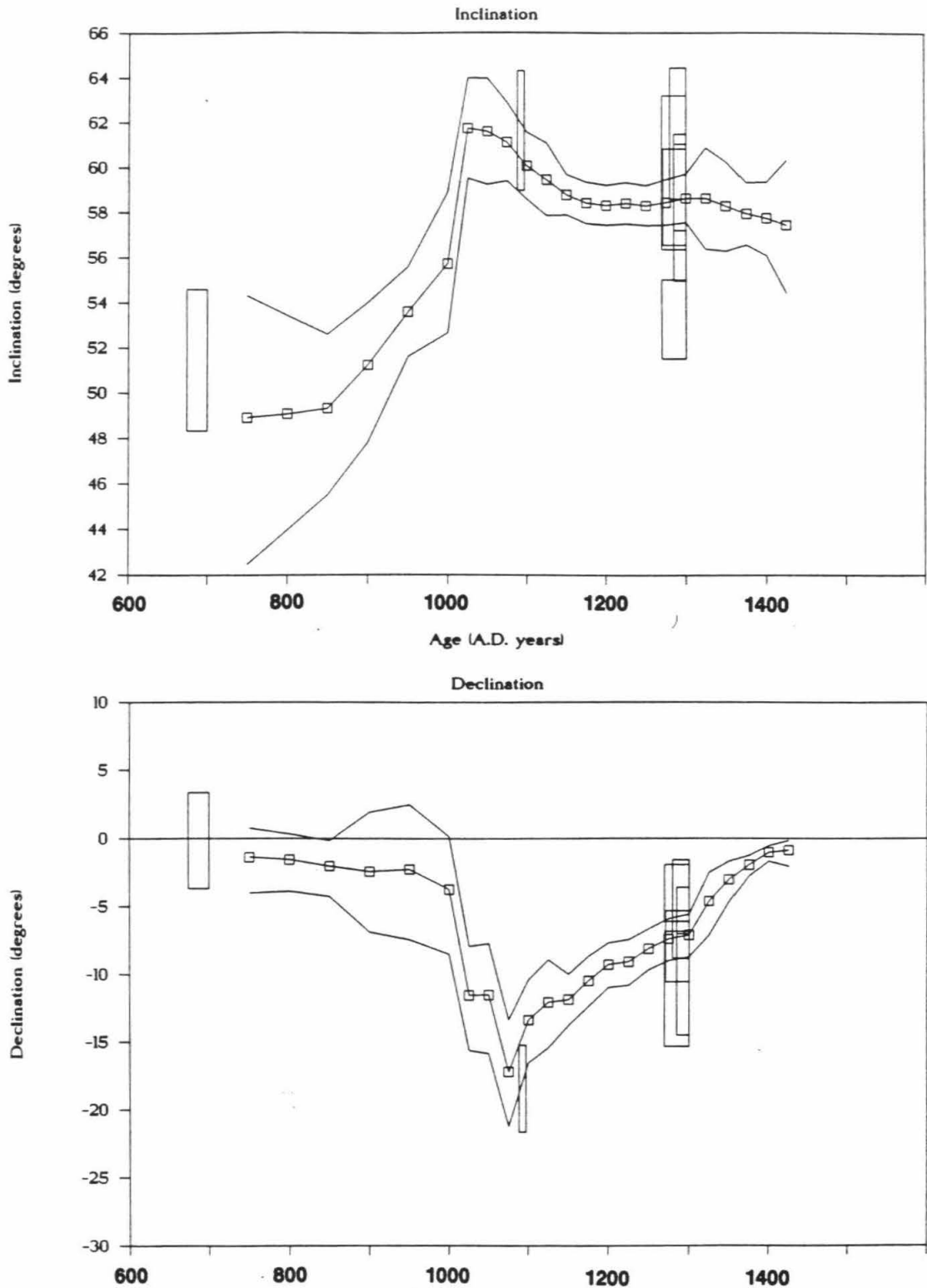


Figure 2

Secular variation (SV) curve from Sternberg (1982) for the southwestern U.S. Points are smoothed data points, adjacent lines are alpha-95 confidence limits, and boxes are the best constrained data used in constructing the SV curve in this chapter.

Table 1
Data Used from Sternberg (1982)

Age Range (A.D.)	Dec.	Inc.	alpha-95	kappa
1271-1300	351.32	58.76	2.3	490
1285-1300	352.94	59.53	2.3	516
1285-1300	348.59	57.86	3.3	288
1270-1300	348.39	59.6	3.7	269
1270-1300	355.91	53.66	1.9	811
1280-1300	352.78	64.12	3	402
674-700	0.04	55.44	3.2	259
1906-1910	11.84	54.8	4.1	158
1088-1097	340.25	62.04	2.8	404

plausible ages of no more than 40 years. In figure 2 these best data points are plotted on Sternberg's smoothed curve and the points lie along along the curve.

The Fish Lake, Oregon, Curve

The best source of a continuous secular variation curve is from a lacustrine sedimentary sequence with a high sedimentation rate. In the western U.S., Verosub and others (1986) utilized seven sediment cores from Fish Lake, Steens Mountain, Oregon, (figure 3) to produce a secular variation curve for the past 13,000 years (figure 4).

The advantage of their curve is its continuity. The disadvantages are poor age constraints, greater uncertainty in measurements of DRM, inclination error due to compaction, and declination errors due to the recovery of unoriented cores. The authors of this curve recognize all of these problems and address them with varying degrees of success.

Two difficulties hamper accurate assessment of the age of the magnetization. First, dendrochronologic dating is impossible, and organic material for radiocarbon dating is sparse. Second, the possibility exists that the paleomagnetic direction does not represent the local field at the time of deposition, because magnetic grains may be free to rotate until the sediment has dewatered. Therefore, the measured field may be the field at a time well after deposition of the sediment, when the water content is low enough to enable binding of the magnetic grains in the

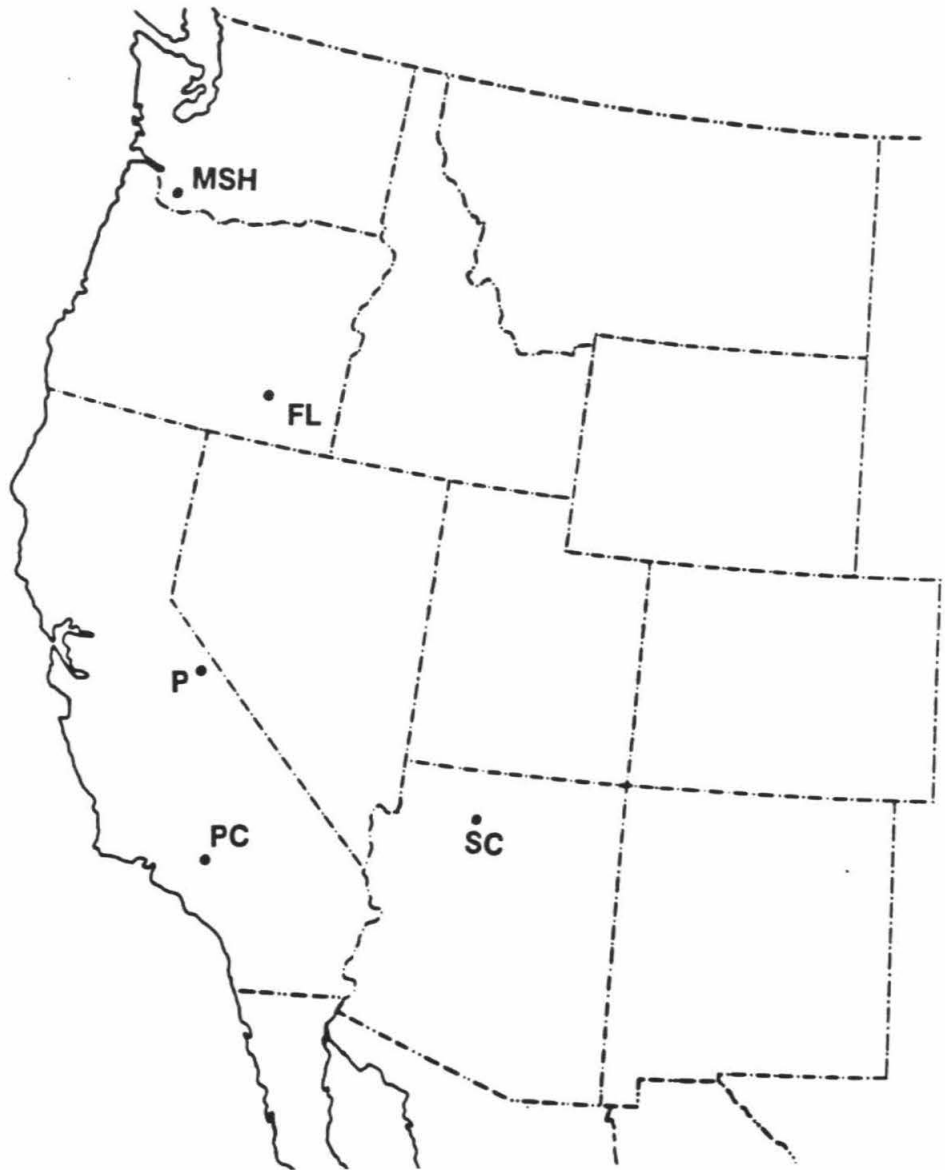


Figure 3

Index map of the western U.S. showing the locations of Fish Lake (FL), Oregon, Panum Crater (P), California, Pallett Creek (PC), California, Sunset Crater (SC), Arizona, and Mt. St. Helens (MSH), Washington.

Verosub and others SV Curve

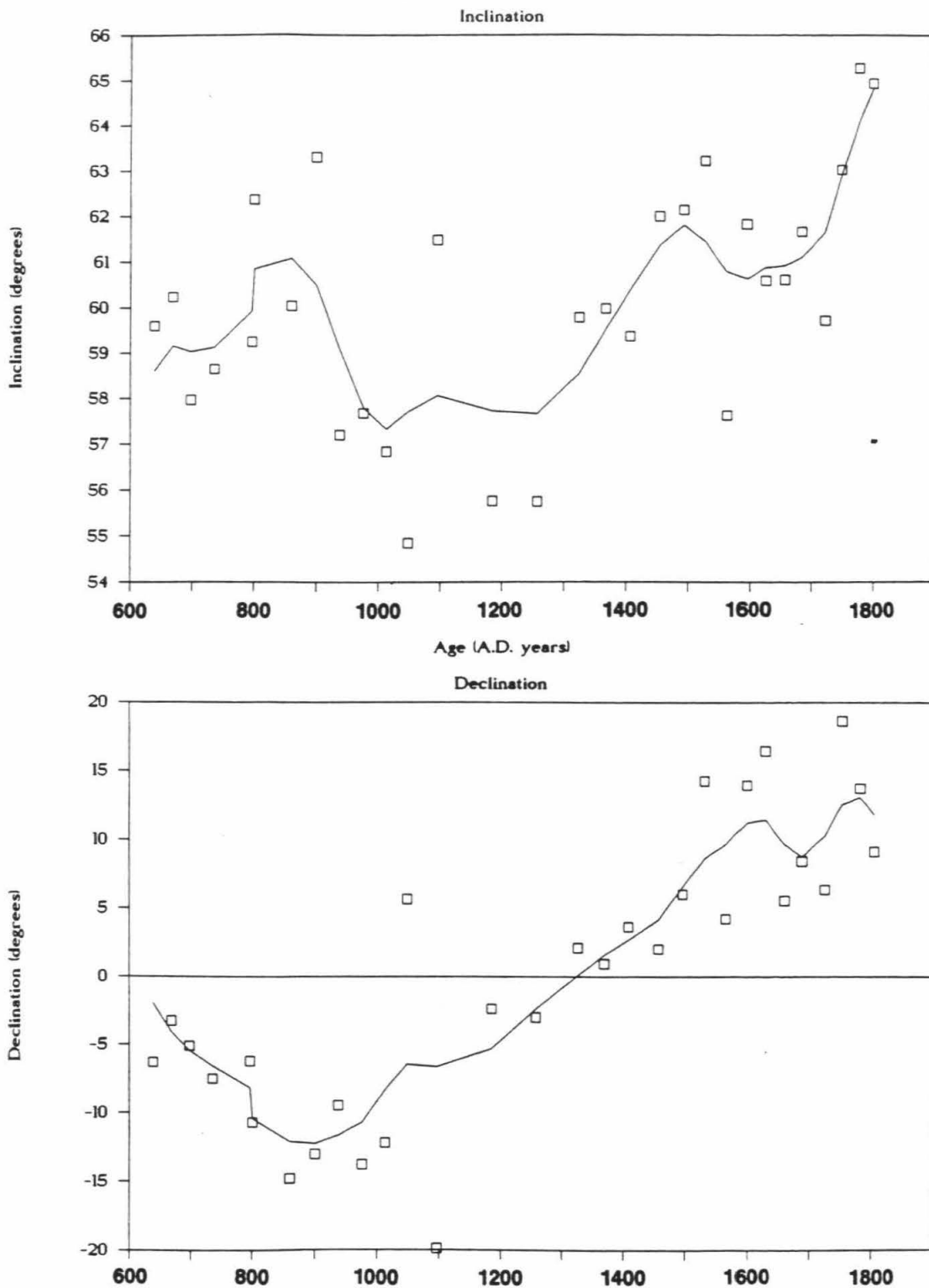


Figure 4

Secular variation (SV) curve from Verosub and others (1986) from Fish Lake, Oregon. Points are data from the sediment cores and the line is a seven point weighted average. Only the most recent 1300 years is shown.

sediment.

Radiocarbon dates constrain the age of the curve over its entire 13,000 year span, and the presence of the Mazama ash provides an additional constraint at about 7000 yrs B.P. However, the portion of the section of the most interest to us, that of the past 2000 years, is constrained by only two radiocarbon dates.

Verosub and others (1986) believe that the second potential source of error, post-depositional magnetization, is not significant. In earlier work Verosub (1977) found that, although sandy sediments were susceptible to a post-depositional remanent magnetization (pDRM), clay and silt showed a true depositional remanent magnetization (DRM). Since the Fish Lake sediments are clays and silts he argues convincingly that the magnetization should be a DRM.

Verosub and others only took one sample at each horizon in a core. Because there is no sample redundancy in a core there is no way to assign uncertainties to the measured directions. To constrain the accuracy of the measurements, Verosub and others processed the data and constructed tests to measure reliability. The cores are correlated using undated but correlable tephra layers to a correlation accuracy of 2 mm. The form of the magnetic signal compares well between the correlated cores. The absolute direction of the cores was established using the known field direction of the Mazama ash. This direction appears to have been accurate, because corrected directions of the most recent

sediments match historical field directions well.

Finally, to help reduce errors due to individual measurements, the magnetic field directions from the different cores are averaged together and this composite curve is smoothed using a seven-point, weighted, averaging function (figure 4). The time span between samples is about 40 years so the seven points average 240 years with the greatest weight on the center point.

Possibly the greatest disadvantage of using sediment cores to construct a secular variation curve is the possibility of inclination error in the sample measurements. The higher scatter of the inclination compared to the declination is most likely due to this error. Although Verosub and others addressed this issue, no reliable method of determining the magnitude of the inclination error is currently known. To try to eliminate the inclination error, a theoretical formulation which corrects all of the measurements by a constant was used (King, 1955).

Verosub and others have two points in their cores where they know the magnetic inclination. The inclination error differs at these two points so they used a constant that was the average of the constants at these two points.

The high scatter of the data points from Verosub and others and the uncertainties discussed above suggest that these data are not well-enough constrained to use in the secular variation curve. Therefore, the Verosub and others curve will be used for comparison only.

Individual Sites

Four individual sites provide additional well-constrained magnetic directions for inclusion in my secular variation curve. Two of these are sites I sampled, Panum Crater and Pallett Creek, and two are well dated volcanic eruptions from other workers, Sunset Crater and Mt. St. Helens.

Panum Crater

To add a well constrained field direction to the secular variation curve constructed later in this chapter, I sampled a block-and-ash-flow deposit from Panum Crater, Mono County, California (figure 3). The combination of the TRM direction and the well-constrained age of this eruption make this an ideal location to measure a direction for a secular variation curve. The details of this study and the conclusions related to the thermal history of the flow are described in detail in Appendix 2. In this section I briefly summarize the details related to the magnetic field direction information.

Panum crater lies at the north end of the Mono craters chain on the east side of the Sierra Nevada. This chain has erupted periodically through the Holocene with the last large eruption between A.D. 1325 and A.D. 1365 (Sieh and Bursik, 1986). The older constraint is the two-standard-deviation confidence limit on a radiocarbon date on organic

material charred by the erupted material. The younger age constraint is from dendrochronologic dating of Jeffrey pine trees growing on younger pyroclastic flows. Miller (1985) showed that these trees were growing on the younger flow by A.D. 1369.

The eruption of Panum crater succeeded all major activity from the main part of the Mono Craters chain (Sieh and Bursik, 1986). Panum crater produced a series of pyroclastic flows and tephra eruptions with a block-and-ash flow as an intermediate stage in the eruptive sequence. This block-and-ash flow probably formed when a predecessor of Panum dome at Panum Crater (figure 5) collapsed while in the process of enlarging and flowed to the northeast (figure 5). This flow is now exposed where streams have incised into it.

The flow is blocky at site 1, composed of blocks from 0.25 to 2 meters in diameter. Two distinct types of blocks are present: angular, grey, glassy lithic blocks and grey, highly vesicular, breadcrusted pumice. These latter clasts have lapilli size fragments of the lithic material embedded in their surfaces and occasionally are warped around the lithic blocks. Therefore, these breadcrusted blocks were soft, and hot, at the time of transport and probably when the flow came to rest.

In the field I drilled ten samples from the breadcrusted pumice blocks. These samples were demagnetized using the progressive AF and thermal steps described in

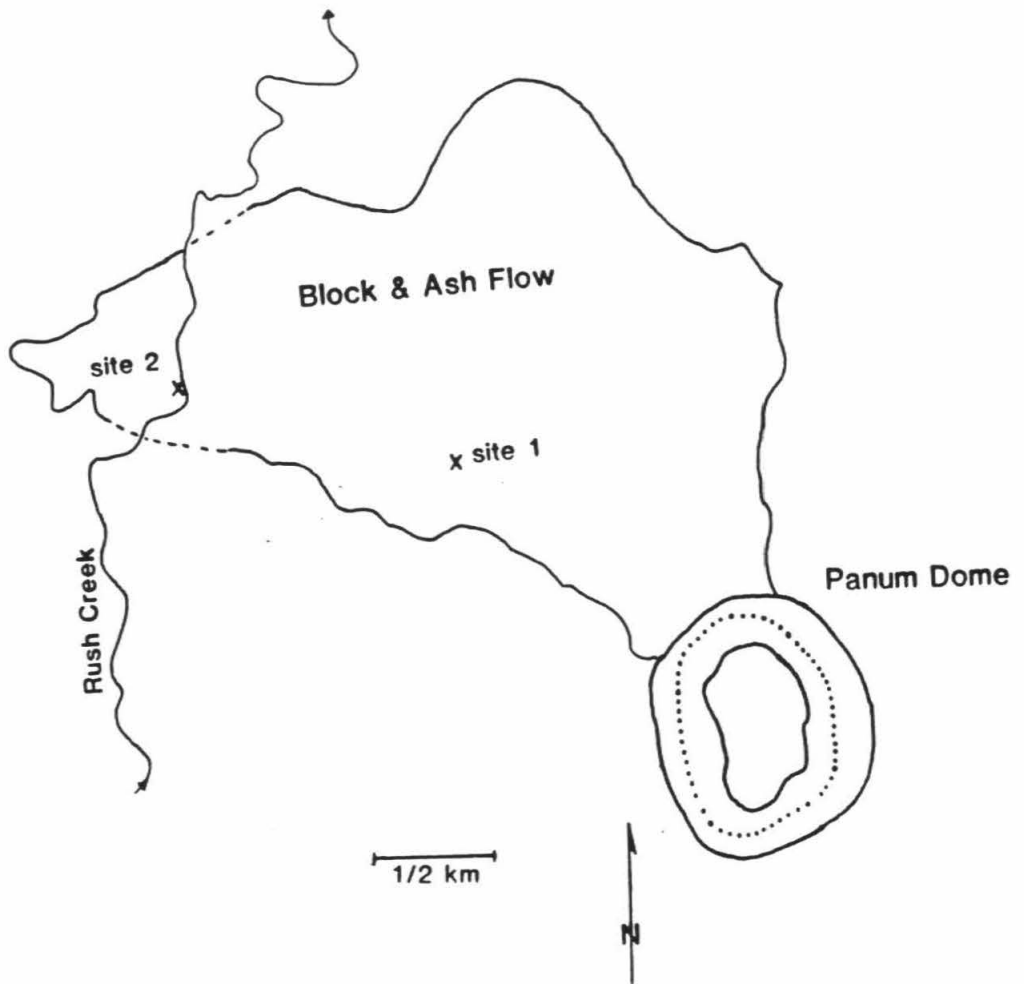


Figure 5

Map of Panum Crater and associated block-and-ash-flow. the sampling sites are marked. (adapted from Sieh and Bursik, 1986)

Appendix 1.

The pumiceous blocks showed the anticipated stable magnetization (figure 6) and six of the sample directions cluster very well with Bingham Kappas of -224.38 and -39.91 and alpha-95 errors of 2.5° and 6° (figure 7). Their direction of magnetization, $D=357.7^\circ$ and $I=61.2^\circ$ will be used in my secular variation curve as the field direction for the period 1325-1365 A.D.

Pallett Creek

The Pallett Creek paleoseismological site is located 55 km northeast of Los Angeles, California, on the San Andreas fault. At this site Sieh (1978, 1984) has excavated a 50-meter-long section of the fault to obtain information on the seismic history of the San Andreas. Sieh has found twelve earthquakes over the past 1800 years. Additional work (Sieh and others, in press) has decreased the errors on the radiocarbon ages of many of the units at Pallett Creek, with the result that the earthquake history is much better constrained.

Because the units are well-dated, this provides another opportunity to obtain a set of well-constrained paleomagnetic directions. There is concern that sediments near an active fault have been deformed and rotated. However, for reasons discussed in Chapter 5, I believe that the directions I present here are unrotated.

I took a group of ten samples from two different units

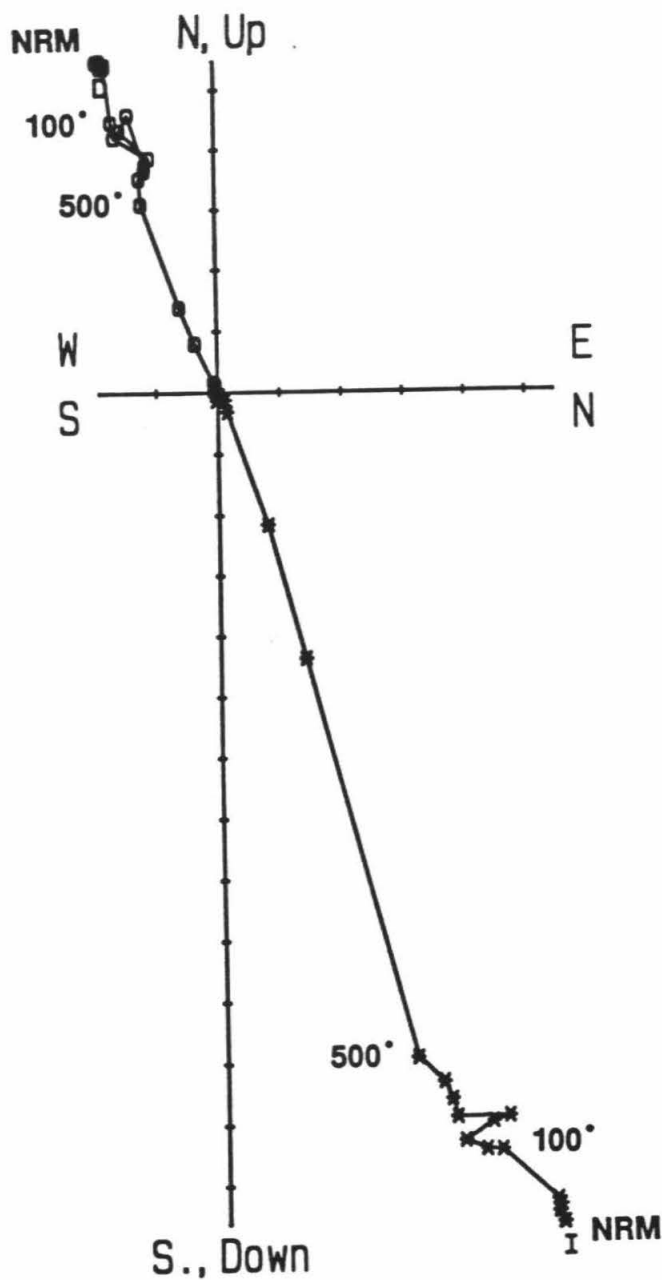


Figure 6

Orthogonal vector demagnetization diagram of a typical breadcrusted pumice sample. The very linear high-temperature demagnetization path shows the stable behavior of these samples. One unit on the axes is 10^{-4} emu. Circles are declination, x's are inclination. An explanation of orthogonal vector demagnetization diagrams is provided in the last section of Appendix 1.

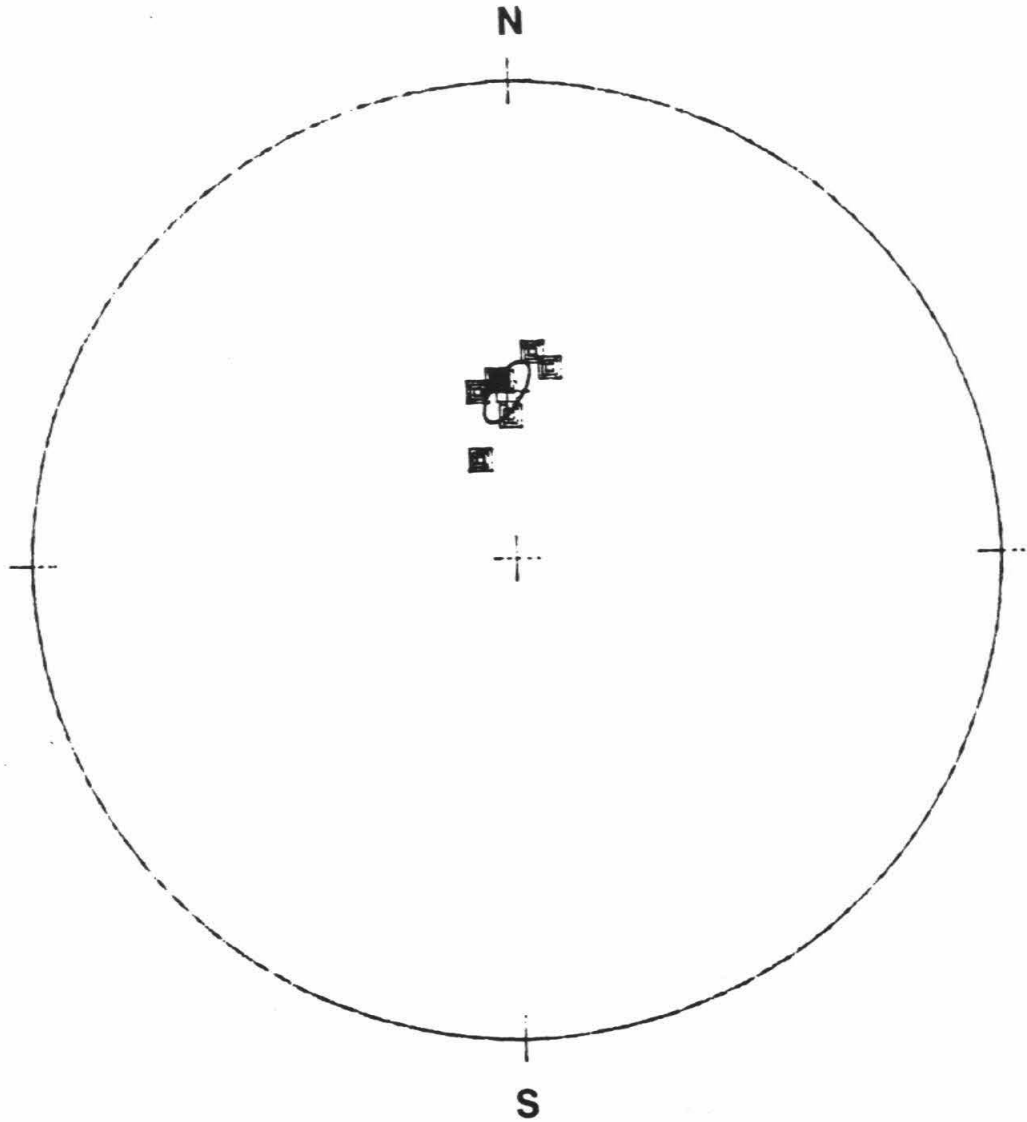


Figure 7

Equal-area plot of the sample directions for seven samples from the breadcrusted pumice with Bingham 95% confidence oval of the mean direction.

between 48 and 49 meters distance from the most recently active trace of the fault. Each of these units showed magnetic stability and the samples' directions cluster well. For middle unit 68, dated at between A.D. 1397 to 1480, the $\text{dec} = -0.65^\circ$, $\text{inc} = 55.1^\circ$ and $\text{alpha-95} = 3.4^\circ$, For unit 71, dated at A.D. 1465 to A.D. 1495 the $\text{dec} = -1.55^\circ$, the $\text{inc} = 60.4^\circ$, and the $\text{alpha-95} = 4.2^\circ$. I discuss these directions further in Chapter 5.

Sunset Crater

Another volcanic eruptive sequence with a well-constrained age is at the Sunset Crater volcanic field near Flagstaff, Arizona, which was studied paleomagnetically by Champion (1980). Dendrochronological studies of buried residences at nearby archaeological sites have shown that the eruption of Sunset crater began after the growing season of A.D. 1064 (Smiley, 1958); unfortunately the end of the eruptive sequence is unconstrained.

These eruptive units gave very tightly clustered magnetic directions. Furthermore, maximum age of these units is also very well-constrained. Champion found that the directions agreed very well with DuBois's SV curve and assigned ages to the flows based on this agreement. Holm and Moore (1987) report different ages for these units based on Champion's directions and their agreement with Sternberg's SV curve.

To use the ages of the units reported by Holm and Moore

in constructing my secular variation curve would be hazardous, because their dates are predicated on the curve of Sternberg. However, because the sequence of eruptive events is known (Holm and Moore, 1987), and because the date of initiation of the eruptive sequence is known to be A.D. 1064, these are still attractive data. The ages reported by Holm and Moore (1987) are consistent with the eruptive sequence. Therefore, I have taken the ages reported by Holm and Moore as reasonable minimum ages. This is consistent with the length of time Holm and Moore suggest the Sunset Crater eruption continued.

Mt. St. Helens

Another well-dated volcanic eruption in the western United States began in the winter of A.D. 1479-1480 at Mt. St. Helens, Washington (Yamaguchi, 1985). From dendrochronology, Yamaguchi (1983, 1985) has shown that the Wn tephra fell after the growing season of 1479 and that the We tephra fell two years later. These two extensive tephra layers mark the initiation of an eruption sequence that probably lasted about a century (Mullineaux and Crandell, 1981). This eruption sequence produced major tephra layers Wn, We, and T, which were dispersed to the north and east. It also produced a series of pyroclastic flows and lava flows that traveled to the southwest (Hoblitt, Crandell, and Mullineaux, 1980). Hoblitt and others (1980) found the only firm constraint on the end of the eruption sequence to be

trees on the last flows that were growing in A.D. 1665. Their estimate of a total eruption sequence of a century allows time for these trees to become established.

Hoblitt (personal communications) found a paleomagnetic direction for the early flows from the eruption beginning in A.D. 1480. The average direction for these flows is $\text{dec}=5$, $\text{inc}=58$, $\text{alpha-95}=1.0$. Hoblitt (personal communications) believes that these flows were erupted in no more than the first 25 years of activity. Many of these flows are bracketed by the Wn and We tephras and so are further constrained to the first two years of eruption. With the bracketed early flows weighting this average of multiple flows towards the initiation of activity in A.D. 1480, the 25-year age span appears reasonable.

Construction of a SVC for southern California

Error in the dipole assumption

The data discussed above provide the material for a secular variation curve. However, since the location of interest for the following chapters of this thesis is southern California and the data are mostly from other locations in the western U.S. the magnetic directions must be corrected to the magnetic direction for southern California. The simplest method would be to correct these data using a magnetic dipole for the earth's magnetic field. However, using this approach introduces additional error

into the magnetic field directions.

Although a dipole is a good first-order approximation, the present geomagnetic field has an appreciable non-dipole (quadrupole and higher) component. One must assume that the prehistoric field also contained a non-dipole component. Therefore, the non-dipole component must be accommodated in geographic corrections.

The best available method of making the geographic correction involves first assuming that the field is a dipole and calculating the virtual geomagnetic pole (VGP) for the site where the magnetic direction was measured. The VGP would be the location of the magnetic pole if the geomagnetic field were a pure dipole. Then, again assuming a dipole field, the VGP is used to calculate the orientation of the magnetic field at the desired location.

Both Champion (1980) and Sternberg (1982) calculated the uncertainty expected from the non-dipole correction. Champion selected six sites with different present geomagnetic field gradients. At each site he calculated the dipole field predicted by the magnetic field direction. From this, he determined how the angular difference between the dipole field and the actual field varied with latitude and longitude as distance from the site increased. Sternberg calculated the variation in the distances between VGP's using the same procedure but did not distinguish between the latitude and the longitude variations.

I have made my own assessment of the variation between

the predicted field and the true magnetic field. For reasons that will become apparent in Chapter 5, I have recalculated the error for declination and inclination independently.

I calculated the declination and inclination of the earth's magnetic field between latitudes 30° N and 50° N on a 5-degree grid using the International Geomagnetic Reference Field for 1985 (IGRF85). For each point I calculated the VGP, and from this I calculated the field direction 5, 10, and 15 degrees away in the four cardinal directions. Frequency distributions of the difference between the calculated field and the actual field were made for 5, 10, and 15 degrees difference in latitude and longitude (figures 8 and 9).

Estimation of confidence limits would be easier if the populations were normally distributed. However, a chi-squared test showed that none of the sample population distributions can be accepted as normally distributed at any reasonable confidence limit (>60%).

Because the sample sizes are large, particularly the longitude calculations, which have 720 data points in each distribution, I assume that the population is adequately sampled. This allows me to say that these sample distributions are very close to the actual population distributions. To get 95% of the variation of the error I determined the upper and lower 2.5%. The region representing 95% of the data falls between these limits (figure 10).

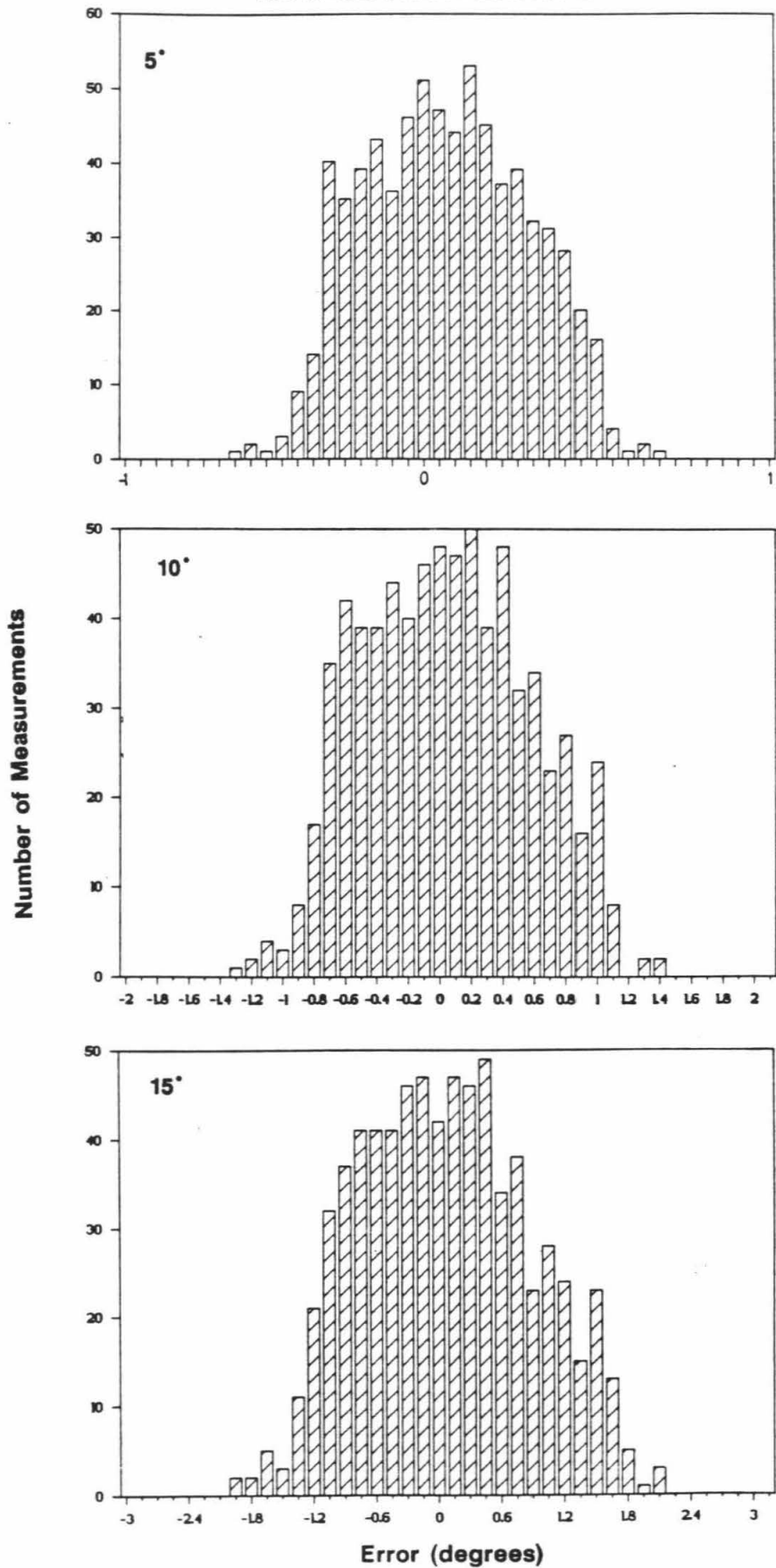
Figure 8

Histograms of translation error distributions for translation in longitude. (a) Error in the inclination. (b) error in the declination. Note that the x-axis, the error in degrees, scales with the translation distance.

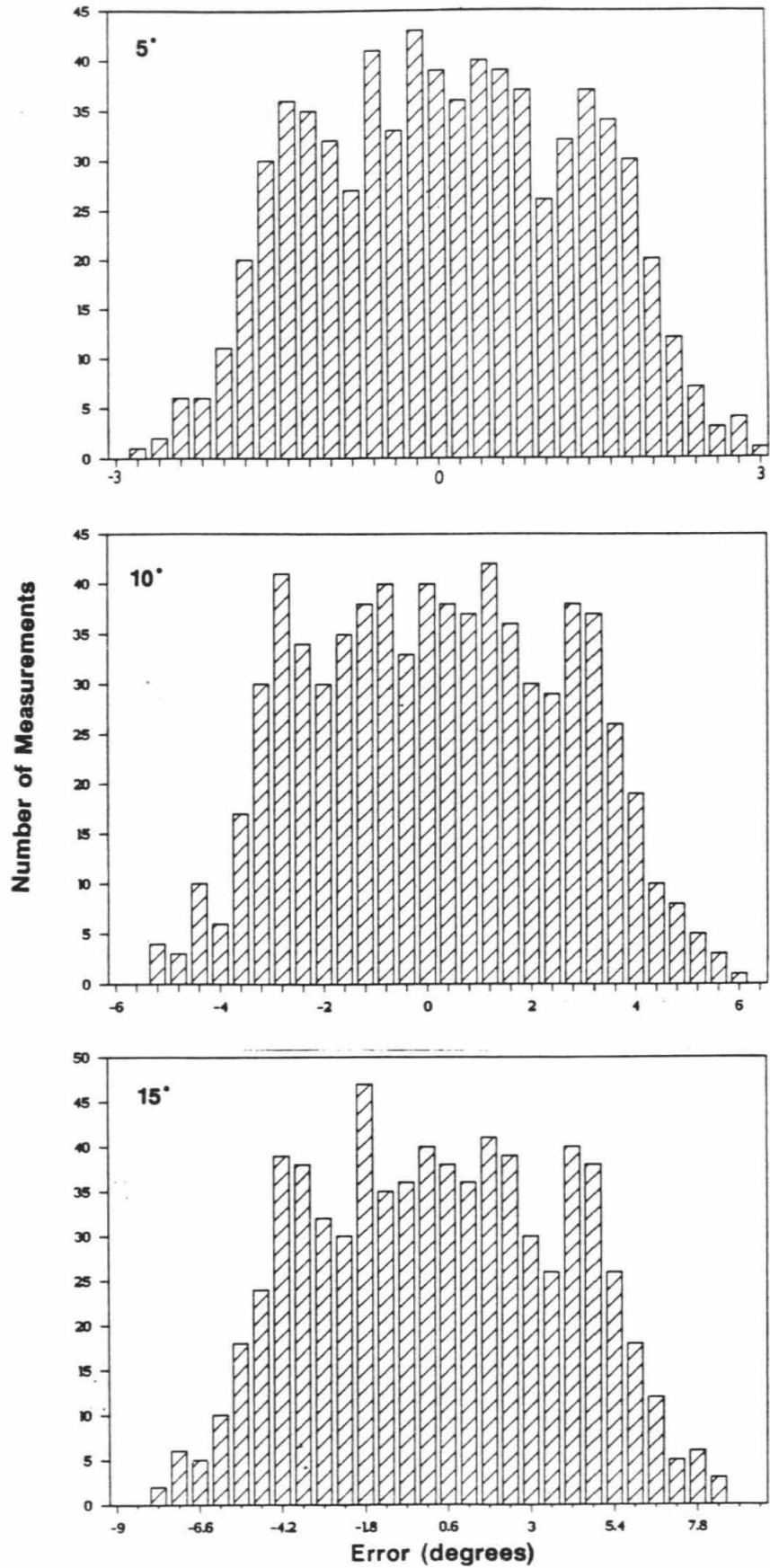
Figure 9

Histograms of translation error distributions for translation in latitude. (a) Error in the inclination. (b) error in the declination. Note that the x-axis, the error in degrees, scales with the translation distance.

8a TRANSLATION ERRORS

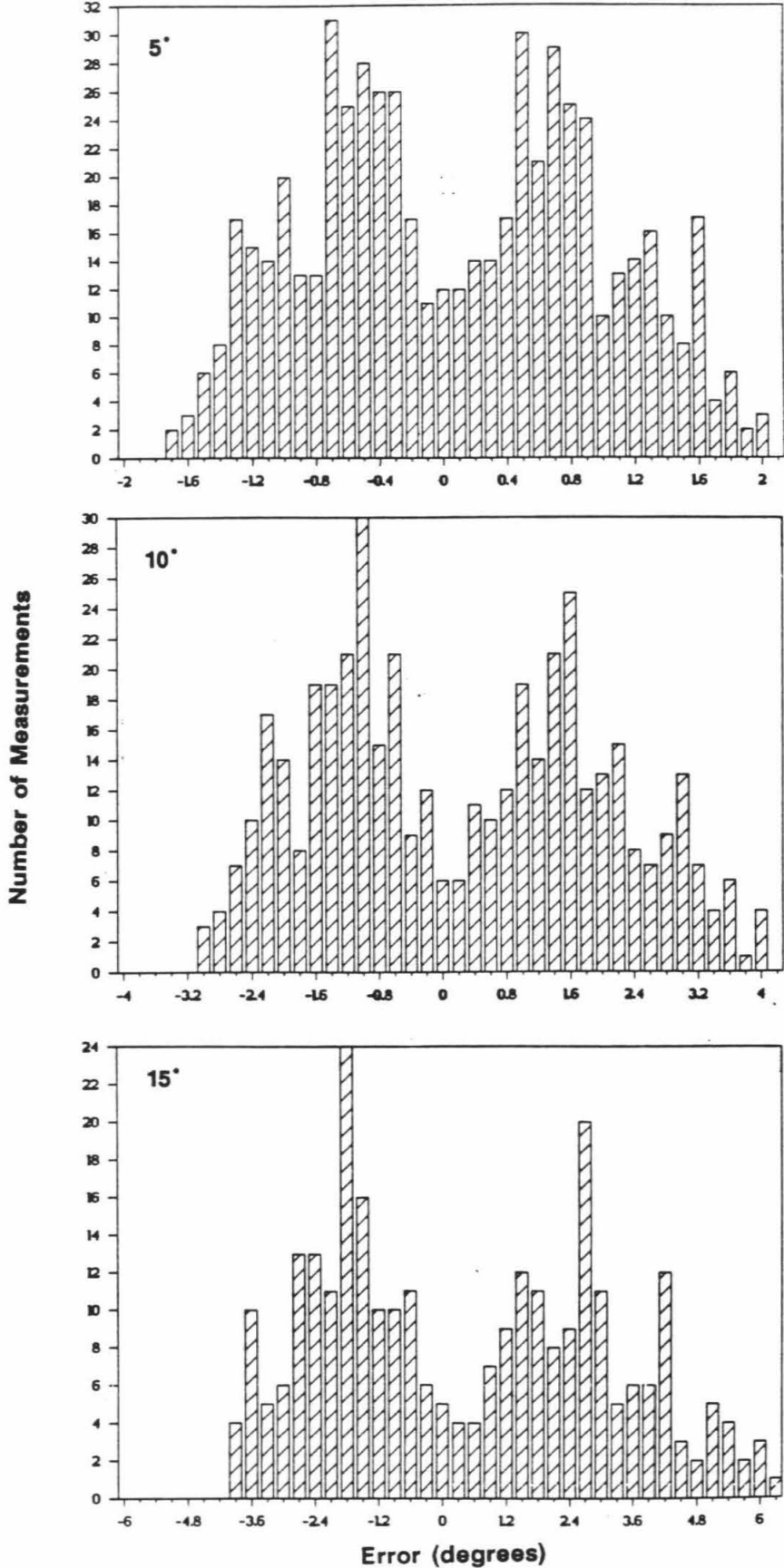


8b TRANSLATION ERRORS

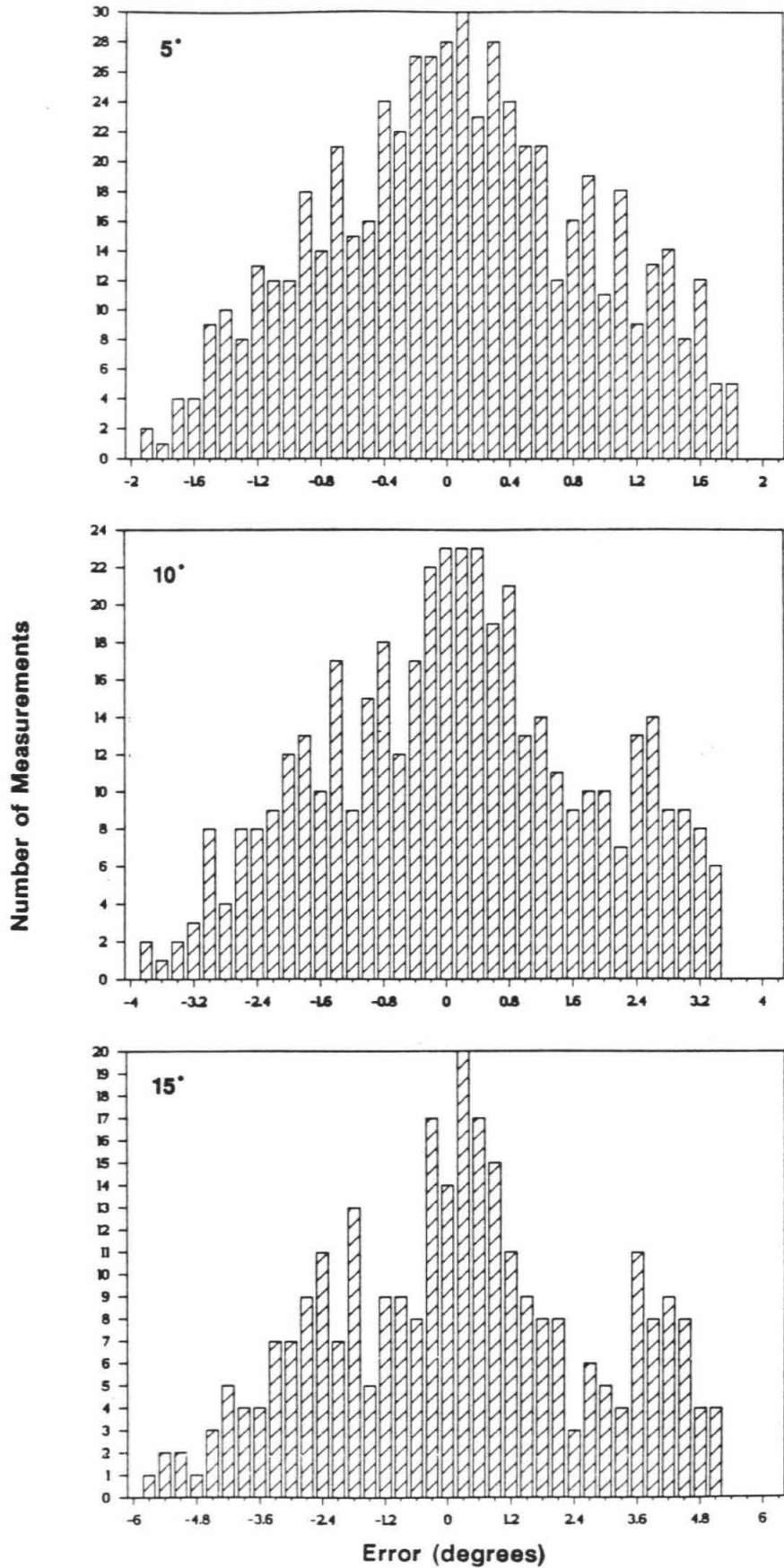


9a Translation Errors

INCLINATION-5 degrees lat-symmetric



9b Translation Errors



10a TRANSLATION ERRORS

Declination

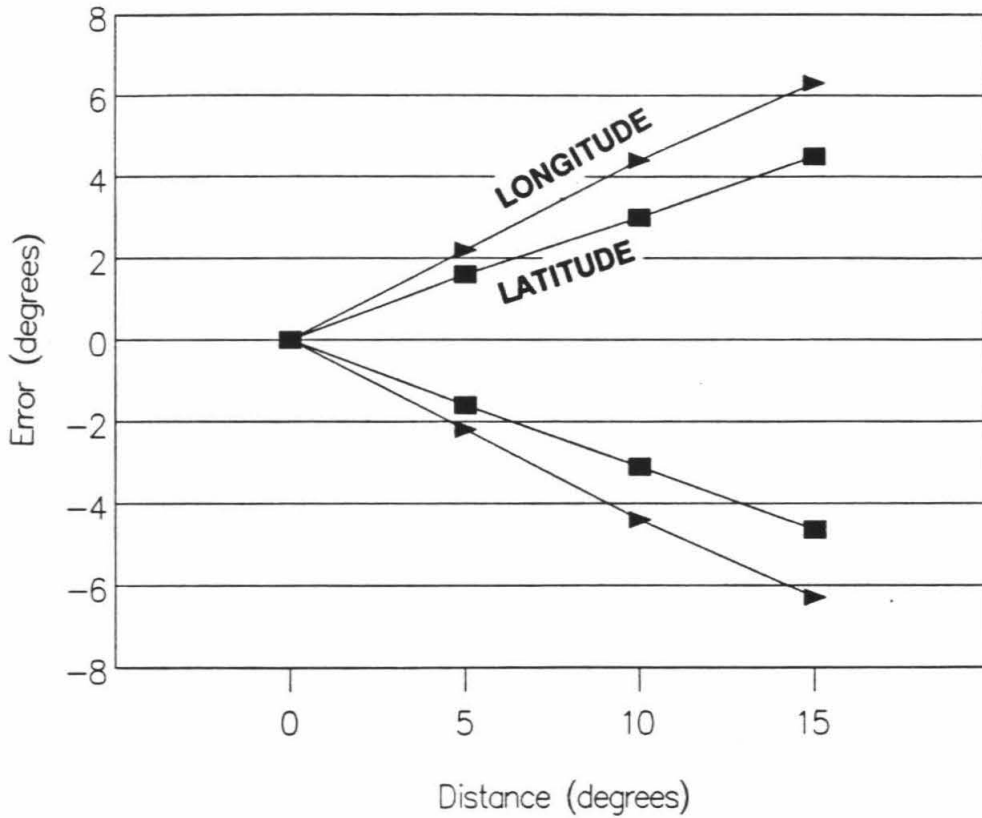
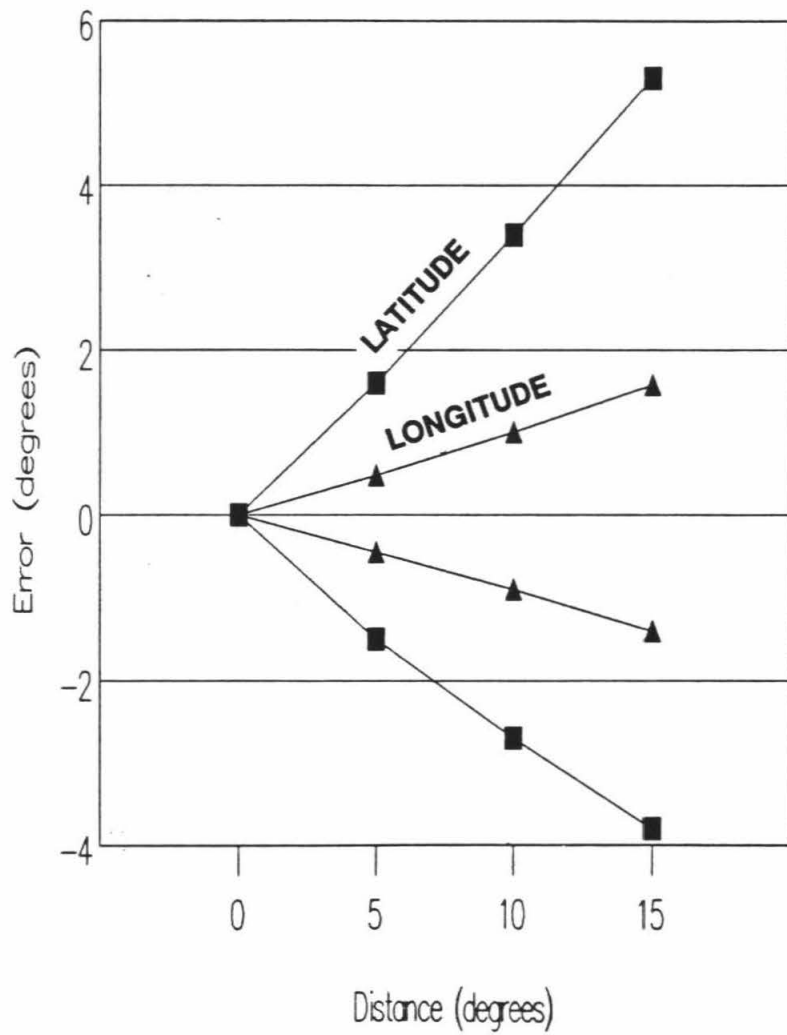


Figure 10
Translation errors for (a) declination and (b)
inclination for 95% of the data.

10b TRANSLATION ERRORS

Inclination



These values are used to place error bars on the directions that are transformed to a new site to construct the curve.

I will illustrate this procedure with one site. Since the Pallett Creek paleoseismological site will be of interest in Chapter 5, I will translate the directions to this locality. Pallett Creek is located at latitude 33.4° N, longitude 244.1° . The direction from Sunset Crater of $\text{dec}=-6.3^{\circ}$ and $\text{inc}=65.0^{\circ}$ with an $\alpha-95$ of 1.67° lies at latitude 35.4° N and longitude 248.6° . The VGP for this direction would be located at $77.2 \pm 1.5^{\circ}$ latitude and $227.3 \pm 8.8^{\circ}$ longitude. At Pallett Creek the dipole field with this magnetic pole would be oriented with $\text{dec}=-4.8 \pm 1.9^{\circ}$ and $\text{inc}=63.8 \pm 1.6^{\circ}$. Since the latitude difference between these two sites is 2° and the longitude difference is 4.5° , this means that the error in the geographic correction is 2.6° for the declination and $+1.1^{\circ}$ and -0.92° for the inclination. The final direction of the magnetic field at Pallett Creek as predicted by Sunset Crater is $\text{dec}=-4.8 \pm 4.5$ and $\text{inc}=63.89 \pm 2.7^{\circ}$.

SV Reference curve for southern California

I have compiled 18 well-dated paleomagnetic vectors from the western U.S. Figure 11 displays these values and serves as our SV reference curve for southern California. Declination and inclination changes are plotted separately rather than as a VGP plot in order to better see changes with time. The size of the box representing each data point

Southern California Secular Variation

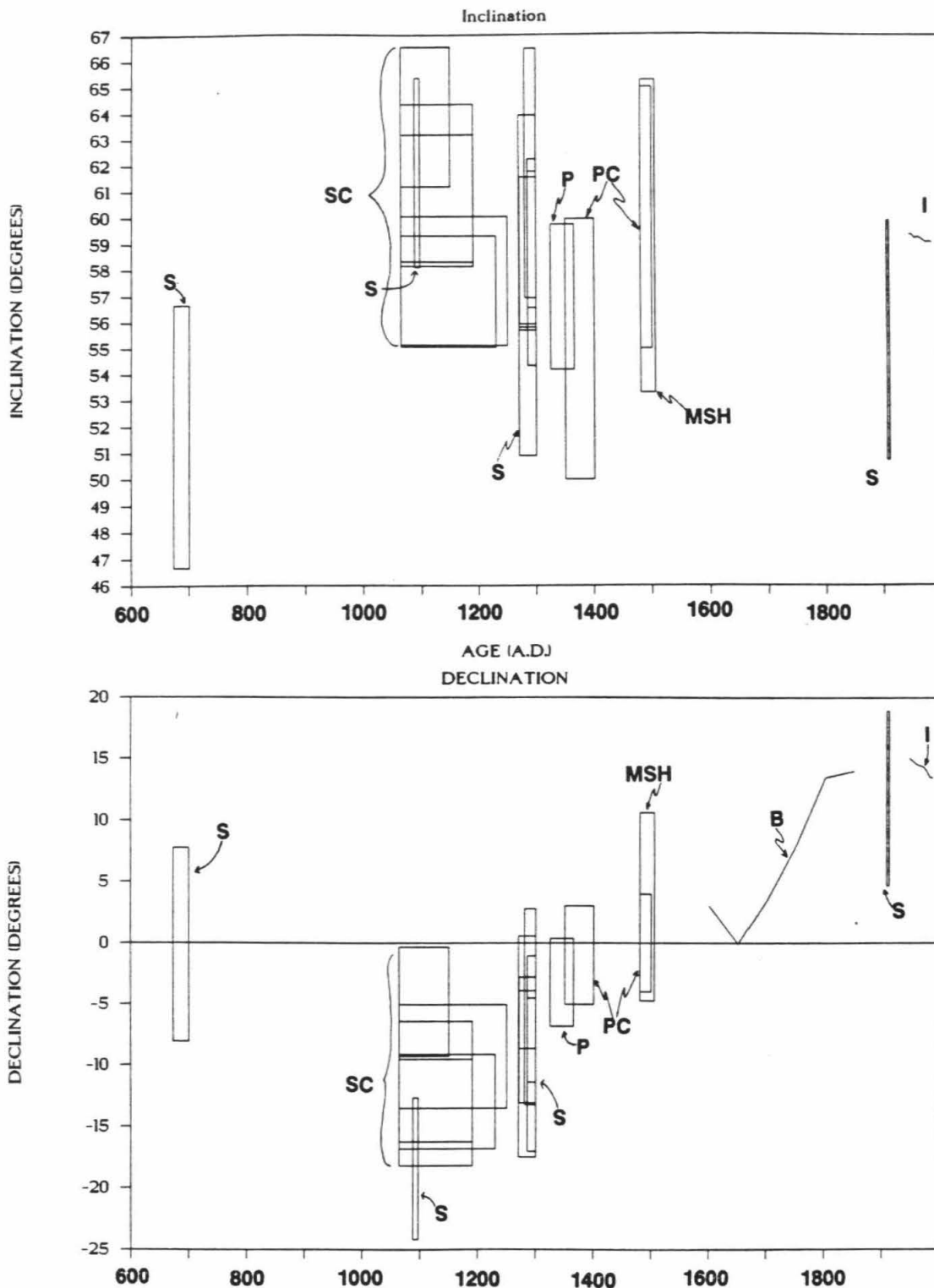


Figure 11

Secular variation curve for southern California. Data from: B-Barraclough, I-IGRF, P-Panum Crater, PC-Pallett Creek, MSH-Mt. St. Helens, S-Sternberg, SC-Sunset Crater.

indicates the uncertainties in both time and direction. These errors combine uncertainty in the original measurements with uncertainty due to geographic translation.

In addition to the points discussed above, magnetic information from two other source is plotted in figure 11. The two lines are from models of the magnetic field calculated for this location and so they are presented as lines with no error limits. The earlier line is from Barraclough's (1974) spherical harmonic inversion of historical magnetic declination data. Barraclough collected historical data on the magnetic field, mostly from maritime navigation records. Because it is from navigation data, only the declination data is sampled well enough to do the inversion. Using these data Barraclough fit up to tenth-order spherical harmonics to obtain the magnetic field at that time. Fields were calculated at 50-year intervals beginning in 1600.

The later line is the International Geomagnetic Reference Field since 1945. This field is very similar to Barraclough's calculated fields but with better sampling and harmonics up to the 10th degree.

Discussion

The basic pattern is in agreement with the three SV curves discussed above. Figure 12 shows each of these curves, geographically corrected to southern California,

Southern California Secular Variation

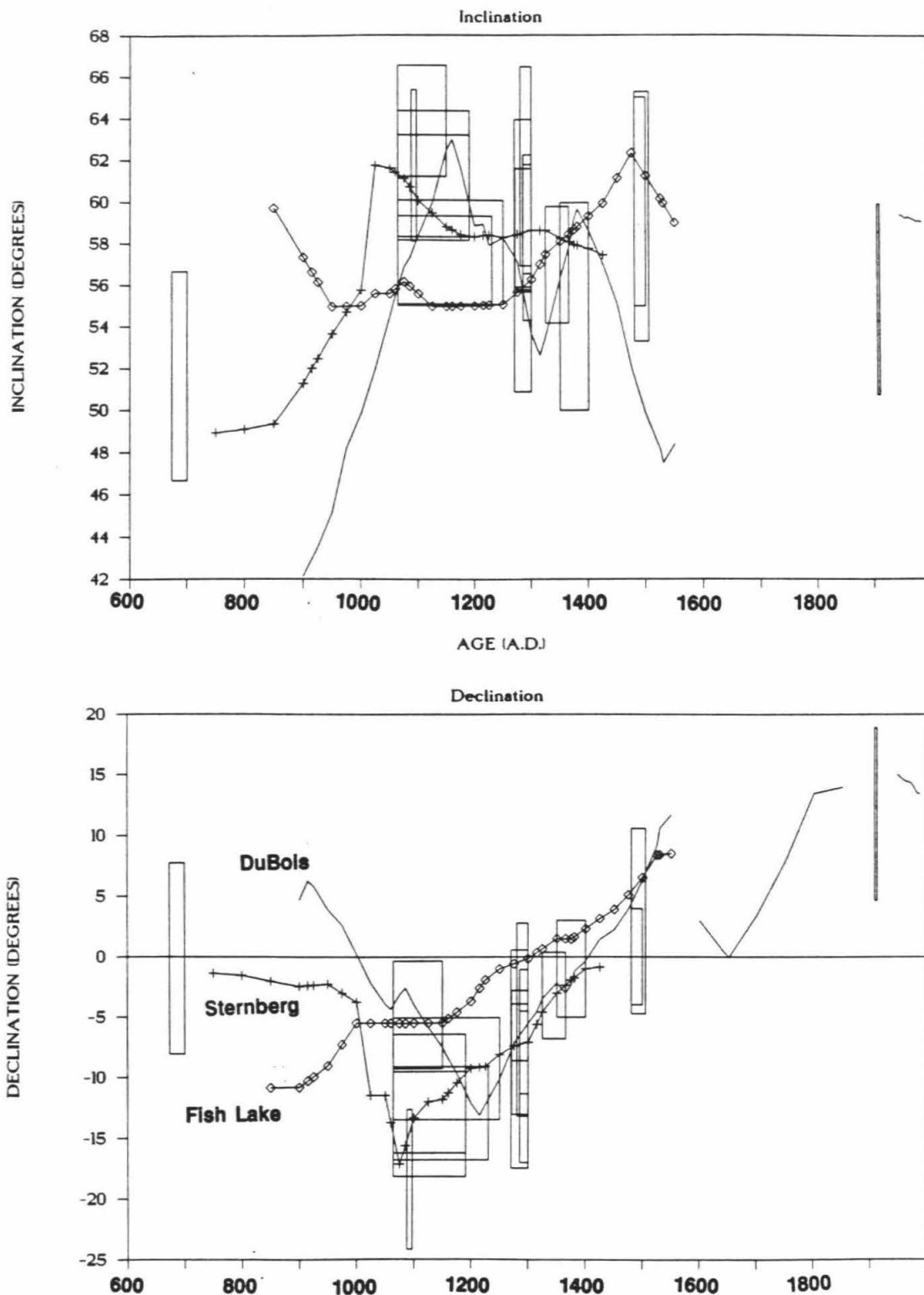


Figure 12

Comparison of the published secular variation curves with the well constrained data points discussed in the text. The published curves have been geographically translated to southern California.

plotted on the data points. In particular, the declination pattern follows closely but with differences in the timing of the peaks. The inclination curves do not follow the data, or each other, as closely. Again, the DuBois and Sternberg curves differ on the timing of peaks but have a similar form. However, the three curves all fit the southern California curve within the scatter of these well-constrained data. Hence, there is no statistically significant difference between the three curves for southern California.

The curve constructed in this chapter has two significant deficiencies. The first is the gaps between the concentrations of data. The most significant of these gaps lies between A.D. 700 and 1064. Although a straight line interpolation between the data points seems reasonable, from observation of the regions where data exists, much detail is probably missing.

The second problem is the large error bounds on the data. For a sample with a magnetic direction of $\text{dec}=-10$ and an $\text{inc}=59$ the possible age range would span A.D. 1064 to 1300. This 250 year uncertainty would make secular variation dating useful for only those samples where no other age control is available. Although this example is extreme, much of the curve would give uncertainties of over 100 years.

For all of the points the translation errors have noticeably increased the confidence limits on the

directions. Future work, concentrated in southern California, will be needed to constrain this curve and reduce the uncertainty added by the translation. Only by sampling close to the location of interest can the error from the geographic correction be minimized.

This curve presents a beginning of a secular variation curve for southern California. In the following chapters I use this curve to analyze paleomagnetic directions. Its use for dating magnetic directions is illustrated in Chapters 3 and 4 and in Chapter 5 I use this curve to help constrain the original directions of well dated, but rotated magnetic directions.

Chapter 3

**Paleomagnetic Correlation and Dating of the
Prehistoric Sediments of Lake Cahuilla and
Measurement of Their Tectonic Rotation**

Abstract

Prehistoric Lake Cahuilla has filled the Salton trough of southern California several times in the past millennium. Paleoseismological studies at two sites along the San Andreas fault make use of faulted Lake Cahuilla sediments, but the correlation of seismic events between the sites has been problematic, due to a scarcity of material for radiocarbon dating at one of the sites. Paleomagnetic directions from these lake sediments enable correlation of lake sediments between the sites. In addition, paleomagnetic rotations near a fault trace at one of the sites confirms structurally predicted deformation.

Introduction

In Chapter 2 I constructed a secular variation curve for southern California as an aid in dating young sediments. In this chapter I apply the secular variation curve and secular variation magnetostratigraphy to correlating and

dating sediments at two paleoseismological sites in southern California.

Over the last 2000 years the Colorado River has occasionally flowed into the Salton trough, filling this closed depression and forming Lake Cahuilla (Sieh, 1986). This lake filled to the overflow height of about 12 meters above sea level and upon diversion of the Colorado River back to the Gulf of California the lake evaporated. During high stand, coastal features such as bars, spits and terraces formed.

The intersection of the San Andreas fault with one of these coastal bars provides good constraints on the fault activity at the Indio paleoseismological site. The Indio site is located on the San Andreas fault near Indio, California (figure 1). Sieh (1986) found 3 earthquakes offsetting bars formed during the last 5 lake highstands.

Williams and Sieh (1987) have been excavating a second site containing Lake Cahuilla sediments near Salt Creek on the east shore of the Salton Sea (figure 1). These are at elevations about 70 meters lower than those at the Indio site. These sediments also include historical beds deposited during the first historic filling of the Salton Sea. This occurred in 1905-1907 when the full flow of the Colorado River was accidentally diverted into a canal to the Salton trough. Incorporation of historical materials, such as railroad ties, demonstrates the youth of these layers.

Correlating lake sediments between these two sites is

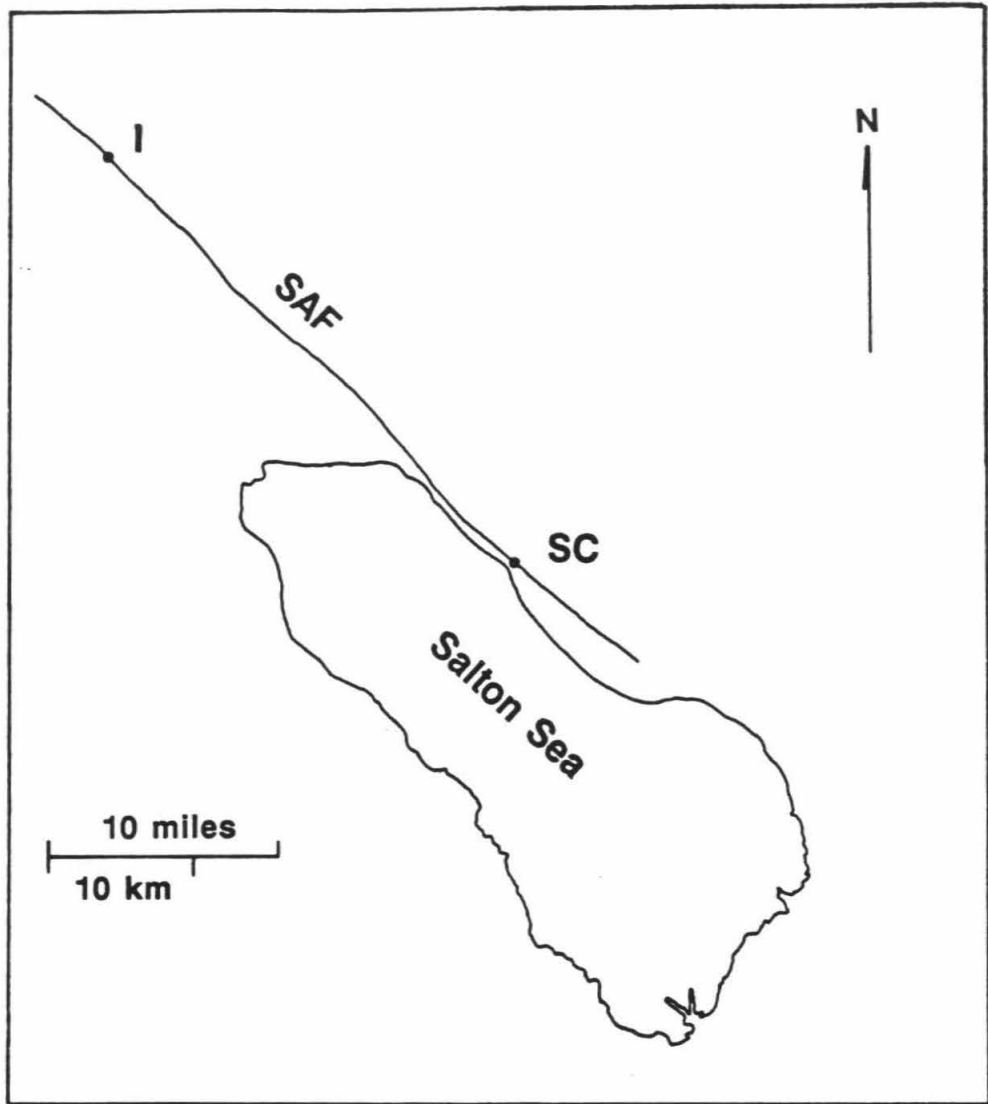


Figure 1

Index map of southern California showing the location of the Indio (I) and the Salt Creek (SC) paleoseismological sites along the San Andreas fault (SAF).

difficult. Because these sites should have experienced similar lake fillings, some of the horizons should be correlative. The paucity of organic materials and inconsistent age ranges makes correlation based on radiocarbon age difficult. In addition, if a lake only partially filled, then sediments would be present at Salt Creek, but not at the Indio site. Alternatively, erosion may have removed lake sediments at these sites. Therefore, correlation strictly on the basis of lake order is not necessarily correct.

Paleomagnetism provides a tool for correlating, and possibly dating, these horizons. Lake sediments that are correlative will have the same paleomagnetic directions. Matching magnetic directions to the secular variation curve from Chapter 2 can provide age constraints on these lakes.

In the excavation of one of the fault strands at the Indio site I had the opportunity to sample next to the fault strand. From the mapping of Sieh the offset and deformation along this strand is well understood. The paleomagnetic measurement of deformation agrees with the deformation predicted by the mapping. I present these data here as an example of the usefulness of this technique and as a prologue to Chapter 5.

Sample Collection

At the Indio paleoseismological site samples were collected from two different areas (figure 2). For the

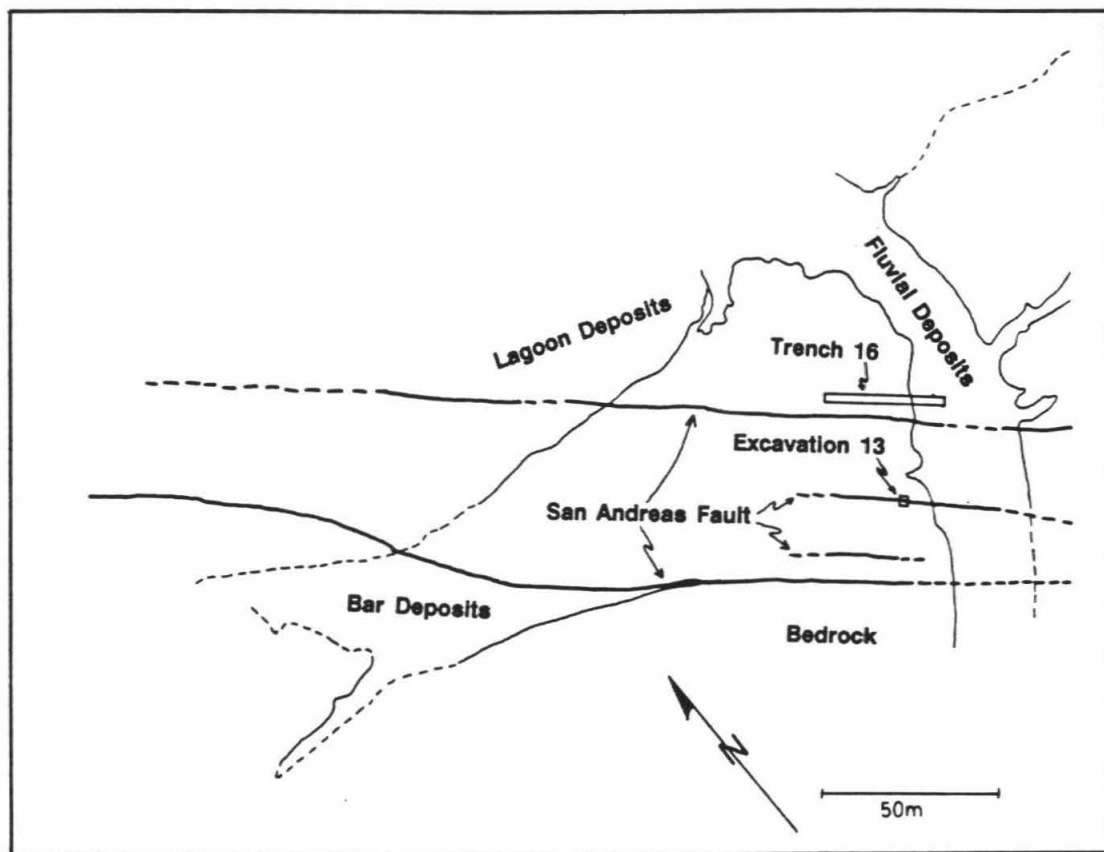


Figure 2

Map of the Indio paleoseismological site showing the major sediment facies, the location of the San Andreas fault strands, and the location of the two sample localities. (modified from Sieh, 1986)

correlation and secular variation study samples were collected from the northeast wall of trench 16, the excavation furthest from an active fault strand. The objective was to reduce the chances of sample rotation due to deformation.

Samples were taken from five units representing four lakes (figure 3). Samples from lake E came from lagoonal silts. Samples from lake C came from the basal bottom-set beds. Lake B samples were taken from basal bottom-set beds. From lake A the samples came from a coarse sand layer in the middle of the unit. Seven samples were taken from each unit except lake B where only three samples were taken.

Along one of the fault strands, four groups of ten samples were taken within two meters of the fault (excavation 13 in figure 2). These sediments were deposited as bottom-set beds in lake B and correlate with the lake B horizon sampled in excavation 16. Later, I discuss the locations of the four groups relative to the fault.

At the Salt Creek paleoseismological site, three groups, with seven samples in each group, were collected (figure 4). Each group was from a different set of lake sediments, but the samples within a group all came from the same horizon.

All of the samples were collected and processed following the standard procedure described in detail in Appendix 1.

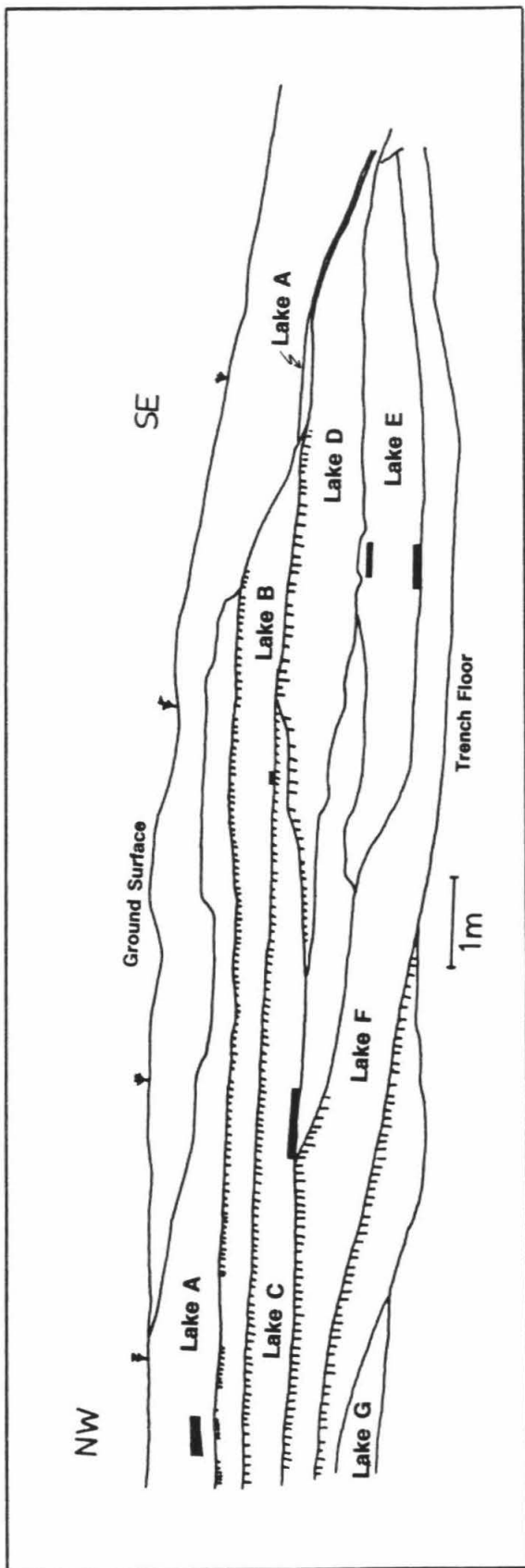


Figure 3
Simplified view of the northeast wall of trench 16 showing the sediments deposited in different lakes. Unlabeled sediment packages are fluvial, or human modified at the top of the section. Rooted horizons indicating beginning soil development during sub-aerial exposure are shown by vertical lines. The sampling locations are shown by the filled rectangles.

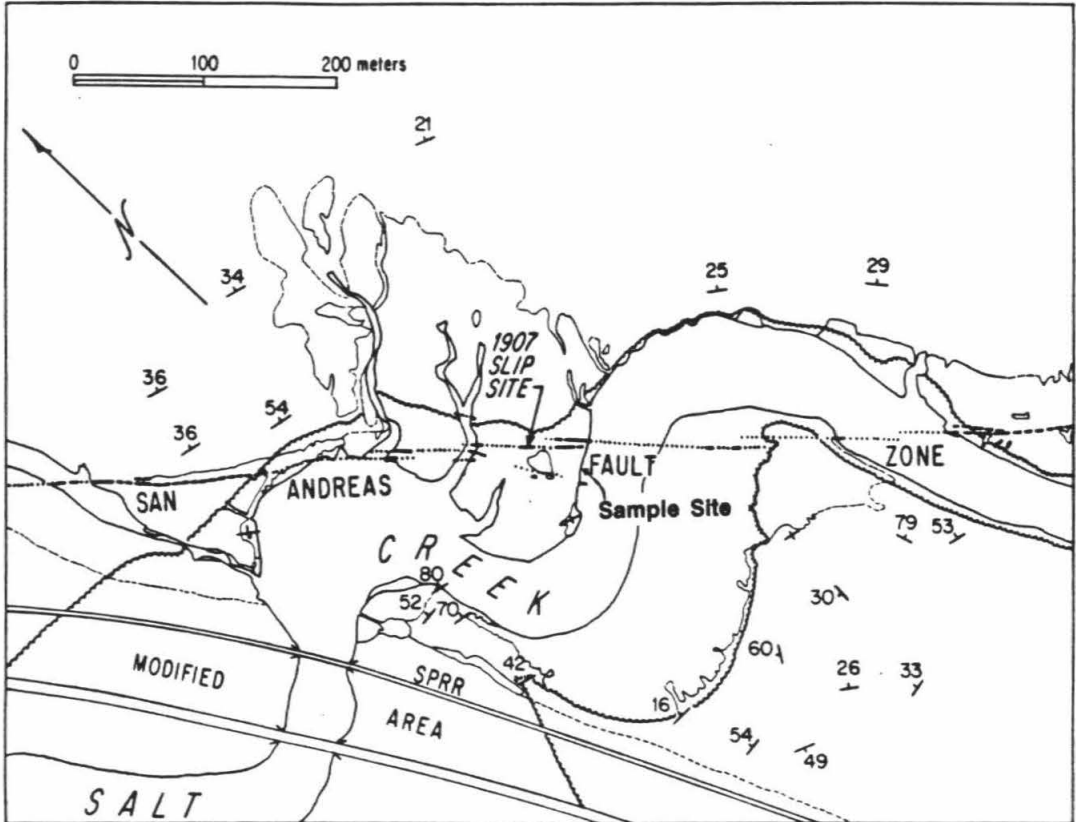


Figure 4

Map of the Salt Creek paleoseismological site showing the trace of the San Andreas fault and the location of sampling.

Correlation and magnetostratigraphy

I will discuss the results from the lakes at each site individually and then correlate the lakes.

Indio-Lake A

These samples showed instability or marginal stability and the few stable directions from these samples scattered widely. Figure 5 shows a typical, unstable sample from lake A. This result is not surprising since this horizon is a coarse sand and probably contains much multi-domain magnetite. No useful results were obtained from these lake sediments.

Indio-Lake B

Of the three samples taken from this lake bed in exposure 16, all showed magnetic stability. Two cluster well and the third is divergent from the other two (figure 6). If all three samples are grouped together they give a Fisher precision constant of 63. I took only three samples from the section distant from the fault because this is the same unit sampled next to the fault at locality 13. Sample group W1 (discussed below), closer to the fault, has a magnetic direction of $\text{dec}=355.6^\circ$, $\text{inc}=57.8^\circ$, and $\text{alpha-95}=4.7^\circ$. This error oval contains the mean of the three clustered points. Since the directions from the two groups

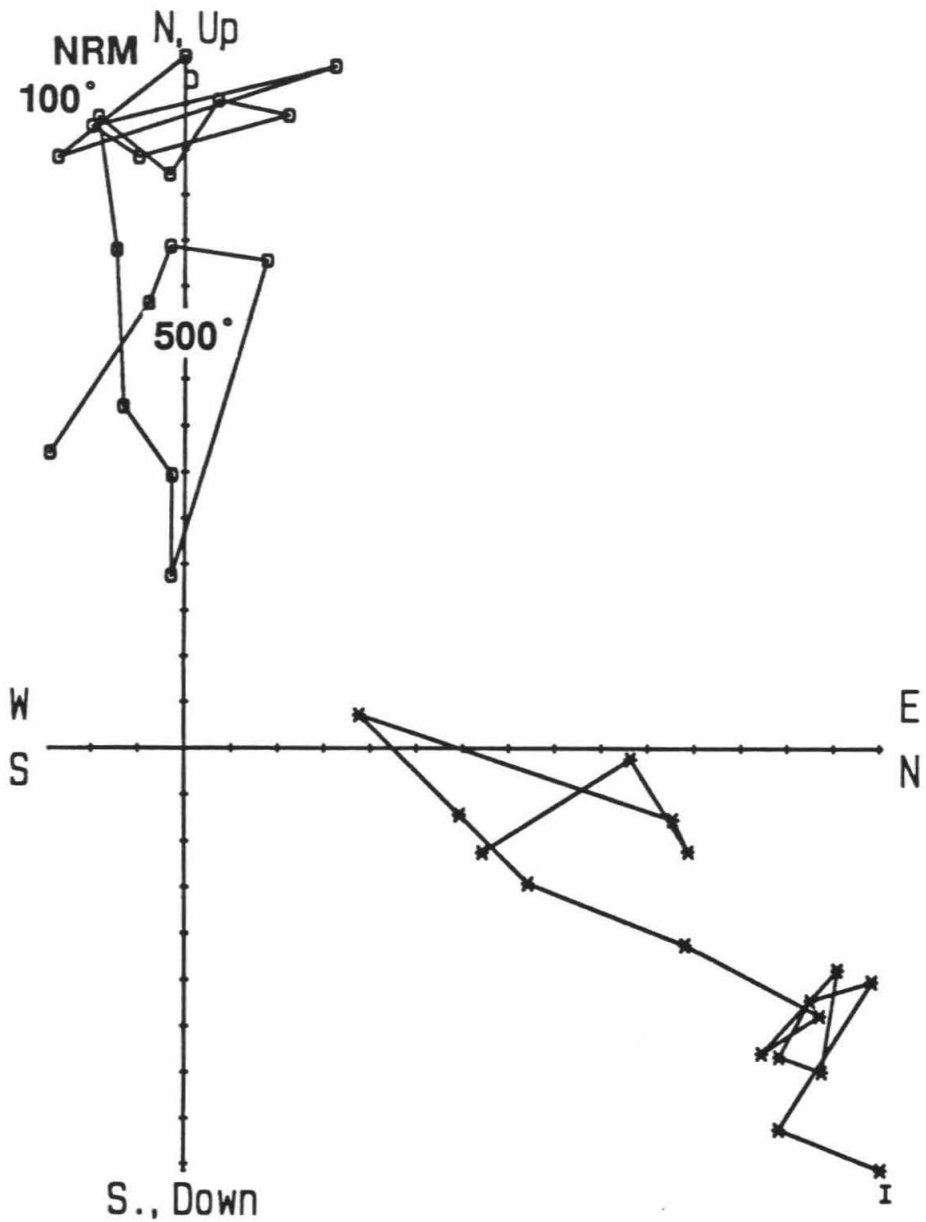


Figure 5

Orthogonal vector demagnetization diagram of a typical unstable sample from lake A. An explanation of orthogonal vector demagnetization plots is provided in the last section of Appendix 1.

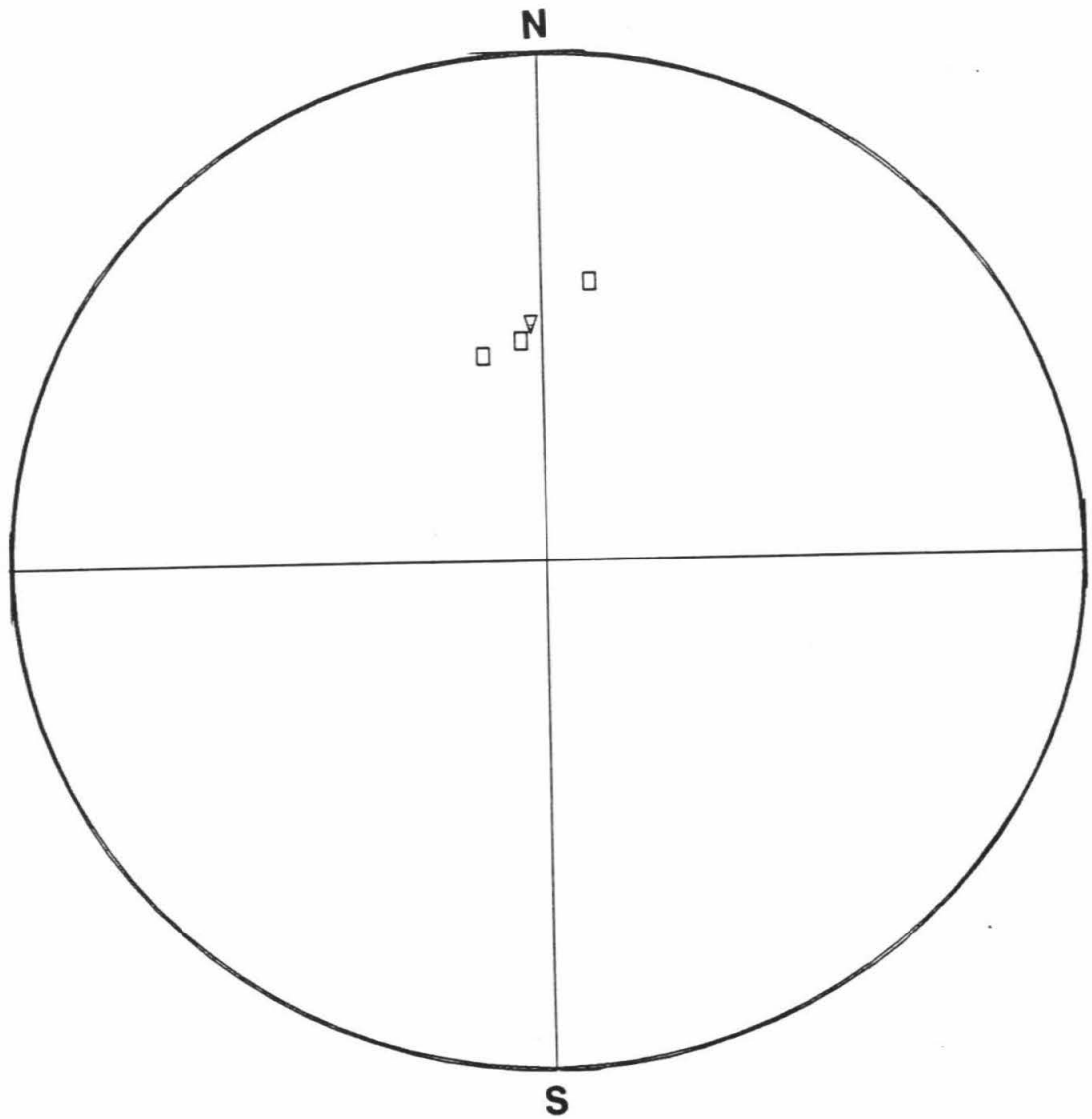


Figure 6

Equal-area plot of sample directions from lake B.
Triangle indicates the mean direction of the three samples.

are indistinguishable I will use the W1 direction for lake B.

Indio-Lake C

This unit showed fair to marginal stability but the directions scattered significantly. Since their Fisher precision parameter was less than 30 I disregard these data and draw no conclusion about the paleomagnetic direction of lake-C sediments.

Indio-Lake E

Two units from this lake showed the best stability of any of the sampled units (figure 7). The samples from the upper horizon from this lake cluster well with a precision parameter of 95.7 (figure 8). By disregarding the two points away from the main cluster, the remaining five points cluster very well with $k=1854$. The $\alpha-95$ of 1.45° reflects this clustering. The resulting direction is $\text{dec}=-6.1^\circ$ and $\text{inc}=35.1^\circ$.

The samples from the base of lake E did not cluster as well as the samples from the top, having a $k=44.4$. In addition, the mean direction differs from the mean direction of the upper lake E group. However, the sample directions in figure 9 do show systematic behavior. In figure 9, both "group a," with the shallow inclination, and "group b," with the high westward declination, are composed of

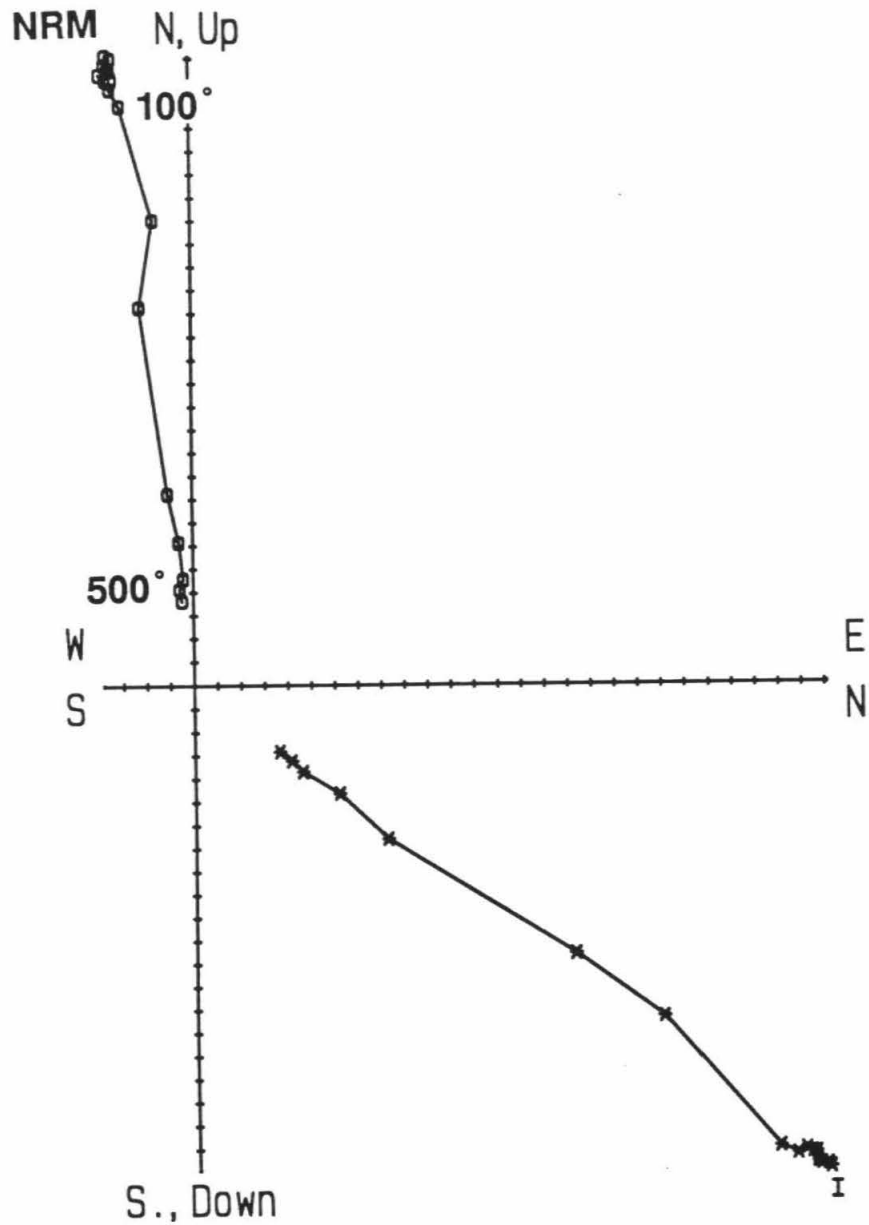


Figure 7

Orthogonal vector demagnetization diagram of a typical sample from the top of lake E. This demagnetization behavior was typical of the stable samples at the Indio site.

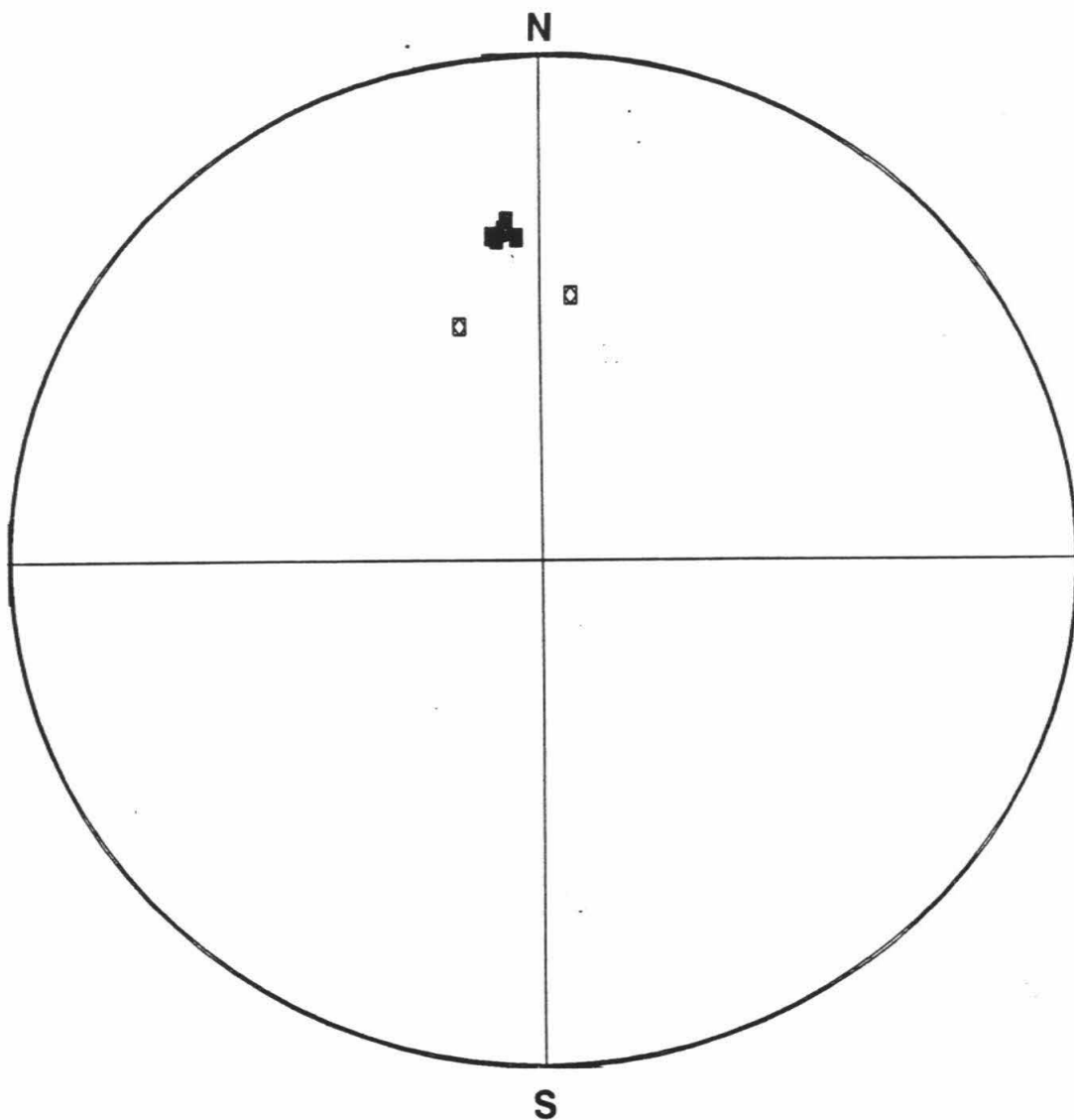


Figure 8

Equal-area plot of sample directions from the top of lake E. The 95% confidence oval of the mean direction for the five well-clustered directions, indicated by the filled squares, is obscured by the data points. The sample directions indicated by open squares were not used in this mean direction.

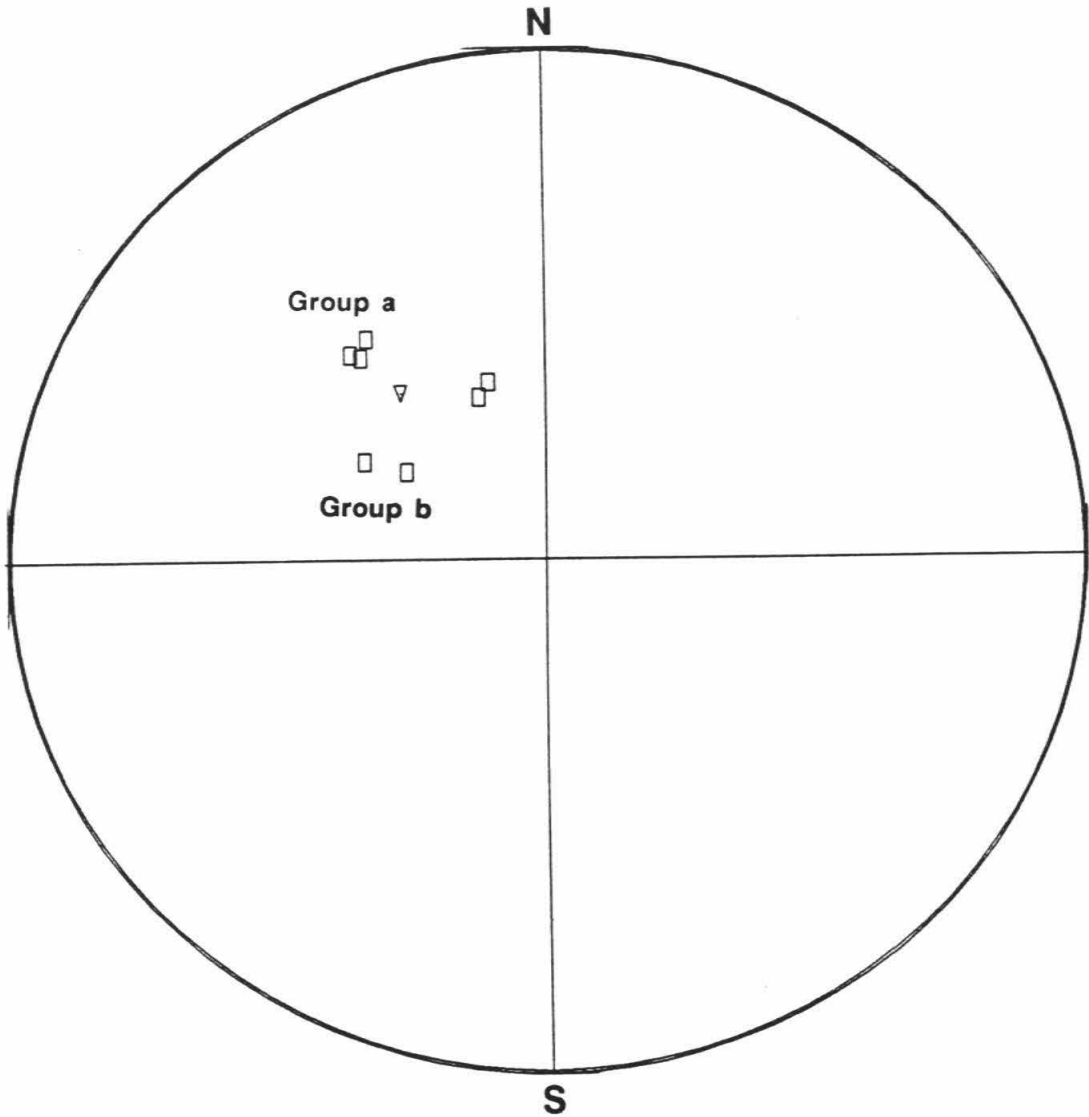


Figure 9

Equal-area plot of sample directions from the bottom of lake E. The mean direction is indicated by the triangle. Group a and group b are discussed in the text.

geographically adjacent samples. The two remaining samples in the unnamed group agree with the upper lake E in declination, but have steeper inclinations.

I propose four possible interpretations, in order of decreasing likelihood. First, after binding of the magnetic grains in the matrix, the layer experienced compaction and sections of the layer moved as coherent slabs. Second, the different directions represent different times at which the different parts of the layer had their magnetic grains bound in place. Third, the different directions represent a Liquefaction Remanent Magnetization, a concept I discuss in Chapter 4. Finally, these directions represent a chemical overprint. Because of the high westward directions of both group a and group b, I consider the first explanation the most likely. Since these directions significantly differ from the usual range of magnetic field directions, these directions probably moved to this position rather than acquiring a magnetic field in this direction. However, this layer does not show structures indicating motion and disruption. If motion occurred it must have been small scale because no obvious indications remain.

Salt Creek-Lakes 3, 2, and 1

At the Salt Creek site the samples from the three lakes all behaved in a stable fashion and the sample groups clustered well. The oldest lake, lake 1, gave a direction of $\text{dec}=-8.3^\circ$, $\text{inc}=35.7^\circ$ with $\text{alpha-95}=5.5^\circ$ and $k=92.3$. Lake

2 has a direction of $\text{dec}=-12.2^\circ$, $\text{inc}=47.8^\circ$ with $\text{alpha-95}=6.0^\circ$ and $k=90.3$. The youngest lake bed sampled has a direction of $\text{dec}=0.2^\circ$, $\text{inc}=43.2^\circ$ with $\text{alpha-95}=4.1^\circ$ and $k=163.9$. Figure 10 shows the samples from each of these groups.

Correlation

The most powerful use of paleomagnetism here is correlation of lake beds between the sites. As I discussed in Chapter 2, the comparison of magnetic directions from distant sites introduces error due to the geographic correction over a non-dipole magnetic field. By comparing sites close together I avoid this error.

The only matching magnetic directions at the two sites is the magnetic direction of lake E at Indio with lake 1 at Salt Creek. The lake 1 error circle completely encloses the lake E error circle (figure 11).

For lake B at Indio, no lake at Salt Creek has a similar magnetic direction (figure 12). There are several possible explanations for this. The most obvious is that there is no correlative for lake B at Salt Creek. Erosion may have removed the sediment or very little sediment was ever deposited here. The upper contact of the lake 3 sediments is erosional, so removal of lake B is quite possible (Williams and Sieh, 1987). Another explanation is that the sampled horizons of the lakes differ enough in age that secular variation of the magnetic field resulted in

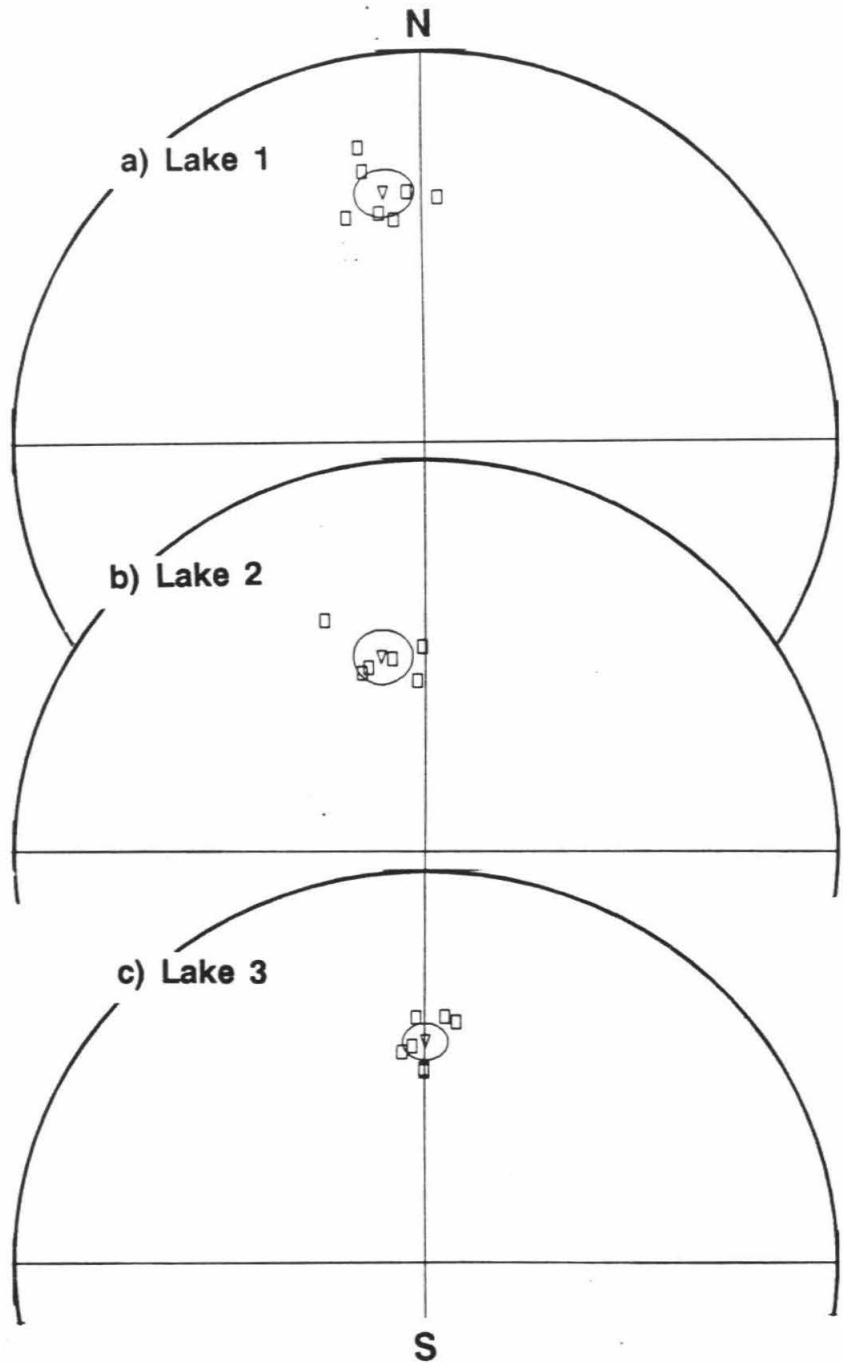


Figure 10

Equal-area plots of the sample directions from (a) lake 1, (b) lake 2 and (c) lake 3 at the Salt Creek site. Mean directions are marked by triangles and the ovals are the 95% confidence regions of the mean.

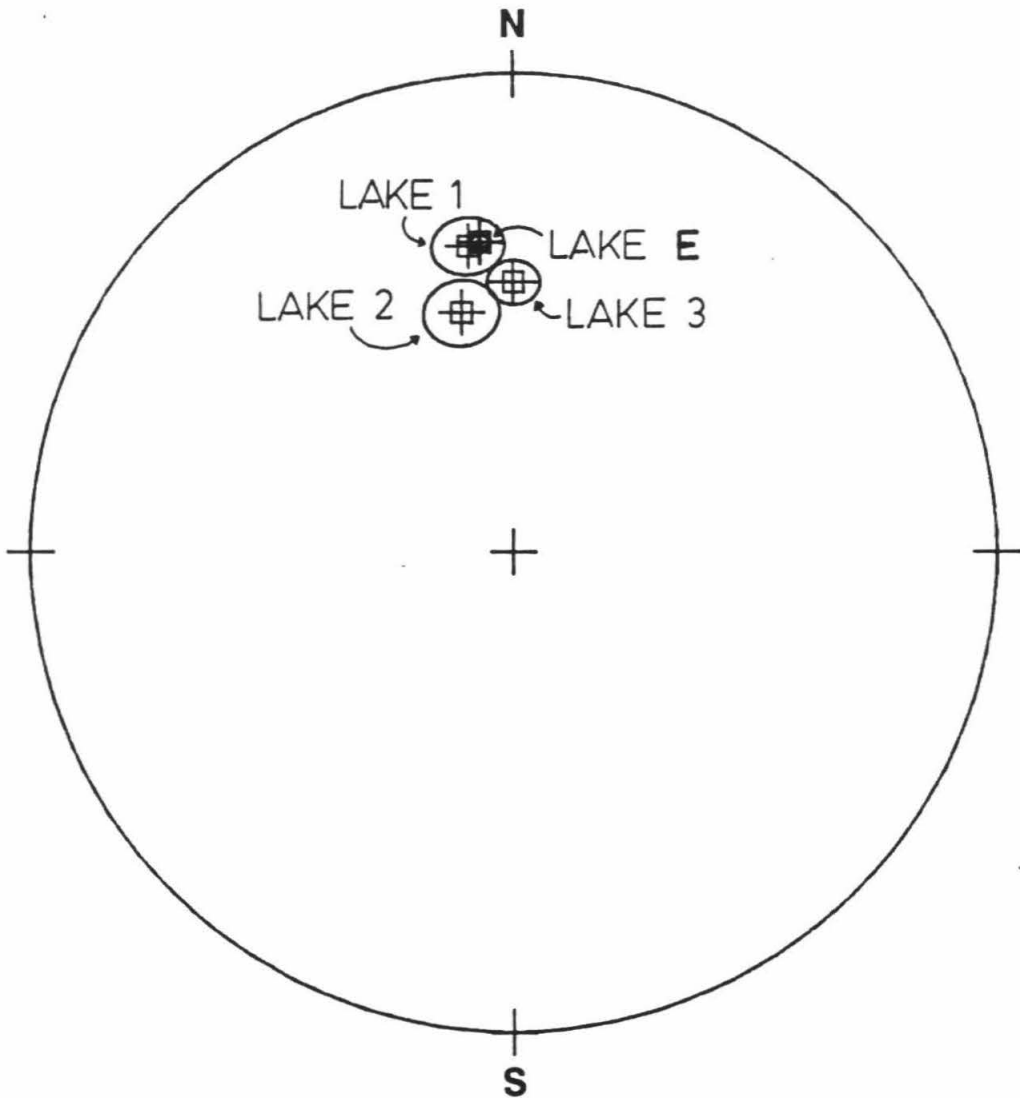


Figure 11

Equal-area plot showing the correlation of lakes 1, 2, and 3 at Salt Creek with lake E at Indio. Ovals are the 95% confidence regions of the means.

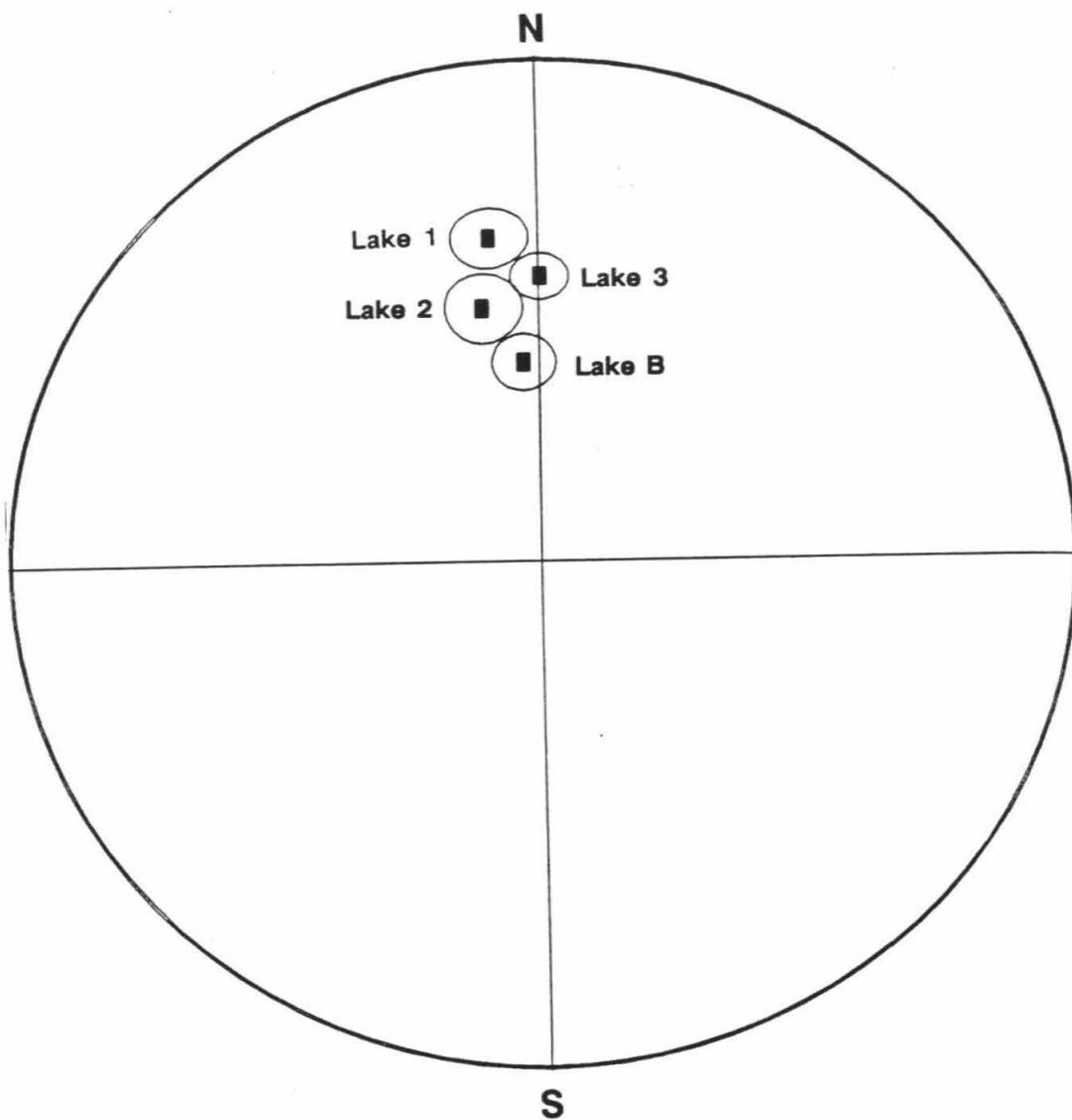


Figure 12

Equal-area plot showing the direction of lake B at the Indio site with lakes 1, 2, and 3 at the Salt Creek site. Ovals are the 95% confidence regions of the means.

differing magnetic directions. In addition, there are the different ways in which the sediments may have acquired a new, secondary magnetic direction. Finally, different amounts of inclination error may account for the lack of a correlative for lake B.

Dating

To determine dates for these units, their magnetic directions are plotted on the secular variation curve I constructed in Chapter 2 (figure 13). The most noticeable characteristic of the Salt Creek magnetic directions, and the direction for lake E, is their shallow inclination. Only lake B overlaps a significant part of the inclination curve and lakes 1 and 3, and lake E miss practically all of the inclination data points. Considering both inclination and declination, for lake B possible age ranges are A.D. 670-700, and 1064-1700. For lake 2, possible age ranges are A.D. 670-700 and 1150-1365.

The shallow inclinations at Salt Creek suggest inclination error of the magnetic direction. This results from the flattening of magnetic grains in deposition and compaction of the sediment (King, 1955). Since these layers have the same composition, a sandy silt, the inclination error should be a constant (King, 1955). In figure 14 I increase the inclinations by 15° so the maximum inclination of lake 2 corresponds with the maximum observed on the

Southern California Secular Variation

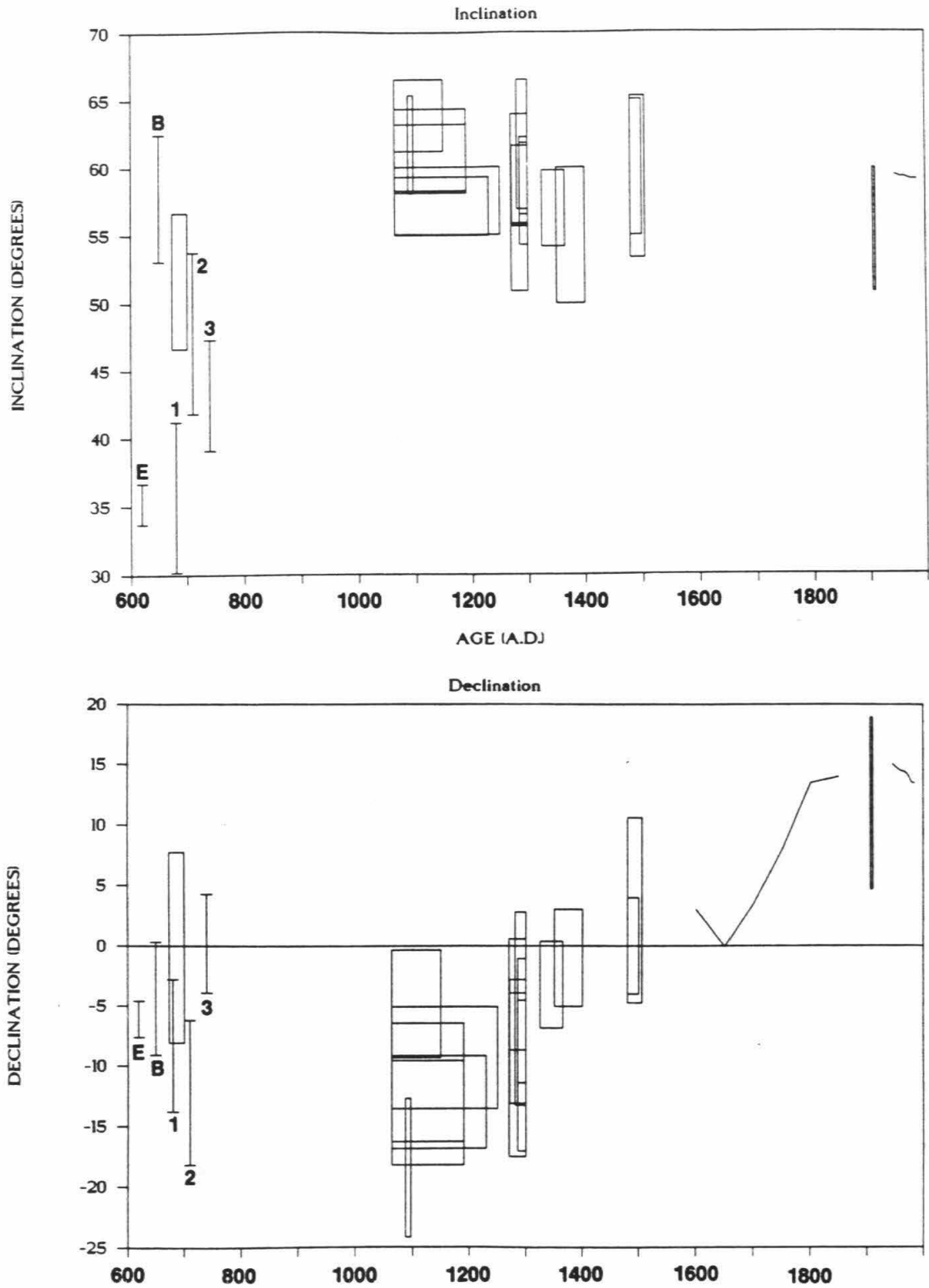


Figure 13

Secular variation curve from Chapter 2 with magnetic directions from lakes E, B, 1, 2, and 3 shown.

Southern California Secular Variation

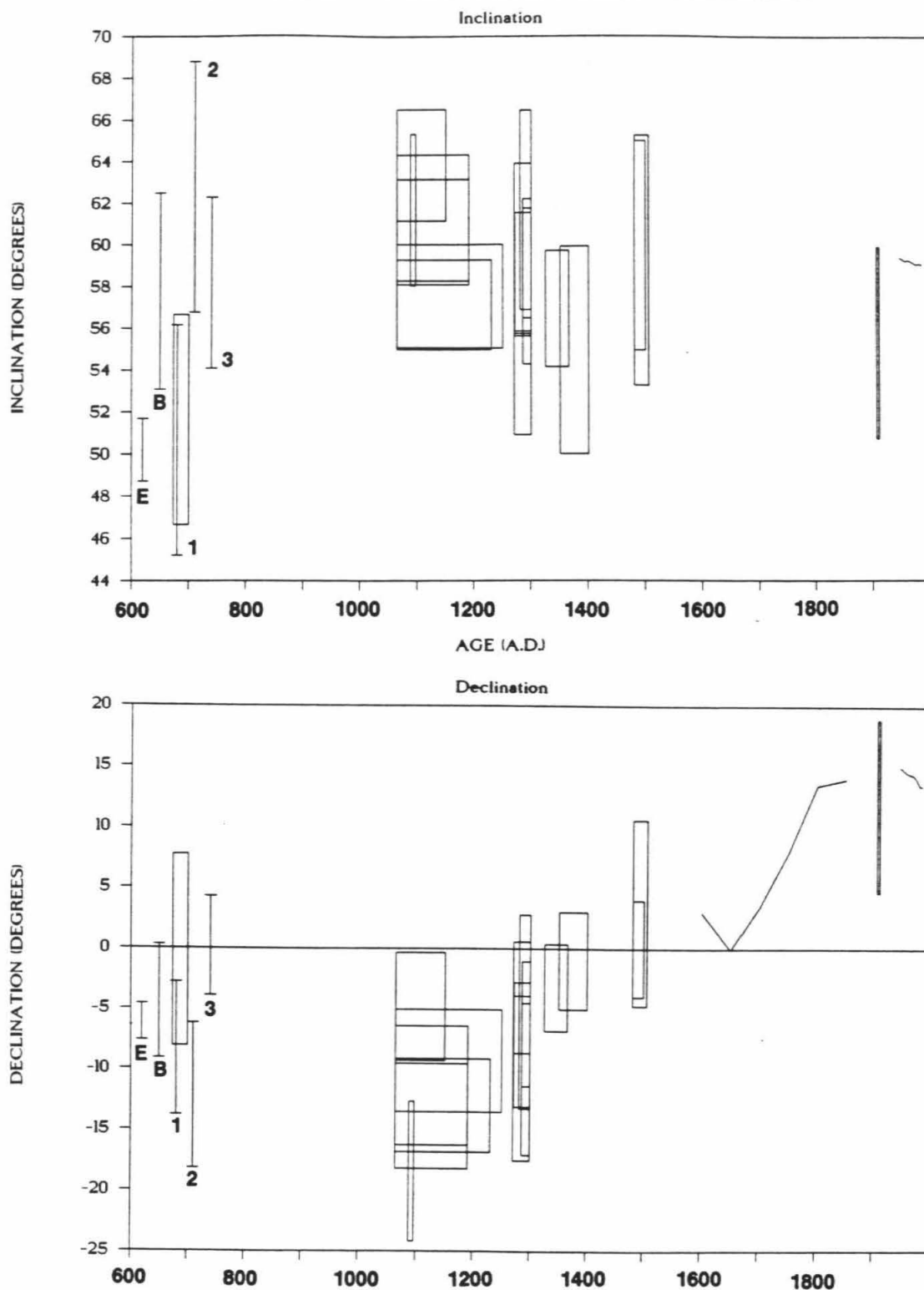


Figure 14

Secular variation curve from Chapter 2 with magnetic declinations from lakes E, B, 1, 2, and 3 and magnetic inclinations of the lake directions increased by 15° to compensate for inclination error.

curve.

Now, the pattern of the magnetic directions from Salt Creek corresponds well with the form of the secular variation curve. The increase in inclination and decrease in declination is seen in the change from lake 1 to lake 2 while from lake 2 to lake 3 the reversal in this trend is apparent. This suggests that the age of lake 1 is in the A.D. 700 to 1100 range, that lake 2 is in the A.D. 1100 to 1300 range, when the declination and inclination reach their extreme values, and that lake 3 is in the A.D. 1300 to 1500 range.

I do not believe that the correlation of lake 1 with lake E is affected by the inclination error. Lake E also has a very shallow inclination and probably suffers from inclination error. In addition, the declination of lake E agrees with lake 1 the best, so I believe this correlation to be the most likely. However, if only the declinations are considered, lake E could also correlate with lake 2.

Using the correlation of lake 1 with lake E, and these broad age ranges, still allows possible sequencing of the Salt Creek lakes with the Indio lake sediments. The broad age range for lake 1 includes the possible radiocarbon ages for lake E of A.D. 995-1040 (Williams and Sieh, 1987). The age range for lake 2 includes the age of Lake D of A.D. 1210-1320. There is no radiocarbon age on lake C, however the age of lake B of A.D. 1410 to 1650 does fall within the range for lake 3. This suggests that lake A and either lake

B or C is not represented at Salt Creek. Because of the lack of a correlation based on magnetic directions with lake B, I would conclude that this lake is not represented. However, because of the uncertainties related to the inclination error this is not certain.

This example demonstrates both the potential usefulness and the problems associated with secular variation magnetostratigraphy and correlation. At these two sites in the Salton trough, there is a possible correlation of Lake E at Indio with Lake 1 at Salt Creek. Because these two sites are close together this correlation is more useful than dating using the secular variation curve constructed in Chapter 2. With this curve, the magnetic directions can only be placed in broad age ranges giving uncertainties of more than a hundred years. A better constrained secular variation curve for southern California will be necessary to reduce these uncertainties.

Measurement of tectonic rotations

As a test of the ability of paleomagnetism to measure non-brittle deformation of fault zones, I conducted a limited test at the Indio paleoseismological site. The samples were taken where good constraints exist on the deformation near the fault. The observed deformation agrees with the predicted rotations.

At the Indio site four individual strands comprise the San Andreas fault zone (figure 4). Along one of these

traces Sieh excavated foreset beds deposited on the prograding end of the bar during the penultimate high stand in about A.D. 1450 (excavation 13 in figure 4). Sieh found 0.7 meters of displacement of piercing points in these foreset beds (figure 15). In addition, the cross-sections in figure 15 show that the piercing points have larger vertical separation at the north end of the excavation than at the south end. This vertical separation yields 6° of southward tilting of the the northeast block relative to the southwest block.

I collected four groups, with ten samples each, from this excavation. Of the two groups on each side of the fault one group came from the first half meter from the fault and the second group came from two meters from the fault (figure 15). I collected the closest group on the east (E1 in figure 15) in the block bounded by the small splay fault to check for rotation of that block.

I collected, processed and analyzed these 40 samples following the standard procedure described in Appendix 1. The samples were magnetically stable and figure 16 shows representative demagnetization paths. The samples contained one component of magnetization and I calculated a best fit direction to these paths using the procedure of Kirschvink (1980). I used Fisher statistics to calculate the group means with the results listed in table 1.

As expected, the group means on the west side of the fault match exactly, indicating relative rotation of $\leq 1^\circ$

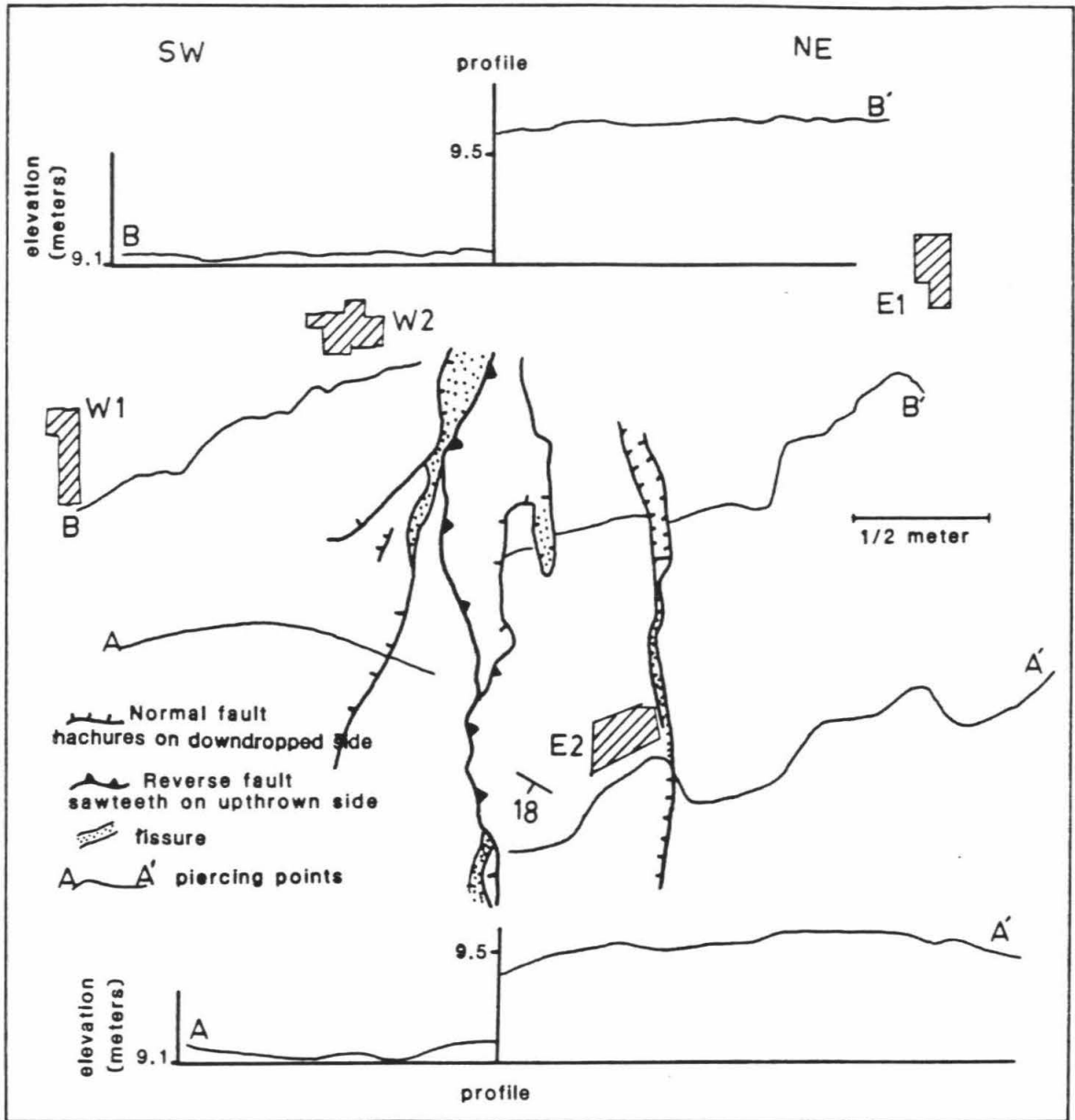


Figure 15

Map of excavation 13 showing locations of sampling sites (cross-hatched boxes) and topographic profiles along the piercing points offset by the fault. The top of the map is towards N40W.

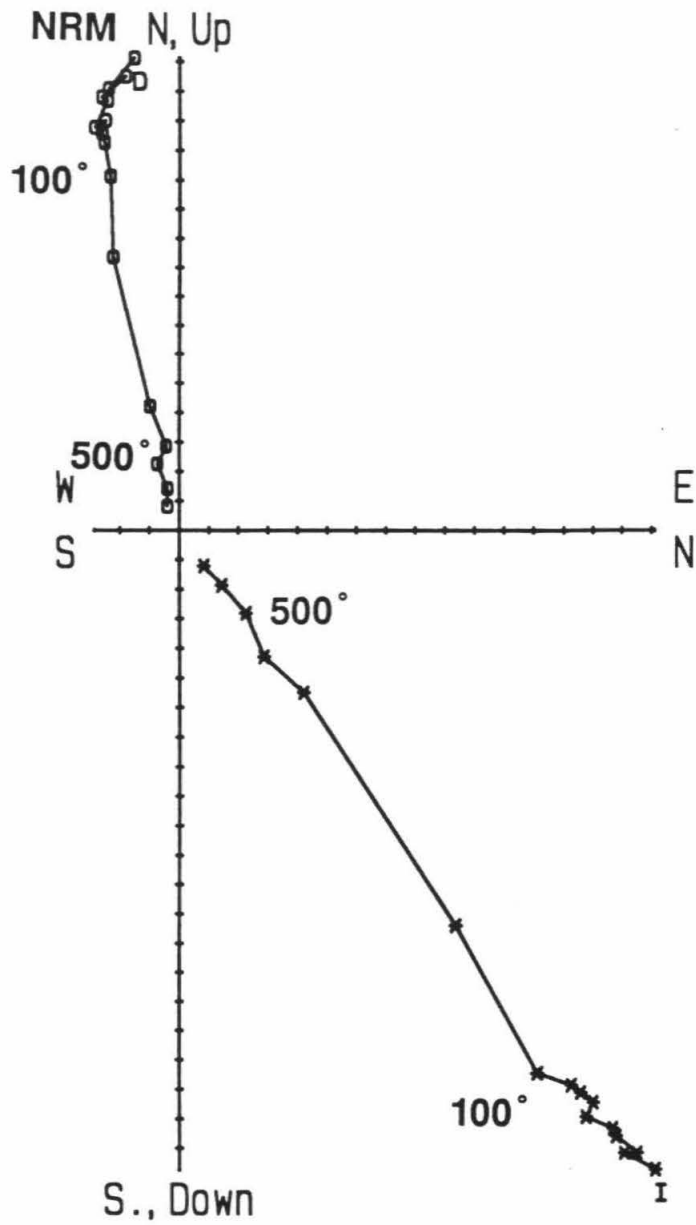


Figure 16

Orthogonal vector demagnetization diagram of a typical sample from the rotation study.

Table 1
Group mean directions

Group	Dec	Inc	Alpha-95
W1	-4.4	57.8	4.7
W2	-3.9	59.4	5.2
E1	-6.9	45.4	4.4
E2	8.0	44.7	8.8

between these groups (figure 17). If rotated by non-brittle deformation the rotation has been as a rigid block. The correlation with the three samples collected away from the fault indicate little, if any, rotation of these groups.

The group far from the fault on the east side shows no rotation relative to the west side of the fault but it does have an inclination shallower by 13° . This amount is higher than the measured southward tilting of 6° . The east group on the block within the fault zone shows an equal amount of inclination shallowing and also shows 11° of clockwise rotation relative to the other three groups. The inclination is not as great as the dip predicted by the tilt of this block but the sense and amount of rotation agree with that observed.

Although this sampling only covers a small distance from the fault, non-brittle deformation is clearly identified. This sample size is too small to make calculations of the non-brittle offset on the fault, but the sampling confirmed the field observations of deformation. However, based on the limited control group collected away from the fault there appears to be rotation only of discrete blocks bounded by splay faults.

This case confirms the ability of paleomagnetism to measure non-brittle offsets in fault zones. I expand on this and present a more detailed study in Chapter 5.

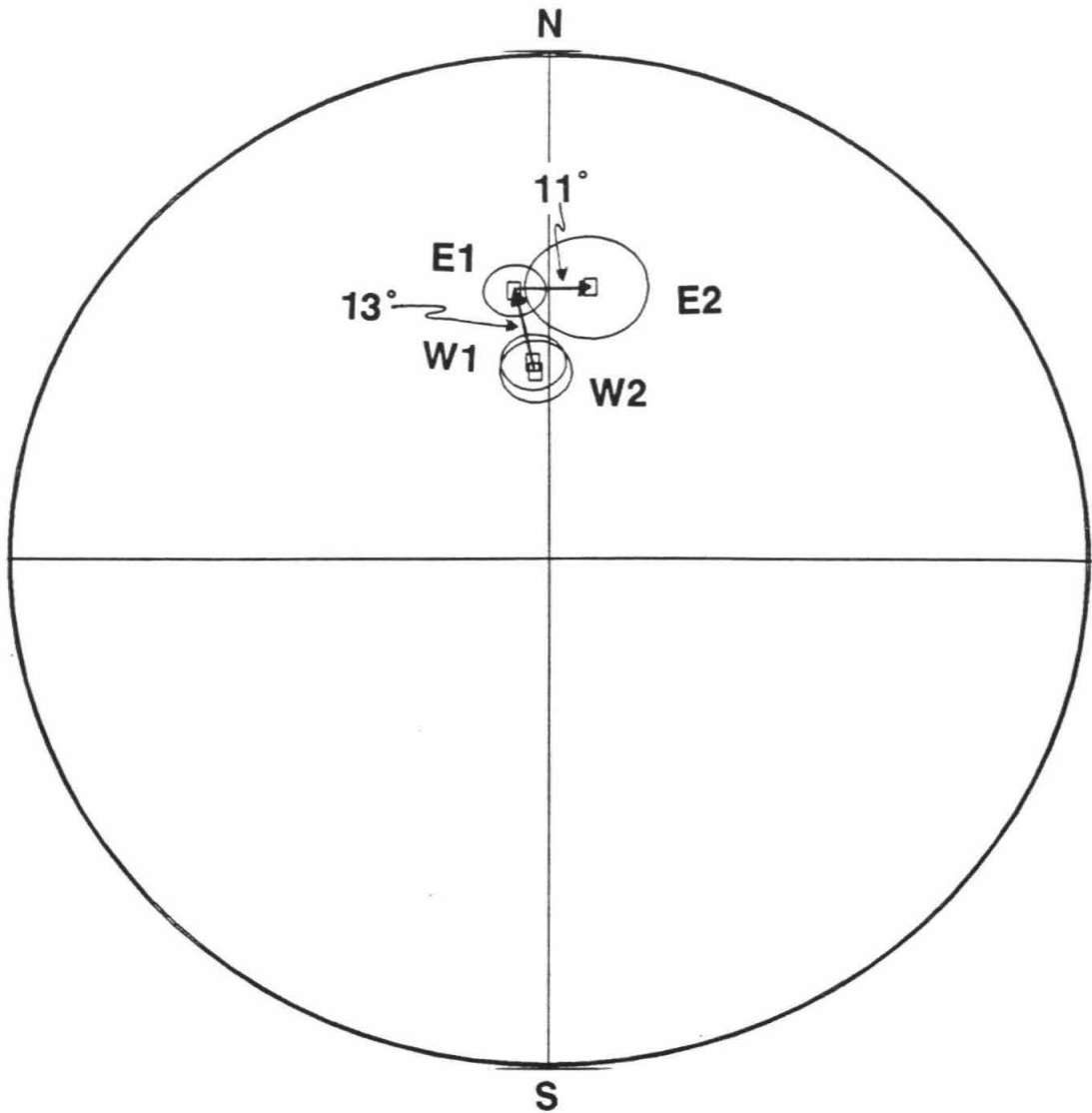


Figure 17
Equal-area plot of the 95% confidence ovals of the groups from the rotation study.

Chapter 4

**Resetting of Detrital Remanent Magnetization
by Liquefaction**

Abstract

The resetting of the magnetic field in mud by physical shock has been documented in adobe bricks. I sampled three types of liquefaction features, a sandbody, soft-sediment diapirs, and sandblows, to determine if a similar process occurs naturally in sediments liquefied by seismic shaking. The samples from the sandbody showed a different magnetic direction than their source beds and a large increase in their NRM intensities. The soft-sediment diapirs and one sandblow showed a stable magnetic direction; however their directions did not differ significantly from the magnetic direction of the source beds. Additionally, both the diapir and sandblow did display higher or lower magnetic intensities than their source beds. Some of the diapirs showed a slight increase in the intensity whereas the others showed a decrease. The sandblow showed a significant increase in the intensity over the magnetic intensity of its source bed. Since all of the liquefaction features showed a magnetic remanence after being physically disrupted, and there was a characteristic increase in the NRM intensity, these bodies show liquefaction resetting of

detrital remanent magnetization or a liquefaction remanent magnetization (LRM).

Introduction

The acquisition of a magnetic moment by a mud slurry subjected to a physical shock has been documented in adobe bricks by Games (1977, 1980). This work shows that the action of throwing mud into a mold produces a shock that causes the mud to acquire a magnetic moment. This moment is parallel to the present field direction and proportional to its intensity.

Because of these results, one might well expect that shocking of slurries in nature should also result in the acquisition of a magnetic moment. Specifically, sediments liquefied during seismic shaking might acquire a remanent magnetization during liquefaction. I have designated this "liquefaction remanent magnetization" (LRM).

Games (1977) clearly showed that the acquisition of magnetic moment by adobe bricks resulted from the shock of throwing the mud into the mold. Neither stirring the mud nor shaking the slurry at 60 Hz. resulted in a magnetic moment. However, throwing the mud into a mold using a mechanical throwing device did result in a magnetic moment. Furthermore, this moment was proportional to the magnetic field intensity. This provided Games (1977, 1980, 1983) with a method of studying the paleointensity of the geomagnetic field. By measuring the magnetic moment of the

adobe brick and then measuring the moment acquired when the brick was liquefied and shocked in a known field, he determined the intensity of the magnetic field at the time the brick was made.

The potential paleoseismologic value of LRM is great. If LRM occurs, then it could provide a method for determining the age of the shaking that produced the liquefaction. By matching LRM directions to the secular variation curve discussed in Chapter 2 the date of the LRM and the shaking could be determined. In many stratigraphic sections where the dates of earthquake horizons are poorly constrained this technique could provide a more precise date for the earthquake. This technique would be particularly useful as a dating technique where organic material for carbon-14 dating is absent.

To test this hypothesis I investigated three groups of once-liquefied sediments at the three localities in southern California shown in figure 1: a sand body in the Elsinore fault zone, a set of soft-sediment diapirs in the sediments of Mono Lake, and sandblows.

Results from a liquefied sand body on the Elsinore fault

It is not uncommon to observe, in exposures of active fault zones, sand-filled fissures and pits produced by the flow of liquefied sand induced by seismic shaking (e.g. Sieh, 1979, 1984). One such pit in an exposure of the Elsinore fault at Glen Ivy, California, (Rockwell and

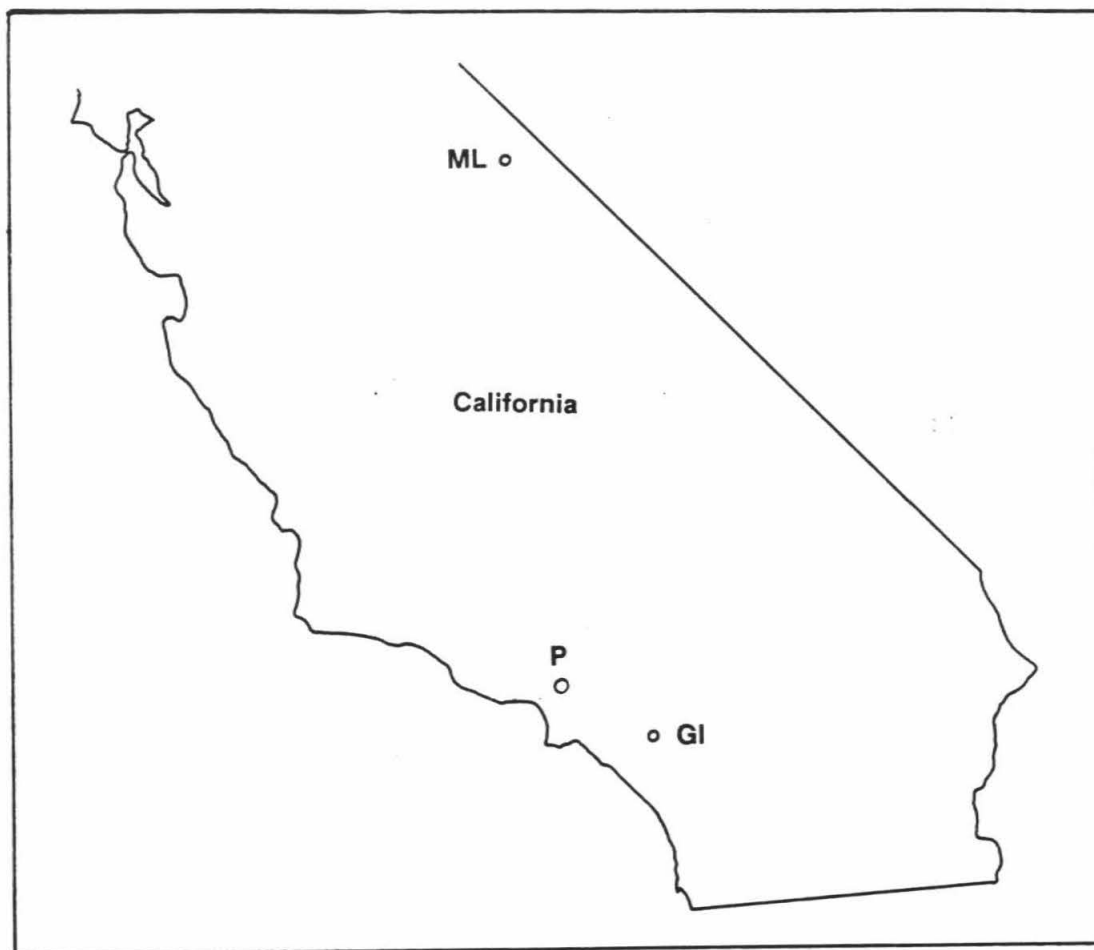


Figure 1

Map of southern California showing the location of the Glen Ivy trench on the Elsinore fault (GI) and Mono Lake (ML). Pasadena (P) is shown for reference.

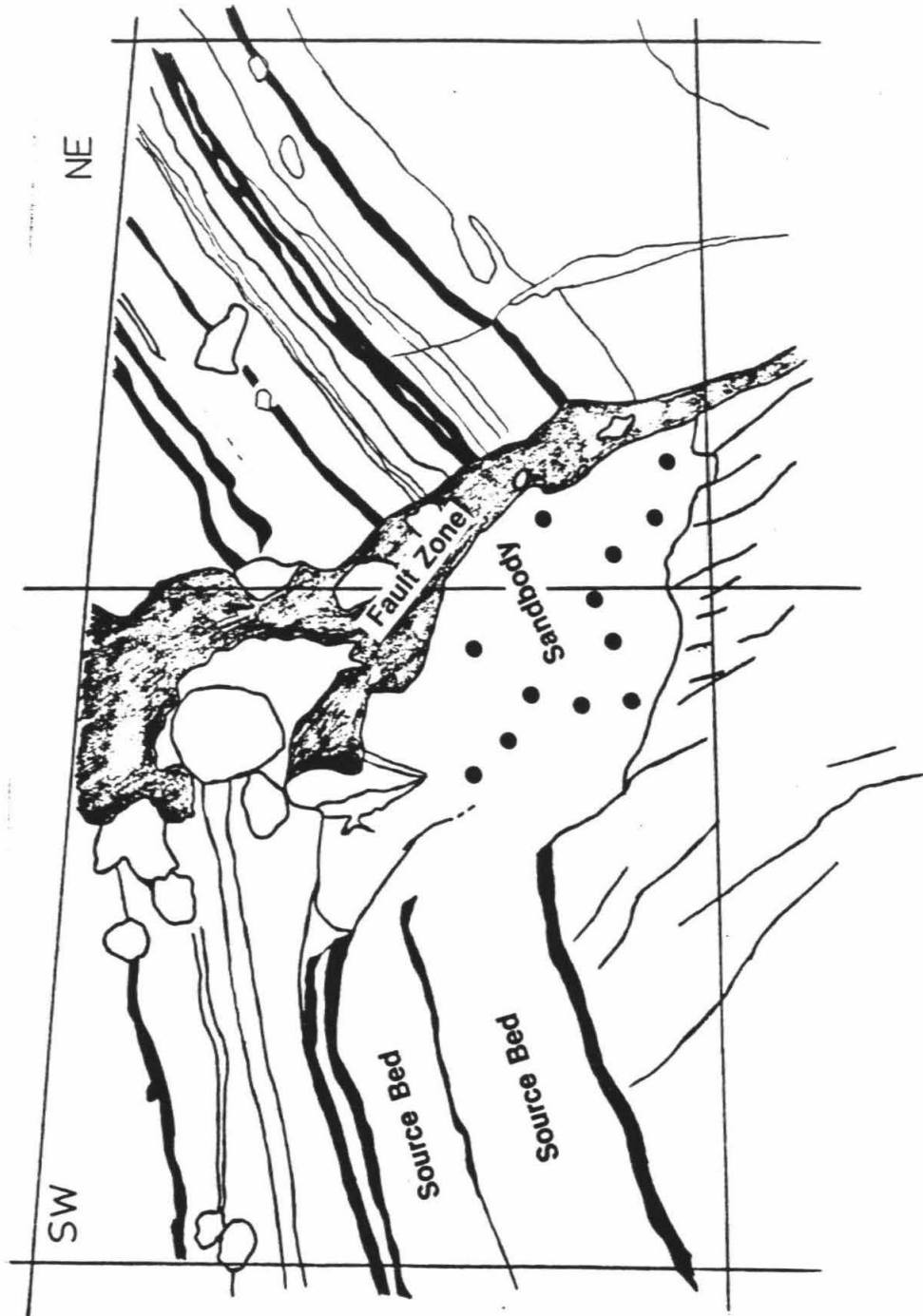
others, 1985) is shown in figure 2.

Studies of this and nearby exposures show that from 3 to 5 earthquakes have involved faulting at this location during the past 700 years (Rockwell and others, 1985).

During the earthquake of A.D. 1310 \pm 50, the sandbody in figure 2 formed. Excavation showed that this sandbody had dimensions of 3 meters along the fault by 0.75 meters across the fault and that it filled a small graben formed in the fault zone (Rockwell, personal communication). The sandbody is made of a well-sorted fine to medium sand and shows no laminations or bedding. In addition, the sandbody contains thin wisps of peat traceable back to the peat layer between the source beds and suggesting flow from the source beds. The material comprising the sandbody is indistinguishable from the sandy layers the sandbody connects with. The structure and material of the sandbody strongly suggest it formed by liquefaction and flow of the associated sandy layers rather than fluvial filling of the graben.

Twelve soft-sediment samples were taken from throughout the liquefied sand body and six samples were taken from each of the source beds. These samples were processed by the standard method described in Appendix 1. Figure 3 shows typical demagnetization paths for a sample from the sandbody and a sample from the lower source bed. The samples from the sand body show one good component of magnetization and were stable to 570° C. The samples from the upper source bed were unstable. Samples from the lower bed were stable

Figure 2
Line drawing of the sandbody and source beds exposed in the wall of the Glen Ivy trench across the Elsinore fault. The grid lines are one meter apart, the view is to the northwest. Individual sample locations are shown by dots. Drawing from a photograph.



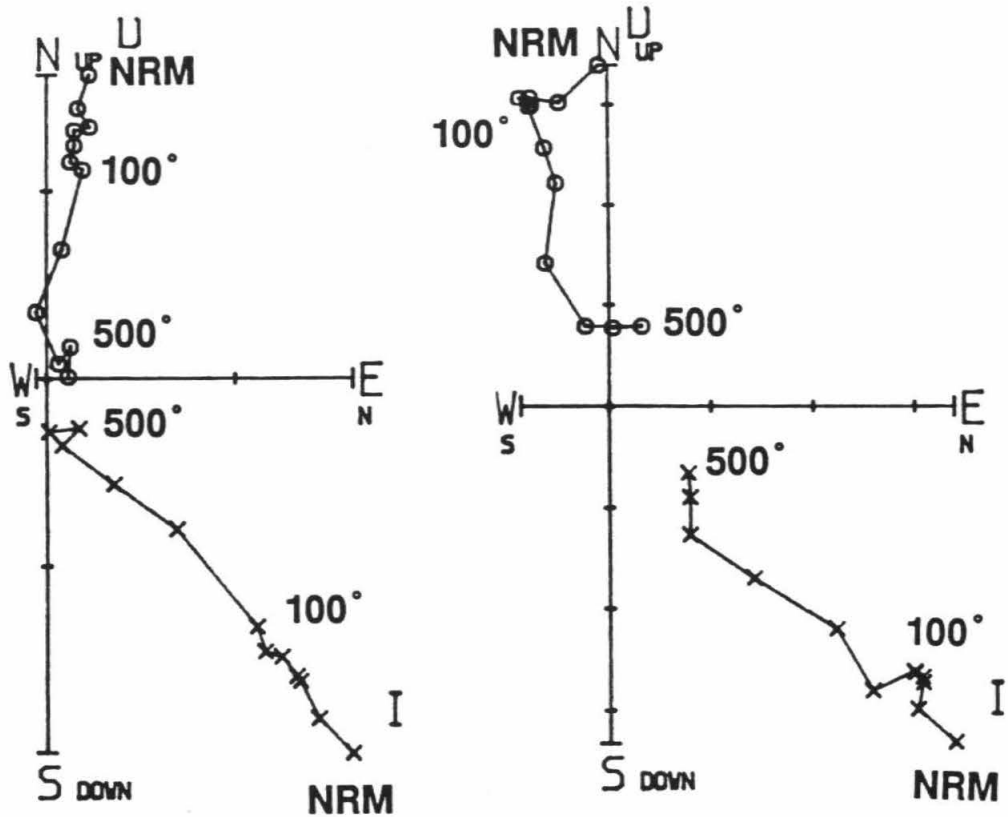


Figure 3

Orthogonal vector demagnetization diagrams for (a) sandbody and (b) lower source bed. One division equals 10^{-5} emu in (a) and 10^{-6} emu in (b). Declination indicated by circles, inclination by x's. An explanation of orthogonal vector demagnetization diagrams is provided in the last section of Appendix 1.

to 400° C. The directions from these six samples cluster well with a Fisher precision parameter of 106.7 ($k=106.7$) (table 1).

The component directions for all twelve samples from the sand body cluster moderately well with $k= 40$. Inspection of the equal-area stereonet plot in figure 4 shows three sample directions away from the main cluster of directions. Rejection of these three samples increases the kappa to $k= 102.5$. These three samples are all from near the base of the sand body, about 5 cm from the lower contact. It is possible that this region sheared as the sand flowed and the magnetic directions of these samples did not efficiently realign. Games (1986) observed a similar effect, and found that samples taken from the corners of the adobe mold frequently do not align well with the magnetic field direction.

In figure 5, the group directions for the sand body and the source bed are both displayed. The mean directions differ and the alpha-95 confidence ellipses do not overlap. In this case, the sand has been disrupted, but it has a strong and stable magnetic direction.

In addition, figure 6 shows the distribution of NRM intensities in the sandbody and the source beds. The NRM intensities of the samples from the sand body are significantly higher than the NRM intensities of the source beds. Assuming that the populations of NRM intensities are normally distributed, the magnitude increase does represent

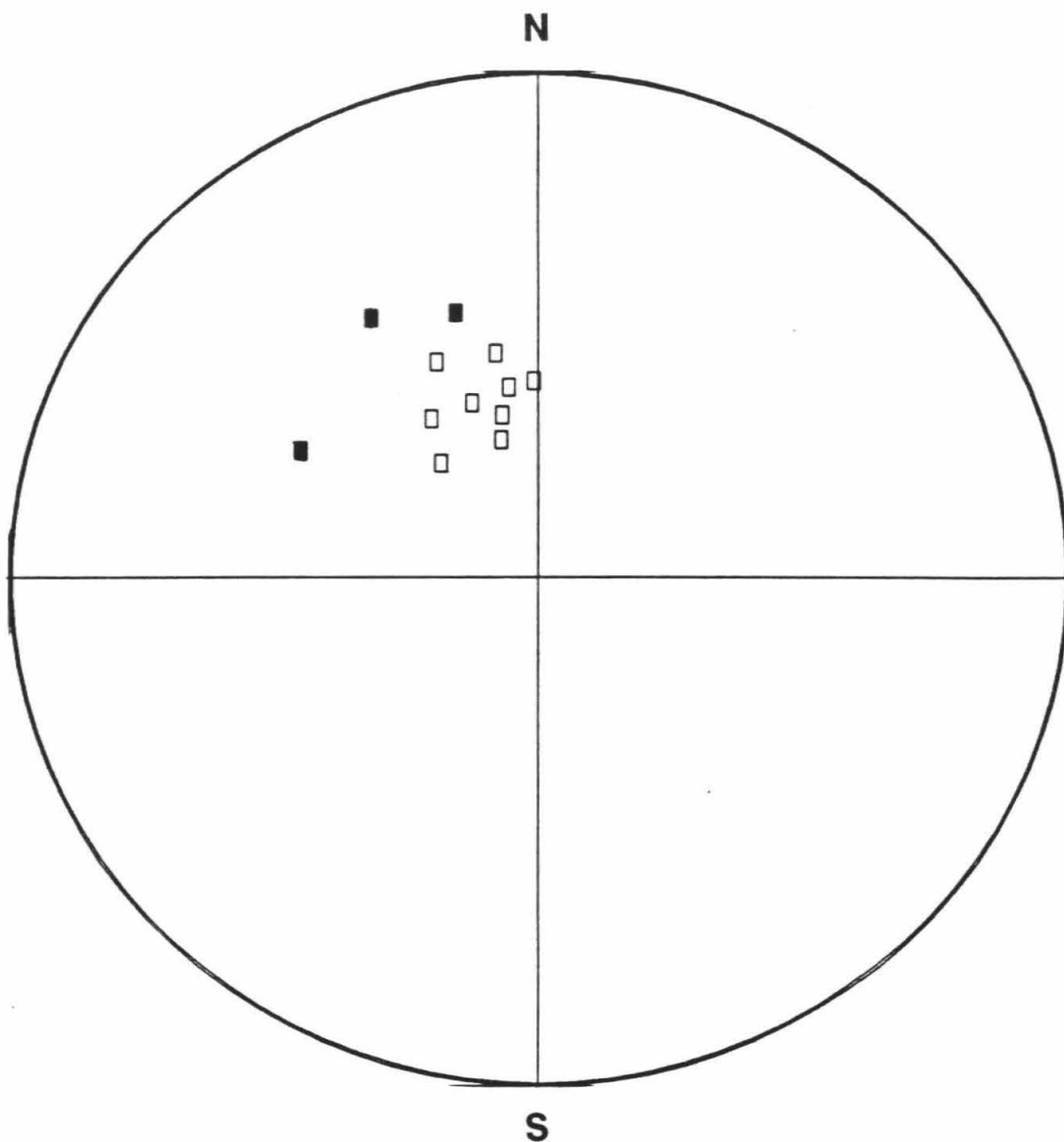


Figure 4

Equal-area plot of all sample directions from the sandbody. The three sample directions marked by the solid squares were discarded, as discussed in the text.

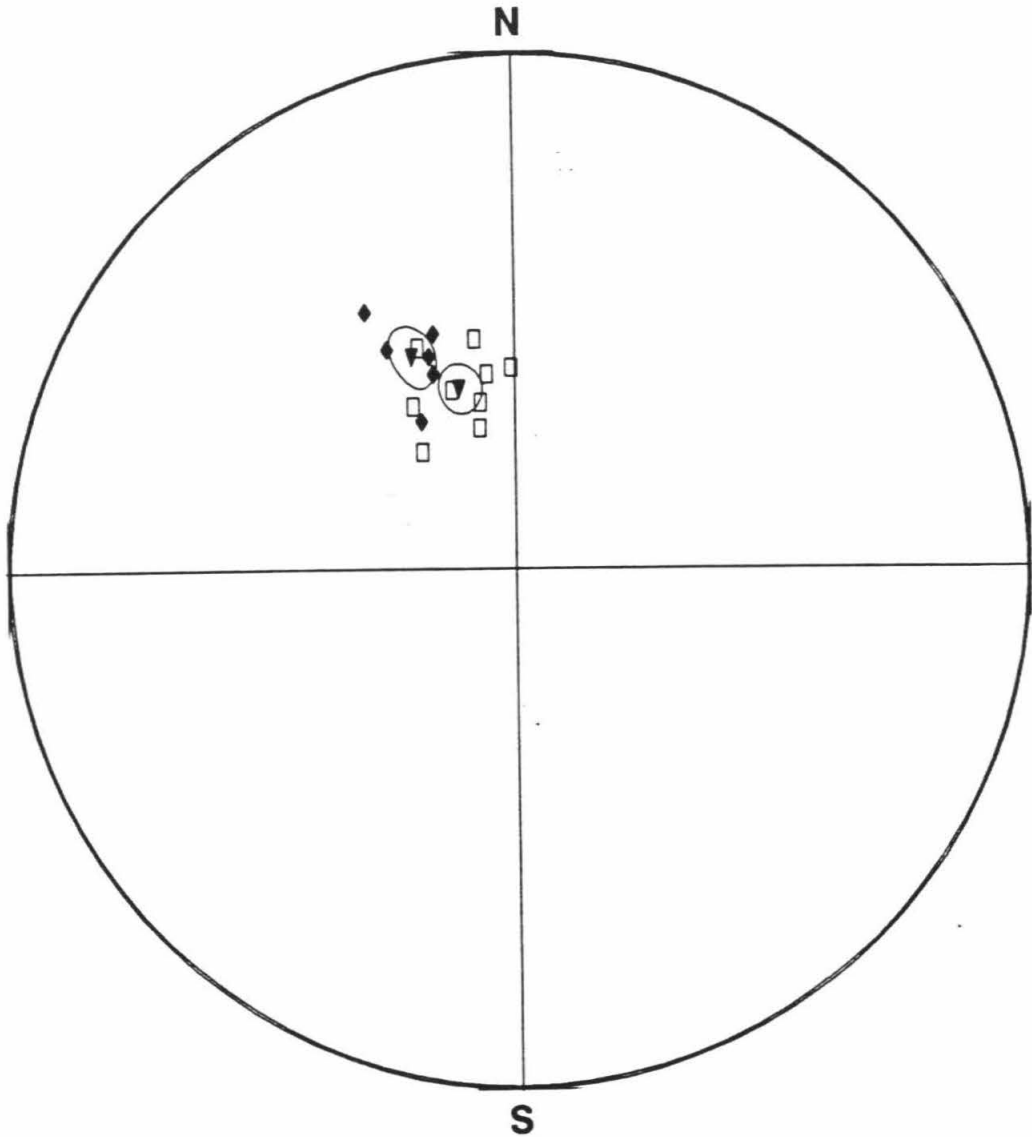


Figure 5

Equal-area plot of the sample directions for the sandbody (open squares) and its lower source bed (filled diamonds) with group means (filled triangles) and 95% confidence limits on the group means.

NRM Intensity

Liquefaction features vs. source beds

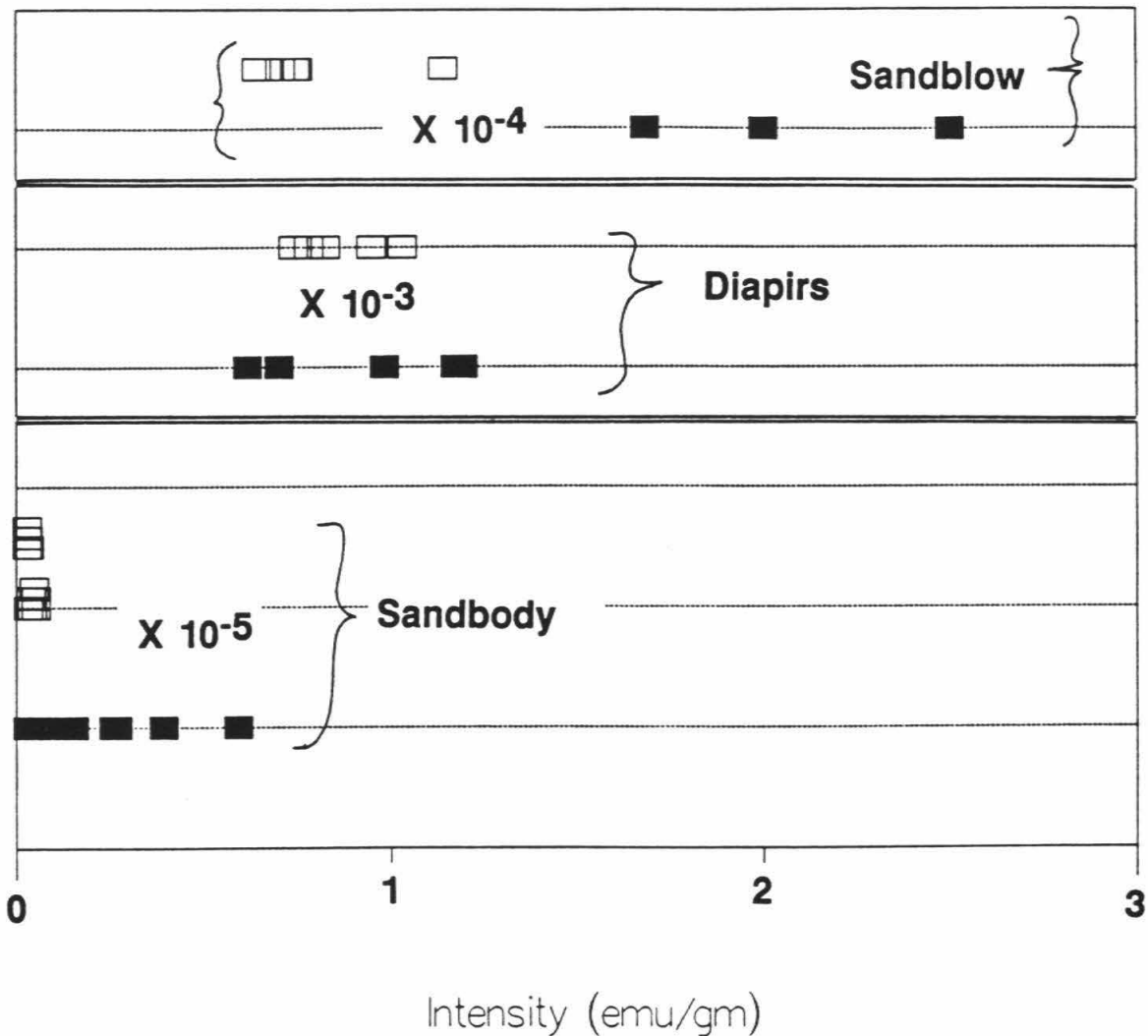


Figure 6

Plot of the NRM intensity variation. For each liquefaction feature the NRM intensities of the samples from the feature (filled squares) are compared to the NRM intensities of the source bed (open squares). The intensity scale is relative and the absolute magnitude of the intensities is given next to the data. The significant increase in intensity in the sandbody and the sandblow is apparent.

a statistically meaningful difference at the 99% confidence limit.

Table 1

Liquefaction Features

Feature	No. of Samples	Kappa	Alpha-95	Mean	
				Dec.	Inc.
Sandbody	9	102.5	4.61	-17.7	60.3
Source beds	6	106.7	6.52	-26.8	52.4
Diapirs	5	177.3	5.8	2.3	59.8
Source beds	5	198.6	5.4	2.4	53.8
Sandblow	3	130	7.09	2.1	48.1

Results from Soft-sediment Diapirs at Mono Lake

Soft-sediment diapirs are a form of deformation commonly seen in recent lake sediments, as well as in older sediments in the geologic record (Blatt, Middleton and Murray, 1980). I sampled five small diapirs exposed in a pit

dug into sediments that until 1981 were submerged beneath the waters of Mono Lake, California (figure 1). At the time the diapirs formed the whole layer probably liquefied. Comparison of the source bed's and diapirs' magnetic directions will show if the DRM was reset at this time, or only rotated in formation of the diapirs.

The sampled layers are composed of volcanic ash from the most recent eruption of the Mono Craters about A.D. 1350. The diapirs represent liquefaction event 2 of Sieh and Bursik (1986). Where undeformed, the sampled bed is a 1.5-cm thick, brown, fine volcanic ash. Where deformed, the ash pierces the overlying unit, a medium to coarse sand size ash (figure 7). In cross section these diapirs are about 2 cm across and 3 cm high, just about the minimum dimensions necessary for sampling.

Five samples were taken from locations where the bed was undeformed and five individual diapirs were sampled, one sample per diapir. Linear demagnetization paths indicated that all of these samples were very stable. Figure 8 shows a representative demagnetization path for a sample from a diapir. The samples from the source bed were also magnetically stable and had similar demagnetization behavior. As seen in figure 9 and table 1, the sample directions from the principal components cluster well for both groups.

Liquefaction probably occurred throughout the source bed, so if an LRM is acquired the source bed and diapirs

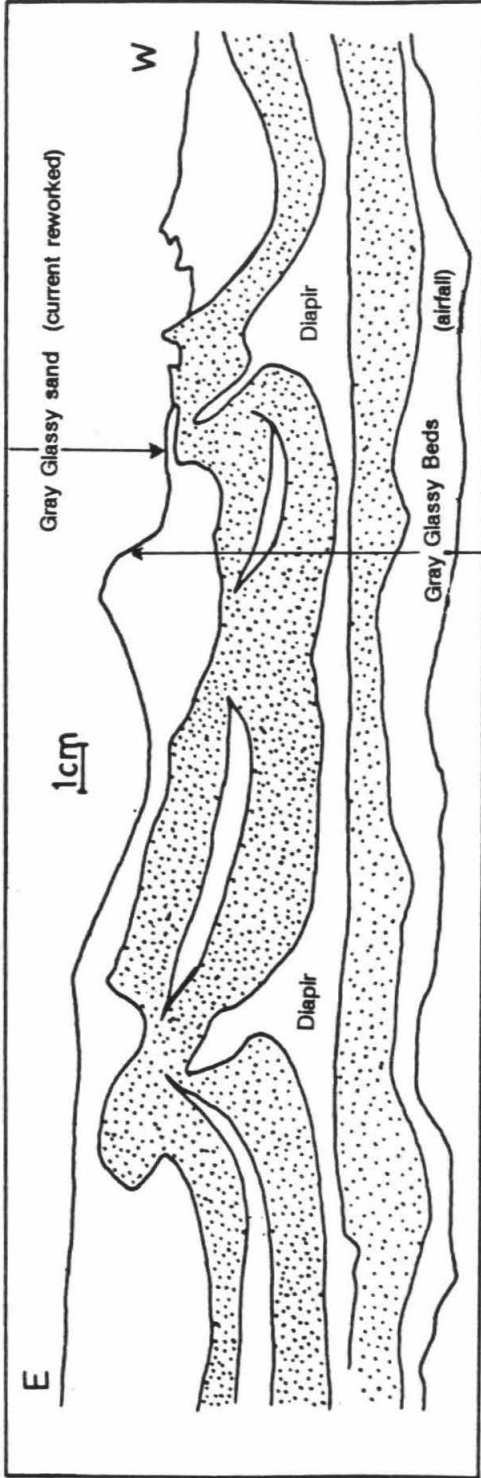


Figure 7
 Drawing of two of the sampled diapirs in Mono Lake sediments. This drawing represents only a portion of the pit wall. Coarser volcanic ash shown by stippled pattern.

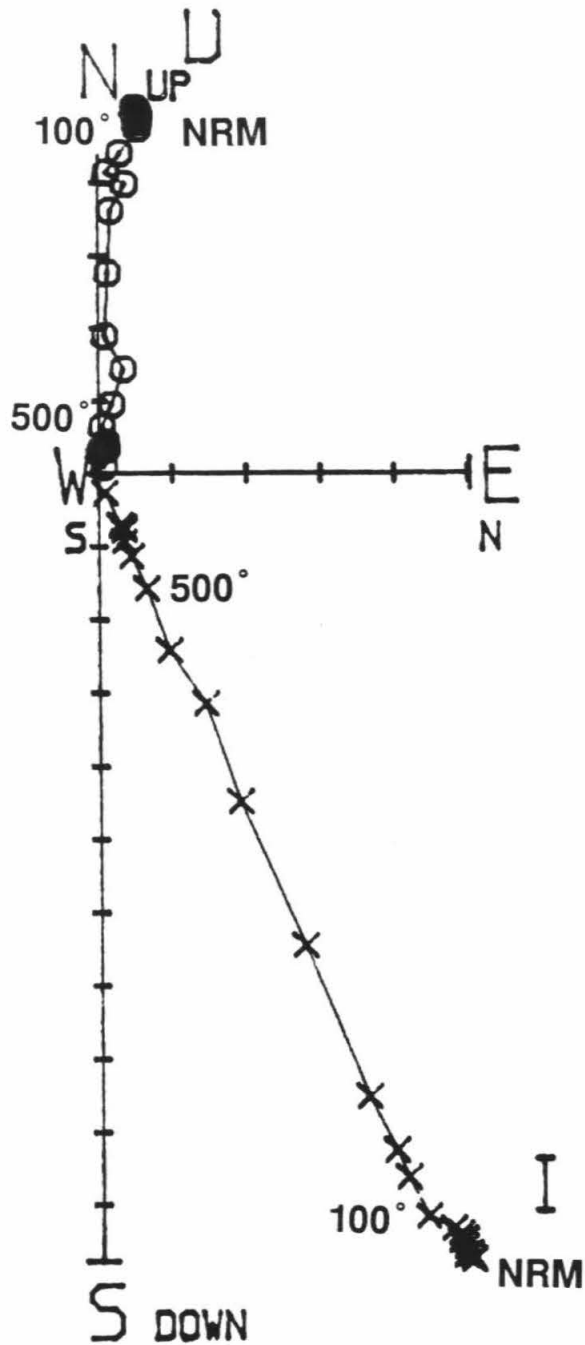


Figure 8

Orthogonal vector demagnetization diagram of a typical diapir sample. Circles are declination, x's are inclination, one division equals 10^{-4} emu.

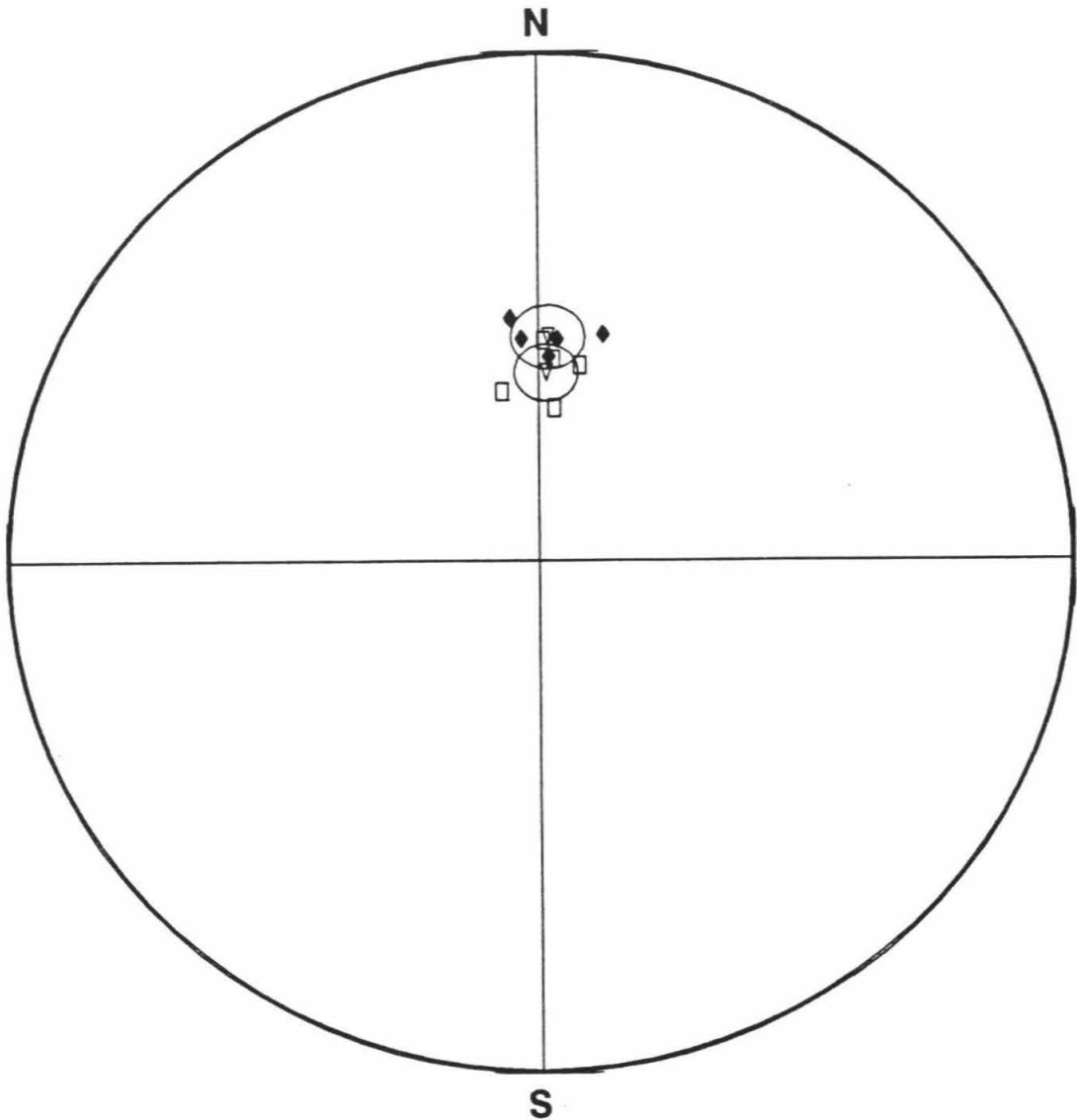


Figure 9

Equal-area plot of sample directions from diapirs (squares) and source bed (filled diamonds). Mean directions shown by triangles and the ovals are 95% confidence limits on these means.

should have the same magnetic direction. This is confirmed, since there is no statistically resolvable difference between the confidence regions of the means of the group directions (figure 9).

Physically, it seems unlikely that a diapir could form and retain its pre-deformation magnetic direction. Diapirs begin as instabilities in a bed overlain by denser material. To achieve complete stability the layers need to reverse their stratigraphic order so the denser material is below the lighter. This is seldom accomplished, but for a large enough density contrast, pieces of the underlying material can flow upward into the denser bed. Seismic shaking can induce or accelerate this process.

This upward motion is best accomplished as a fluid-like flow. Initial formation and continued building of the diapir requires horizontal flow of the material into the diapir from the sides. The material accumulates, and when the diapir becomes large enough it flows upward. This transport of material would be very difficult with rigid blocks and so this possibility seems unlikely.

Another alternative to the interpretation that the magnetic moment is an LRM is that this section has a post-depositional remanent magnetization (pDRM). This magnetization would have been acquired after liquefaction and during the compaction of the sediments. After deposition the possibility exists that the magnetic minerals have the freedom to change orientation. If this happens,

the sediment records the magnetic field direction at the time the compaction restricts their motion. If this happened after the diapirs formed, the source beds and the diapirs will have the same directions.

It is unlikely that magnetic directions are a pDRM acquired much later than deposition. These units were deposited within a few months to a year or two of the Panum Crater block and ash flow discussed in Appendix 2. The close agreement between these two remanence directions argues against a delayed remagnetization event.

The intensity differences between the diapirs and the source bed is not as large as for the sandbody. As shown in figure 6, the diapirs only have a slightly greater range of intensities than the source bed does. The two groups do not represent two different populations when tested at the 95% confidence level. This agrees with the interpretation that both the source bed and the diapirs liquefied. Furthermore, the sample NRM intensities shown in figure 6 appear bimodally rather than normally distributed. The diapir intensities cluster at the ends of the source bed intensity range, suggesting that the diapir formation produced two different effects. In some of the samples there was enhancement of the resetting and a corresponding intensity increase. In other diapirs shearing dominated and the intensity decreased. With only five samples it is difficult to test this but the pattern is suggestive.

In light of the intensity comparison it is unlikely

that the source bed and the diapirs acquired their magnetic moments as a pDRM. Rather, the remanence of the diapirs appears to be a modification of the magnetization of the source beds. The diapirs show a large amount of deformation and for them to have retained an original magnetic moment through that deformation is unlikely. Since the eruption was over a period of only a few months to years (Sieh and Bursik, 1986) it is likely that the time interval separating the deposition and the disruption was short enough that the magnetic field had not changed a significant amount.

Results from Sandblows

Sandblows are another common manifestation of liquefaction, and are formed by the ejection of liquefied sand onto the ground surface. Since material is transported as individual grains and not as a block there is no doubt that any magnetic direction is post-emplacement. However, the material most commonly found in sandblows is fine to coarse sand. This can be because either these source beds are suited to being overpressurized and brought to the ground surface, or because this material is deposited in the sandblow and the fines transported away. Since medium to coarse sand is typically not magnetically stable, sandblows are not good targets for paleomagnetic sampling.

Of twenty samples taken from five different sandblows and clastic dikes feeding sandblows, only three samples, all from the same structure, showed magnetic stability.

Unstable samples were taken from sandblows in the Mono Lake sediments and a clastic dike at Pallett Creek. Some of these samples showed marginal stability, but the samples in a group from the same structure were significantly scattered, possibly a result of shearing during flow.

The stable samples came from a sandblow exposed in the same pit in which the diapirs were exposed. The sandblow consists of medium lapilli-size volcanic ash and represents liquefaction event 5 of Sieh and Bursik, 1986. The sandblow is the top layer in the sequence of volcanic deposits that accumulated at this site in, at most, a few years (Sieh and Bursik, 1986), and post-dates deposition of the ash associated with the third Inyo eruption of about A.D. 1365 (Miller, 1985). The lack of sublacustrine reworking of the Inyo ash, and a lack of accumulated organic deposits between the ash and the sandblow, indicate that the sandblow must have been deposited soon after the eruption. Because of this short time interval I expected no difference in direction between the sandblow and its source bed.

Both the sandblow and its source bed were sampled. The three samples from the sandblow cluster with $k=130$ and an alpha-95 of 7.09 (table 1). The source beds were not magnetically stable but the immediately overlying unit (the source bed for the diapirs) was stable. Sieh and Bursik (1986) concluded that this series of volcanic ash layers accumulated rapidly and so the period of time between the deposition of the sandblow's source bed and the deposition

of the source bed of the diapirs was small. The samples from the diapir source bed cluster with $k=199$ and an alpha-95 of 5.4. Figure 10 shows that the mean directions are separated but the error ovals overlap.

Because sandblow emplacement requires complete mobilization and disarticulation of the source bed, its DRM must have been reset. Since the time interval between source bed deposition and liquefaction is short, the fact that the resetting is not reflected in differing directions is not surprising. Since the declinations are nearly identical, the shallower inclination of the sandblow can easily be due to inclination error in the sediments.

As with the samples from the sandbody in the Elsinore fault zone, the NRM intensities differ by a statistically significant amount (figure 6). Samples from the sandblow have intensities close to an order of magnitude higher than the source beds. If the populations are normally distributed this difference is verified at the 99% confidence limit.

Discussion

The most intriguing result from this study of liquefied sediments was the increase in the NRM intensity of the liquefied samples over their source beds. In the case of the sandbody and the sandblow this is an increase of up to an order of magnitude. At least two plausible mechanisms that could cause this increase require mobilization of the

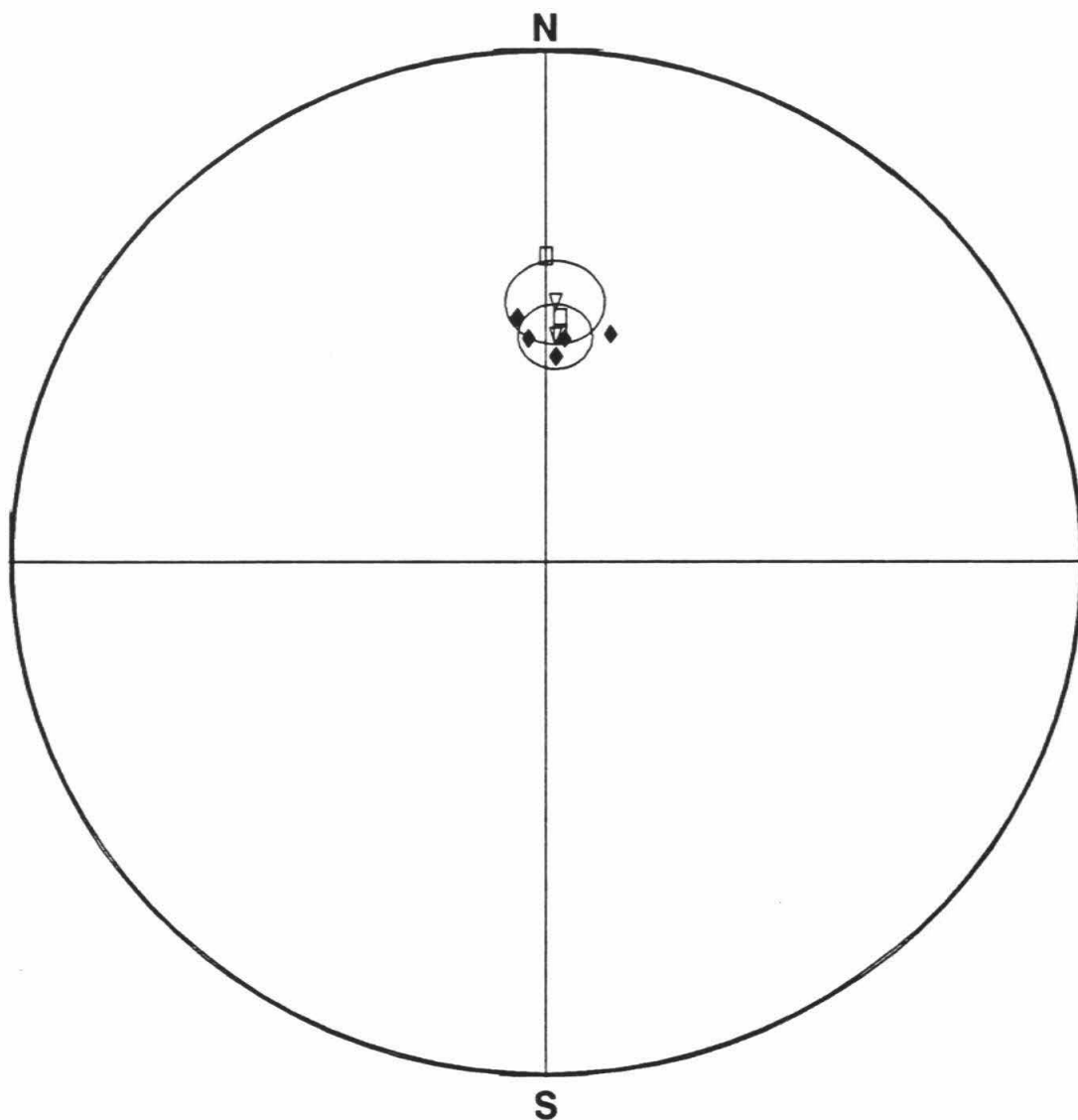


Figure 10

Equal-area plot of sample directions from sandblow (squares) and a bed of same age as the source bed (filled diamonds). Triangles are mean directions and the ovals are 95% confidence limits on these means.

material and are worth brief consideration here. These are: 1) the composition of the material is the same, but the liquefaction has improved the alignment of the magnetic minerals in one of the units and/or scattered the alignment in the other and 2) the liquefied unit has changed composition by sorting and has increased the content of magnetic minerals so the unit can hold a greater magnetic moment.

One argument for the latter is that the units showing the largest increase in intensity are the units transported the furthest and so they have the greatest opportunity to undergo sorting. However, because these units were transported the furthest, they have also had the greatest mobilization of the magnetic grains and the greatest opportunity for realignment. The possibilities can be distinguished by measuring the saturation magnetization of each of the units.

That these three liquefied and disrupted units show a magnetic remanence demonstrates that resetting of the detrital remanent magnetization by liquefaction, or a liquefaction remanent magnetization (LRM), exists. In addition, the LRM appears to have an associated increase in the magnetic intensity of the material over the NRM intensity. Further work could tell us the association of this LRM to the intensity of the shaking and whether it is a faithful recorder of the magnetic field direction.

If the liquefied body has not experienced significant

rotation or deformation, then the LRM direction holds the potential to date seismic events. This would be accomplished by matching the LRM direction to the secular variation curve constructed in Chapter 2.

As a test of this technique each of the LRM directions discussed in this chapter are plotted on this southern California secular variation curve (figure 11). The sandbody shows a significant westward declination but the declination and inclination directions both coincide with the curve between A.D. 1064 and 1300. This agrees well with the radiocarbon age of A.D. 1310 \pm 50.

The diapir and sandblow directions were previously compared with the Panum block and ash flow direction, one of the directions used to construct the curve. The geologic constraints indicate that these liquefaction features are temporally close to the Panum eruption. The declination and inclination of the diapir LRM agrees well with the Panum crater direction. The declination of the sandblow LRM also agrees well with the Panum direction. Although the sandblow inclination intersects the Panum direction the inclination is significantly shallower, and, as discussed before, may be a result of inclination error.

The diapir and sandblow directions agree with a large portion of the secular variation curve, not just the Panum direction. Additional age ranges include A.D. 675-700, 1060-1160, 1275-1300, 1350-1400, 1475-1500, and 1904-1910. Interpolating between the data points the diapir and

Southern California Secular Variation

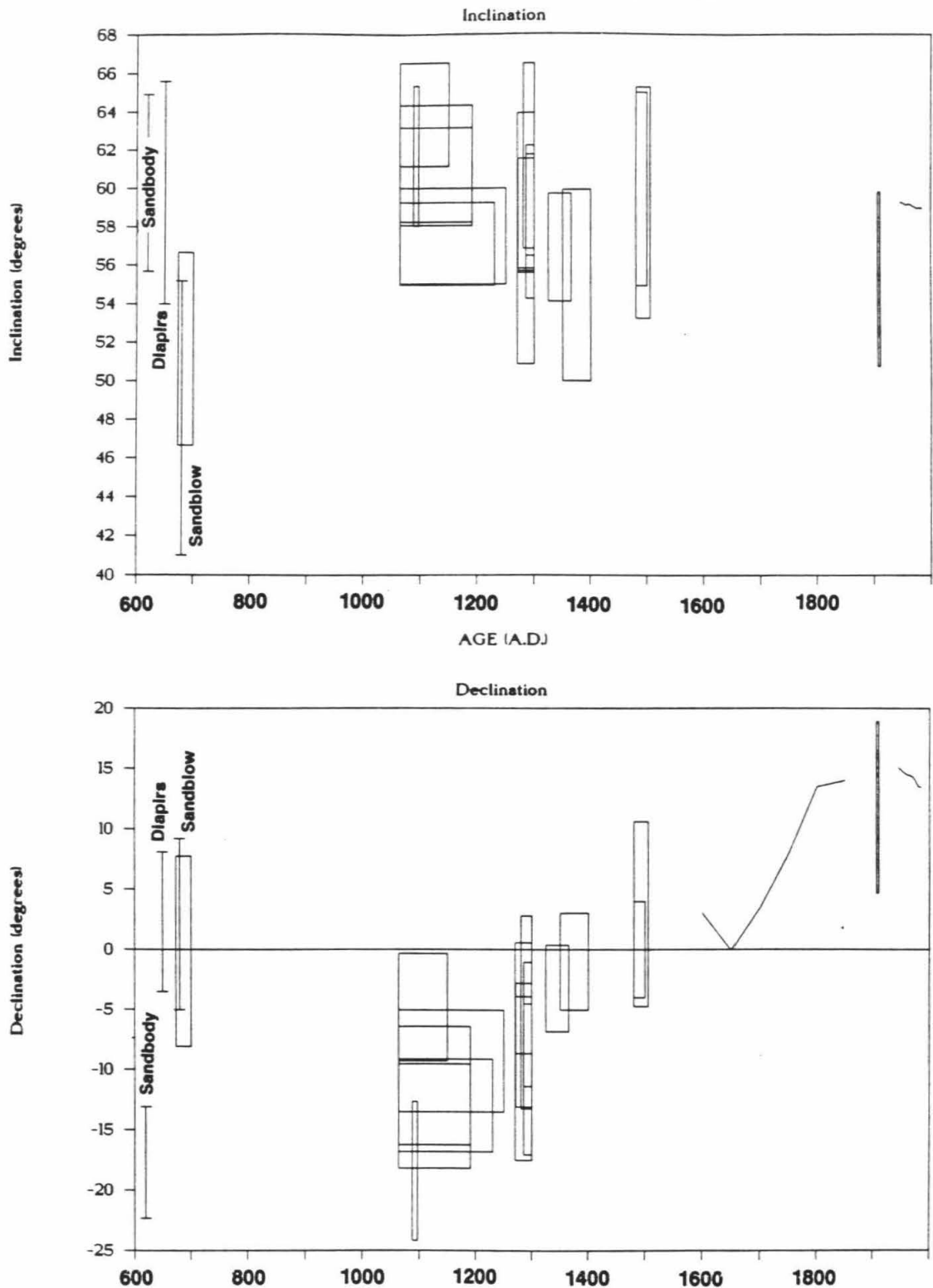


Figure 11

Secular variation curve for southern California from Chapter 2. The LRM directions from this chapter are plotted on the left side of this curve.

sandblow would correspond with the whole age range A.D. 1275 to 1910. This uncertainty reflects the large errors on both the directions of liquefaction features and the translation error in the secular-variation-curve data points. This reaffirms the need to construct secular variation curves based on local data to reduce the geographical translation errors discussed in Chapter 2.

Another problem that may be related to the large westward declination of the sandbody is the possibility of deformation in the fault zone. The Elsinore fault has a right-lateral sense of offset so "fault drag" would produce eastward rotations. However, close to the fault complexity could produce westward rotations. This could be a problem because of the tendency for liquefaction features to occur in fault zones. This could render LRM directions useless. However, if there is no possibility of deformation, as in the case that the liquefaction occurred in the most recent earthquake, then LRM directions provide a useful technique for dating seismic events.

Chapter 5

**Paleomagnetic Measurement of Non-brittle Deformation
Across the San Andreas Fault at Pallett Creek**

Abstract

In this chapter I use paleomagnetism to address a problem at the Pallett Creek paleoseismological site. The brittle long-term slip-rate is a quarter of the expected value and the best explanation for this deficiency is that the additional slip is accumulating as non-brittle deformation. I collected 264 paleomagnetic samples from two units bracketing the third earthquake back, which occurred in about A.D. 1480. These samples span 53 meters of the fault zone perpendicular to the trend of the fault. Control groups of ten samples, collected from each unit at the furthest point from the fault, appear to be unrotated. Groups of samples have mean declinations of up to 30° ; the older group shows higher declinations. Interpreting this deformation as block rotation, the older unit has 14.0 ± 2.9 meters of right-lateral, non-brittle offset and the younger unit has 8.5 ± 1.0 meters of non-brittle offset. Combined with the brittle offset across the fault plane, the last three events had offsets of 5.5, 6.25 and 6.25 meters, with a long-term average slip-rate of 35.6 ± 6.7 mm/yr.

Introduction

Motion across a fault zone may result in two types of deformation. Brittle deformation is expressed as discrete offset across narrow fault planes and fractures. Non-brittle deformation is expressed as rotations within the fault zone.

Because it is more difficult to recognize and quantify, non-brittle deformation is only rarely evaluated in paleoseismic and neotectonic studies. This omission may result in an underestimation of offset magnitude associated with individual faulting events and in underestimation of fault slip rates.

Such underestimates may significantly affect kinematic interpretations and evaluation of seismic hazard. For example, calculation of recurrence intervals for earthquakes, by division of measured brittle slip by a geodetically determined slip rate, may yield intervals far shorter than actual intervals. Variations in the slip rate of a fault, determined from studies at different locations along strike, may be misinterpreted as having regional tectonic significance, when, in fact, the variations are due to variable amounts of undetected non-brittle deformation.

Measurement of non-brittle deformation is usually difficult and often impossible. In pervasively deformed rocks, distortion of fossils, pebbles, and other shapes with known original dimensions may enable estimation of non-brittle deformation (Ramsay and Huber, 1983). Anomalous

bends in reference lines that cross faults at high angles may also be used to estimate non-brittle deformation, but this is hampered by the fact that the initial linearity of such features is difficult to prove.

The best use of deformed reference lines for this purpose may well be Thatcher and Lisowski's (1987) use of fence-lines that were disrupted by the San Andreas fault in the 1906 San Francisco earthquake. These fences, shown in figure 1, show that 0 to 60 % of the total right-lateral deformation across the fault zone occurred as non-brittle warping.

Traditional methods of paleoseismology and neotectonics only measure the brittle offset across a fault. The non-brittle deformation of the fault zone is the largest unknown in the estimation of the total slip-rate across a fault.

In some cases, paleomagnetism provides a method of measuring the non-brittle deformation in a sediment or rock. A synchronously deposited body of rock or a stratum should acquire the magnetic field direction existing at the time of its deposition. Deformation or wholesale rotation of the rock mass or stratum will result in changes of the orientation of its magnetic moment. Comparison of these altered paleomagnetic directions with the original unrotated direction should enable quantitative analysis of the total rotation and deformation.

In this chapter, I apply this paleomagnetic tool to a significant problem of non-brittle deformation in late

NE

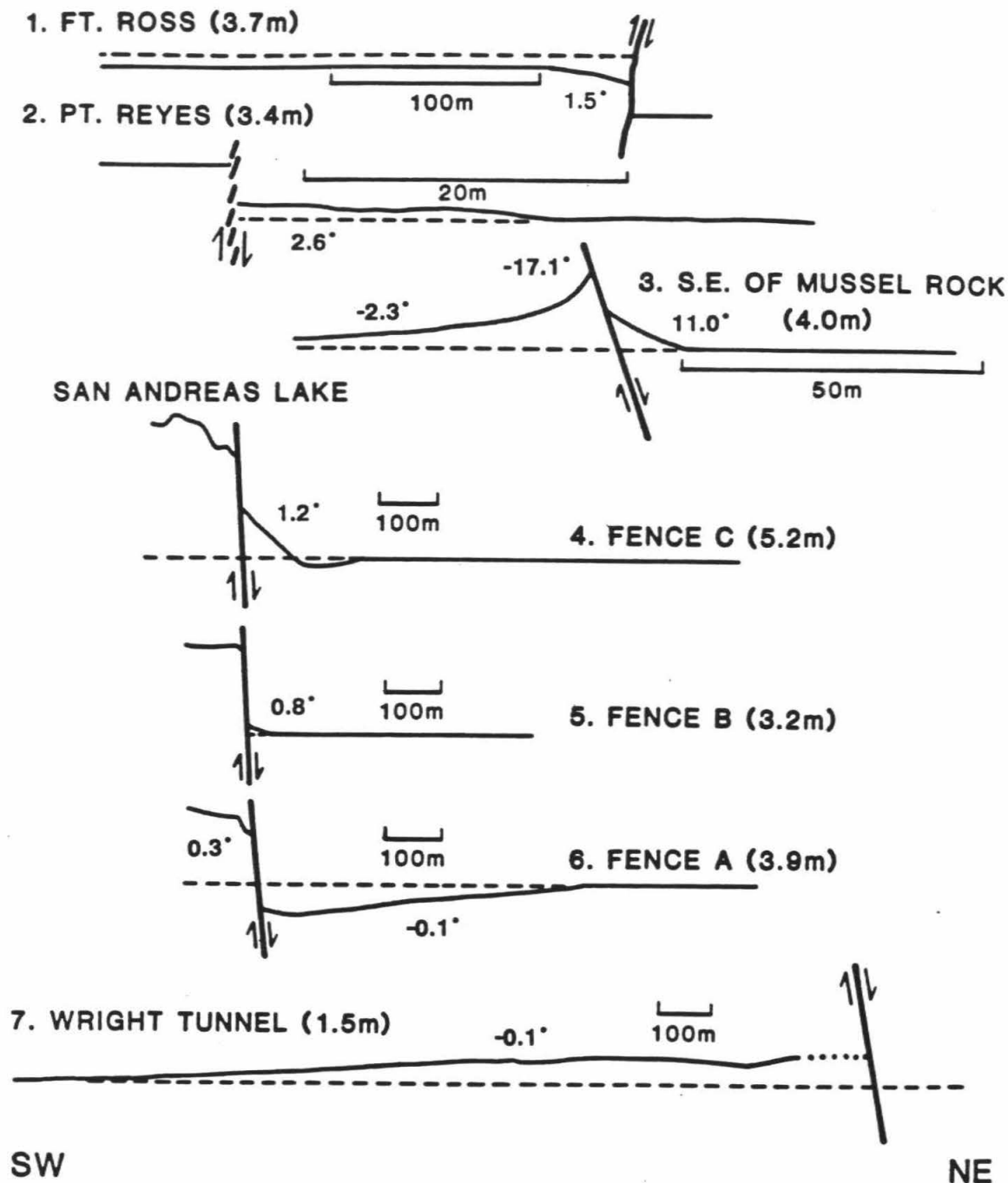


Figure 1

Fence lines from Lawson and others (1908) analyzed by Thatcher and Lisowski (1987). The tectonic, structural line rotation is indicated next to each fence. The horizontal scale is marked and the vertical scale is given by the brittle offset listed in the figure.

Holocene sediments along the San Andreas fault.

Problems at Pallett Creek

The Pallett Creek paleoseismic site, 55 kilometers northeast of Los Angeles, has for several years presented a disturbing problem. Although the 8-meter-thick series of unconsolidated sediments there provides an astounding record of the latest 12 large earthquakes (Sieh, 1978, 1984; Sieh and others, in press), the rate of right-lateral fault slippage determined there is only about 9 mm/yr. This is less than estimates derived elsewhere along the San Andreas fault (Weldon and Sieh, 1985; Schwartz and Weldon, 1987) and far less than values seemingly required by plate-tectonic models and geodetic data (Minster and Jordan, 1987). Slip measured for the past three earthquakes, using various piercing points excavated out of the sediments, are only 2, 2, and 1.5 meters (Sieh, 1984), less than half of the values suggested from offset landforms along the same fault trace several kilometers to the northwest (Sieh, 1978b).

The location of the Pallett Creek site near a major left step in the recent trace of the San Andreas fault (figure 2) led Sieh (1984) to suspect that significant non-brittle deformation was present at the site. He speculated that dextral warping in the blocks adjacent to the fault would account for the unexpectedly low slip-rate determined from the offsets he measured and dated across faults there.

Fence number 1 in figure 1 is situated in a very

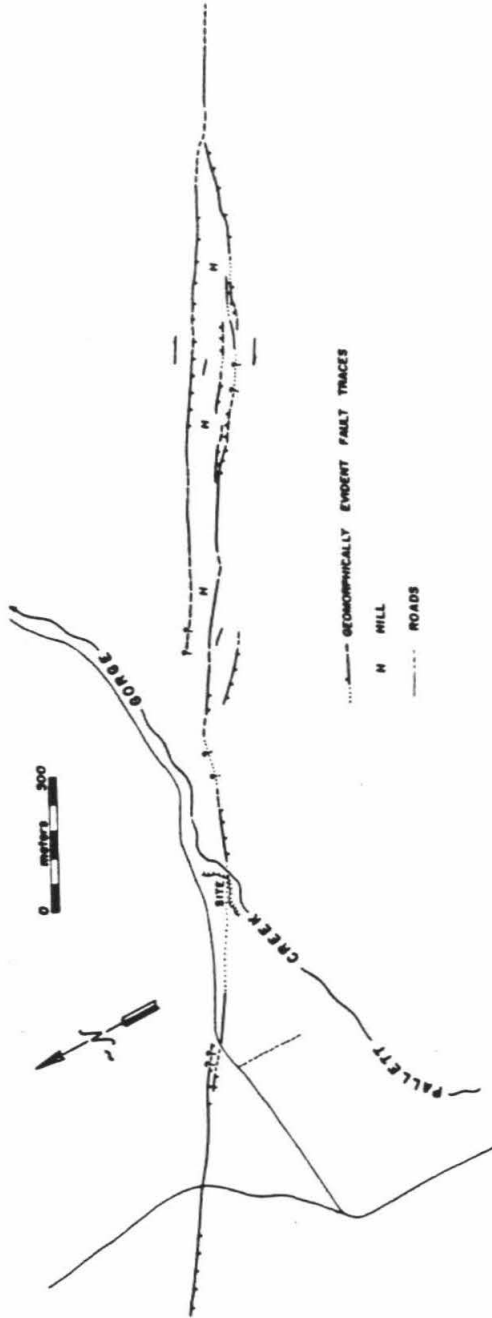


Figure 2

Geometry of the San Andreas fault in the area of the Pallett Creek paleoseismological site. Pallett Creek and roads (light lines) are also shown. The San Andreas fault is making a "left-step" to the southeast of the Pallett Creek site. (from Sieh, 1978)

similar setting near a left-stepover in the recent fault trace. There 38% of the total offset that occurred in 1906 occurred as dextral warp in a 130 m wide zone between the brittle offset and the extension of the adjacent fault trace.

Study Site

Three criteria must be met for a paleomagnetic study of recent rotations to succeed. The unit sampled must be magnetically stable, isochronous, and laterally extensive.

The necessity for magnetic stability is obvious, as the samples must have recorded the magnetic field at the time of deposition and not had this direction altered or overprinted. Unfortunately, stable magnetization of Holocene sediments adjacent to fault zones is rare. A previously attempted separation of magnetite from one peaty unit at Pallett Creek produced no magnetite (S.-B. R. Chang, personal communication). In other samples, secondary mineralization and multi-domain magnetite caused magnetic instability. I have found a large variation in the number of stable units at the sites I have sampled. At some sites a very small percentage of the units showed stability, whereas at other sites most of the units were magnetically stable.

The second requirement, that the unit be isochronous, is the most important and the most difficult to meet. The orientation of the earth's magnetic field changes by as much

as 5° in 50 years (see Chapter 2), so sampled horizons must be deposited in far less time than this. If samples from within a unit are not isochronous, differences in magnetic orientation may be due to secular variation of the magnetic field rather than tectonic rotation.

Finally, the unit must be laterally extensive, in order to sample across as much of the zone of deformation as possible. And, in order to determine the orientation of samples before rotation, unrotated samples from beyond the fault zone must be collected.

There is a fourth criterion which, although not necessary, I considered highly desirable for this pilot study. Conducting the study at a location where large deformation is suspected would help assure a measurable amount of rotation.

Sediments that have experienced only one earthquake may not have accumulated enough rotation to be measurable by paleomagnetism. Figure 1 shows the 8 structures from Lawson and others (1908) that Thatcher and Lisowski (1987) used to measure the non-brittle deformation. On this figure I have indicated the rotation of these structures by the non-brittle deformation. If the sensitivity of paleomagnetism to rotations is $\pm 4^\circ$ then only the most extreme deformation, that of fence 3 with 11° and 17° of rotation, will have enough to be visible by paleomagnetism. However, after repeating the deformation in two or three earthquakes, more of the fence lines will have accumulated enough deformation

to be visible. Therefore, paleomagnetism has the potential to measure deformation on these scales.

The Pallett Creek paleoseismological site meets all four of the criteria -- the sampled beds are magnetically stable, they are isochronous, laterally extensive, and large non-brittle deformation is suspected.

Since about B.C. 100, fluvial and marsh sediments have accumulated fairly continuously across the San Andreas fault zone at Pallett Creek. Only two "major" hiatuses occurred during this period. The first occurred during a major incision of the creek into the sediments between about A.D. 1100 and 1200 (Sieh and others, in press). The second began about A.D. 1910 (Sieh, 1978) and continues to the present day.

The accumulated sediments alternate between black, organic-rich layers and light brown to dark brown silts to coarse sands (figure 3). Sieh (1978) found the composition of the peat layers to be mostly of marsh plants. He suggested that during the times of organic accumulation the creek flowed through this area as a broad, diffuse sheet with abundant plant growth in this marshy area.

Excavation of these sediments revealed 12 individual faulting events in the last 1800 years (figure 3). Since many features characteristic of earthquakes are present at the times of these movements, aseismic motion is not a likely explanation for these events (Sieh, 1978).

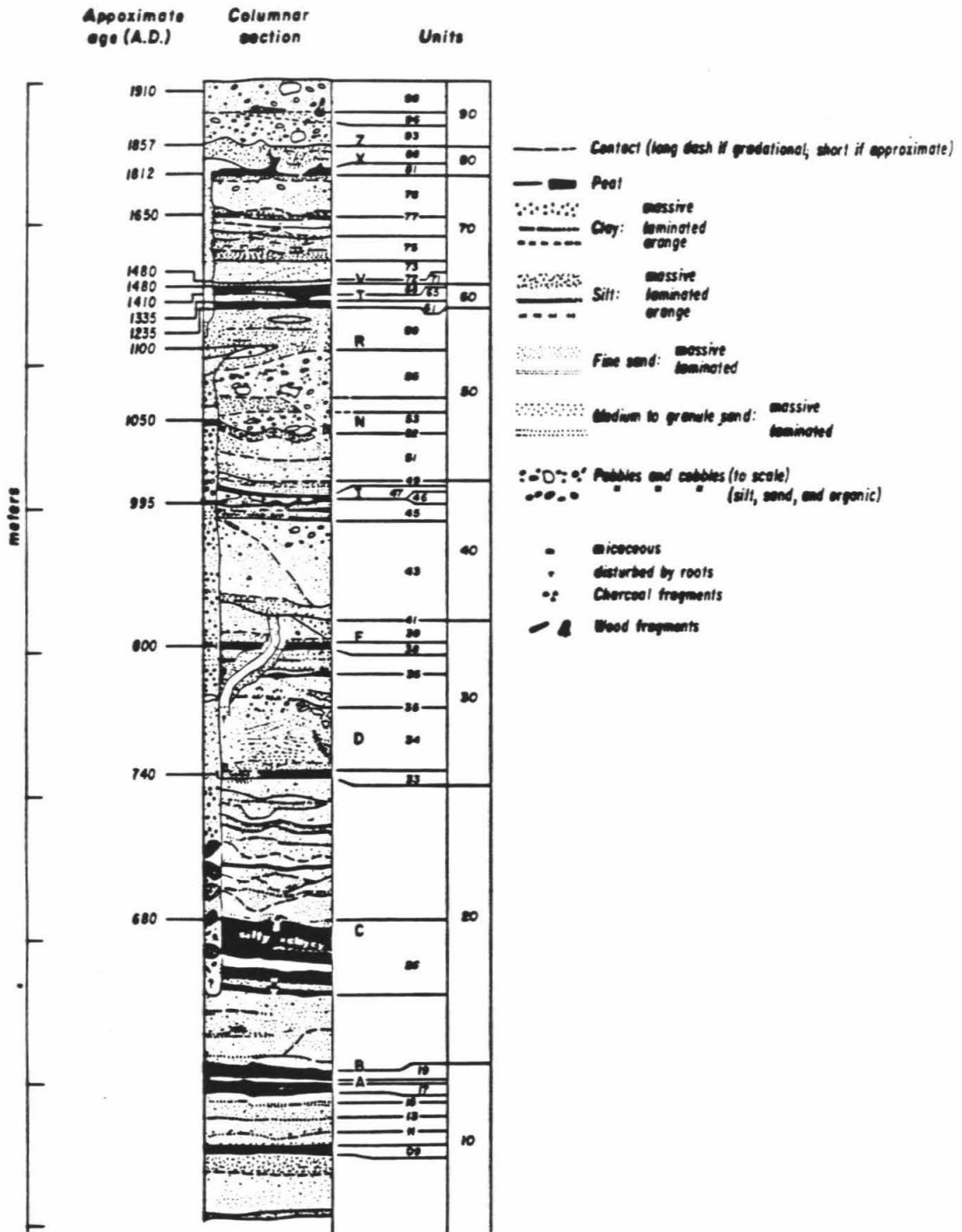


Figure 3

Stratigraphic section at Pallett Creek. Ages of selected units are indicated at the left. The base of the letters on the right are one the location of the ground surface at the time of that earthquake. (from Sieh and others, in press)

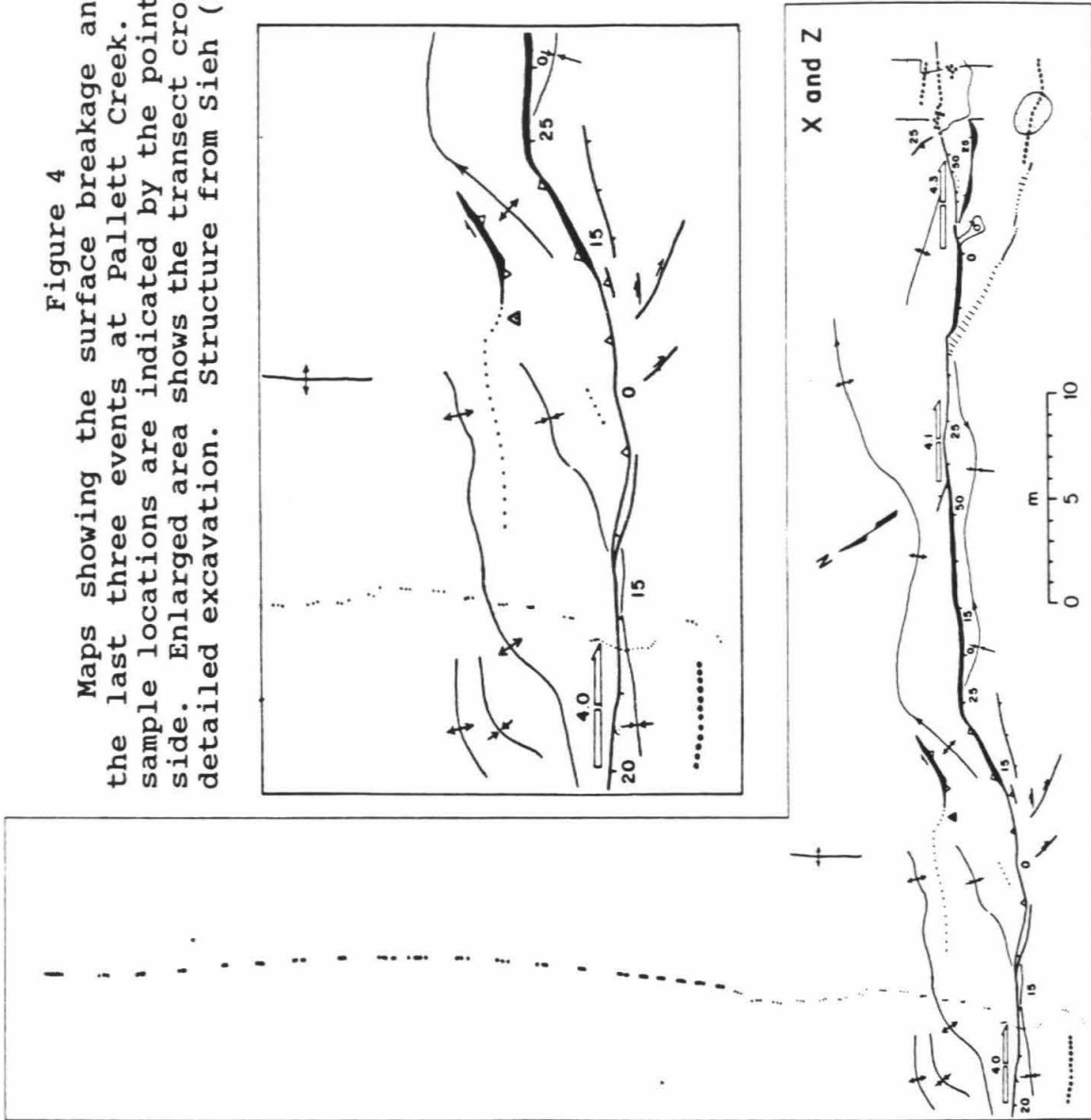
Data Collection

Initial analysis of samples from several different stratigraphic units at Pallett Creek showed that only a few units were magnetically stable (Salyards, unpublished data; E. Shoemaker and D. VanAlstine, personal communication). Of the magnetically stable units, units 68 and 71 post-date the A.D.-1100 incision, and so they are laterally extensive. Coincidentally, these units bracket the horizon of event V, the third earthquake back. Thus, the older of the beds, unit 68, has experienced three large earthquakes, and the younger, unit 71, has experienced only two. The top of unit 68 represents the peaty ground surface at the time of event V; it was deposited within the period A.D. 1479-1503; the base of unit 68 was deposited within the period A.D. 1397-1419 (Sieh and others, in press).

Unit 71, a 2- to 4-cm thick, eolian, very fine sandy silt (Sieh, 1978), is present throughout the area and immediately overlies unit 68. Unit 72, a thin peat immediately overlying unit 71, was deposited within the period A.D. 1457-1489. The merged ages of upper unit 68 and unit 72 constrain the age of unit 71, and event V, to A.D. 1480 ± 15 (Sieh and others, in press). The expressed uncertainty is at a 95%-confidence level.

I collected samples from an excavation cut perpendicular to the most recent trace of the fault (figure 4). This excavation extended fifty meters northeastward and

Figure 4
Maps showing the surface breakage and deformation in the last three events at Pallett Creek. The individual sample locations are indicated by the points along the left side. Enlarged area shows the transect crossing the area of detailed excavation. Structure from Sieh (1984).



three meters southwestward from the fault. The property line limited sampling to the northeast. To the southwest incision of Pallett Creek early in the twentieth century eroded and removed all but the three meters of the bed nearest the fault.

Figure 4a shows the lateral offsets and vertical deformation associated with the latest two events. About 2 meters of dextral slip occurred across the sampling transect during each of these events (Sieh, 1984). Figure 4b shows the lateral offsets and vertical deformation associated with the third event back. Note that no discrete rupture occurred across the transect, even though as much as 1.5 meters of dextral slip occurred only a few tens of meters to the southeast.

Dextral deformation of unit 71 should be added to the 4 meters of discrete dextral slip across the fault to derive a more complete measurement of the total dextral slip associated with events X and Z. Dextral deformation of unit 71, subtracted from that of upper unit 68 will give the total value of offset across the transect associated with event V.

From the excavation, I took groups of samples at regular intervals from the fault. The sampling scheme was the same for units 68 and 71. In the meter nearest the fault I took one sample every 10 cm. Between one and twenty meters from the fault, I collected a group of three samples every meter out to 20 meters. I collected a group of three

samples every two meters between 20 and 46 meters from the fault. Between 48 and 49 meters I collected ten samples from each unit. I hoped that the magnetic direction of this group collected at the farthest distance from the fault, would represent the magnetic direction of undeformed sediments. The larger number of samples in this control group was intended to provide a mean direction with a smaller uncertainty. Each sample locality was surveyed with a three-component electronic surveying instrument (Wild TC2000 "total station") accurate to ± 1 mm.

In addition, I collected a group of ten samples from a locality thirty meters from the fault at the southeast end of the site. These were collected as part of the pilot study to locate magnetically stable layers.

Collection, measurement and analysis followed the procedures described in detail in Appendix 1. Figure 5 shows typical vector demagnetization diagrams. The samples, in general, showed high stability with one good component of magnetization. From unit 68, 110 of 132 samples showed stable demagnetization, and 118 of the 132 samples from unit 71 were stable.

Because of previous observations that peat layers are magnetically unstable, I chose not to sample uppermost unit 68; instead I sampled a siltier zone in the center of unit 68. Unfortunately, but unavoidably, this led to poorer control on the age of the sampled stratum, because the age constraints on unit 68 are on the uppermost and lowermost

VECTOR DEMAGNETIZATION PATH

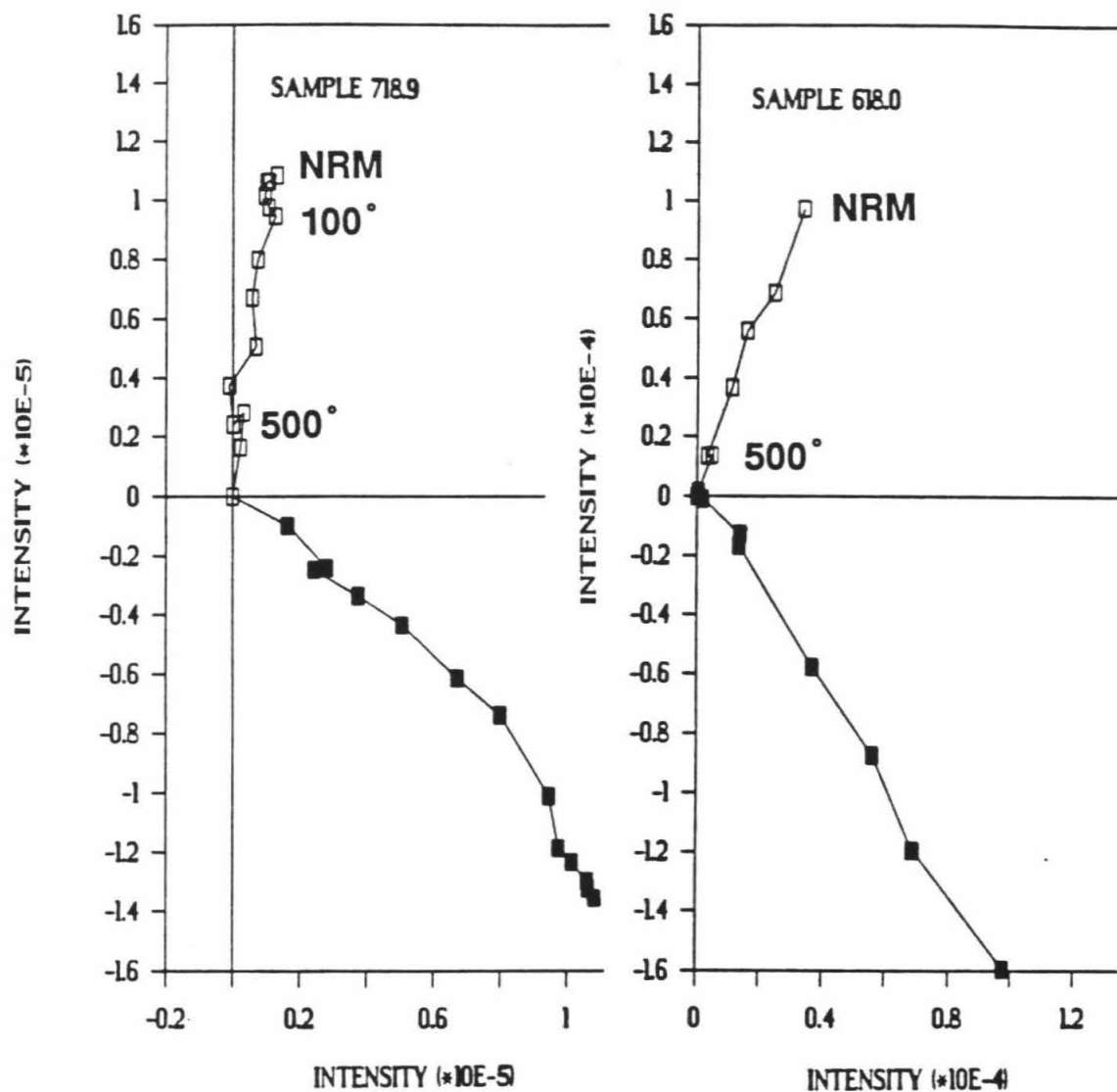


Figure 5

Orthogonal vector demagnetization diagrams for representative samples from unit 71 (left) and unit 68 (right). Open squares are declination, solid squares are inclination. An explanation of orthogonal vector demagnetization diagrams is provided in the last section of Appendix 1.

horizons. These dates only bracket the age of the center of the unit. In addition, by sampling in the center of the unit there is greater uncertainty in the synchronicity of the samples. A unique time horizon in unit 68 partially resolves this second concern. In places, the center of unit 68 is a brilliant orange color. This suggests burning of the normally black peat in a brush fire. This hypothesis is supported by the NRM intensities of the samples. These intensities range to values as high as 10^{-2} emu/gm, three orders of magnitude greater than the usual NRM intensities of a good detrital unit (like unit 71). Acquisition of a TRM in a prehistoric brush fire provides the most likely explanation for this orange layer within unit 68. Thus, our samples of burned unit 68 acquired their magnetization almost instantaneously and are remarkably magnetically stable.

Unfortunately, the peat was not burnt everywhere, and so the orange layer is not ubiquitous. I attempted to maintain synchronicity of the samples, however, by sampling a siltier horizon at locations within unit 68 where the burn layer does not exist. This siltier septum appears to be contemporaneous with the horizon containing the burn.

For each group that consists of two or three oriented samples, I average the sample directions determined by calculating a least-squares fit to the sample demagnetization path (Kirschvink, 1980). For unit 68 there are 9 groups with three stable samples, 23 groups with two

stable samples, 2 groups with one stable sample, and no groups with no stable samples. For unit 71 there are 10 groups with three stable samples, 19 groups with two stable samples, 4 groups with one stable sample, and one group with no stable samples.

I did not group together the samples collected at ten centimeter intervals within one meter of the fault to calculate a group mean declination. Within this short distance from the fault I wanted to avoid averaging out any rapid changes in rotations.

To eliminate spurious directions due to mis-oriented or overprinted samples I formulated a simple consistency test. If two of the three samples differ in direction by less than 5° and the third direction is more than 15° away, I considered this third sample an outlier and disregarded this direction. Although this is not a very elegant method, difficulties exist in constructing a more refined outlier test for groups of only three samples.

Results

I expected that the deformation at Pallett Creek would be similar to the pattern of deformation of the fence line from near Fort Ross, California, deformed during the 1906 San Francisco earthquake (figure 6). As discussed above, the Ft. Ross fence provides a historical example of the non-brittle deformation that can occur at an en echelon step in the fault. At Fort Ross the largest deformation occurred in

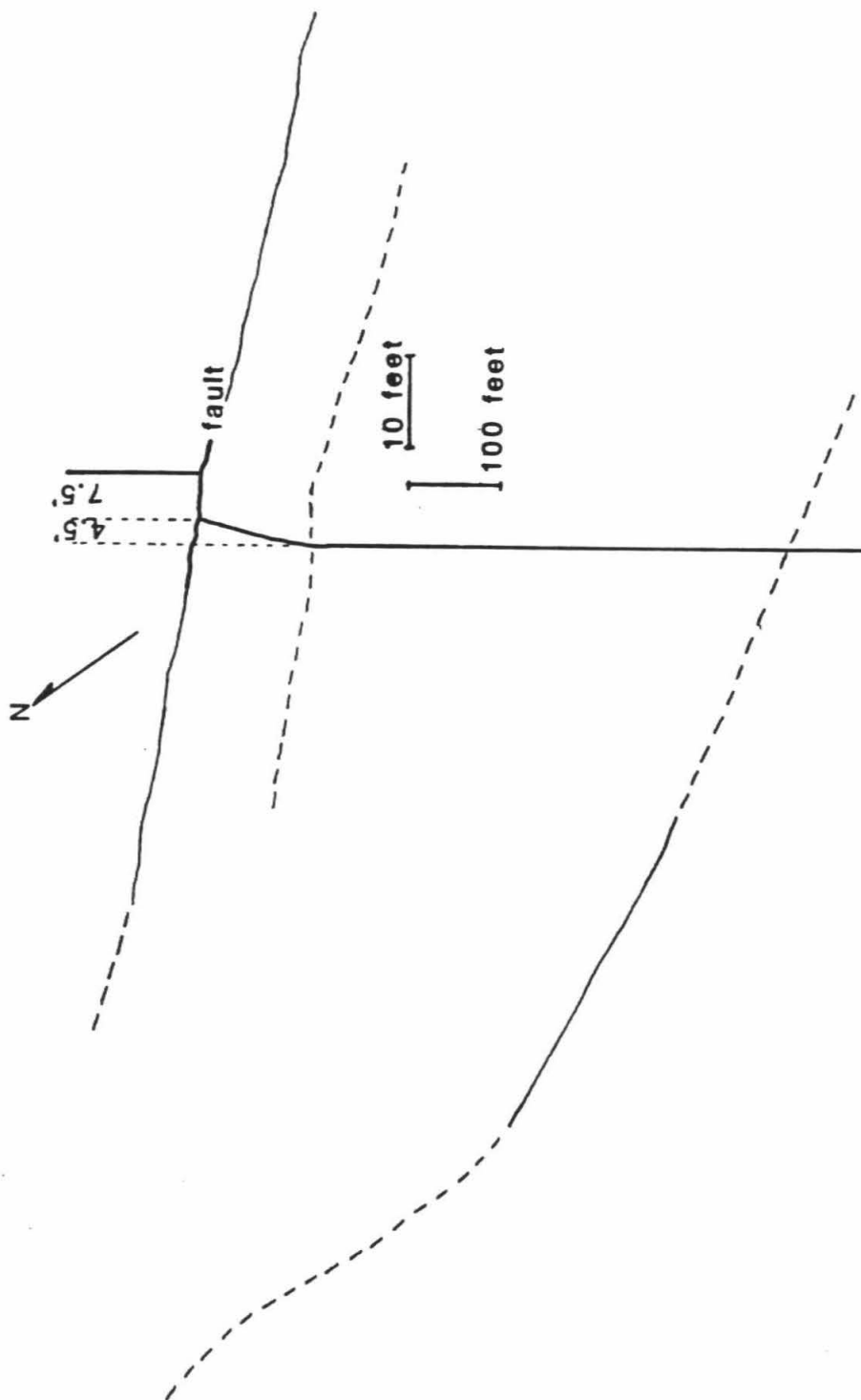


Figure 6

Offset and warping of a fence line near Fort Ross, California, during the April 18, 1906 earthquake. Fault geometry is mapped without exaggeration; the offset and warping of the fence line are exaggerated ten times, scale shown by the horizontal scale. The geometry of the fault is similar to the left-step at Pallett Creek. (from Prentice, unpub. mapping, Lawson and others, 1908; Brown and Wolfe, 1972)

the region between the fault trace and the extension of the left-step in the fault, and the magnitude of the deformation decreased away from the active trace. The sampling pattern at Pallett Creek was designed to maximize sampling where I expected, from this analogy, the largest deformations.

The pattern of deformation at Pallett Creek (table 1, figure 7) shows several characteristics. The declinations generally increase in eastward declination as samples approach the fault, however, the scatter also increases. The declinations are mostly eastward, indicating clockwise rotation and right-lateral deformation. Furthermore, unit 68 shows greater clockwise declinations than unit 71, an expected result because of the greater number of earthquakes experienced by unit 68. However, unlike the Fort Ross analogy, the section of the transect showing the most groups with large eastward declinations, representing the greatest clockwise rotation, occurs between 20 and 40 meters from the active trace of the fault.

At site two the two groups of samples each clustered well but have a noticeable westward declination. The mean for unit 68 is $D=350^\circ$, $I=43^\circ$ with an alpha-95 of 7.5° . The mean for unit 71 is $D=352^\circ$, $I=51^\circ$ with an alpha-95 of 7.2° . These directions are not useful for directly measuring the non-brittle offset, but the occurrence of this high counter-clockwise rotations will be compared to numerical results in the interpretation section.

Before the data can be translated into dextral warp a

Table 1a

Group Averages
Unit 68

Group	Number in group	Avg. Dec.	Group	Number in group	Avg. Dec.
-3	2	0.1	17	3	20.0
-2	2	2.3	18	2	20.6
-1	1	13.4	19	3	23.1
-0.9	1	-6.8	20	2	20.4
-0.8	1	-18.2	22	3	27.4
-0.7	1	0.3	24	2	15.8
-0.4	1	0.1	26	2	9.3
-0.3	1	37.1	28	2	13.4
-0.1	1	41.5	30	2	36.5
0.1	1	48.2	32	2	37.7
0.2	1	0.4	34	3	31.4
0.4	1	-52.0	36	2	-1.2
0.6	1	13.0	38	2	32.5
0.7	1	-2.8	40	2	28.6
0.8	1	-7.0	42	2	13.4
0.9	1	40.4	44	3	2.4
1	1	-10.4	46	3	-1.2
2	2	31.4	48	9	-0.7
3	2	2.2			
4	3	12.4			
5	2	-0.7			
6	2	18.8			
7	2	-9.6			
8	2	-9.9			
9	2	9.8			
10	2	-11.0			
11	2	3.9			
12	1	8.0			
13	3	-0.3			
14	1	16.4			
15	3	23.9			
16	2	6.8			

Table 1b

Group Averages
Unit 71

Group	Number in group	Avg. Dec. (degrees)	Group	Number in group	Avg. Dec. (degrees)
-3	2	0.6	26	2	22.1
-2	1	6.9	28	2	13.9
-1	1	-0.8	30	1	12.0
-0.9	1	-2.7	32	1	8.9
-0.8	1	5.1	34	2	15.4
-0.7	1	-5.9	36	0	NA
-0.6	1	0.8	38	1	0.8
-0.5	1	-2.2	40	3	18.6
-0.3	1	12.3	42	3	12.5
-0.2	1	14.3	44	2	1.9
-0.1	1	16.5	46	3	7.8
0.3	1	2.4	48	6	-1.5
0.4	1	1.6			
0.5	1	-6.0			
0.7	1	21.0			
0.8	1	-3.0			
0.9	1	-28.7			
1	1	1.6			
2	3	5.5			
3	2	-1.0			
4	3	12.3			
5	2	19.0			
6	2	27.8			
7	2	4.3			
8	3	14.1			
9	2	1.1			
10	2	4.3			
11	2	-5.8			
12	2	8.1			
13	2	7.4			
14	2	2.6			
15	2	4.3			
16	3	3.7			
17	3	-3.1			
18	2	-6.6			
19	3	8.0			
20	3	9.7			
22	2	2.6			
24	2	9.7			

Group Declination

Unit 68 and Unit 71

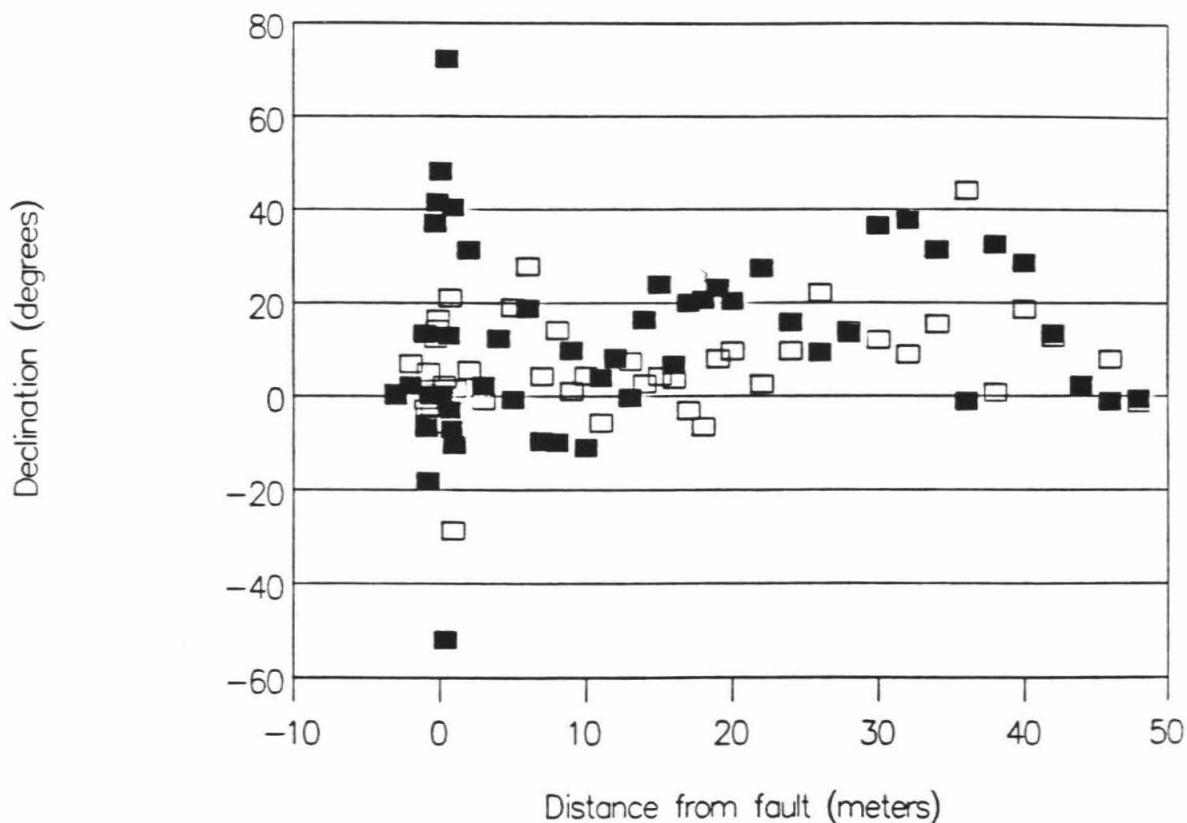


Figure 7

Group declinations for unit 68 (filled squares) and unit 71 (open squares). Unit 68, which has experienced three earthquakes, usually shows greater eastward declination, and therefore rotation, than unit 71.

discussion of errors is necessary.

Error analysis

In this measurement of sediment rotation in a fault zone, the quantity of interest is the magnetic declination of the sediments. Several sources of error are present in these measurements. Because the sampled horizon in unit 68 contains a burn unit, and the units bounding unit 71 have indistinguishable ages, both of these units appear to be isochronous. Therefore, the problem of different parts of the horizon acquiring detrital remanent magnetization at different times is not a problem. However, where the sampling horizon is thinner than the sample size some of the adjoining material must be sampled. The resulting magnetic direction is an average of all of the directions. However, in all of my samples the accidentally-sampled material is only a small fraction of the total volume, so the discrepancy should be minor.

A more serious problem is the possibility of chemical overprinting. The formation of secondary iron oxides after deposition of the unit may alter the Natural Remanent Magnetization of the sample. With varying amounts formed at different times the effect is random. This problem is minimized, but not completely eliminated, by the analysis by thermal demagnetization.

The final source of error is in the process of collecting and measuring the samples, as there is the

potential for mis-measuring or mis-recording the data at every step. Although samples which are mis-oriented during collection probably have the greatest errors, they are the easiest to recognize and eliminate. Similarly, the problem with measurement error is minimized by multiple readings of each component during the specimen measurement process, and by conducting a large number of progressive demagnetization steps on each sample.

However, in spite of these precautions, scatter is still present in the data. Taking three samples in each group allows application of the consistency test and permits averaging of the data to reduce the random errors. An analysis of the errors is needed to further understand these results.

I begin with the assumption that the data are from a population having a Fisher distribution (Fisher, 1953), which is one of several distributions which are asymptotically normal on a spherical surface, but is circularly symmetric about the mean. The Fisher distribution is commonly used for paleomagnetic directional data (e.g. Irving, 1964; McElhenny, 1973; Tarling, 1983).

Block Errors

To obtain an initial assessment of the random error in the data, I will first group the data into blocks of similar data. First, I will make the naive assumption that all of the data have a uniform rotation, and therefore are

scattered about a uniform declination. Grouping together all of the data between -3 and 46 meters gives the statistics listed in table 2. As would be expected, the scatter is high with $k=26.93$ for unit 68 and $k=47.56$ for unit 71. Nevertheless, it is reassuring to note that the declination of 12.1° for the older unit, 68, is greater than the declination of unit, 71, 7.1° .

As a refinement of this "block" treatment, I next group together the samples from adjacent groups that show similar declinations. Because any rotation should affect unit 68 and unit 71 over blocks of the same dimensions, these groups are the same for each unit. These statistics are listed in table 3. In most cases, this treatment is an improvement over the the one-block approximation; however, in each unit, one block shows greater scatter.

This analysis provides one measure of the error in the samples. Because the rotations are of interest, and the inclinations are all indistinguishable on these blocks, I will continue this analysis using only the declinations. In this case the data are assumed to follow a Von Mises distribution, the circular form of the spherical Fisher distribution.

Independent groups

I first assume that each sample group is independent and has its own mean and standard deviation. For each group that has two or three samples, I calculate the mean and

Table 2
Single block rotation

	Dec.	Inc.	N	k	Alpha-95
Unit 68	12.1	41.9	91	26.9	2.9
Unit 71	7.1	40.1	89	47.6	2.2

Table 3
Block Rotation

	Dec.	Inc.	N	k	Alpha-95
Unit 68					
-3 to -0.4 m	0.4	38.8	9	28.8	9.7
-0.3 to -0.1 m	38.8	42.2	2	52.1	35.3
0.1 to 3 m	12.9	44.0	13	17.0	10.3
4 to 8 m	10.4	42.8	7	47.7	8.8
9 to 14 m	1.8	38.9	10	35.4	8.2
15 to 19 m	21.0	41.7	13	55.9	5.6
20 to 42 m	21.2	42.2	26	32.0	5.1
44 to 49 m	2.1	40.7	17	66.6	4.4
48 to 49 m	-0.7	40.7	9	142.7	4.3
Unit 71					
-3 to -0.4 m	-0.6	39.4	9	23.9	10.7
-0.3 to -0.1 m	14.2	39.1	3	106.6	12.0
0.1 to 3 m	0.4	41.3	12	71.7	5.2
4 to 8 m	15.6	40.0	12	58.2	5.7
9 to 14 m	2.8	37.9	12	93.8	4.5
15 to 19 m	2.0	40.7	13	78.5	4.7
20 to 42 m	12.2	40.9	22	48.0	4.5
44 to 49 m	1.8	38.5	10	132.2	4.2
48 to 49 m	-1.6	37.9	5	95.6	5.6

standard deviation. For the samples within one meter of the fault I use the sample to either side of a sample to make a group of 2 or 3 samples and calculate the standard deviation at that location.

Figure 8 shows the data with the one standard deviation error bars and table 4 lists these values. Note that the error bars are quite large. To reduce these uncertainties, I attempt a "group mean centered" analysis.

Group mean centered

Samples from the same layer, but in different groups, should experience the same effects, except for the magnitude of rotation, and so have similar random error. Hence, it seems reasonable to expect the samples should have a similar level of angular scatter around the mean direction.

In this case, I assume that all of the groups have the same distribution but have been rotated smoothly so as to yield different mean values. Mardia (1972) shows that for circular data, distributions remain constant through uniform rotation. To center each group to a constant mean I rotate each group so they all have the same mean, arbitrarily set to be zero. In a one dimensional situation, for example, centering the means from two groups with values of 5, 6, and 7, and another with 8, 9, and 10 would yield two centered groups of -1, 0, 1. Observation of these centered values shows that the two groups have the same standard deviation. By combining these values into one group a standard

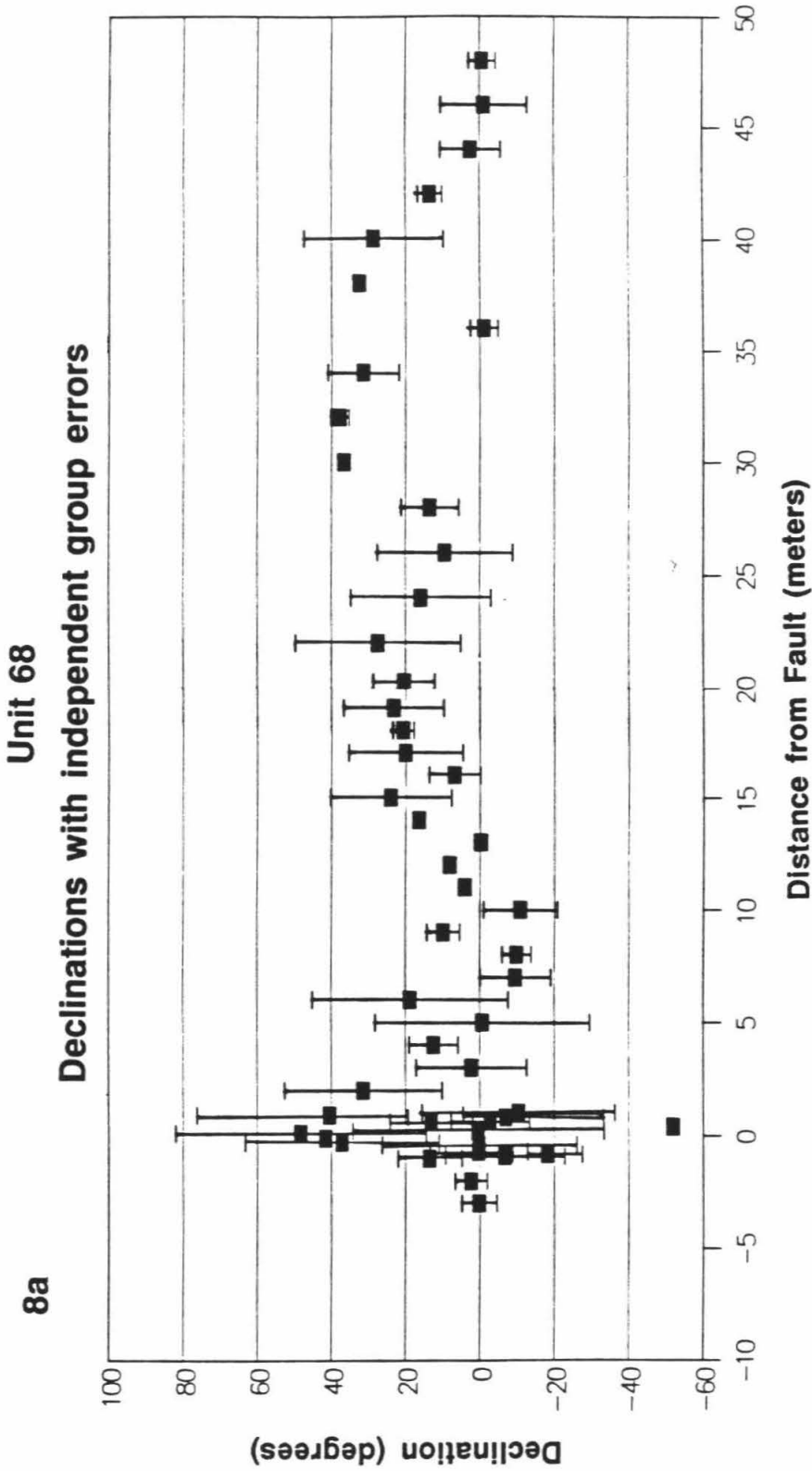


Figure 8

Group mean directions with one standard deviation error bars calculated using the independent group method. (a) unit 68, (b) unit 71.

Unit 71
Declinations with independent group errors

8b

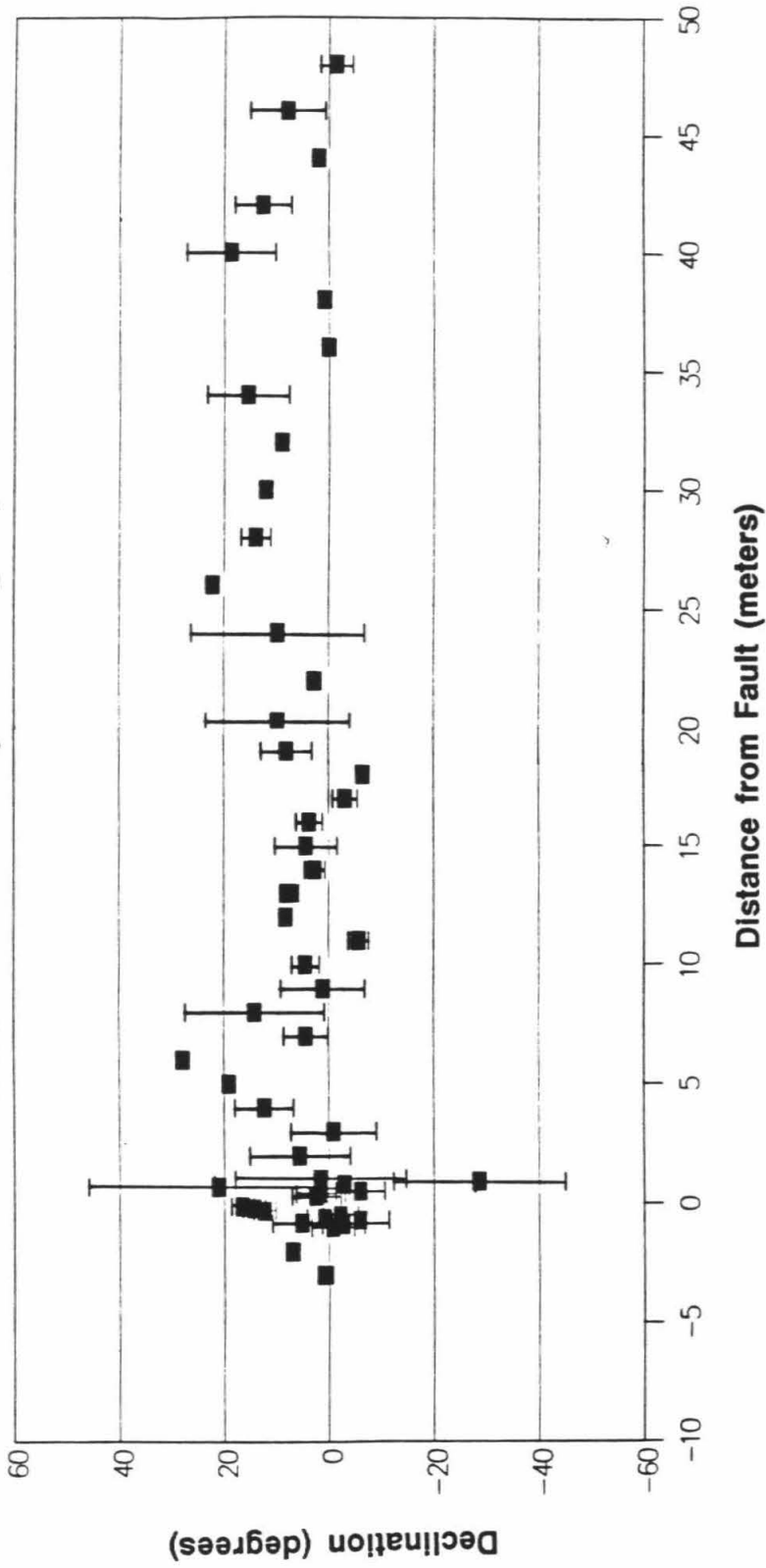


Table 4a

Unit 68
Independent Group Statistics

Group	Dec (Degrees)	Sigma (Degrees)
-3	0.1	4.7
-2	2.3	4.2
2	31.4	21.3
3	2.2	14.8
4	12.4	6.6
5	-0.7	28.8
6	18.8	26.4
7	-9.6	9.5
8	-9.9	3.8
9	9.8	4.4
10	-11.0	9.9
11	3.9	1.3
12	8.0	
13	-0.3	1.7
14	16.4	
15	23.9	16.3
16	6.8	6.9
17	20.0	15.4
18	20.6	2.8
19	23.1	13.5
20	20.4	8.3
22	27.4	22.3
24	15.8	18.9
26	9.3	18.2
28	13.4	7.8
30	36.5	0.8
32	37.7	2.4
34	31.4	9.5
36	-1.2	3.7
38	32.5	0.5
40	28.6	18.8
42	13.4	3.3
44	2.4	8.1
46	-1.2	11.6
48	-0.7	3.6

Table 4b
Unit 71
Independent Group Statistic

Group	Dec	Group Independe	Group	Dec	Group Independe
-3	0.6	1.4			
-2	6.9		30	12.0	
-1	-0.8		32	8.9	
-0.9	-2.7		34	15.4	7.8
-0.8	5.1		36	NA	
-0.7	-5.9		38	0.8	
-0.6	0.8		40	18.6	8.5
-0.5	-2.2		42	12.5	5.4
-0.3	12.3		44	1.9	0.6
-0.2	14.3		46	7.8	7.2
-0.1	16.5		48	-1.5	3.1
0.3	2.4				
0.4	1.6				
0.5	-6.0				
0.7	21.0				
0.8	-3.0				
0.9	-28.7				
1	1.6				
2	5.5	9.6			
3	-1.0	8.1			
4	12.3	5.6			
5	19.0	0.7			
6	27.8	0.7			
7	4.3	4.2			
8	14.1	13.3			
9	1.1	8.0			
10	4.3	2.6			
11	-5.8	1.9			
12	8.1	0.1			
13	7.4	1.8			
14	2.6	1.9			
15	4.3	5.9			
16	3.7	2.5			
17	-3.1	2.3			
18	-6.6	0.2			
19	8.0	4.8			
20	9.7	13.8			
22	2.6	1.3			
24	9.7	16.5			
26	22.1	0.6			
28	13.9	2.8			

deviation for the six measurements can be found. The standard deviation for each group of three samples is 1.22 whereas the standard deviation of the combined group of six is 0.980. By combining the groups I achieve a reduction in the standard deviation, because I have more fully sampled the population. This happens for use of the unbiased $N-1$ weighting of the standard deviation but not the N weighting (for N samples).

For the sample directions, I used those groups with two or three samples and the larger groups at 48 meters. The samples within one meter of the fault were not used. Unit 68 has a standard deviation of 4.60 degrees for 82 samples. Unit 71 has a standard deviation of 5.19 degrees for 73 samples. Figure 9 shows these error bars on the group directions. Note that the uncertainties are much less than in the previous analysis.

Comparison

Many of the groups have standard deviations that appear similar. Having a standard deviation of the centered groups, the independent group standard deviations can be tested against them. I used the F-test of standard deviations at the 95% confidence level to test if a standard deviation significantly exceeded or fell short of the whole group value. If the ratio of the variances (standard deviations squared) exceeds the value of the F distribution at the $1-0.95$ level for $n-1$, $n-1$ degrees of freedom, the

9a

Unit 68

Declinations with mean centered errors

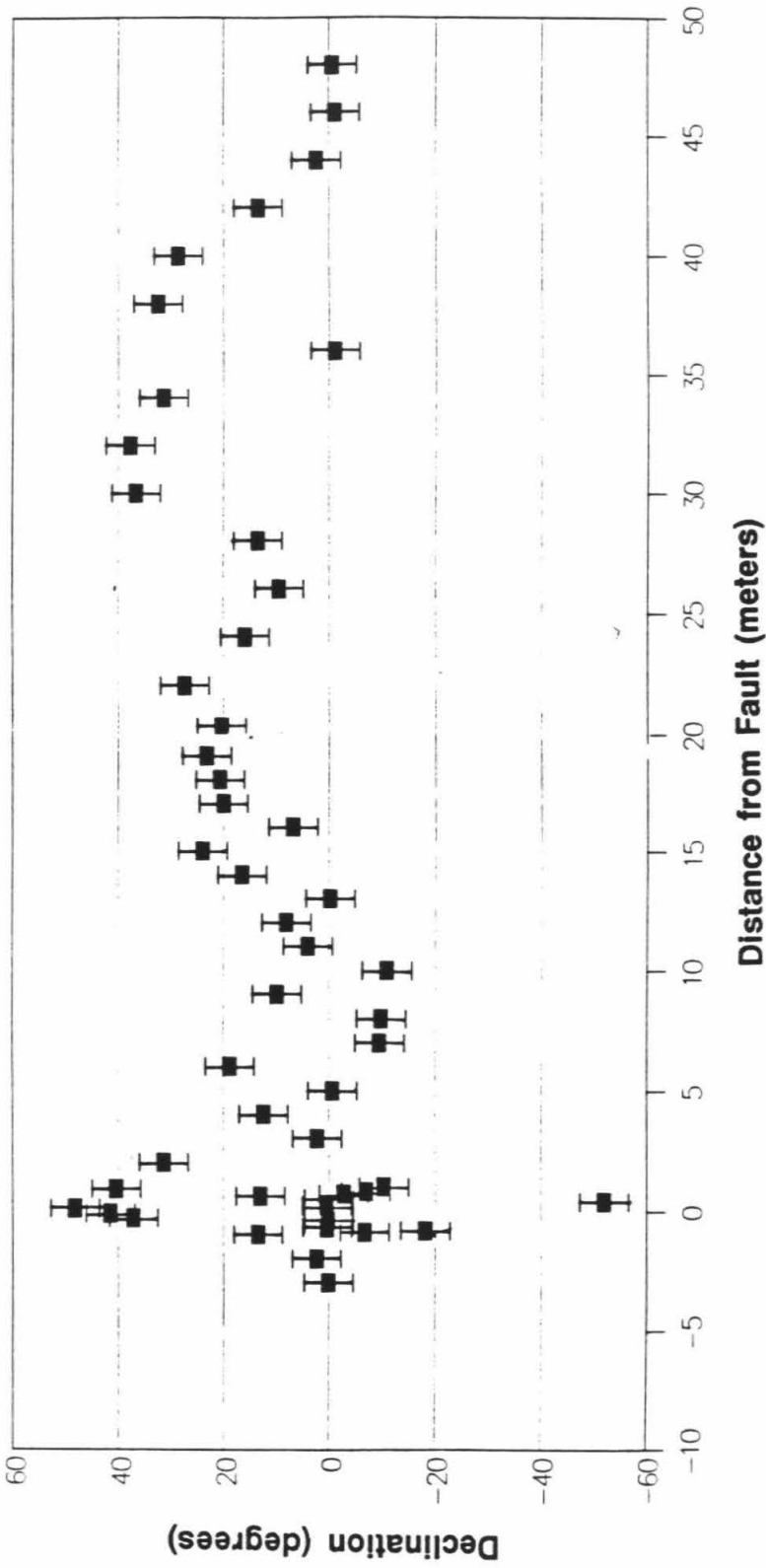
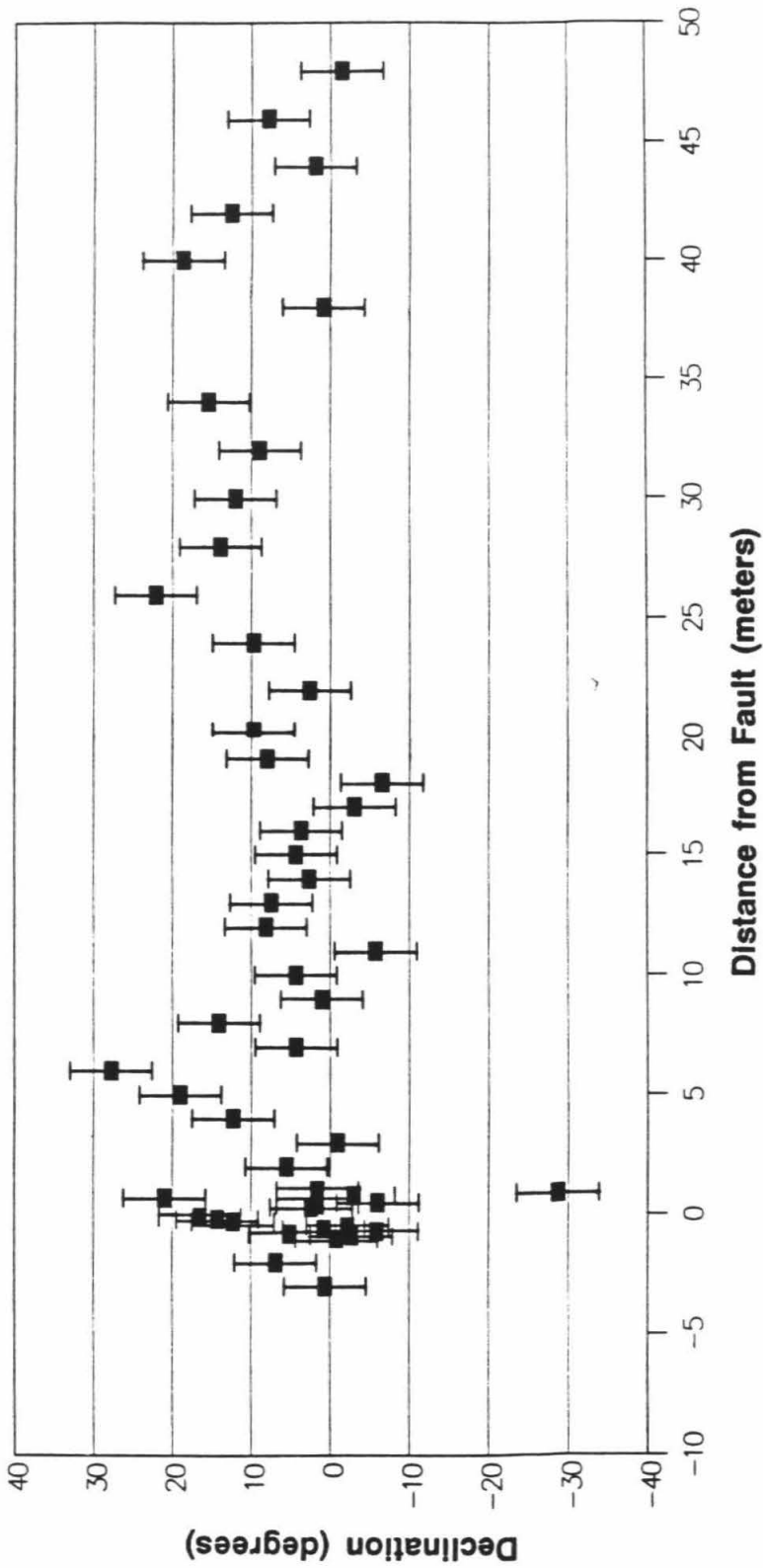


Figure 9

Group mean directions with one standard deviation error bars calculated by the centered group mean method. (a) unit 68, (b) unit 71.

Unit 71
Declinations with mean centered errors

9b



standard deviations are judged to be different (where the n 's are the number of samples in each group) (Mardia, 1972).

For the independent group values for unit 68 I found that for 18 of the groups I could not reject the groups having the same value as the whole centered population. For 15 of the groups I could accept that the standard deviations of the groups are higher than the whole population.

For the individual group values for unit 71 I found that for only six of the groups could I accept that they differed from the whole population value, four groups higher and two groups lower.

This suggests that unit 68 contains multiple populations and a group approach best describes the scatter of the directions. For unit 71, with such a high number of groups being statistically indistinguishable from the whole population, the whole population standard deviation probably represents the individual groups well.

Based on these tests, I conclude that the independent group standard deviations best represent the group standard deviations for unit 68.

For unit 71 the group mean method appears to provide the best result. The high rejection rate of groups for the test of unit 68 convinces me that the sensitivity of the F-test is high enough, and the low rejection rate for unit 71 suggests that this population is adequately described by the group mean standard deviation.

Absolute rotation

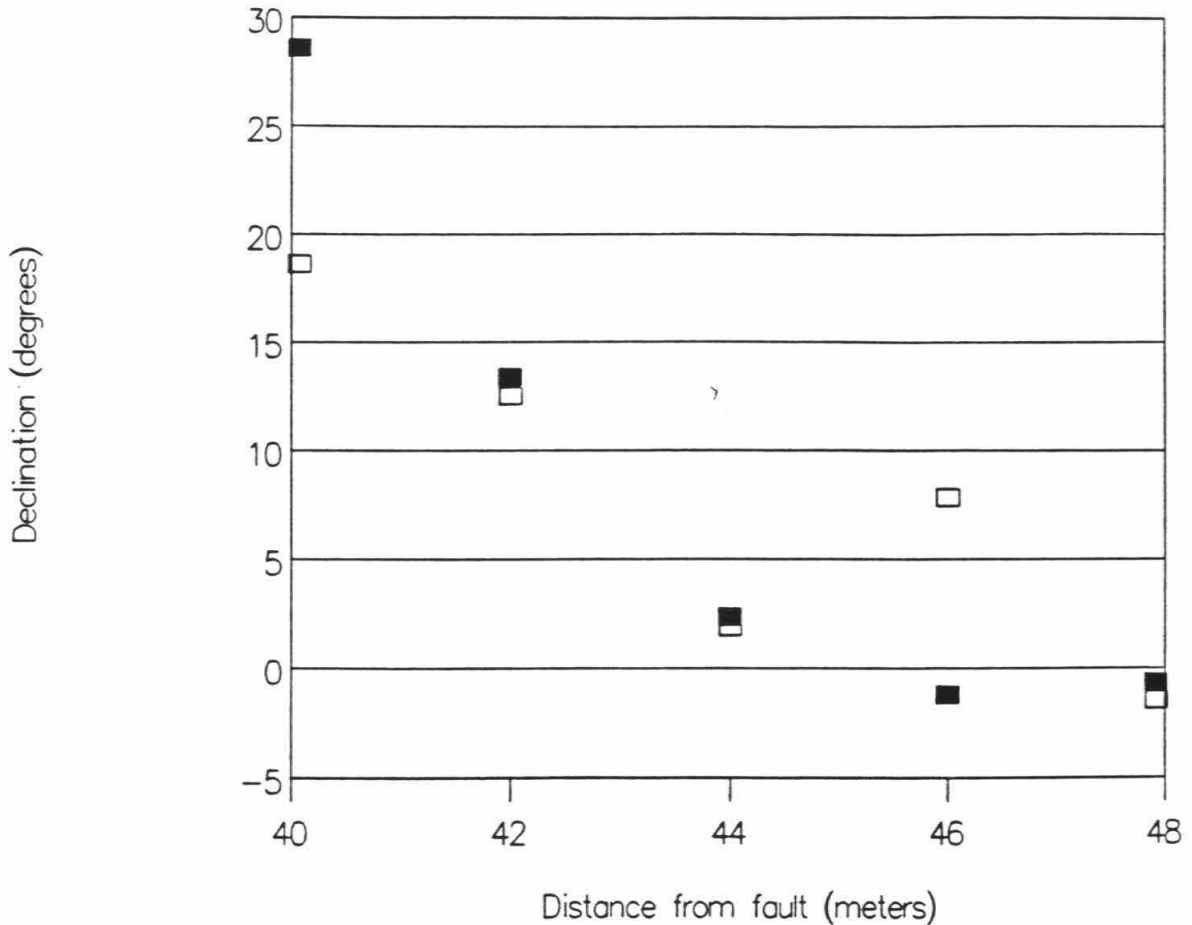
In order to determine the absolute rotation of an individual group I must establish the "unrotated" direction for both unit 68 and unit 71. The larger sample groups at 48 meters from the fault were collected with this objective. Because these samples are from points farthest from the fault, they should have the greatest chance of being unrotated.

These groups give a direction for unit 68 of $\text{dec} = -0.68^\circ$ and $\text{inc} = 40.7^\circ$ and for unit 71 of $\text{dec} = -1.6^\circ$ and $\text{inc} = 38^\circ$. Three lines of evidence suggest that these directions are unrotated.

First, from the mapping of Sieh (1984) the ancient stream gorge of A.D. 1100-1200 ends close to this point. Although the exact location of the gorge wall is unknown, Pleistocene bedrock is exposed at 53 meters, 5 meters beyond the control groups. So the control groups are close to the consolidated bedrock. Rotations of bedrock in a single earthquake would likely be less than those in unconsolidated sediment.

Second, as we move towards the fault trace the first one or two groups encountered yield the same direction as does the control group. (Figure 10 shows the details of these rotations.) This suggests that the material filling the ancient gorge near the wall is deformed less, perhaps through the stabilizing influence of the adjacent Pleistocene strata.

Group mean declinations

**Figure 10**

Detail of the group mean declinations for unit 68 (solid squares) and unit 71 (open squares) near the reference location at 48 meters. The declination generally decreases towards the 48 meter value and some of the adjacent values are very close in direction.

Finally, these directions are fully consistent with the secular variation curve developed in Chapter 2. Even though these directions were used in constructing the secular variation curve in Chapter 2 there are other directions in this time interval in full agreement with these directions. Hence, the directions of the control groups have probably not been rotated.

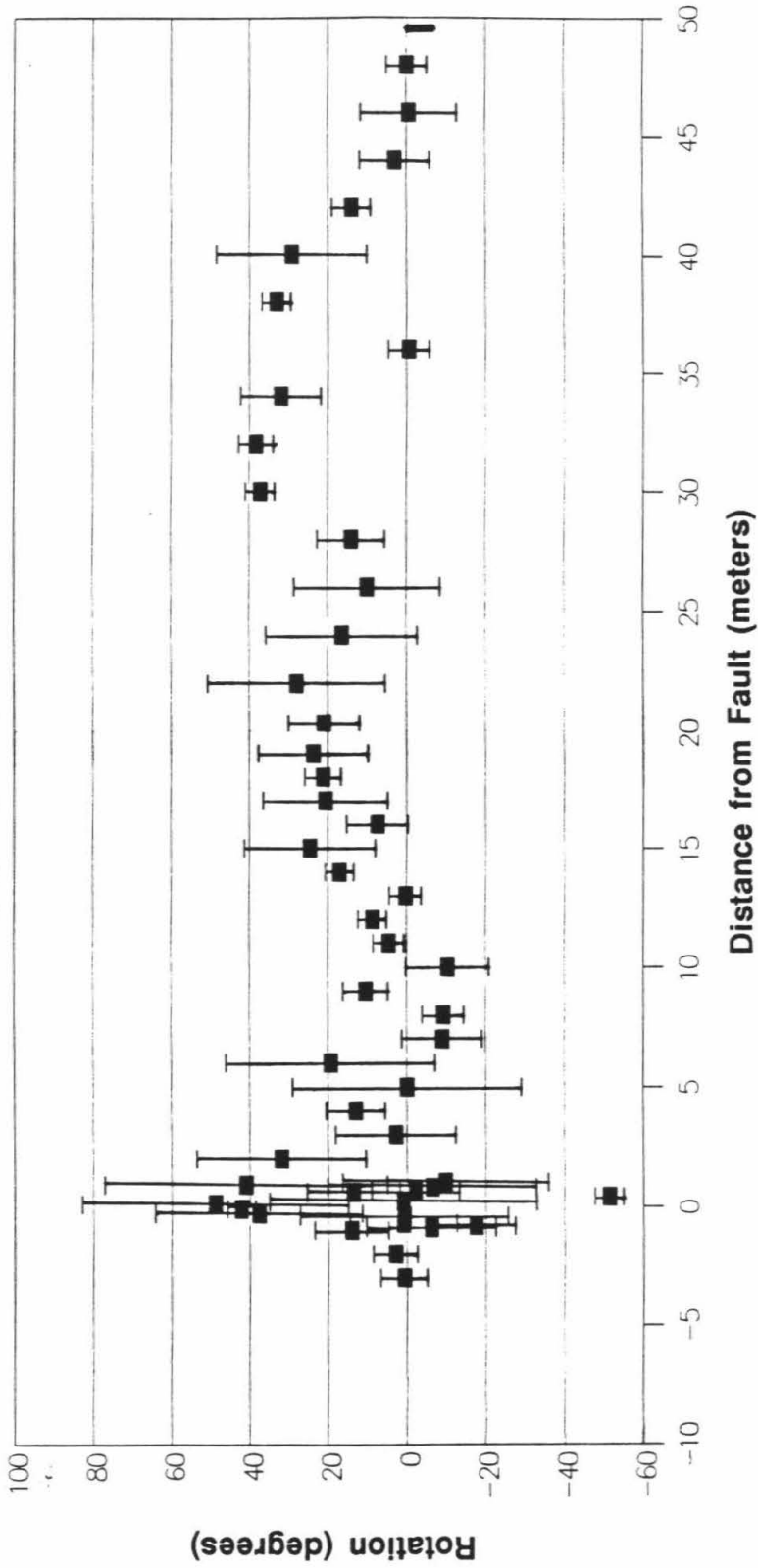
Using these, and the error bars developed above, figure 11 and table 5 shows the relative declination difference, of rotation, at each group location. Since these directions are subtracted the error bars are calculated from the sum of the variance of the reference group and the rotated group.

The maximum possible rotation of the control groups is constrained by the Panum Crater and Mount St. Helens magnetic directions from Chapter 2. Taking the extremes of the 95% confidence limits gives the range of possible rotation. The unit 68 control group could be rotated clockwise 9.8° or counter-clockwise 5.3° . The unit 71 control group could be rotated clockwise 10.1° or counter-clockwise 15.8° . However, since no detachment of unit 71 from unit 68 is seen, and for a rotation direction that does not vary from one earthquake to the next, the rotation of unit 71 can be no more than the rotation of older unit 68.

If the control groups are rotated, the rotations shown in figure 11 would be shifted upward or downward uniformly. The bars on the right edge of the figure shows the range of the Panum and Mount St. Helens declinations, and therefore

11a

Unit 68 - Rotations



Distance from Fault (meters)

Figure 11

Group rotations with one standard deviation error bars. (a) unit 68 (b) unit 71. The bars on the right side of the plots show the control directions from (a) Panum Crater and (b) Mount St. Helens.

11b

Unit 71 - Rotations

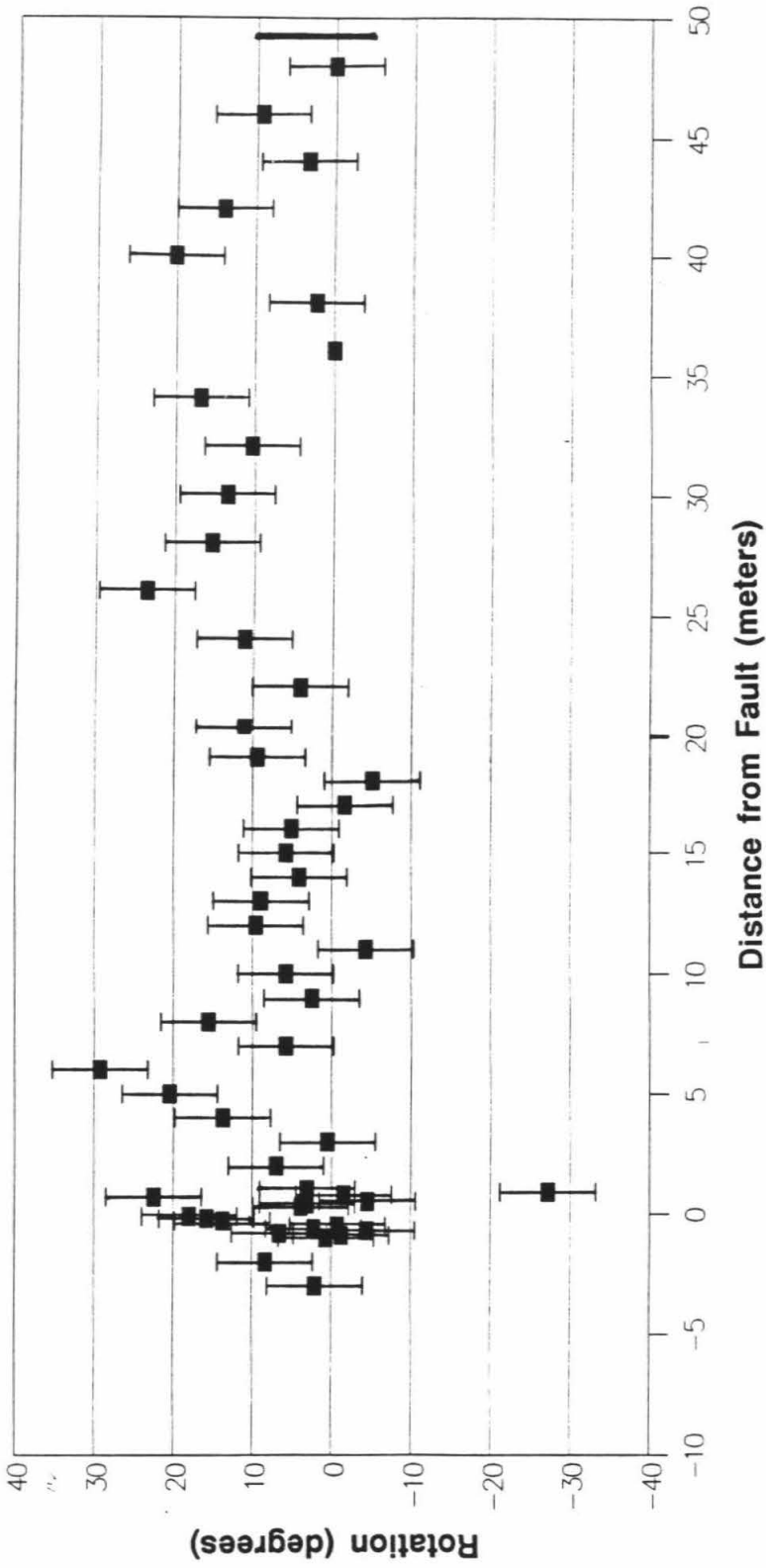


Table 5
Rotations

Unit 68			Unit 71	
Group	Rot.	Sigma	Rot.	Sigma
-3	0.8	5.9	2.1	6.0
-2	3.0	5.6	8.4	6.0
-1	14.1	9.3	0.7	6.0
-0.9	-6.1	16.4	-1.2	6.0
-0.8	-17.5	10.0	6.6	6.0
-0.7	1.0	13.6	-4.4	6.0
-0.6			2.3	6.0
-0.5			-0.7	6.0
-0.4	0.8	26.4		
-0.3	37.8	26.4	13.8	6.0
-0.2			15.8	6.0
-0.1	42.2	3.6	18.0	6.0
0				
0.1	48.9	34.0		
0.2	1.1	34.0		
0.3			3.9	6.0
0.4	-51.3	3.6	3.1	6.0
0.5			-4.5	6.0
0.6	13.7	11.7		
0.7	-2.1	11.1	22.5	6.0
0.8	-6.3	26.5	-1.5	6.0
0.9	41.1	36.1	-27.2	6.0
1	-9.7	26.1	3.1	6.0
2	32.0	21.6	7.0	6.0
3	2.9	15.3	0.5	6.0
4	13.0	7.5	13.8	6.0
5	-0.0	29.1	20.5	6.0
6	19.4	26.6	29.3	6.0
7	-8.9	10.1	5.8	6.0
8	-9.2	5.3	15.6	6.0
9	10.5	5.7	2.5	6.0
10	-10.3	10.5	5.8	6.0
11	4.6	3.8	-4.3	6.0

12	8.7	3.6	9.6	6.0
13	0.3	4.0	8.9	6.0
14	17.1	3.6	4.1	6.0
15	24.6	16.7	5.8	6.0
16	7.4	7.8	5.1	6.0
17	20.6	15.8	-1.6	6.0
18	21.3	4.6	-5.1	6.0
19	23.8	14.0	9.4	6.0
20	21.0	9.0	11.2	6.0
22	28.0	22.6	4.1	6.0
24	16.5	19.2	11.2	6.0
26	10.0	18.5	23.6	6.0
28	14.1	8.6	15.4	6.0
30	37.2	3.7	13.5	6.0
32	38.4	4.3	10.4	6.0
34	32.0	10.2	16.9	6.0
36	-0.5	5.2		
38	33.1	3.6	2.3	6.0
40	29.3	19.2	20.1	6.0
42	14.1	4.9	14.0	6.0
44	3.0	8.9	3.4	6.0
46	-0.5	12.2	9.3	6.0
48	0.0	5.1	0.0	6.0

the amount of shift possible. Figure 11 is accurate for the rotation of the other groups relative to the control groups. However, for the reasons stated above, I believe that rotation of the control groups is much less than the extremes calculated above, and probably very small to negligible.

Interpretation

The existence of two possible modes of deformation of these sediments complicates the calculation of the non-brittle offset from the rotations. Block rotation is the simpler of these forms of deformation (Nur and others, 1986). In this form of deformation the material rotates as a coherent rigid block (figure 12a). The second form of deformation is the deformation of a continuum. In this form of deformation the material rotates as small independent rigid blocks on the surface of a deforming fluid (figure 12b). This applies even for continuous deformation that includes the surface. For a pure fluid the rigid blocks are of infinitesimal size.

For the case of block rotation, calculating the offset across the block uses simple geometry. The offset will be $O = D \tan \theta$ with offset O , distance D and rotation angle θ (figure 12a). For small θ , in radians, this reduces to $O = D \theta$.

In the case of continuum deformation the rotations are

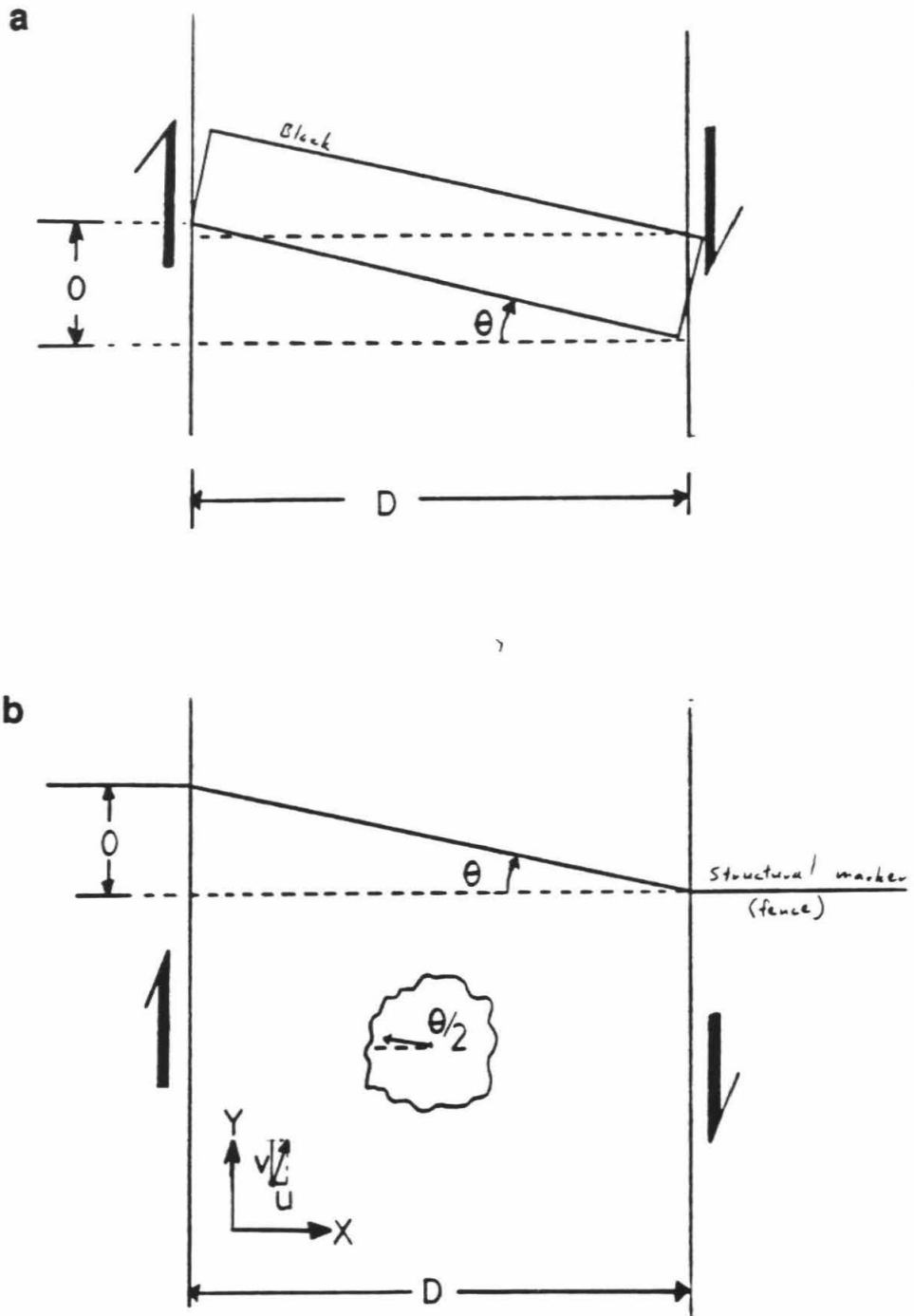


Figure 12

Cartoons of block rotation deformation (a) and continuum deformation (b) showing style of deformation and coordinate system and variables discussed in text.

half of the vorticity of the deforming fluid (McKenzie and Jackson, 1983). This can be expressed as $\theta = I/2$ where $I = \partial v / \partial x - \partial u / \partial y$ with rotation θ , and material velocities u in the x direction and v in the y direction (McKenzie and Jackson, 1983).

Simple shear represents one possible form of deformation. In this case the deformation is only in one direction, in figure 12b the y direction, means that the velocity in the other direction equals zero. Therefore the vorticity $I = \partial v / \partial x$ and $\theta = \frac{1}{2} \partial v / \partial x$. In simple shear this gradient remains constant across the fault zone so $\partial v / \partial x = O/D$ and so $\theta = \frac{1}{2} D$. This means that the rotation for the simple shear case is half the rotation in the block rotation case for the same offset.

Both of these forms of deformation have been reported in studies of non-brittle deformation of fault zones using paleomagnetism. Nelson and Jones (1987) interpreted the rotations they measured near the Las Vegas Valley Shear Zone of southern Nevada as being continuum deformation. These samples, mainly from the Las Vegas range, north of the shear zone, demonstrated paleomagnetic rotations in the non-brittle deformation. These rotations systematically increased from 0° of rotation more than 24 km north of the shear zone to greater than 50° of rotation at the closest sites to the shear zone, about 10 km north. Based on geologic evidence, Nelson and Jones concluded that the non-brittle deformation occurred as rotation of small

independent blocks, less than 5 km in size, on a deforming viscous continuum. They found that this conclusion supports the use of non-Newtonian viscous plate models to model deformation of the crust.

In an area near the Nelson and Jones study Ron and others (1986) came to a different conclusion. On the north side of Lake Mead, Nevada, they found counter-clockwise rotations of 29° on blocks bounded by northeast trending left-lateral faults and northwest trending right-lateral faults. These right-lateral faults include the Las Vegas Valley Shear Zone. Ron and others argued that these 20 km scale blocks rotated as rigid bodies between the fault zones and not on a deforming material below.

Block rotations

I will first calculate the non-brittle offset across the transect for the case of the block rotation interpretation. As I discussed above, the offset across an individual block equals $D \tan \theta$. Figure 13 shows the deformation calculated in this manner. Each individual segment is centered on the group location at which the rotation of that segment was measured at. I have used the groups at 48 meters from the fault as being unrotated so the summation of deformation begins at the end of that segment at 47 meters from the fault.

To calculate the error on the sum I have used the standard deviations calculated above. However, the quantity

13a

Palsett Creek Offset

Unit 68

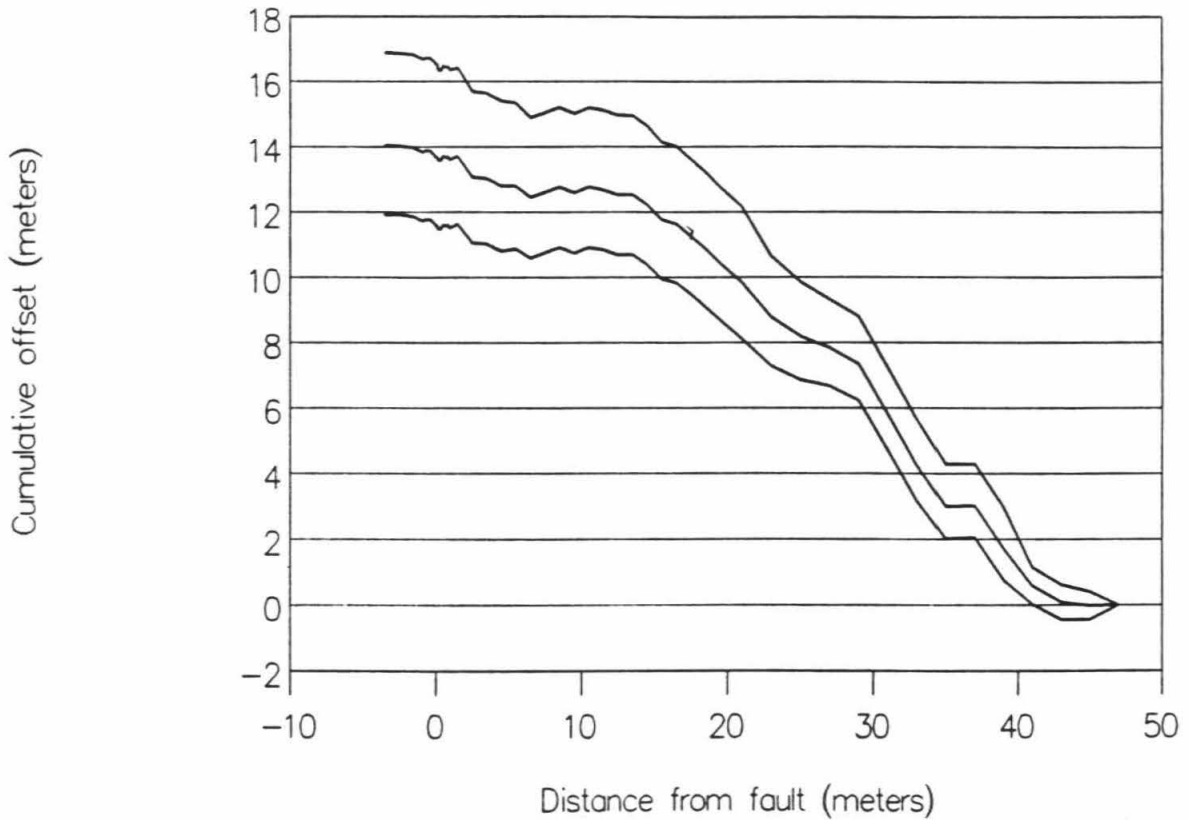


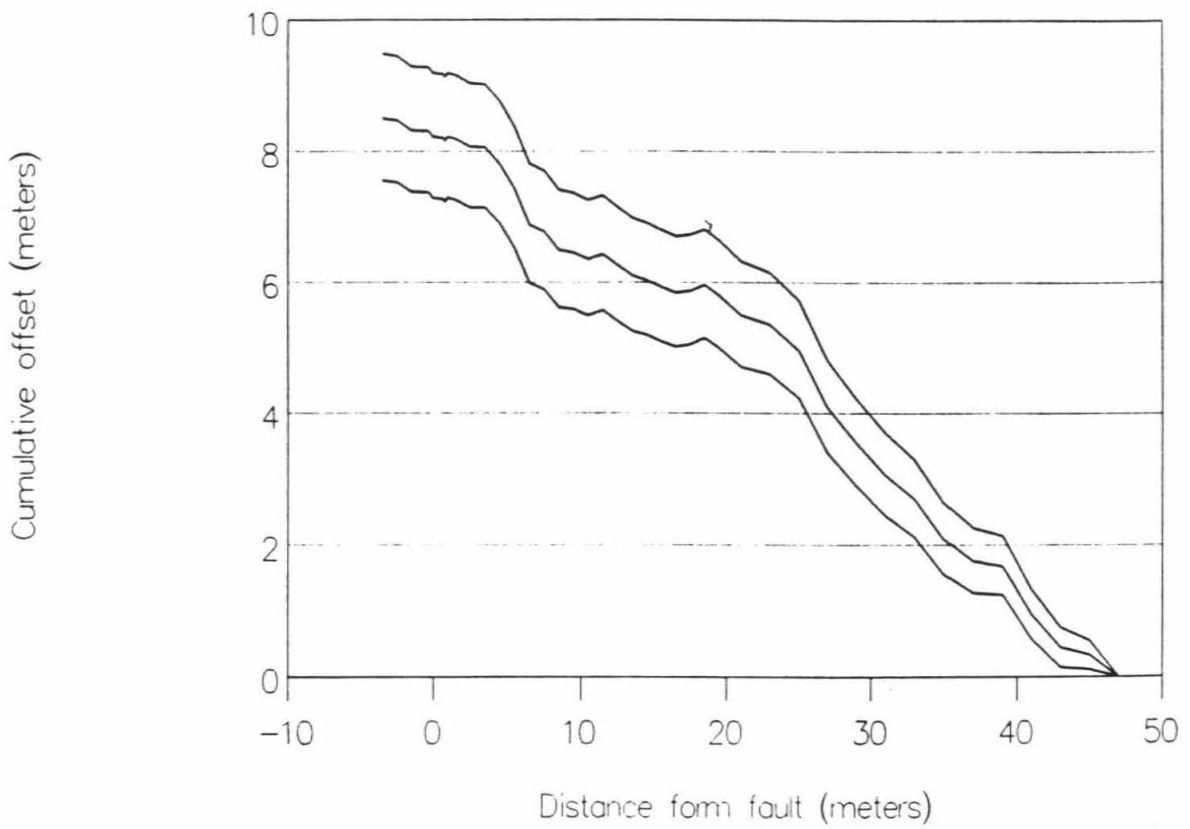
Figure 13

Cumulative non-brittle offset of (a) unit 68 and (b) unit 71 (center line) with one standard deviation error bars. The deformation was calculated using the block rotation model discussed in the text.

13b

Pallett Creek Offset

Unit 71



from above is in degrees and the quantity being measured is in meters, so a non-linear conversion is required. I have simply taken the standard deviation of the rotation, added and subtracted it from the rotation angle measured, and calculated the new block offset. To get the error, I then subtract the block offset without the error from this. Now, since the summation is a linear combination, the total variance of the sum is the sum of the individual variances.

From this summation, unit 68 shows $14.0+2.8$, -2.1 meters of non-brittle offset (figure 13a). Unit 71 shows $8.5+1.0$, -0.9 meters of non-brittle offset (figure 13b). The confidence limits are one sigma errors.

Continuum deformation

The alternate interpretation of continuum deformation is complicated by the need to know the displacements in both the x and y directions. As discussed above, the interpretation of simple shear gives a result twice the block-rotation value. Certainly, in a restraining jog in the fault this interpretation simplifies the situation.

Interpreting the offset as simple shear gives offsets of 28.0 meters and 17.0 meters for unit 68 and unit 71 respectively. These values were calculated by doubling the values calculated for block rotation. In the coordinate system used to calculate the vorticities a clockwise rotation has a negative value. This can be seen from the vorticity equation $I = \partial v / \partial x - \partial u / \partial y$. For a right-lateral

strike-slip offset with fault displacement in the y direction v , the velocity in the y direction (figure 12b), will decrease with increasing x . Therefore $\partial v / \partial x < 0$ and in simple shear I will be less than zero. By observation of the vorticity equation, for a constant vorticity, a value of $\partial u / \partial y > 0$ will reduce the value of $\partial v / \partial x$ necessary to maintain that constant vorticity. This means that less fault offset is necessary to produce the same rotations.

To find the rotation in a more complicated deforming fault geometry I calculated some finite-element models. I used the program DLEARN (Hughes, 1987) to calculate the deformation of an 11 x 11 node grid. The grid is square and the nodes equally spaced in the grid. The calculation used an incompressible material in plane-strain deformation. I calculated the grid with a variety of initial conditions and boundary conditions. The computation ran for only one time step, representing a single earthquake. I scaled the boundary force to produce a six meter offset across a 100 meter wide fault zone.

From the calculated displacements, and hence the material velocities, I calculated the vorticities. Using the velocity at each nodal point, the difference of these values gives the velocity gradient between these points. In figure 14 the gradient of u equals $u_{12} - u_1$ and $u_{13} - u_2$. The V gradient equals $v_2 - v_1$ and $v_{13} - v_{12}$. These gradients are assigned to points half way between the nodes (figure 14). This results in the two different gradients, $\partial u / \partial y$ and

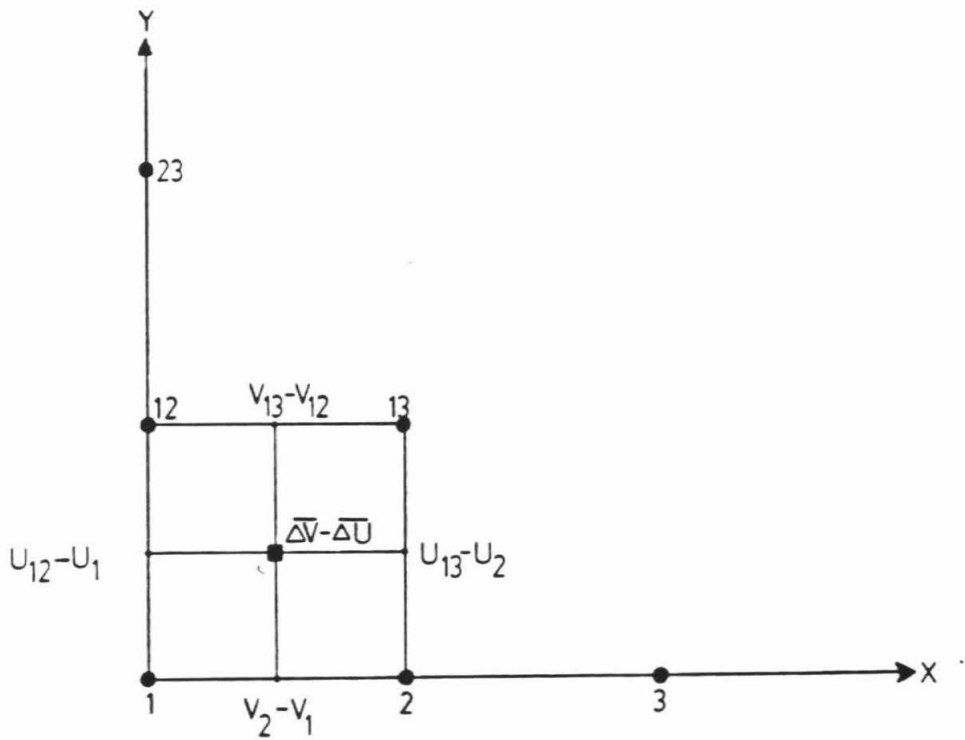


Figure 14

Diagram illustrating lower left corner of finite-element grid. Nodes are large circles, gradient points are small circles, and averaged gradient point the square.

$\delta v / \delta x$ centered between different nodes. The first are centered between nodes in the y direction and the second are centered between nodes in the x direction. To get these gradients to coincide I average gradients on opposite sides of the square and center this value between the two points (figure 14). The result is values for both the u and v gradients at the center of a square formed by four nodes. With a value for the two gradients at the same point I subtract them to get the vorticity. Halving this value gives the rotation.

The simplest model that I ran tested the simple shear case. In this model I applied a uniform force along each boundary. The scaling of this force resulted in a displacement across the fault zone of almost 6 meters right lateral. I constrained the ends and sides of the grid to move only in the y direction. Figure 15 shows the resulting particle displacements. Using these displacements to calculate the vorticity gives a result very close to the expected value of 1.78 degrees of rotation for 6 meters of displacement across a 100 meter wide fault zone (figure 15). The slight variation of $\pm 0.05^\circ$ appears to be an edge effect at the sides. The profiles in figure 15b show no variation with position in the y direction so the calculation probably is influenced by the sides. As with any numerical solution of this nature the best results exist in the center farthest removed from the edges.

In the next set of models, I used the same boundary

CONTINUUM DEFORMATION

ROTATIONS

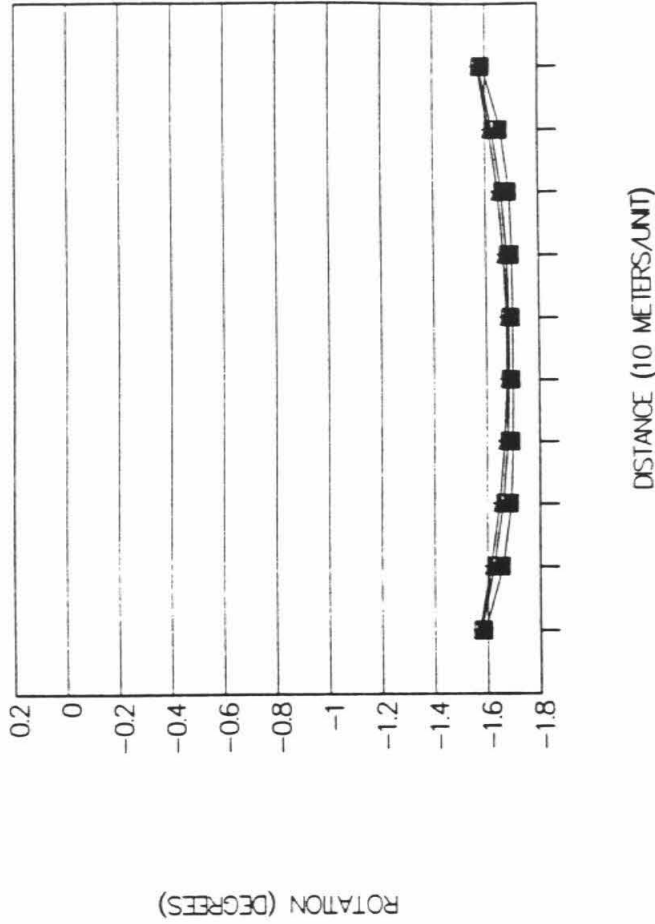
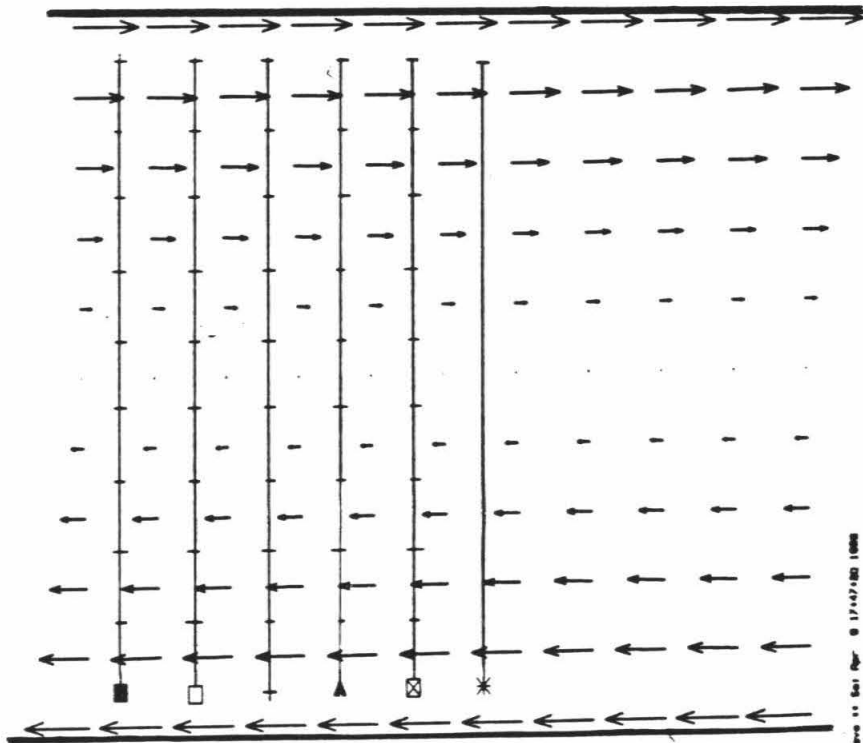


Figure 15 Particle displacements (left) and material rotation (right) for simple-shear deformation. Location of profiles are shown on the particle displacement map with symbol designating profile on left end of profile. Profile data points are located at tick marks. Largest arrow is scaled to 3 meters of displacement.

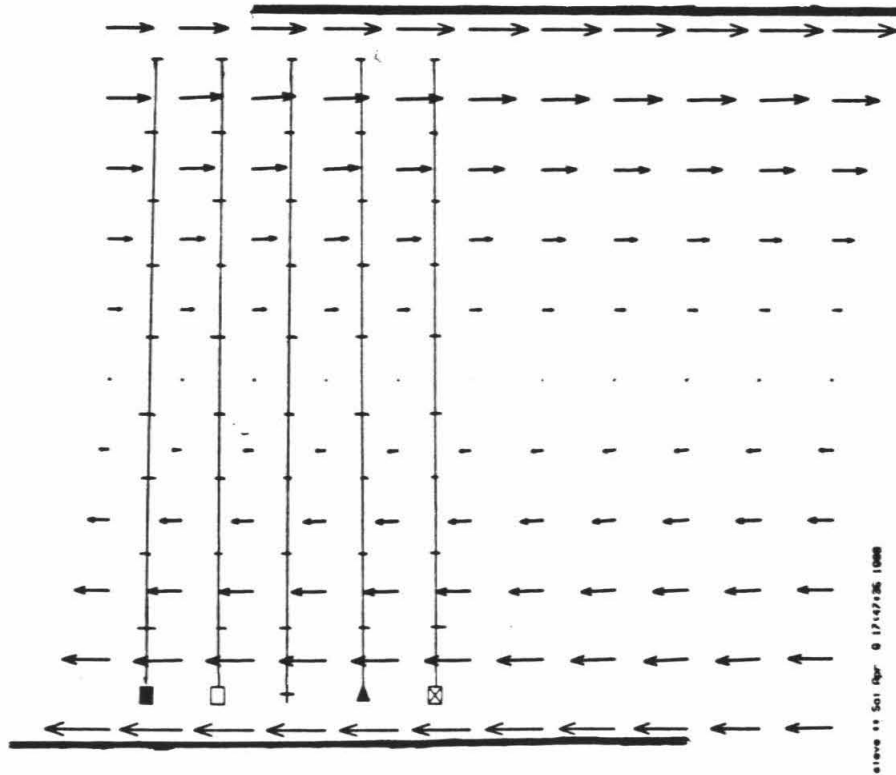
conditions but applied the force to sequentially less of each side. I scaled the forces to maintain the 6 meters of right lateral displacement. Figure 16 shows the results of this calculation. As the tips of the two strands of the fault first approach and then pass the solution diverges from the simple shear case. In general the largest rotations occur near the active side of the deforming block. In addition, the vorticity at the center of the deforming block decreases and the rotation angle becomes less than the -1.78° of the simple-shear case. In these models the rotation only increases above the simple-shear solution near the fault and at the ends. Because of edge effects I do not consider the significant rotations in the corners realistic.

Finally, I investigated the result of relaxing the boundary conditions. Figure 17 shows the results of first constraining the ends but not the sides, and then reversing the restriction. Here for the first time rotations of greater magnitude than -1.78° occur away from the corners.

These profiles suggest interpretations of the rotation data in figure 11. The region between the fault and 20 meters has the appearance of the profiles in figure 16c. The increase in rotation approaching the fault appears similar in form. A second location where a similarity exists lies between 20 and 40 meters from the fault. In this region the rotations are relatively constant at about 20 degrees for unit 68 and 10 degrees for unit 71. This suggests either the simple-shear case for continuum

CONTINUUM DEFORMATION

16a



51000 111 Sci Rep 6 17:47:26 1000

ROTATIONS

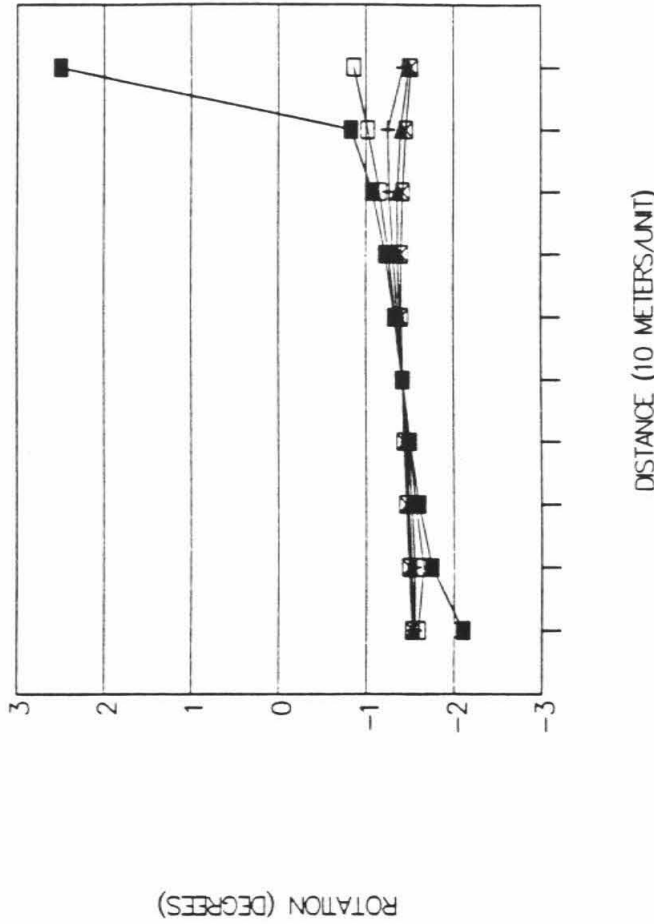
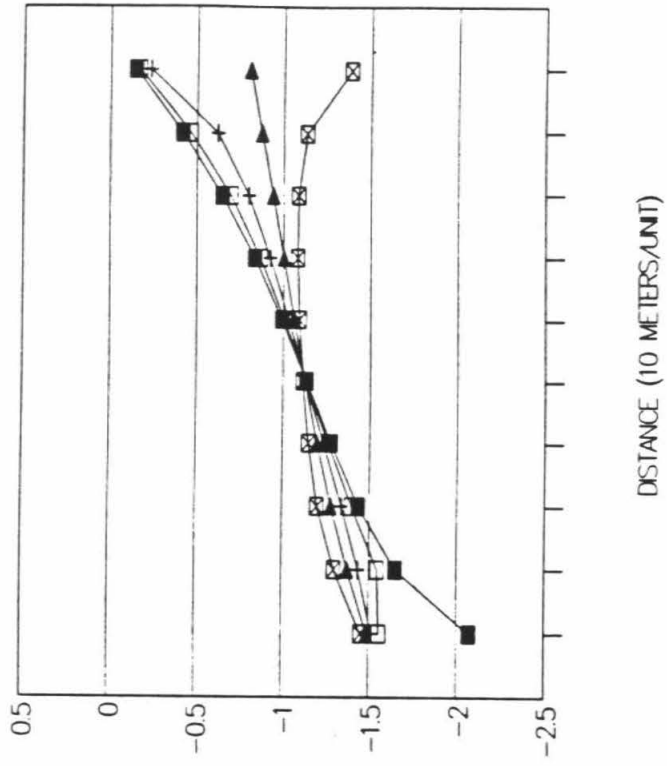
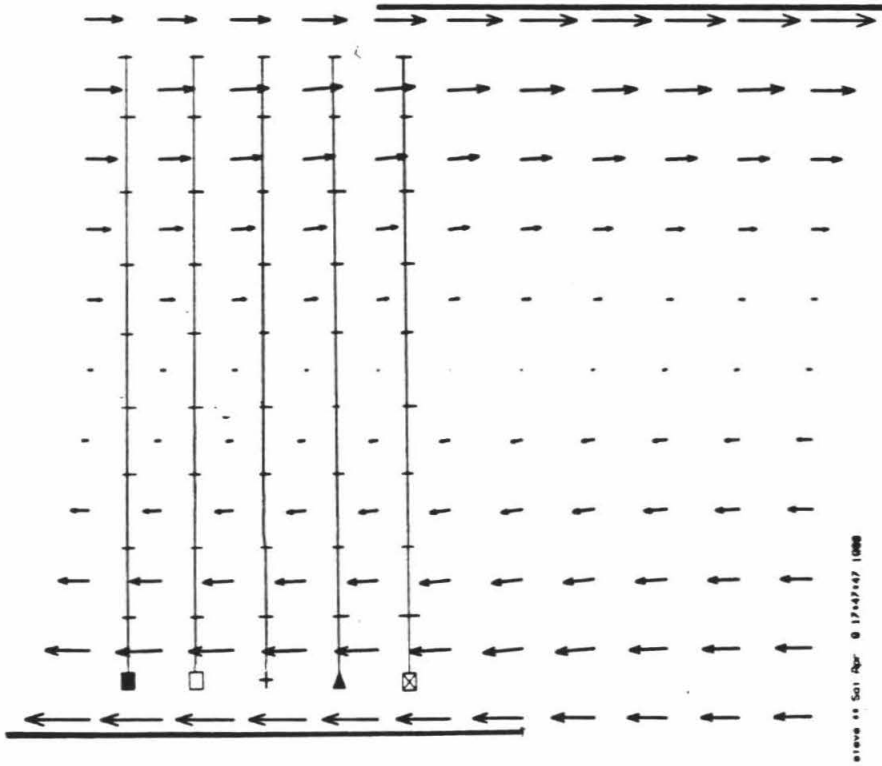


Figure 16 Particle displacements (left) and material rotation (right) for various left-step fault geometries. Extent of fault traces are indicated by heavy-lines on edges of map. Location of profiles are shown on the particle displacement map with symbol designating profile on left end of profile. Profile data points are located at tick marks. Largest arrow is scaled to 3 meters of displacement.

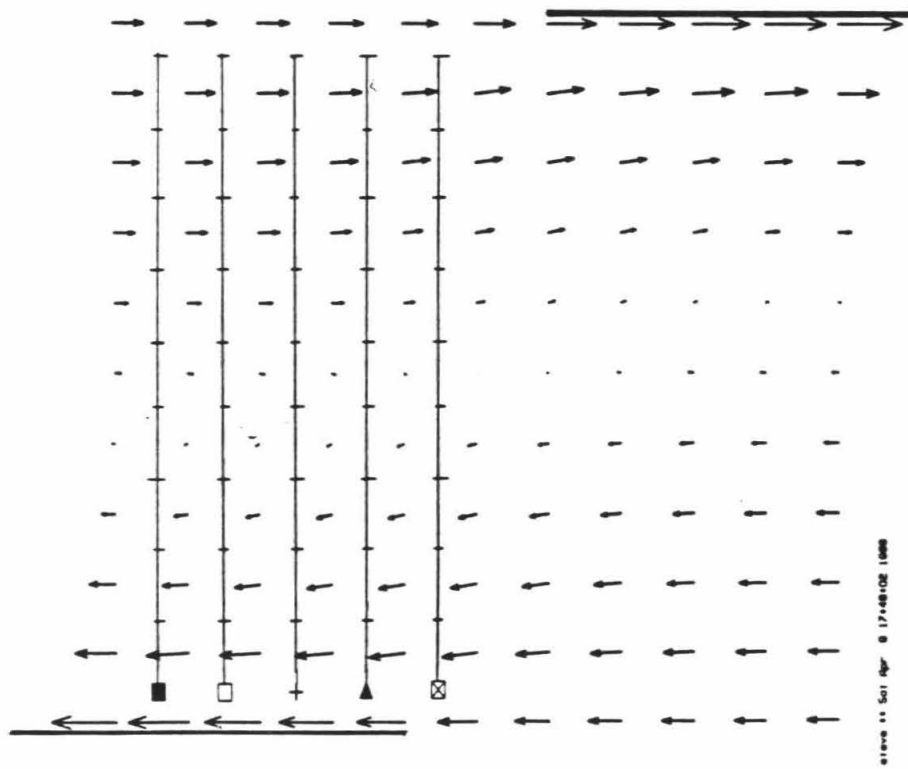
CONTINUUM DEFORMATION ROTATIONS

16b

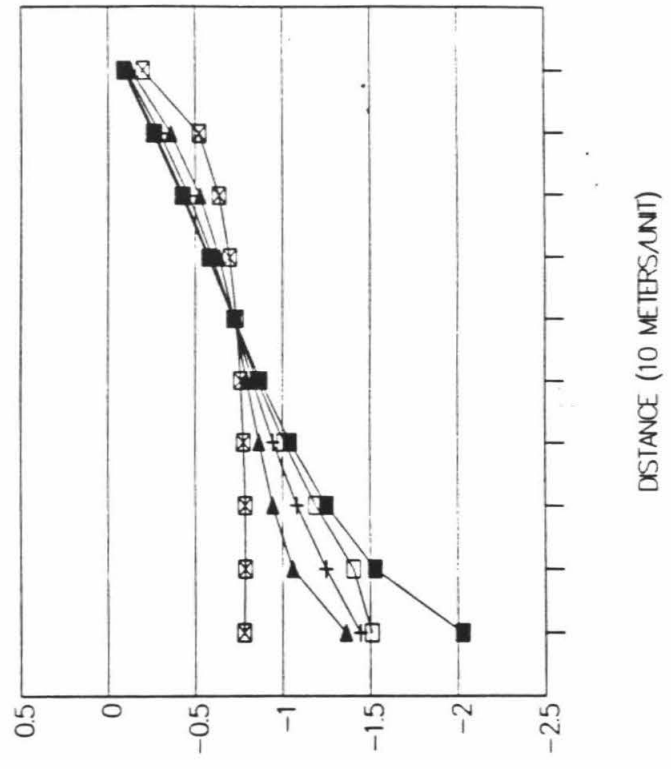


CONTINUUM DEFORMATION ROTATIONS

16c

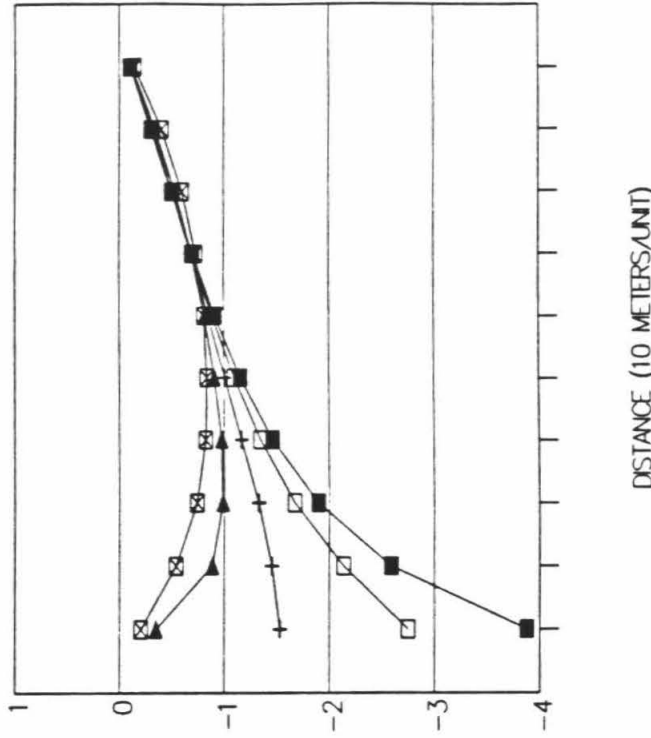


sigma = 501 MPa @ 17.48E102 1000



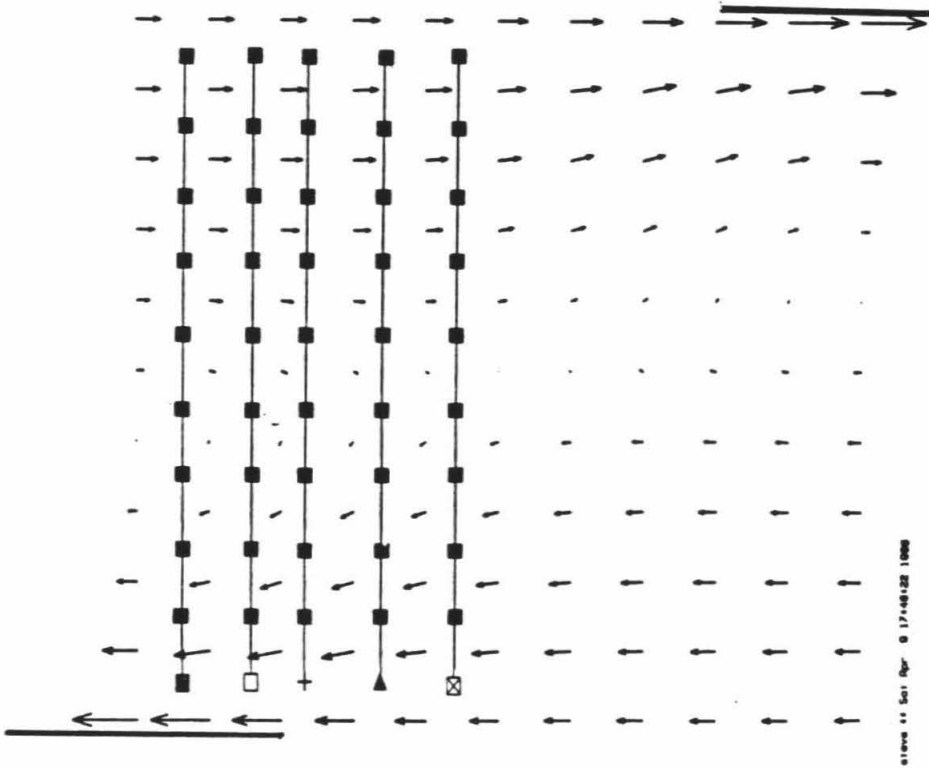
CONTINUUM DEFORMATION

ROTATIONS



16d

ROTATION (DEGREES)



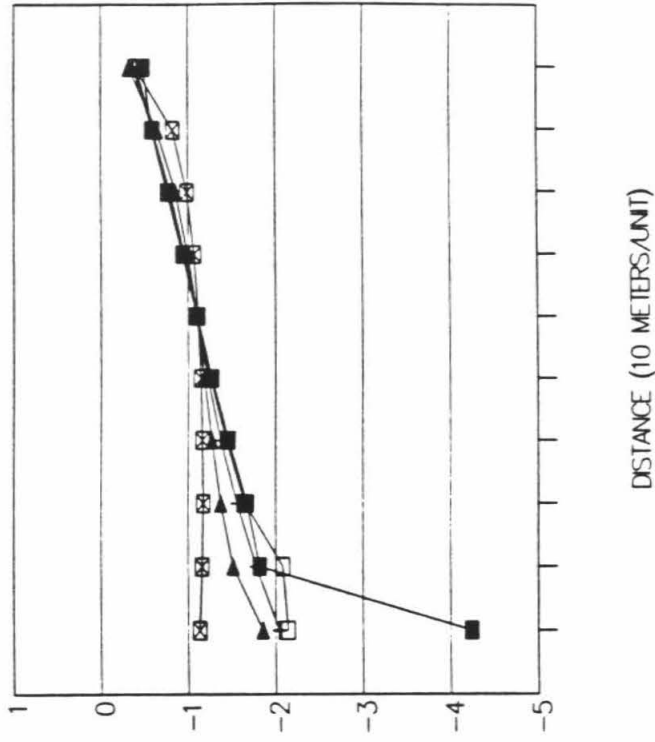
SIERRA 4.1 Sep 89 17:48:22 1000

Figure 17

Particle displacements (left) and material rotation (right) for different boundary conditions. (a) only ends constrained to displacement in the y-direction. (b) only sides constrained to motion in the y-direction. Fault geometry shown by heavy lines on edges of map. Location of profiles are shown on the particle displacement map with symbol designating profile on left end of profile. Profile data points are located at tick marks. Largest arrow is scaled to 3 meters of displacement.

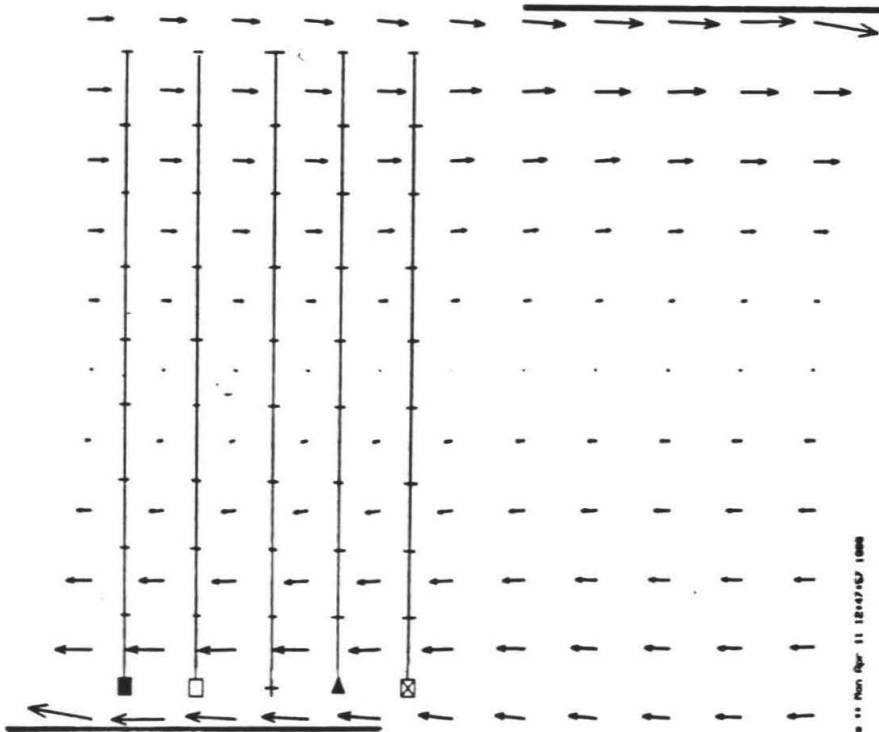
CONTINUUM DEFORMATION

ROTATIONS



17a

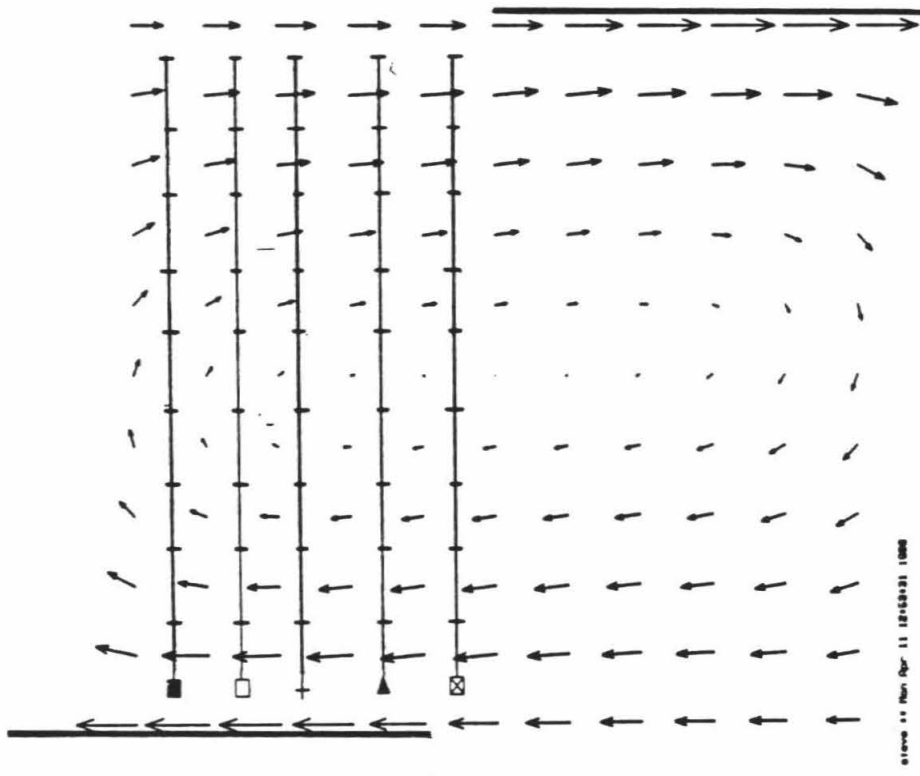
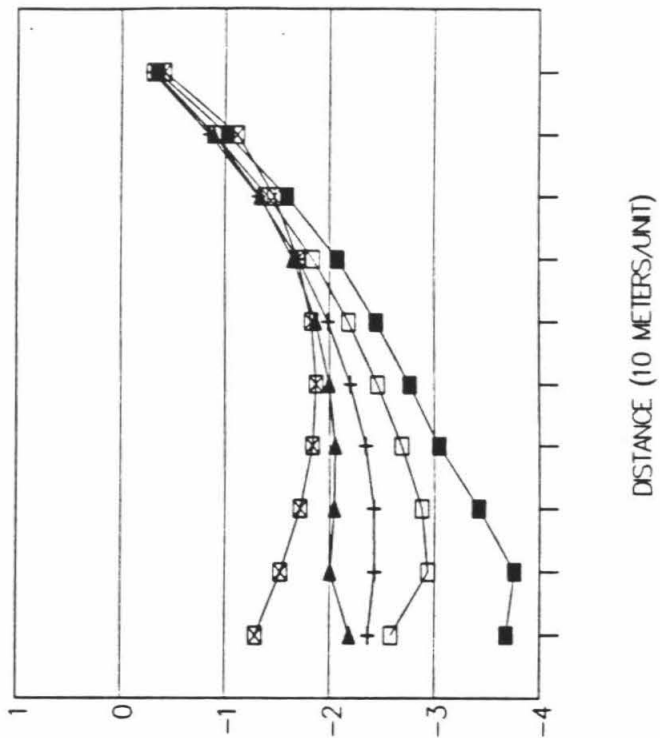
ROTATION (DEGREES)



CONTINUUM DEFORMATION

17b

ROTATIONS



deformation or the block rotation case.

These continuum deformation calculations provide answers to the order of magnitude of the two gradients but does not provide numbers that translate into a non-brittle offset across the fault. The first reason for this is because a very simple geometry was used. As discussed below the increased rotations between 20 and 40 meters correlate with stratigraphic features. This added complexity is not present in these models. Secondly, the deformation was approximated by plane-strain. Nowhere did positive (counter-clockwise) rotations occur similar to the rotations seen at site two. This plane-strain approximation is probably the main simplification leading to this failure of the model.

More work, beyond the scope of this study, is needed to resolve these questions. This work includes more complex modeling of this fault geometry with better material properties and the provision for thickening and thinning included. In addition, more paleomagnetic measurements to better cover the site would be useful. These both would contribute to a better understanding of the material behavior in this fault geometry.

Discussion

The data alone do not suggest one or the other of these

models. The sediments do not have cohesion and so having rigid blocks rotate on the underlying fluid does not appear reasonable. However, these ductile sediments do suggest that they might act as a fluid themselves and so continuum deformation seems like a very reasonable model. A few lines of evidence, however, suggest interpreting the rotations as block rotations.

The first of these is the reasonableness of the average slip rate these values yield. Using the block rotation offset of 14.0 meters for unit 68, plus the brittle offset on the fault of 4 meters for these three earthquakes gives a total offset of 18.0 meters. From Sieh and others (in press), the earthquake cycle began in 1346 ± 17 with event T and ended with event Z in 1857. This gives an average slip rate of 35.6 ± 6.7 mm/yr (figure 18).

For simple shear this value would be double at 71 mm/yr, a value significantly larger than any other proposed slip rate for the San Andreas. Furthermore, the plane strain model demonstrated that this slip rate would be even larger for the left step that I modeled. This unacceptably large rate argues against the validity of the simple-shear model and in favor of the block-rotation model.

The possible existence of regions of left-lateral shear also suggests the validity of the block-rotation model. If the block rotation model accurately represents the deformation, then regions of left shear should be present at the boundaries between the blocks. Except for the main

Pallett Creek Cumulative Offset

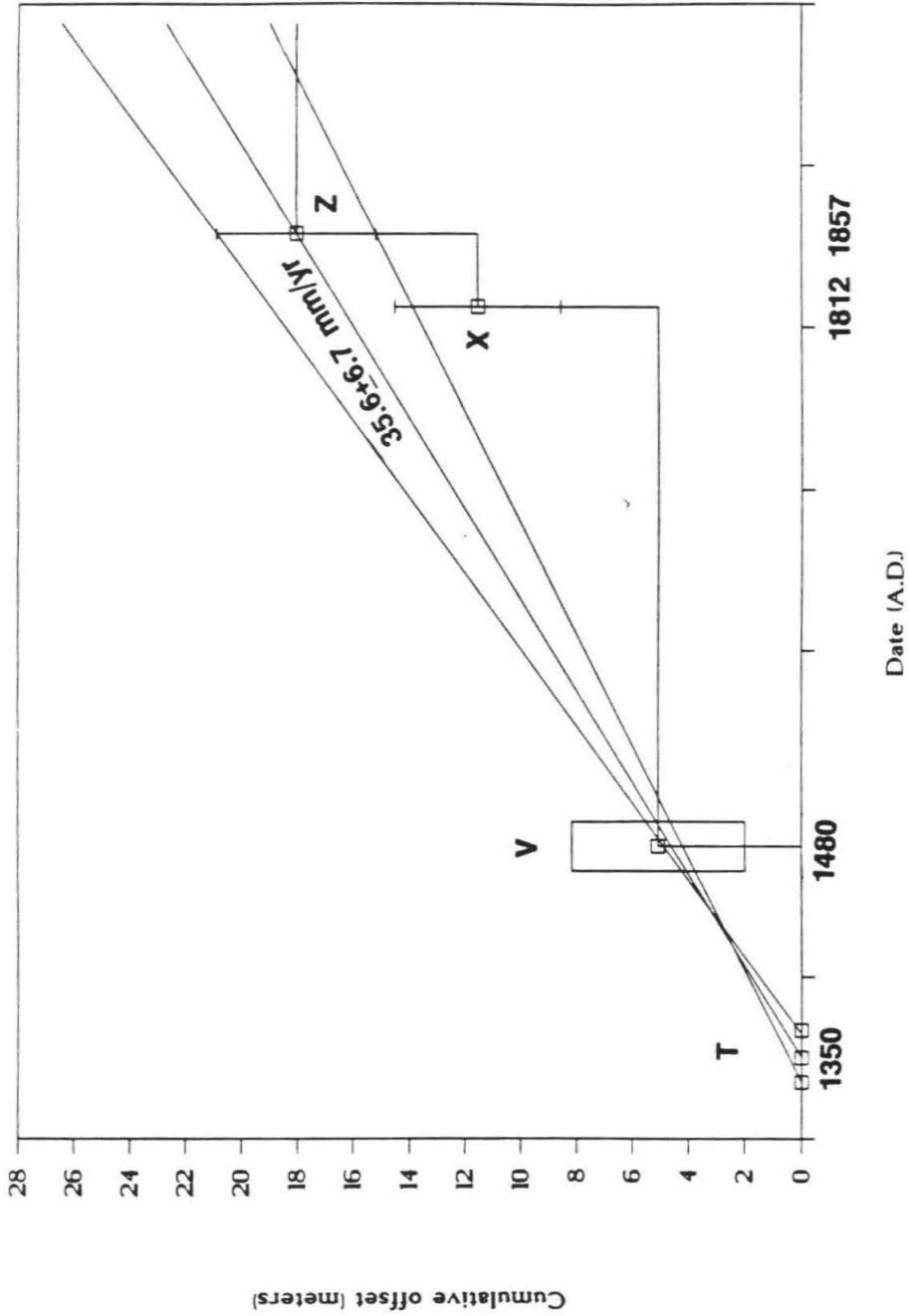


Figure 18

Pallett Creek fault slip history based on earthquake dates from Sieh and others (in press) and individual event offsets. Offsets are combination of non-brittle offset and the brittle offset on the fault trace where the sampling transect crosses (from Sieh, 1984).

trace, no discrete fault planes appear in the excavation, but the noticeable smaller spike in rotation at 36 to 38 meters may represent one of these locations.

The block rotation model, therefore, is the preferred model. This model is the simpler of the two and yields the anticipated average slip-rate. A more sophisticated model of the continuum deformation may show these large rotations possible, but on the basis of the models studied none can generate rotations large enough based on the approximate size of the seismic offsets.

In reality, the actual deformation may be a hybrid form of deformation. In this case there could be some block behavior and some fluid behavior, plain strain or otherwise. This is beyond the scope of this study and will require further work.

I can analyze the three individual events without knowing the precise offset in each. If the region deforms by block rotation, the offsets are known. If the region deforms by continuum deformation, the modeling shows some variation in rotation. I will assume that this variation in rotation is small and that the non-brittle deformation is a multiple of the block rotation offset. I will refer to the non-brittle offset in terms of unspecified "units."

As shown in figure 4, the discrete fault plane had two meters of offset in each of the last two earthquakes, events X and Z. In event V however, the point on the discrete fault plane where this transect crosses showed no brittle

offset. With 14.0 units of non-brittle offset in events V, X, and Z and 8.5 units of offset in events X, and Z, there were 5.5 units of offset in event V alone. Since events X and Z had identical amounts of brittle offset at this point a reasonable assumption is that the non-brittle offset was also the same at 4.25 units.

So the last three events appear to have similar offsets but with different amounts of brittle and non-brittle offset. Event V had 5.5 units of offset, event X had 4.25 units + 2 meters, and event Z had 4.25 units + 2 meters. When the brittle offset is smaller the non-brittle offset is larger. If these units are interpreted as meters the last three events had nearly identical offsets of about 6 meters.

Implications

These similar offsets occur in earthquakes with widely differing recurrence intervals. Between event T and event V, a recurrence interval of about 130 years, between event V and event X, 332 years, and between event X and event Z, 44 years.

This variation suggests two end-member models of fault behavior. If strain accumulation is taken to be constant then the offset in each event is independent of the time between events, and the offset would be a function of the material properties of the fault zone. Alternatively, strain accumulation may vary, in which case the fault zone has a characteristic strength and when a certain stress is

reached the fault moves with a characteristic offset.

Whichever model of rotation is most appropriate the largest rotation generally occurs between 20 and 40 meters from the fault. This coincides with the ancient stream channel. Two possible reasons for this localization present themselves.

First, this region between 20 and 40 meters might represent the subsurface extension of the trace of the fault whose surficial expression ends to the southeast (figure 19a). In the excavation, no discrete fault planes were exposed beyond the main fault zone. However, due to the incision of the ancient channel much of the record is missing. Therefore, three earthquakes may not represent enough time and movement for the second trace to re-establish a discrete plane through this thick fill. The location of the fault in the stream channel may be a coincidence or it may represent stream erosion along a favorable line.

An alternative model is that the whole block is under shear but the younger, less consolidated channel fill is taking most of the shear (figure 19b). In this case the fault zone has two blocks of differing stiffness and the less stiff block deforms the most. If the shear across the fault zone at depth is uniform then one problem is the need for a detachment at depth. This uniform motion must be translated into variations in the deformation and so the surface must be decoupled from the fault zone at depth.

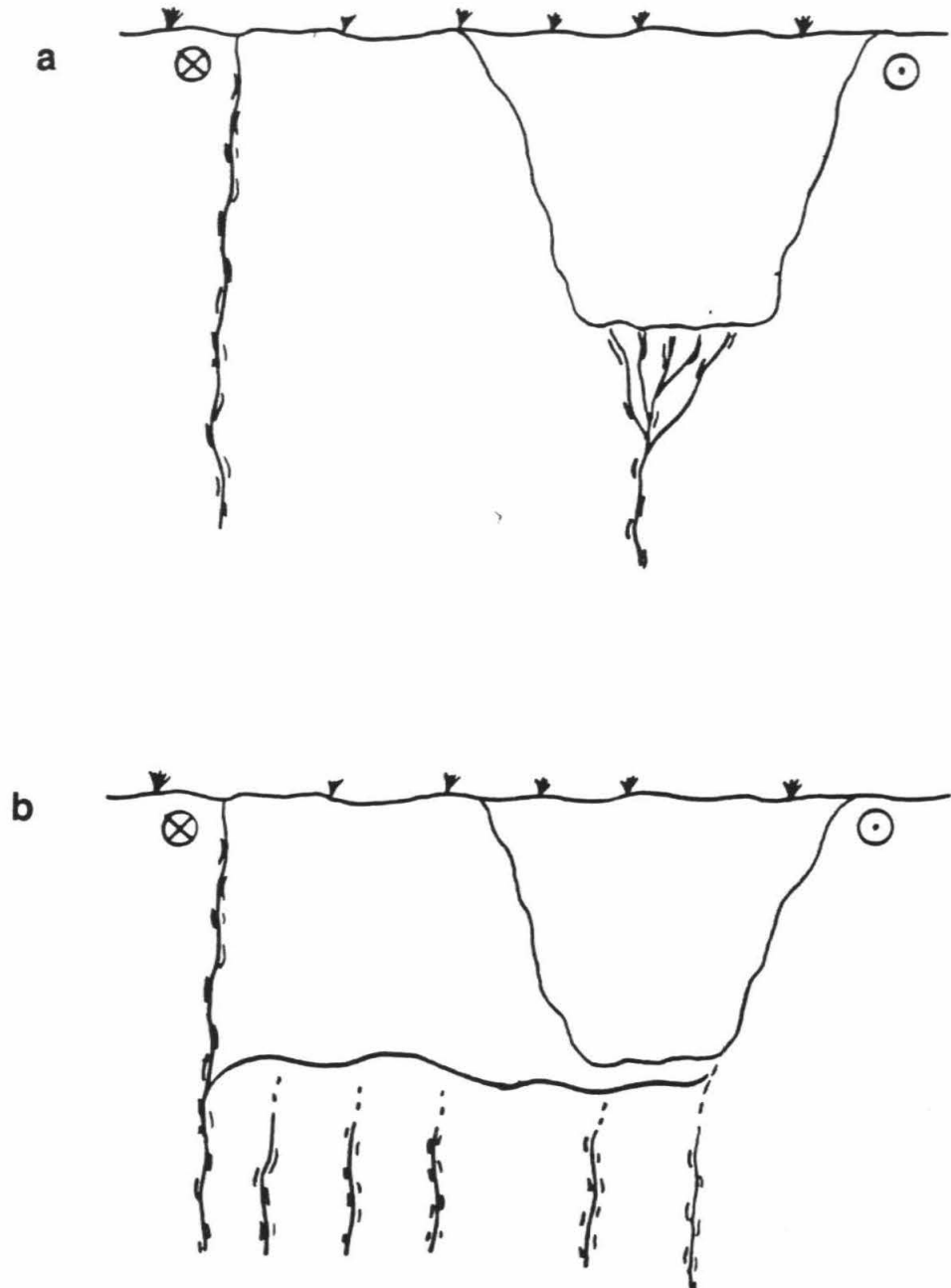


Figure 19

Cartoons of possible models explaining large deformations between 20 and 40 meters. (a) Discrete fault-plane coincides with ancient stream channel and brittle shear is translated into non-brittle deformation of stream fill. (b) Whole fault zone is under distributed shear and shear is concentrated in channel fill because of lower stiffness.

Because of the coincident location with the stream channel, I consider the more likely possibility that the deformation is taking advantage of the less stiff fill of the stream channel. In this case the whole region is under shear but there are two adjoining blocks of different stiffness. Between zero and about 20 meters from the fault the older material has had time to consolidate and stiffen. Between 20 and 40 meters from the fault the younger material has not had the time to consolidate and is not as stiff.

The question that can not be accurately answered pertains to the amount of deformation to the southwest of the fault. Since Pallett Creek has removed the section here there can be no definitive answer to this problem. However, the analogy of the Fort Ross fence in 1906 suggests no further non-brittle deformation. The measurements of Lawson and others (figure 6) showed no deformation of the fence on the northeast side of the fault. The fault geometry at Fort Ross resembles the geometry at Pallett Creek with a step in the fault as it forms a restraining bend. This suggests that I have sampled the whole region containing non-brittle deformation and little more would have be found if the section to the southwest was present.

The fence lines of Thatcher and Lisowski (1987, figure 1) also suggest that no further deformation exists. These fence lines tend to steadily decrease in deformation away from the fault. There are seldom significant oscillations in this decreasing trend. Since the group 3 meters

southwest of the fault has reached the unrotated direction, the behavior of the fences in figure 1 suggest no further deformation beyond 3 meters.

This pattern is, however, violated by the groups to the northeast of the fault. After decreasing from high rotations near the fault, to near zero rotation at about 10 meters, the rotations increase again between 20 and 40 meters. The chances of the pattern being violated again beyond 50 meters is probably very low since the Pleistocene bedrock is about three meters beyond that point. Therefore, the fence lines suggest that all of the deformation has been included on the northeast side of the fault.

The deformation, offsets and slip rate calculated above all represent minimum estimates of these quantities. If the control groups are rotated clockwise (the most likely case in a right-lateral fault zone), or the deformation has not been completely sampled, or the deformation is fluid and not block rotation, the amount of deformation across the fault zone will be larger.

Summary

From these results I have demonstrated that paleomagnetism can be a useful tool in identifying and measuring non-brittle deformation in young sediments within fault zones. Specifically, if the block-rotation model is correct, then the non-brittle long-term offset rate at the Pallett Creek site is about 26 mm/yr and the total average

long-term slip-rate at this site is 35.6 ± 6.7 mm/yr.

In addition, paleomagnetism provides a method of measuring deformation in individual earthquakes and identifying regions of greatest deformation. This latter application may be useful in locating buried, active fault traces.

References

- Barraclough, D. R., 1974, Spherical harmonic analyses of the geomagnetic field for eight epochs between 1600 and 1910: *Geoph. Jour. of the Royal Astron. Soc.*, v. 36, p. 497-513.
- Blatt, Harvey, Middleton, Gerard, and Murray, Raymond, 1980, *Origin of sedimentary rocks*. Prentice-Hall, Englewood Cliffs, New Jersey, 782 p.
- Brown, Robert D., Jr., and Wolfe, Edward W., 1972, Map showing recently active breaks along the San Andreas fault between Point Delgada and Bolinas Bay, California: U.S. Geol. Surv., *Miscellaneous Geologic Investigations*, Map I-692.
- Champion, Duane Edwin, 1980, *Holocene geomagnetic secular variation in the western United States: Implications for the global geomagnetic field*: Ph.D. Thesis, California Institute of Technology, Pasadena, 314 p.
- Creer, K. M., and Tucholka, P., 1982, The shape of the geomagnetic field through the last 8,500 years over part of the northern hemisphere: *Jour. of Geophys.*, v. 51, p. 188-198.

DuBois, R. L., 1974, Secular variations in southwestern United States as suggested by archeomagnetic studies, in Fisher, R. M., Fuller, M., Schmidt, V. A. and Wasilewski, P. J., eds., Proceedings of the Takesi Nagata Conference: University of Pittsburg, p. 133-144.

Ehlers, Ernest G., and Blatt, Harvey, 1982, Petrology: Igneous, Sedimentary, and Metamorphic, W. H. Freeman, San Francisco, 732 p.

Fisher, R. A., 1953, Dispersion on a sphere: Proc. of the Royal Soc., v. A217, p. 295-305.

Games, Kenneth P., 1977, The magnitude of the palaeomagnetic field: a new non-thermal, non-detrital method using Sun-dried bricks: Geophys. Jour. Royal Astron. Soc., v. 48, p. 315-329.

Games, Kenneth P., 1980, The magnitude of the archaeomagnetic field in Egypt between 3000 and 0 BC: Geophys. Jour. of the Royal Astron. Society, v. 63, p. 45-56.

Games, Kenneth P., 1983, Magnetization of adobe bricks, in K. M. Creer, P. Tucholka, and C. E. Barton, eds.,

Geomagnetism of baked clays and recent sediments, Elsevier, Amsterdam, p. 22-26.

Hoblitt, Richard P., Crandell, Dwight R., and Mullineaux, Donal R., 1980, Mount St. Helens eruptive behavior during the past 1500 yr.: *Geology*, v. 8, p. 555-559.

Holm, Richard F., and Moore, Richard B., 1987, Holocene scoria cone and lava flows at Sunset Crater, northern Arizona, *in* Stanley S. Beus, ed., Centennial Field Guide, Rocky Mountain Section of the Geol. Soc. of Amer., v. 2, p. 393-398.

Hughes, Thomas J., 1987, *The finite element method: Linear static and dynamic finite element analysis*, Prentice-Hall, Englewood Cliffs, New Jersey, 803 p.

Irving, E., 1964, *Paleomagnetism and its application to geological and geophysical problems*, Wiley, New York, 399 p.

King, R. F., 1955, Remanent magnetism of artificially deposited sediments: *Mon. Not. R. Astron. Soc. Geophys. Suppl.*, v. 7, p. 115-134.

Kirschvink, Joseph L., 1980, The least-squares line and plane and the analysis of paleomagnetic data: *Geophys.*

Jour. of the Royal Astron. Soc., v. 62, p. 699-718.

Lawson, Andrew C.(ed.), 1908, The California earthquake of April 18, 1906, in Report of the State Earthquake Investigation Commission, Carnegie Institution of Washington, Washington, D.C., 2 vol., 641 p.

Lund, S. P., and Banerjee, S. K., 1979, Paleosecular variations from lake sediments: Rev. Geophys., v. 17, p. 244-248.

Lund, Steve P., and Banerjee, Subir K., 1985, Late Quaternary paleomagnetic field secular variation from two Minnesota lakes: Jour. of Geoph. Res.,v. 90, p. 803-826.

Mardia, K. V., 1972, Statistics of directional data, Academic Press, New York, 357 p.

McElhinny, M. W., 1973, Paleomagnetism and plate tectonics, Cambridge University Press, 358 p.

McKenzie, Dan, and Jackson, James, 1983, The relationship between strain rates, crustal thickening, palaeomagnetism, finite strain and fault movements within a deforming zone: Earth and Planet. Sci. Let., v. 65, p. 182-202.

- Miller, C. Dan, 1985, Holocene eruptions at the Inyo volcanic chain, California: Implications for possible eruptions in Long Valley caldera: *Geology*, v. 13, p. 14-17.
- Minster, J. Bernard, and Jordan, Thomas H., 1987, Vector constraints on western U.S. deformation from space geodesy, neotectonics, and plate motions: *Jour. of Geoph. Res.*, v. 92, p. 4798-4804.
- Mullineaux, Donal R., and Crandell, Dwight R., 1981, The eruptive history of Mount St. Helens, in U.S.G.S. Prof. Paper 1250, p. 3-15.
- Nelson, Michael R., and Jones, Craig H., 1987, Paleomagnetism and crustal rotations along a shear zone, Las Vegas Range, southern Nevada: *Tectonics*, v. 6, p. 13-34.
- Nur, A., Ron, H., and Scotti, O., 1986, Fault mechanics and the kinematics of block rotations: *Geology*, v. 14, p. 746-749.
- Ramsay, John G., and Huber, Martin I., 1983, The techniques of modern structural geology: v. 1, Strain analysis, Academic Press, New York, 302 p.

- Rockwell, T. K., Lamar, D. L., McElwain, R. S., and Millman, D. E., 1985, Late Holocene recurrent faulting on the Glen Ivy north strand of the Elsinore Fault, southern California: Geol. Soc. of Amer. Abs. with Prog., v. 17, p. 404.
- Ron, Hagai, Aydin, Atilla, and Nur, Amos, 1986, Strike-slip faulting and block rotation in the Lake Mead fault system: Geology, v. 14, p. 1020-1023.
- Schwartz, David P., and Weldon, Ray J., 1987, San Andreas slip rates: Preliminary results from the 96 St. site near Littlerock, CA.: GSA Abs. with Prog., v. 19, p. 448.
- Sieh, Kerry E., 1978, Prehistoric large earthquakes produced by slip on the San Andreas fault at Pallett Creek, California: Jour. of Geophys. Res., v. 83, p. 3907-3939.
- Sieh, Kerry E., 1978b, Slip along the San Andreas fault associated with the great 1857 earthquake: Bull. of the Seismol. Soc. of Amer., v. 68, p. 1421-1428.
- Sieh, Kerry E., 1986, Slip rate across the San Andreas fault and prehistoric earthquakes at Indio, California: EOS, v. 67, p. 1200.

- Sieh, Kerry E., 1984, Lateral offsets and revised dates of large prehistoric earthquakes at Pallett Creek, southern California: Jour. of Geoph. Res., v. 89, p. 7641-7670.
- Sieh, Kerry, and Bursik, Marcus, 1986, Most recent eruption of the Mono Craters, eastern central California: Jour. of Geoph. Res., v. 91, p. 12,539-12,571.
- Sieh, Kerry E., Stuiver, Minze, and Brillinger, David, in press, A very precise chronology of earthquakes produced by the San Andreas fault in southern California.
- Smiley, Terah L., 1958, The geology and dating of Sunset Crater, Flagstaff, Arizona: New Mexico Geol. Soc. Field Conference, no. 9, p. 186-190.
- Sternberg, R. S., 1982, Archaeomagnetic secular variation of direction and paleointensity in the American southwest, Ph.D. Thesis, University of Arizona, Tucson, 307 p.
- Sternberg, R. S., 1983, Archaeomagnetism in the southwest of North America, in K. M. Creer, P. Tucholka, and C. E. Barton, eds., Geomagnetism of baked clays and recent sediments, Elsevier, Amsterdam, p. 159-167.

Tarling, D. H., 1983, Paleomagnetism: Principles and applications in Geology, Geophysics, and Archaeology, Chapman and Hall, New York, 379 p.

Thatcher, Wayne, and Lisowski, Michael, 1987, Long-term seismic potential of the San Andreas fault southeast of San Francisco, California: Jour. of Geoph. Res., v. 92, p. 4771-4784.

Verosub, Kenneth L., 1977, Depositional and postdepositional processes in the magnetization of sediments: Rev. Geoph. Space Sci., v. 15, p. 129-143.

Verosub, Kenneth L., and Mehringer, Peter J. Jr., 1984, Congruent paleomagnetic and archeomagnetic records from the western United States: A.D. 750 to 1450: Science, v. 224, p. 387-389.

Verosub, Kenneth L., Mehringer, Peter J. Jr., and Waterstraat, Paul, 1986, Holocene secular variation in western North America: Paleomagnetic record from Fish Lake, Harney County, Oregon: Jour. of Geoph. Res., v. 91, p. 3609-3624.

Weldon, Ray J. II, and Sieh, Kerry E., 1985, Holocene rate of slip and tentative recurrence interval for large

earthquakes in the San Andreas fault, Cajon Pass, southern California: Geol. Soc. of Amer. Bull., v. 96, p. 793-812.

Williams, Patrick L., and Sieh, Kerry E., 1987, Decreasing activity of the southernmost San Andreas fault during the past millennium: Geol. Soc. of Amer. Abs. with programs, v. 19, p. 891.

Wolfman, D., 1979, Archaeomagnetic dating in Arkansas: Archaeo-Physika, v. 10, p. 522-533.

Yamaguchi, David K., 1983, New tree-ring dates for recent eruptions of Mount St. Helens: Quat. Res., v. 20, p. 246-250.

Yamaguchi, David K., 1985, Tree-ring evidence for a two-year interval between recent prehistoric explosive eruptions of Mount St. Helens: Geology, v. 13, p. 554-557.

Appendix 1

Collection, Preparation, and Measurement of Soft-sediment Paleomagnetic Samples

Introduction

This appendix serves a twofold purpose. First, it sets forth in one complete and independent section the methods and processing sequence used for the samples in this thesis. Second it records the current "state of the art" of handling soft-sediment paleomagnetic samples. As an evolving technique this is not the final word, but rather a statement of the current techniques for those who wish to use and improve them.

SAMPLING

Tools

Sampling is performed using many of the same tools used for traditional paleomagnetic sampling. These are: a brass orienting sleeve, pocket transit (such as a Brunton compass), and a "sun compass."

The sun compass consists of a plastic plate with two orthogonal leveling bubbles, a protractor mounted horizontally on the plate, and a straight metal wire that mounts vertically in the center of the protractor. The compass measures the angular difference between the sun and the strike of the orienting sleeve. A computer program

later converts this angle, using the date, time and site location, into the strike of the orienting sleeve. Although necessary at locations where the difference between magnetic and true north is unknown, its use at other times provides useful redundancy in the measurements.

The non-traditional tools are a "sampling tube," a brass "pounding sleeve," a teflon plunger, and quartz-glass sample tubes. The sampling tube is made from specialty non-magnetic steel. A 10-inch-long section of this 1-inch-outside-diameter (the same diameter as a drilled paleomagnetic sample) steel pipe is sharpened at one end. In addition, straight lines are scribed on opposite sides of the outside of the tube parallel to the axis of the tube. One of these lines is inked red for reference and another ink line is made around the circumference of the tube about one inch from the sharpened end of the tube.

The brass pounding sleeve is a cylindrical piece of brass three inches long and 2 inches in diameter, with a indentation in one end that fits over the blunt end of the sampling tube. This indentation is about 1.0 inches deep, so the sleeve is stable over the end of the sampling tube. The plunger is made from a plastic, like teflon, and is about one inch longer than the sampling tube. It is also cylindrical, but with an outside diameter less than the inside diameter of the sampling tube. The plunger fits closely inside the sampling tube, but should still be able to slide freely.

The sample tubes are cylinders of quartz glass. We have found that tubes closed at one end work better than tubes open at both ends, but both are usable. The tubes are 1 inch long and slightly less than one inch in diameter, giving an inside diameter close to the inside diameter of the sampling tube.

Sampling procedure

1) The glass sample tube is prepared by marking an ink arrow on the outside of the tube, parallel to the cylindrical axis of the tube. The arrow points towards the open end of the tube. If both ends are open, the end at the tail of the arrow is covered with "Parafilm." Finally, the sample tube is labeled with the sample identification number.

2) The sharp end of sample tube is pushed into the trench wall, either by strong manual pressure or by pounding. The red line is on the top of tube, as close to vertical as possible. There should be no rotation of the tube as it is pushed into the exposure. I found that rotating the tube can be avoided by applying the force to the brass cap allowing it to rotate independently of the sampling tube.

3) The brass cap is removed and the brass orienting sleeve is placed over the exposed end of the tube, the top mark on the sleeve aligned with the red line on the sampling tube. The angle of the red line from vertical is measured.

This is the "twist correction," the error in placing the red line exactly at the top of the tube when the tube is pushed into the outcrop. The convention used in the Caltech lab is that "clockwise" or "counter-clockwise" describes the direction necessary to turn the orienting sleeve to go from vertical to the position of the red line.

4) The right-handed orientation (strike and dip) of the plate on the orienting sleeve is taken. This means that the strike, pointing to the right on the plate, is taken. Therefore, taking the vector product of the dip vector cross the strike vector will give the orientation of the sampling tube pointing outward from the outcrop. The sun compass strike, and time of reading, are also taken.

5) The orienting sleeve is removed and the plunger placed inside the sampling tube. The plunger is pushed into the tube until the sample is contacted, but not compacted.

6) The sampling tube is removed from the exposure. Pulling the tube straight out frequently fails to detach the sample from the exposure, so the removal of the tube is best preceded by lateral rocking, but not rotation, of the tube.

7) Upon removal, the end of the tube containing the sample is tilted upward. At this time the plunger should be held in place so it supports the sample and does not fall out. The glass sample tube is placed over the end of the metal sampling tube aligning the head of the ink arrow with the red line. Now, forcing the plunger upward transfers the sample to the sample tube. Again, rotation of the plunger

should be avoided to prevent rotating the sample.

8) When enough of the sample has been pushed into the glass sample tube to fill it, the two tubes are lowered together to horizontal. Continuing to push on the plunger provides extra sample material above the rim of the sample tube. As the glass tube is separated from the sampling tube it is quickly turned vertical, but avoiding disruption of the sample.

9) The open end of the sample tube is capped with "Parafilm," a flexible paraffin film.

10) The sample tube is wrapped in paper and stored for transport back to the lab.

PREPARATION

To cement the sample together for processing we use a 10:1 water to sodium silicate solution (waterglass) mixture. I perform all "silicating" in the shielded room to prevent grains from rotating to the ambient field direction if they should become suspended.

After unwrapping the samples, I apply the silicate solution with a pipette, a few drops at a time. Depending on the permeability of the sediment I may apply up to five drops at one time. I usually silicate 20 samples in a group, adding solution to each sample in order. When I reach the last sample, I begin again with the first sample. With the glass tubes, the advance of the silicate solution through the sample can be seen. I continue adding solution

until the silicate solution completely permeates the sample, but not until solution is standing in the bottom of the tube. When the whole sample is moist, and solution from the sample begins to moisten the side of the tube, I halt silicating. For samples with good permeability, this procedure of five drops of solution repeated every 1.5 minutes will saturate the sample in about 45 minutes.

Modification of the procedure is necessary for less permeable samples. In this case, it may be necessary to let solution stand on the top of the sample so it can slowly soak in. For an impermeable sample, it is difficult to avoid standing solution in the bottom of the tube. These samples may require a few days to silicate, adding more solution to the top of the sample every hour or so.

After I stop adding silicate solution to the sample, I allow the sample to dry at least three days. This assures that the center is solid and does not fall apart with handling.

When the sample is dry, I seal the open end(s) of the sample tubes with a high-temperature, ceramic cement. We use Zircar alumina cement. A thin cap of the cement is placed over the open end of the tube and allowed to dry, usually about 4 hours. This must be done in a shielded area since this cement can acquire a strong magnetic moment if dried in an ambient field (Salyards, unpublished research).

Finally, the sample tube is labeled with high temperature white ink. The ink from the felt tip markers

used in the field vaporizes at temperatures between 300° and 350° C, so the sample must be labeled before heating to these temperatures.

At this time the "twist correction" is made. Using a template, the twist measurement from the field notes is measured on the sample tube and a new arrow marked on the side of the tube. This arrow is at the location of the true top of the sample when collected.

When all of this has dried, the sample is ready for processing.

MEASUREMENT

Facilities

The paleomagnetism laboratory at the California Institute of Technology has a modified SCT cryogenic SQUID magnetometer with electronics from 2G Corporation. The whole measurement process is computer automated using an IBM-compatible system. The computer controls the lowering of the sample into the measurement region and the rotation of the sample in the measurement region, as well as the acquisition of data from the SQUID electronics. In addition, the alternating field (AF) demagnetization is completely computer controlled.

The magnetometer and samples all reside in a room shielded with a double layer of molypermaloid metal (mu-metal). The samples remain in this room through the whole measurement process. The AF coils, mounted on the top of

the magnetometer, are further shielded with three more layers of mu-metal. The thermal demagnetization oven is shielded in two layers of mu-metal and is accessible through a port in the wall of the shielded room, so samples do not leave the shielded space during thermal demagnetization.

Demagnetization procedure

On any sample, the NRM is the first measurement. After this, the sample is usually demagnetized by progressive alternating-field demagnetization steps up to 10 mT. This is a static, three-axis AF demagnetization using a vertical solenoid to demagnetize the cylindrical axis of the sample and a transverse solenoid to demagnetize the two horizontal axes of the sample. Placement in the coils, peak field levels and field decay rate are all computer controlled. Usually, samples are demagnetized in 1.25 mT steps, but if several samples from a unit show stable demagnetization, the steps for remaining samples may be increased to 2.5 mT.

Next, the samples are thermally demagnetized. Again, samples are usually demagnetized in 50°C steps, but if the unit is stable, remaining samples may be heated in 100°C steps. At a minimum, samples will be heated to, and measured at 100°, 200°, 300°, 400°, 500°, 550°C. Samples of volcanic rock are heated in small steps; particularly around the Curie temperature of magnetite, about 570°C, where steps may be as small as 15°C. Heating continues until: 1) the magnetic moment is <5% of the NRM intensity, or 2) the

sample has been heated to 675°C, or 3) the sample is judged to be unstable and no useful information is to be gained by further effort.

INTERPRETATION

After demagnetization, components of magnetization are found using a principal component analysis of the demagnetization directions (Kirschvink, 1980). Typically I will calculate component directions for several different sets of measurement steps. Using all of the measurement steps gives a direction that assumes no overprinting. A component based on the low temperature steps, up to 350° or 400°C, provides an estimate of the viscous magnetic component or the chemical component from secondary iron mineralization. A component direction using the high temperature measurement steps hopefully yields the direction of the original magnetization direction carried by detrital magnetite and hematite. Usually, these three components are fairly close and I consider the component using all of the sample points a reliable primary direction for the sample.

ORTHOGONAL VECTOR DEMAGNETIZATION DIAGRAMS

Orthogonal vector demagnetization diagrams allow representation of three dimensional vector information on a two dimensional plot. The information of interest in paleomagnetism is declination, inclination and intensity of the magnetic field in a sample. These three quantities

uniquely describe the magnetic field vector.

At each demagnetization step these three values are measured so the demagnetization of a sample can be described by this set of vectors, one vector per demagnetization step.

In analyzing the demagnetization behavior of a sample, the vector of interest is the one representing the change between demagnetization steps; this quantity is found by subtracting the magnetic field vector at a given step from the vector direction of the preceding step.

The orthogonal vector demagnetization diagram shows these vectors in the sequence in which they were removed, the first vector being furthest from the origin.

This diagram shows two different projections of the string of vectors on a shared set of axes.

First, the vectors are projected onto a horizontal plane passing through the origin. Accordingly, the axes for this projection are the four cardinal directions: North, South, East, and West.

Second, the vectors are projected onto a vertical plane passing through the origin; in this thesis I use a north-south trending plane. For this projection the vertical axis is up-down and the horizontal axis is north-south or east-west.

The two projections are labeled "D" for the declination projection onto the horizontal plane and "I" for the inclination projection onto the vertical plane.

In practice the construction of this diagram is

simpler than this description of its significance would suggest. The magnetic field vector for each measurement step is plotted with its tail at the origin. Only a symbol representing the location of the head of the vector is plotted. By connecting one vector head to the preceding vector head the two vectors are subtracted graphically.

For declination D , inclination I , and magnetic intensity M , the Cartesian coordinates of the first projection are $x = M \cos I \sin D$ and $y = M \cos I \cos D$. The coordinates of the second projection are $x = M \cos I \cos D$ and $y = -M \sin I$.

In reading orthogonal diagrams there are two important concepts to remember. First, the declination angle appears undistorted, but inclination and magnetic intensity will be distorted by the projections. Second, significant magnetic components will appear as straight sections of the demagnetization path made up of one or more vectors removed by demagnetization steps (provided magnetic components do not have overlapping coercivity ranges).

Appendix 2

Paleomagnetic Constraints on the Depositional and Thermal History of a Block-and-Ash Flow from Panum Crater, California**Abstract**

Paleomagnetic directions of clasts within a block-and-ash flow deposit near Panum crater, California, tightly constrain the local direction of the magnetic field about A.D. 1350 and illuminate the cooling history of the flow. The magnetic directions of bread-crusteD pumice blocks within the flow yield a field direction of $dec=357.7^\circ$ and $inc=61.2^\circ$. Tight clustering of paleomagnetic directions and unidirectional demagnetization paths prove that the pumice blocks were emplaced at temperatures well above 600°C and that all in situ settling occurred while the samples were hotter than 600°C . Surprisingly, the magnetic directions of nearby non-pumiceous, angular blocks also indicate emplacement at temperatures above 600°C . One subset from within this population of blocks records a mean direction similar to the direction of the pumiceous blocks, but with substantially more scatter. This suggests that slight, random settling of these blocks occurred after they had cooled to temperatures of $\leq 100^\circ\text{C}$. A second subset of the angular blocks displays low-temperature components of magnetization identical to the direction recorded by the

pumice, but substantially different high-temperature components. This indicates that these blocks settled as they cooled from about 600° to about 500° C, but were stable during the remainder of their cooling history. These results confirm and quantify field observations that indicate the clasts within the flow deposit were emplaced as a variety of temperatures and with diverse rheologic properties.

Introduction

A block-and-ash flow deposit associated with the 600-year-old eruption of Panum Crater, near Mono Lake, California, is a particularly attractive target for paleomagnetic study. there are three reasons for this: First, stable volcanic rocks possess a thermal remanent magnetization, which is typically a more reliable form of remanent magnetization than other types. Second, the age of this volcanic deposit is unusually well-constrained by radiocarbon and dendrologic dates to A.D. 1340±25. Third, the deposit contains two types of volcanic clasts, which appear to have experienced markedly different cooling histories.

The volcanic nature of the deposit and its precise date give us hope that we could determine a well-constrained point for a late Holocene paleomagnetic secular variation curve for southern California. The interesting textural variety of clasts within the deposit led us to believe that

paleomagnetic data might enable quantification of the cooling history of the deposit.

Setting

The Mono and Inyo craters are in eastern central California, at the boundary of the Sierra Nevada and Basin-Ranges provinces (Figure 1). This forty-kilometer-long chain of domes and flows is the product of about 35,000 years of silicic volcanic activity.

The most recent large eruption from the chain occurred about A.D. 1345. Sieh and Bursik (1986) showed that this episode, the north Mono eruption, began with several plinian eruptions from vents along the northern six kilometers of the chain. Pyroclastic flows occurred after the plinian eruptions, and these were followed by extrusion of several rhyolitic domes and flows. Within no more than a couple of years, a similar sequence occurred to the south, along the Inyo Craters.

The northernmost member of the Mono-Inyo chain, Panum Dome, is one of the domes and flows that was erupted during the North Mono eruption. Prior to extrusion of the dome, but after the plinian phases of the eruption, a pyroclastic flow emanated from the crater now plugged by the dome, and flowed northwestward, toward Mono Lake. Figure 2 displays the geometry of this pyroclastic flow and its relationship to Panum dome.

At site one, 1.5 km from the crater, this deposit is a

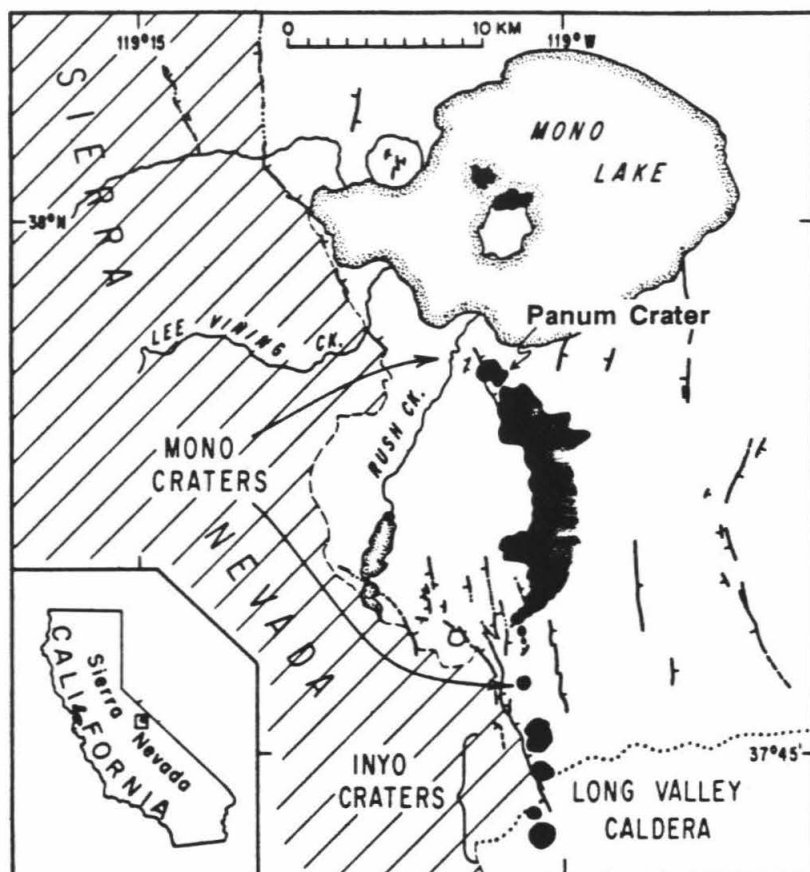


Figure 1

The Mono and Inyo craters and volcanoes of Mono Lake (in black) lie along the active east flank of the Sierra Nevada. The block-and-ash flow studied in this chapter lies to the northwest of Panum Crater. (modified from Sieh and Bursik, 1986)

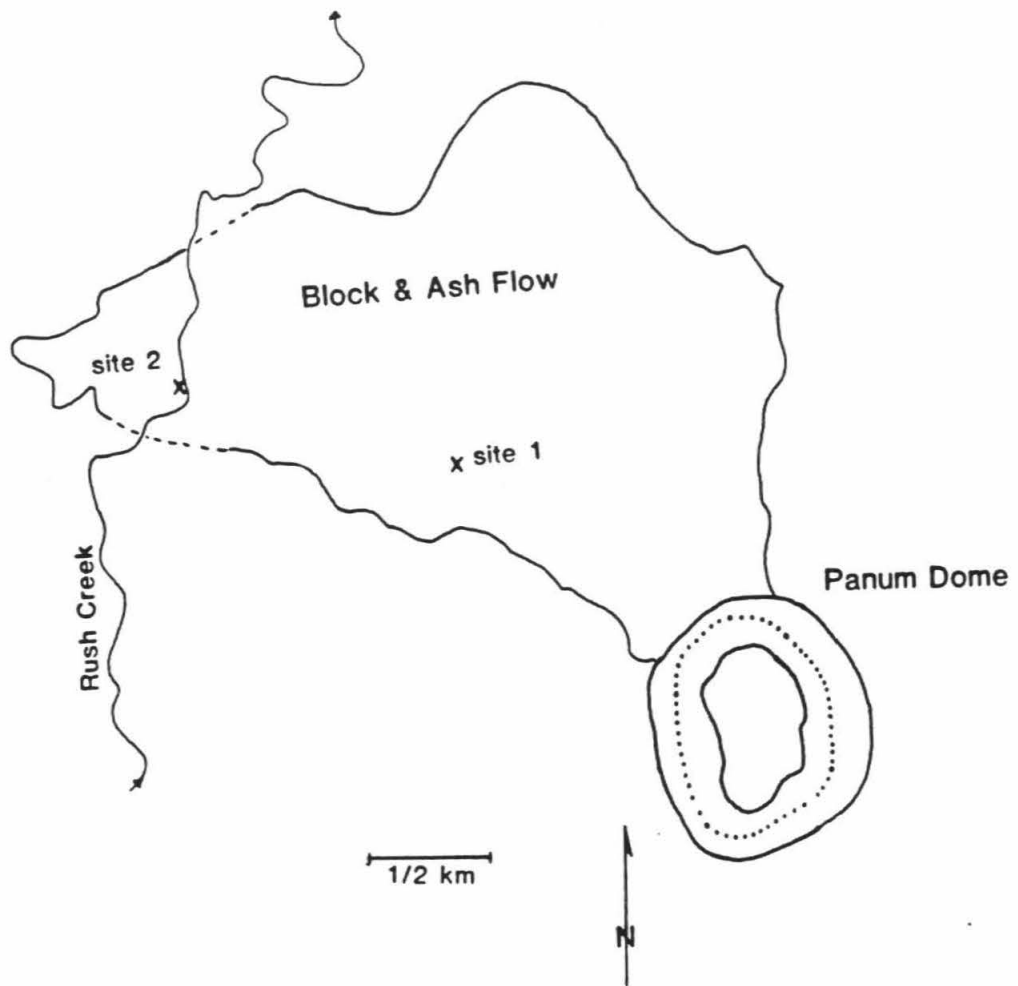


Figure 2
Map of Panum Dome and the associated block-and-ash flow showing the sampling sites. (adapted from Sieh and Bursik, 1986)

heterogeneous, unsorted mixture of three distinct types of clasts--lithic, pumiceous and obsidian blocks. The majority of the clasts at this locality are dense gray, glassy "lithic" blocks ranging in size from a few centimeters to a few meters. These clasts are angular and most are non-pumicious. The surfaces of these clasts are commonly pink, but show white powder marks that Sieh and Bursik (1986) interpret to be percussion marks from impact with other clasts during transport. These observations demonstrate that the lithic blocks were solid at the time of their creation, probably during their creation by fragmentation of a cryptodome or exogenous dome in Panum Crater.

About 10% of the clasts are highly vesicular pumiceous blocks with breadcrusted surficial textures. They range in size from a centimeter to a meter across. The surfaces are rounded and commonly contain embedded lapilli of the lithic material. In addition, these clasts are occasionally molded around larger lithic clasts. Clearly the pumiceous clasts were still molten and gaseous at the time of their creation.

At site two, about 2.5 km from Panum Crater, Rush creek has incised 2 meters into the flow deposit. At this locality the flow is composed principally of rounded 1- to 20cm pumicious clasts in an ashy matrix. Vertical degassing pipes occur throughout the flow deposit and the upper meter of the flow is pinkish in color. A thicket of charred brush rests beneath and within the lower several centimeters of the deposit. These observations indicate abrasion of

solidified pumiceous clasts during transport, but a high emplacement temperature for the deposit.

The blocky nature of the flow deposit at site one indicates that it is the comminuted remains of a dome that resided within Panum Crater prior to the emplacement of the dome that now resides there. The lithic blocks represent degassed, solidified portions of the cooling dome. The breadcrusted pumice originated as hotter and more fluid material, probably deeper within the dome. The dome may have been an exogenous feature, similar to present Panum Dome, that suffered sudden collapse or explosive disintegration. Alternatively, it may have been a cryptodome, deeper within the crater or vent, that was comminuted into blocks by an explosion.

The Problem

Field evidence indicates that the pumiceous blocks at site 1 solidified after emplacement in the flow deposit. I anticipated, therefore, that paleomagnetic directions of samples from these blocks would be tightly clustered and would represent the direction of the magnetic field at the time of the eruption. The abraded nature of the pumiceous clasts at site 2 suggest they were solid during transport, but other evidence described above clearly indicated emplacement at high temperatures. We did not know what the paleomagnetic characteristics of these samples might be.

Field evidence suggested that the lithic blocks at site

1 were solid during transport. Therefore, we expected magnetic directions to be randomly distributed in all quadrants.

Data Collection and Results

At site 1 I sampled ten blocks of both the pumicious and the lithic blocks. I drilled core samples in the field and trimmed them in the lab before processing. Demagnetization consisted of progressive AF and thermal steps as described in Appendix 1.

As anticipated, the pumice blocks are magnetically stable (figure 3), and seven of the ten sample's high temperature directions cluster very well, with Bingham Kappas of -224.38 and -39.91 and alpha-95 errors of 2.5 and 6 (figure 4). The mean direction of these seven samples is $\text{dec} = 357.7^\circ$ and $\text{inc} = 61.2^\circ$. Two of the three samples whose directions are not used were mis-oriented in the field. The third sample was later shown to be from a block that was not in original emplacement position.

The magnetic behavior of the lithic blocks is not as anticipated. The blocks are magnetically stable, but all show directions in the northern hemisphere and downward. Hence, they had not cooled below 600°C prior to their turbulent transport in the flow.

The lithic blocks display two types of demagnetization paths. The first type, shown in figure 5, has no component of magnetization near the present field direction. Four of

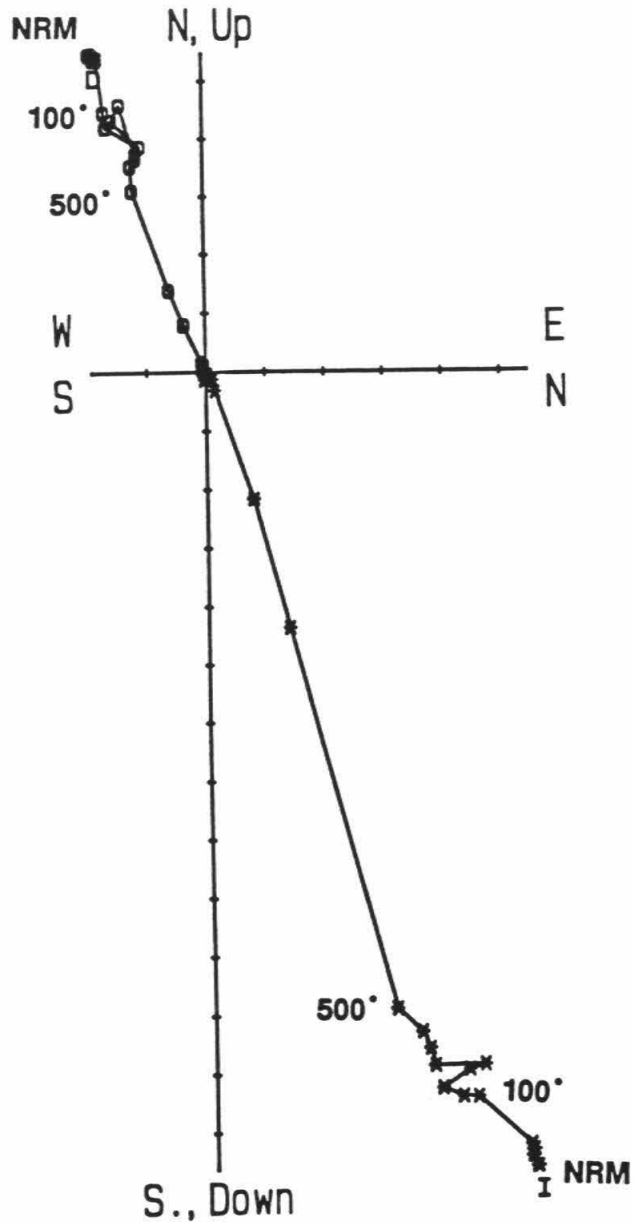


Figure 3

Orthogonal vector demagnetization diagram of a typical sample of breadcrusted pumice. The lower temperature component of magnetization is a viscous component and the very linear high temperature component shows the stability of this sample. One unit on the axes is 10^{-4} emu. Circles are declination, stars are inclination.

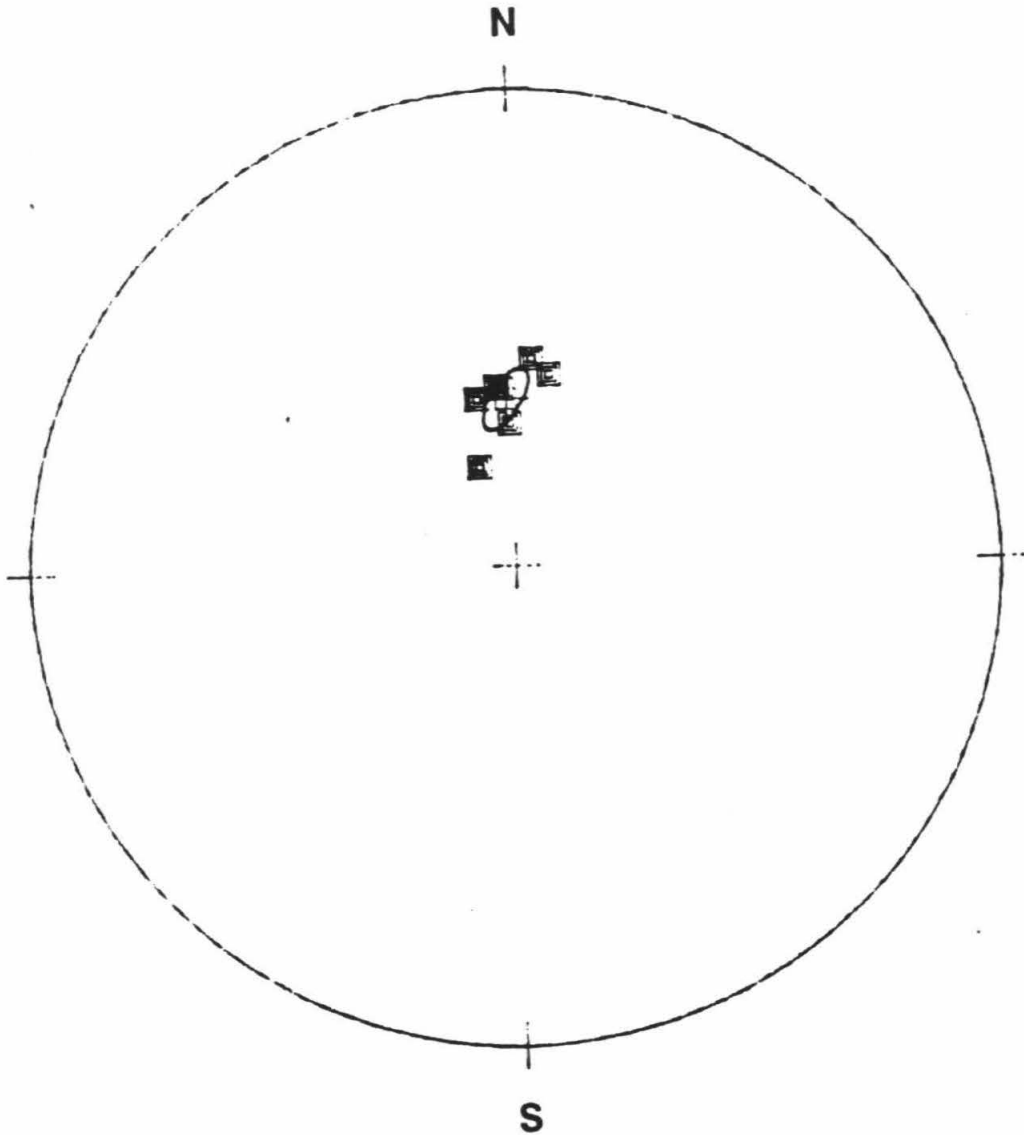


Figure 4

Equal-area plot of the sample directions for seven samples from the breadcrusted pumice. Oval is the Bingham 95% confidence limit on the mean direction.

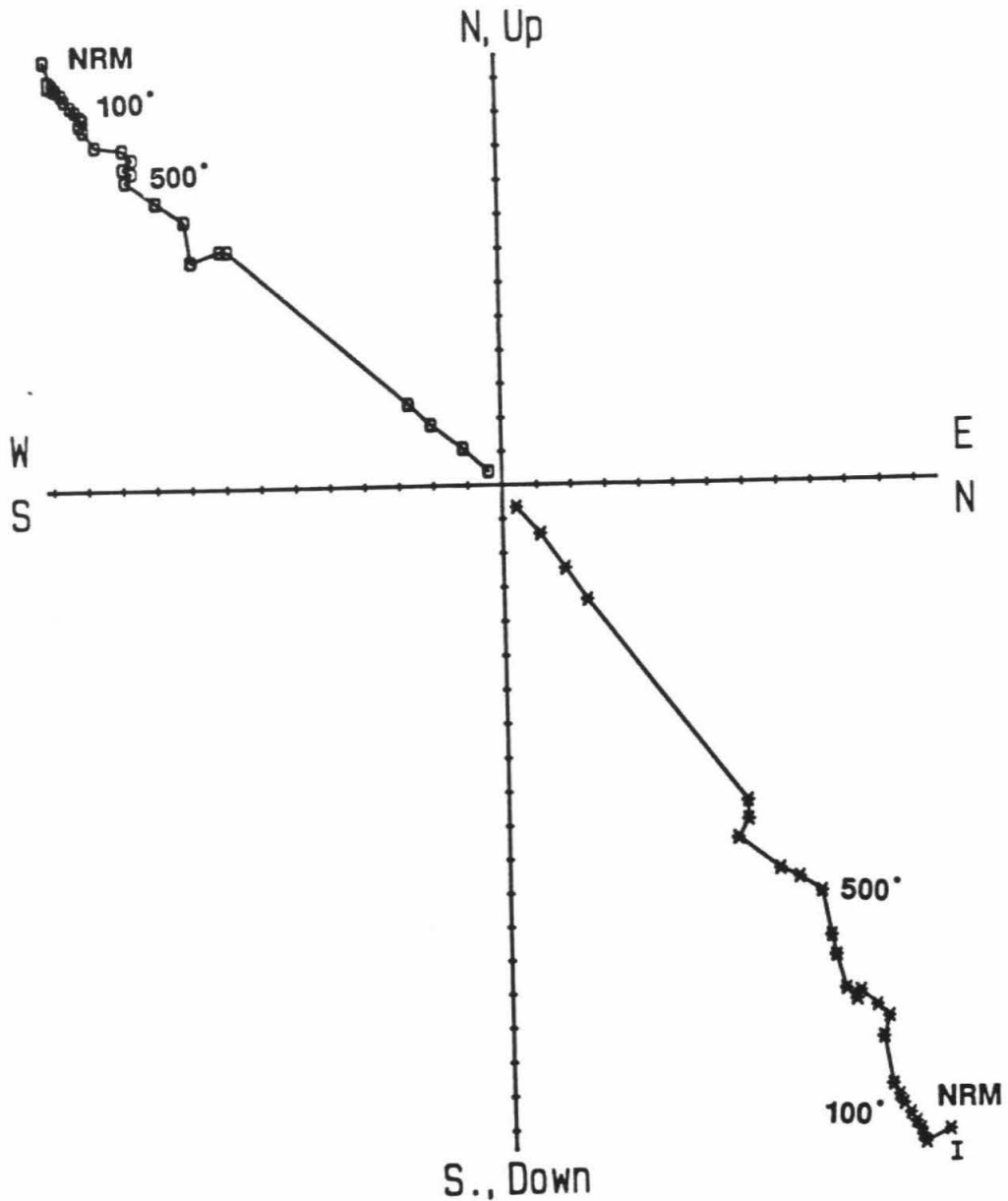


Figure 5

Orthogonal vector demagnetization diagram of a typical sample of a lithic block. Because the lower temperature component of magnetization differs markedly from the present field direction, it is interpreted to be of cooling origin. The very linear high temperature component shows the stability of this sample. One unit on the axes is 10^{-3} emu. Circles are declination, stars are inclination.

the samples show this pattern, or only one component of magnetization. The second type, shown in figure 6, shows at least two components of magnetization and only the lower-temperature components of these samples are coherent. Four samples show this type of behavior. Figure 6a shows the most extreme difference in direction between these two components, whereas figure 6b shows a more typical example. The transition between the two components is at 450° to 500° C. The remaining two samples are too strong to measure with the Caltech SQUID cryogenic magnetometer.

Equal-area plots of the magnetic directions these two types of blocks are shown in figures 7 and 8. The scatter of the incoherent samples (figure 7) is high and significantly greater than that of the pumiceous samples. The scatter of the high temperature component of the two component samples (figure 8a) is also high but the low temperature components cluster very well (figure 8b) with Bingham Kappa's of -6018 and -27.95. The dimensions of the alpha-95 error oval are 0.6 and 9.5 degrees.

At site 2, five samples were taken from pumiceous clasts in the pink upper zone and five more from the lower zone. These are called group one and group two respectively. These were taken as oriented block samples and cores were drilled from them in the lab.

The vector demagnetization paths shown in figure 9 indicate that all of these samples are magnetically stable and show one component of magnetization. The presence of

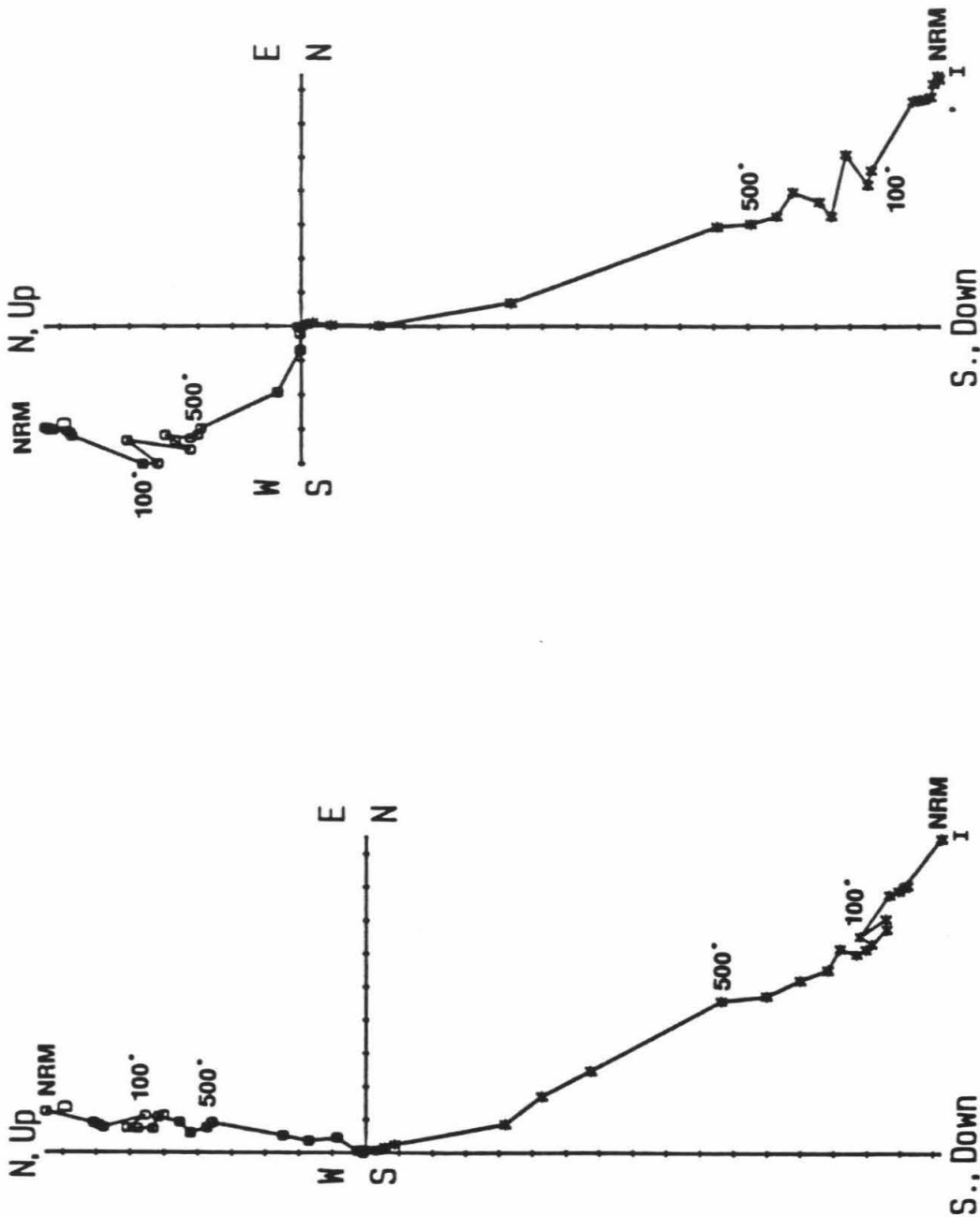


Figure 6

Orthogonal vector demagnetization diagrams showing two component samples with the coherent low temperature direction. (a) shows an extreme difference between the components and (b) shows a typical sample with a small angular difference between the components. One unit on the axes is 10^{-3} emu. Circles are declination, stars are inclination.

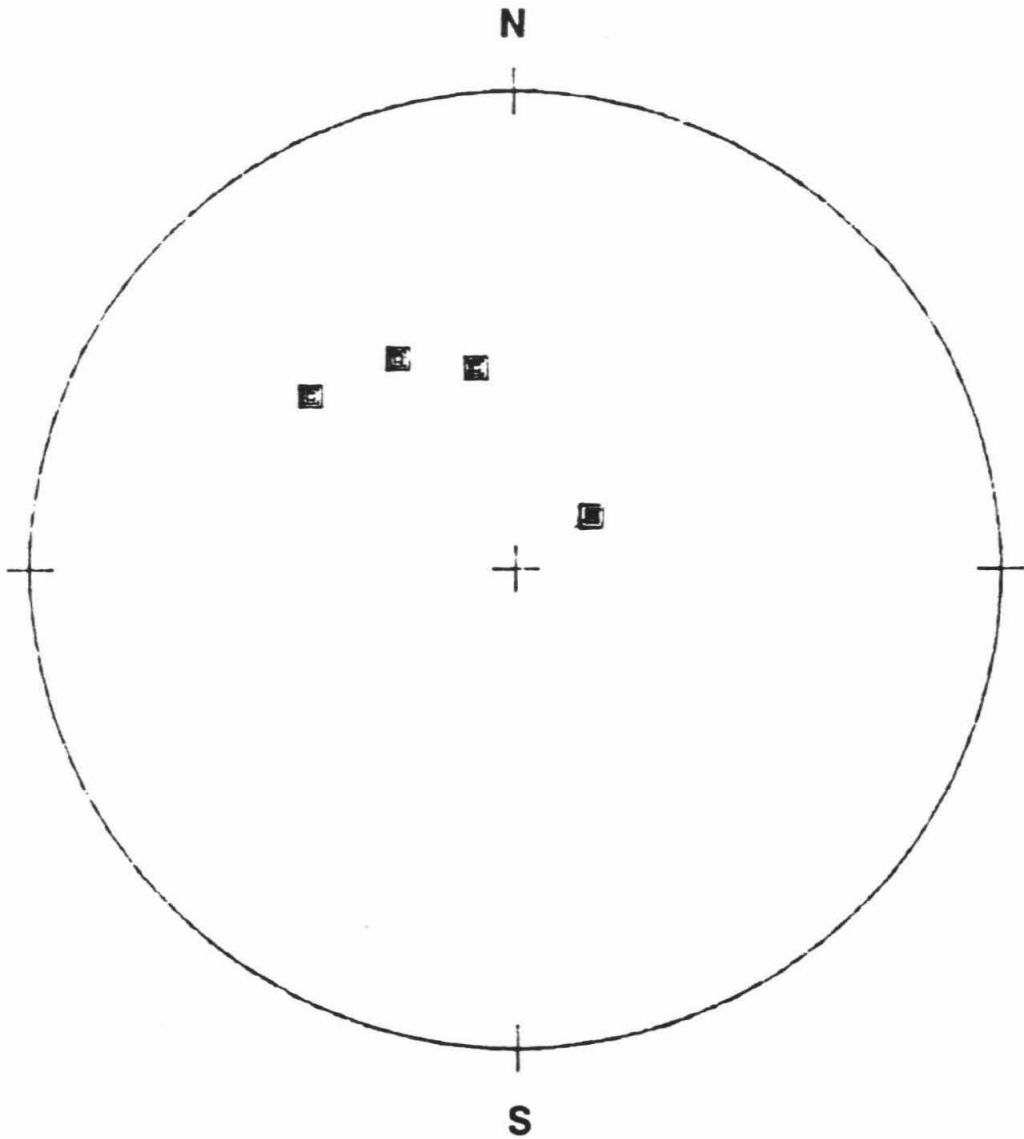


Figure 7

Equal-area plot of the sample directions of the four samples showing one component, or all components away from the pumice direction.

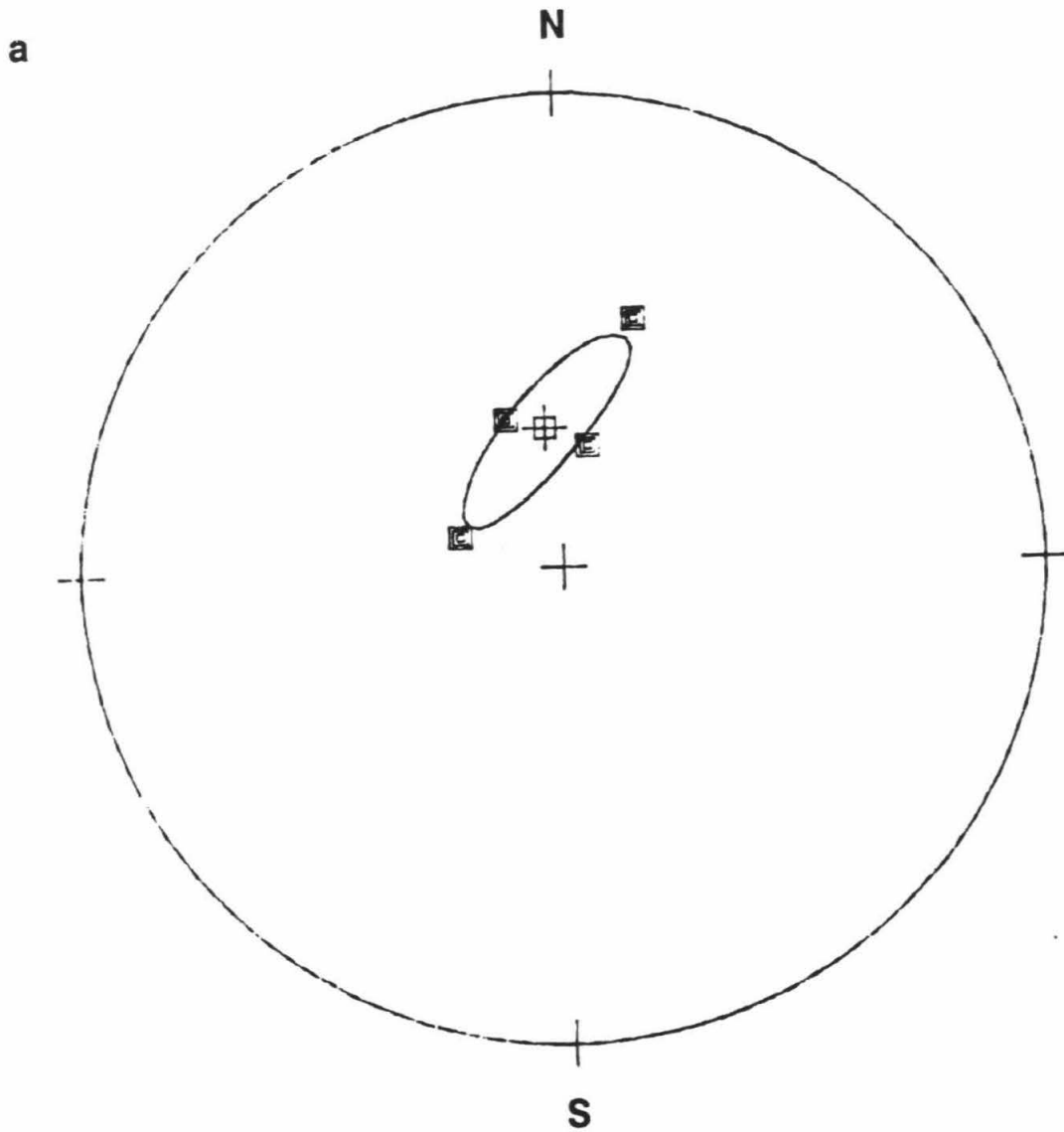
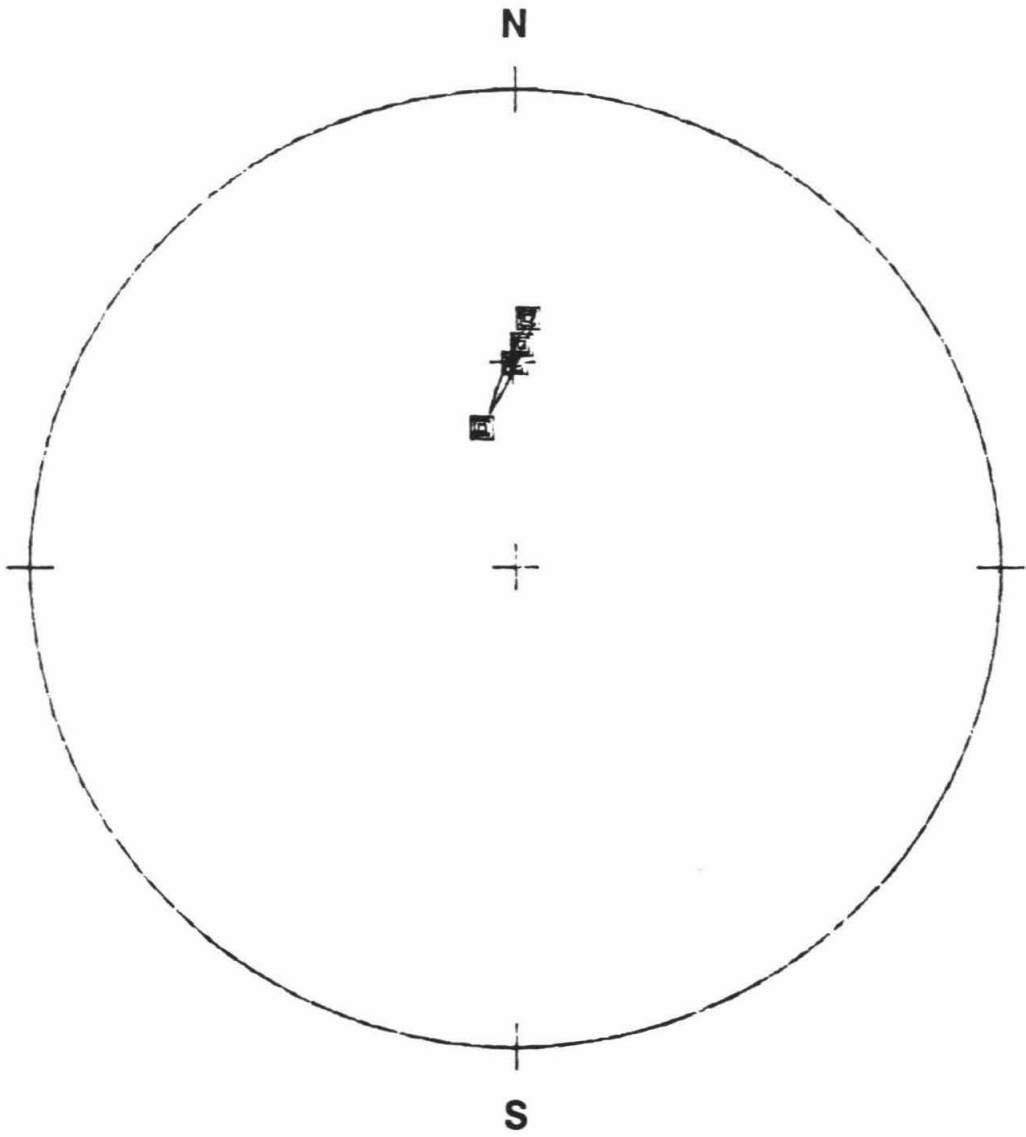


Figure 8

Equal-area plot of (a) the high temperature component directions of the four lithic samples showing two components and (b) the low temperature component directions.

b

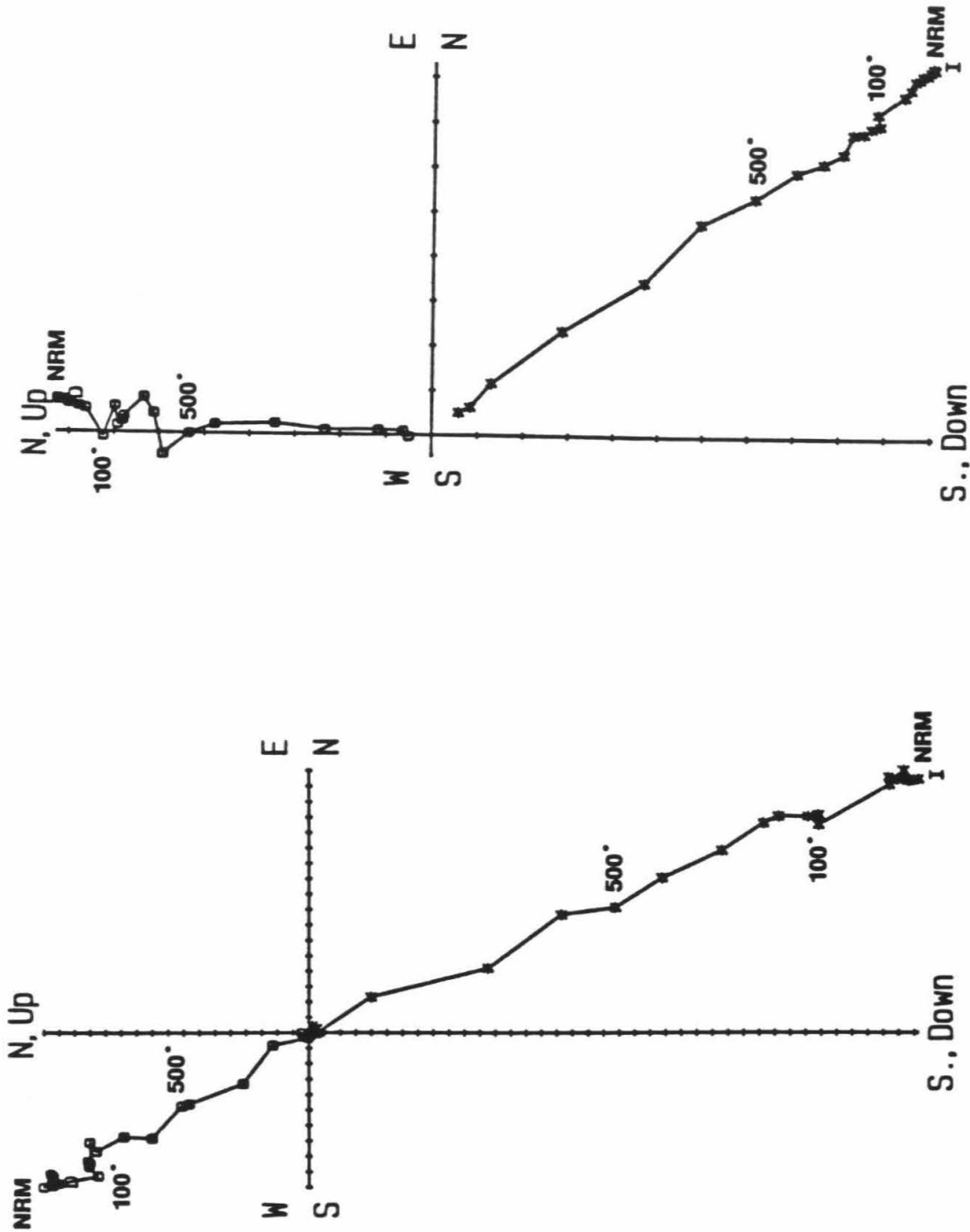


Figure 9

Orthogonal vector demagnetization diagrams of typical samples from site 2. The greater distance from the origin of the group one sample (a) than the group two sample (b) shows the presence of hematite. One unit on the axes is 10^{-4} emu. Circles are declination, stars are inclination.

hematite in group one is indicated by the existence of a noticeable magnetic moment after progressive demagnetization to 610°C. Group two samples have a negligible moment after attainment of 580°C. The Curie Temperature (the temperature at which a mineral loses its ability to hold a magnetic moment) of magnetite is about 570°, whereas the Curie Temperature of hematite is about 660°. Group two samples, therefore, appear to contain no appreciable hematite. Group one samples, however, do appear to contain hematite. This is consistent with the pink color of the upper meter of the flow deposit, from which group one samples were collected.

These samples have only a fair clustering (figure 10) but the mean directions of the two groups are indistinguishable. Group one clusters with Bingham precision parameters of -47.2 and -30.5 and with error oval dimensions of 6.0 and 7.2 degrees. Group two clusters with Bingham precision parameters of -24.23 and -15.72 with error oval dimensions of 9.4 and 11.7.

Discussion

All of the blocks sampled showed magnetic directions north and downward. If the blocks were cool at the time of emplacement, the chances of all of the blocks coming to rest with their magnetic directions in this quadrant would be vanishingly small. The similar magnetic orientation of all the sampled blocks indicates that all were at temperatures above 600° C at the time of emplacement.

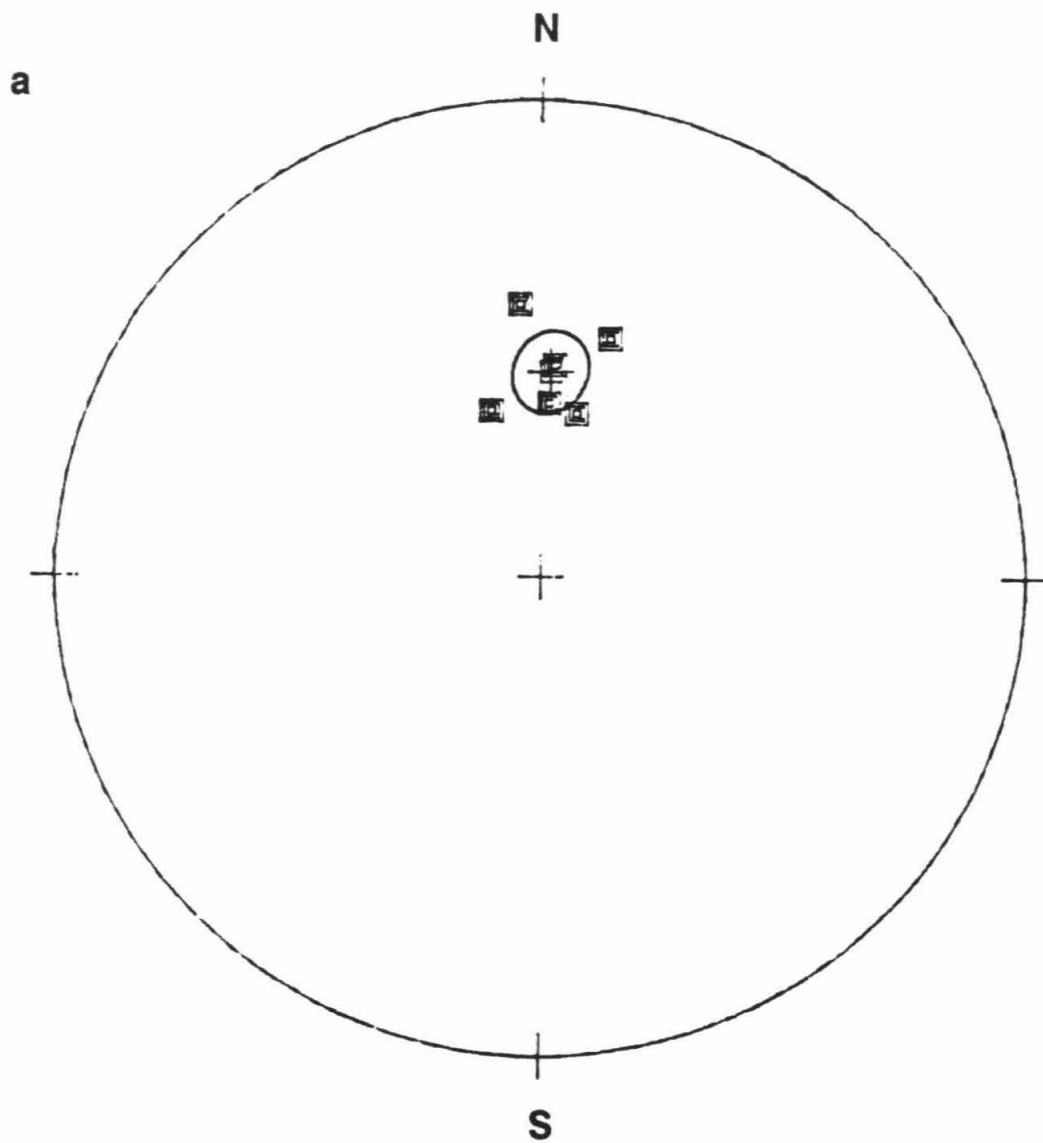
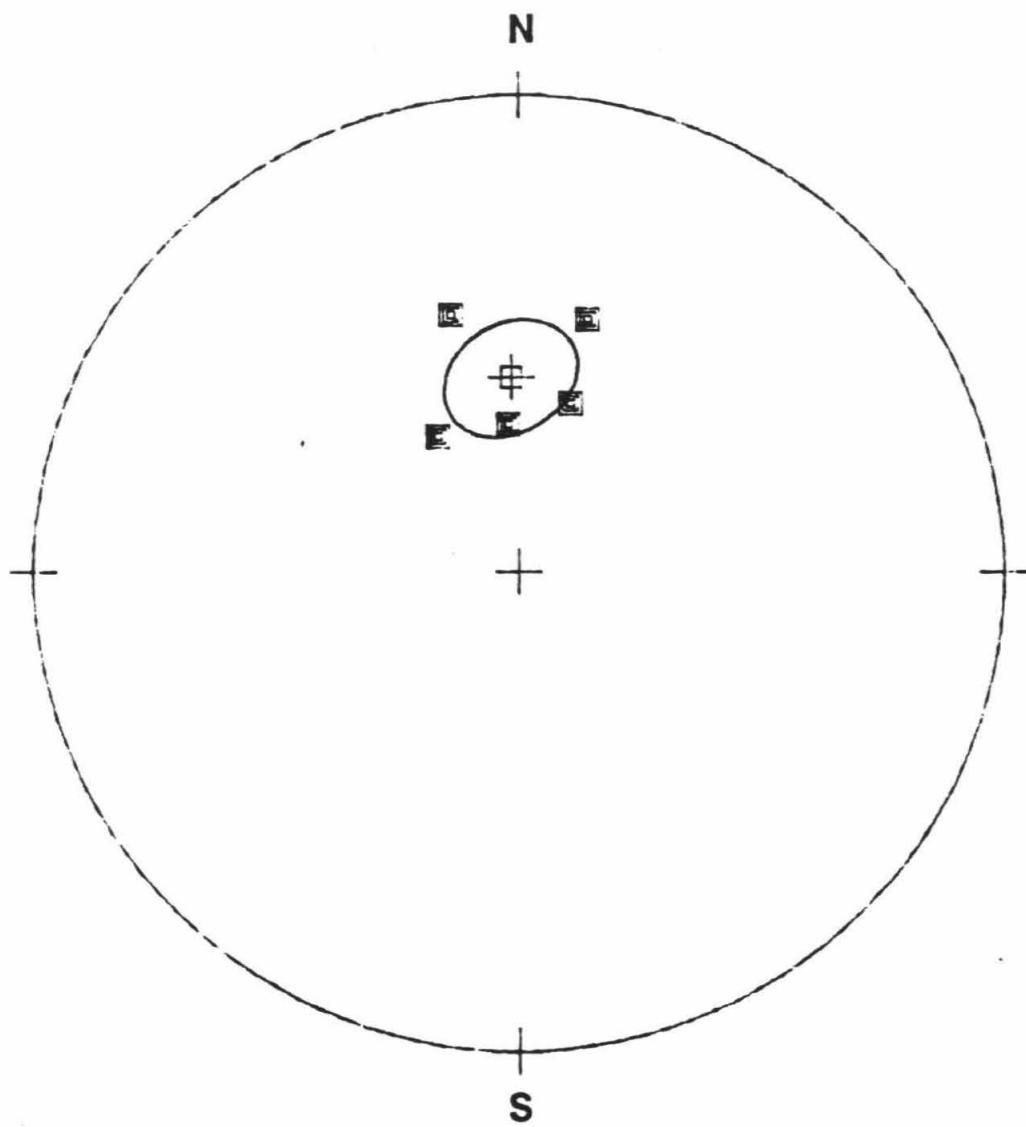


Figure 10
Equal-area plot of sample directions from (a) group one
and (b) group two at site 2.

b

An alternative interpretation is that the coherent magnetic components, being near the average field direction, represents a viscous magnetic direction. However, there are no observable compositional differences between the samples with the coherent components and the samples showing scattered directions. Therefore, it is unlikely with similar samples that some would acquire a viscous component and others would not.

The very good clustering of the breadcrusted pumice at site 1 indicates that these blocks had become physically quite stable before they cooled below 600°C. Likewise, the tight clustering of the lower-temperature component of the two-component lithic samples indicates that these blocks had become physically stable before reaching 450°C. The scatter of the higher-temperature components of these samples, however, suggests that they settled somewhat as they cooled through the 600° to 450°C range. The poor clustering of the one-component lithic samples and samples from site 2 indicates that minor settling occurred after the samples has cooled to a temperature of 150°C.

The confidence ovals of all these disturbed samples overlap the pumice direction (figure 11). Because the mean direction of these blocks agrees with the mean direction of the pumice, I conclude that no systematic physical disruption of the blocks occurred. Instead, the blocks experienced minor random tilting as the flow cooled.

I draw three major conclusions from this interpretation

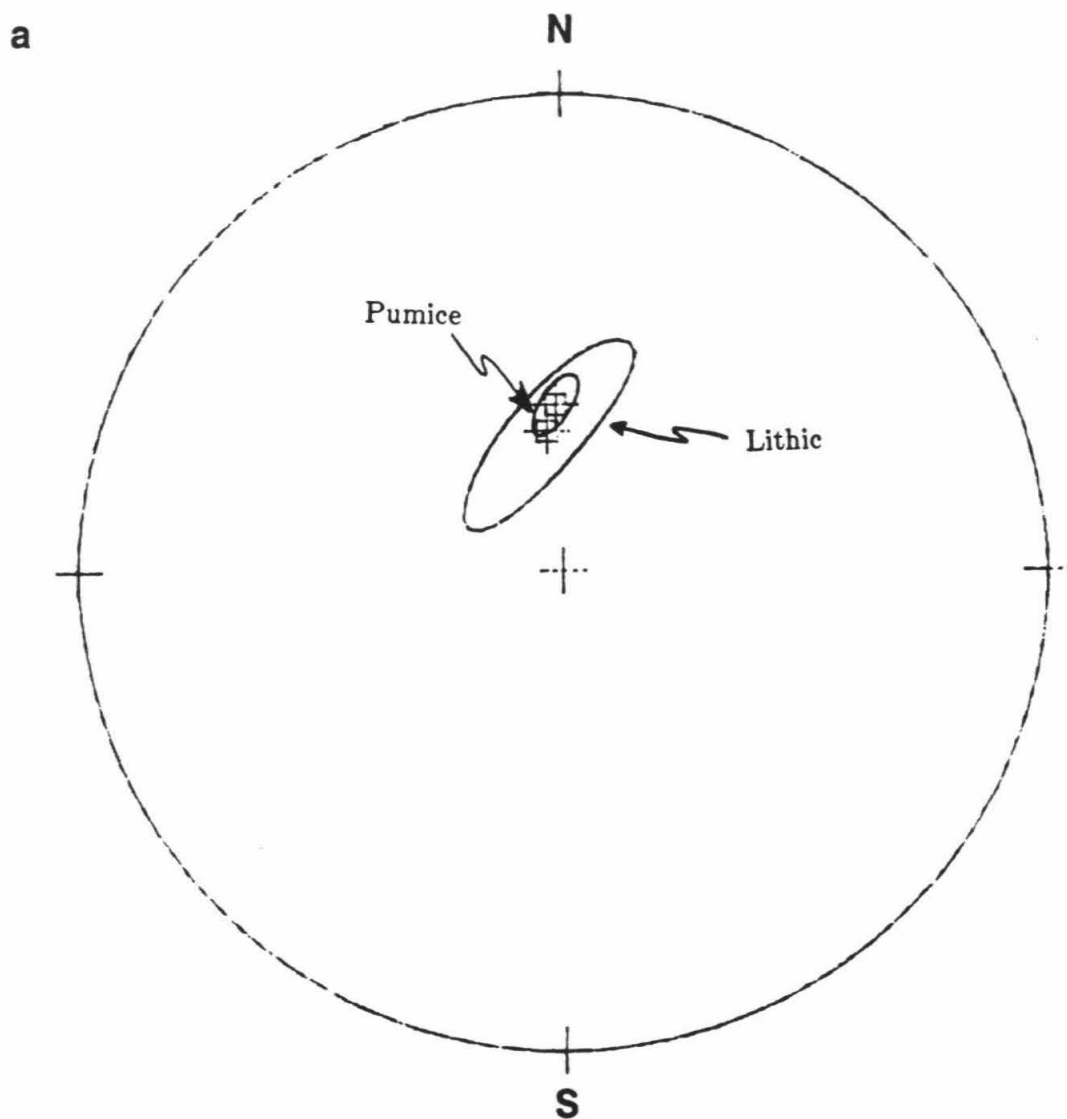
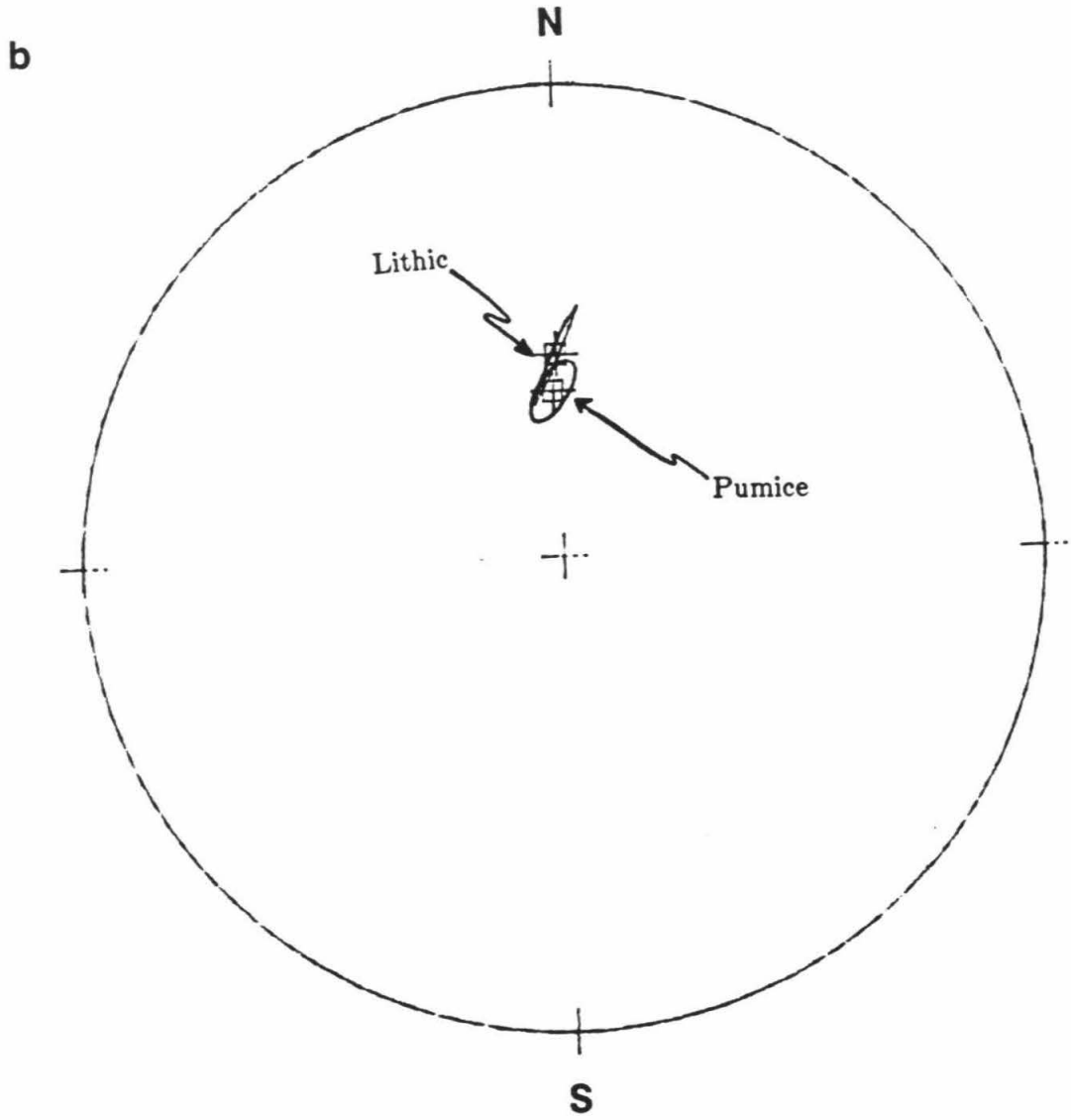
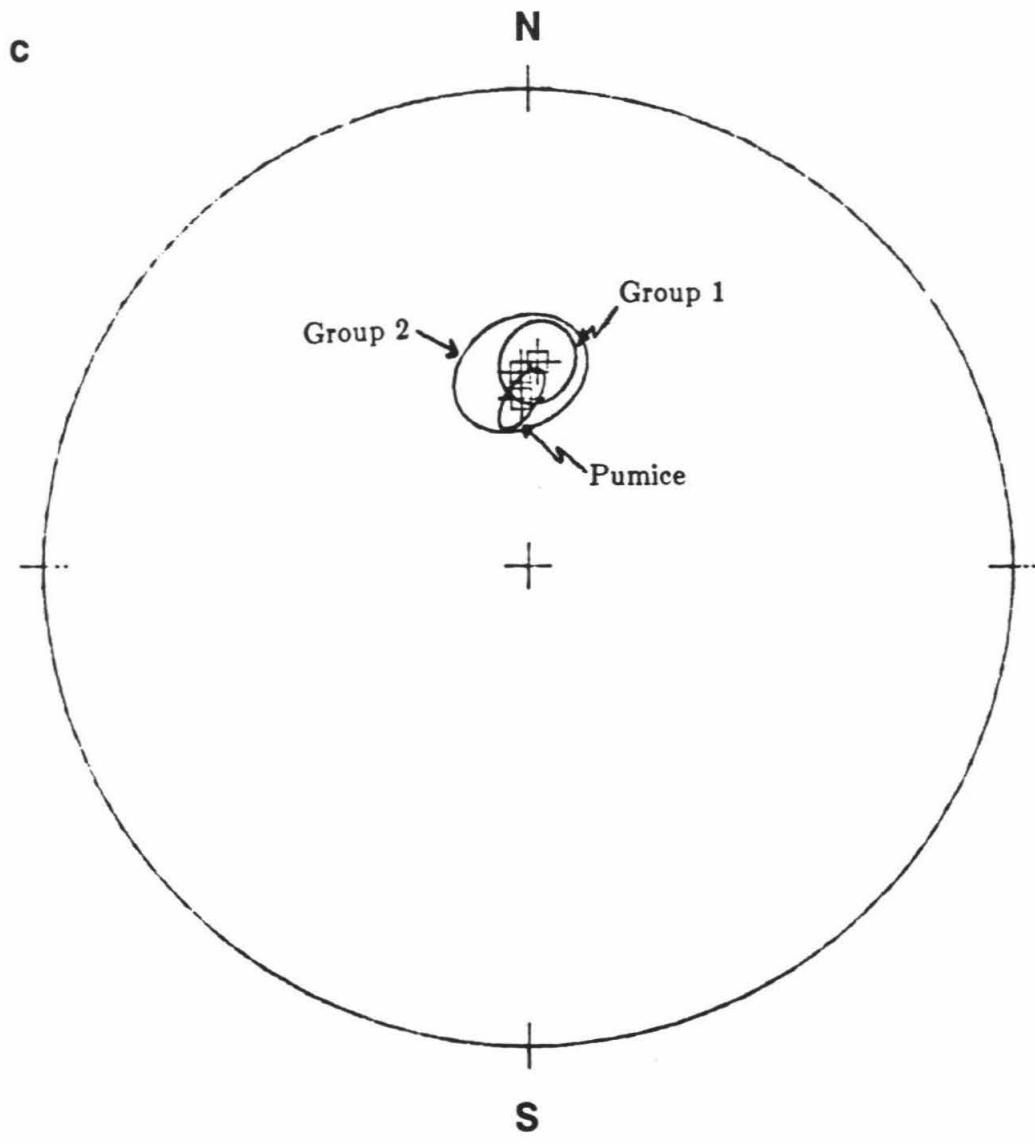


Figure 11

Comparison of means and confidence intervals of (a) low temperature lithic component directions, (b) high temperature component directions, and (c) the samples from site 2, with the pumice direction.





of the data. First, although some of the blocks were solid at the time of collapse, transport and emplacement, all of these blocks were at temperatures $\geq 600^{\circ}$ C. This implies that the dome from which the blocks were derived had not cooled below 600° C prior to its fragmentation by collapse or explosion.

Second, the flow deposit experienced substantial settling following emplacement. For 2 meter diameter blocks to rotate by 10° or more requires significant lack of compaction of the surrounding material. I recognize no correlation of the amount of rotation with the clast size, so the whole flow must have experienced this substantial settling. The results at site two indicate that the rotations during settling were not as large as at site one, but did occur. This is consistent with the greater percentage of ash between large clasts at site 2.

Finally, the clasts were emplaced at different temperatures. If the clasts cooled at similar rates the clasts with scattered directions were at the lowest temperatures at the time of emplacement. Even so, these coolest clasts were emplaced at temperatures greater than 600° C. The blocks showing a coherent low-temperature direction began at a relatively higher temperature, but had cooled to 450° C by the time the scattered direction clasts were less than 100° C. Finally, the breadcrusted pumice blocks were still soft at the time of emplacement (probably between 700° and 900° C, depending on the water content

[Ehlers and Blatt, 1982]) and had not cooled below 600°C when the lithic blocks had reached 500°C.